Towards Thick Battery Electrodes and Interdigitated Cell Architectures Via Micro-structured Carbon Nanotube Forests

by

Richard Bertram Church

B. Eng, McGill University (2016)
M. Eng, McGill University (2018)

Submitted to the Department of Materials Science and Engineering in partial fulfillment of the requirements of the degree of

Doctorate of Philosophy

at the

MASSACHUSETTS INSTITUTE OF TECHNOLOGY

September 2023

Authored By: Richard Bertram Church
Department of Materials Science and Engineering
August 18, 2023

Certified by: Anastasios John Hart
Professor of Mechanical Engineering
Thesis Supervisor

Certified by: Carl V. Thompson
Professor of Materials Science and Engineering
Thesis Reader

Accepted by: Robert J. Macfarlane
Associate Professor of Materials Science and Engineering
Chair of the Departmental Committee on Graduate Studies

THIS PAGE IS LEFT INTENTIONALLY BLANK

Towards Thick Battery Electrodes and Interdigitated Cell Architectures Via Micro-structured Carbon Nanotube Forests

by

Richard Bertram Church

Submitted to the Department of Materials Science and Engineering on August 18, 2023 in partial
fulfillment of the requirements for the degree of Doctorate of Philosophy

Abstract

The growing demand for electric vehicles and portable electronics has created a significant interest in the scalability, recyclability, and economics of both traditional and emerging battery technologies. Although lithium-ion batteries (LiB) are approaching their theoretical energy density they will remain a widespread and promising technology as alternative (e.g., Li-metal) chemistries and solid-state architectures are still in relatively early stages of commercial scale-up. In the meantime, LiB performance can be improved by redesigning the cell geometry to incorporate thick 3D electrodes. Using thick electrodes increases the cell level energy density by minimizing the volume and mass contributions of inactive components, including the current collectors and separator. However, batteries with thick planar electrodes suffer from capacity limitations due to increased mechanical fatigue, Li-ion diffusion distances, and tortuosity. 3D electrode designs compensate for this weakness by providing micro-scale channels within the electrode to enable rapid charge transport and accommodate active material expansion. To meet these criteria, the materials used in 3D electrodes must be mechanically robust, electrically conductive, and processable in a manner enabling precise control over geometry and porosity.

In this thesis we first develop thick 3D “honeycomb” battery electrodes using patterned, vertically aligned carbon nanotubes (VA-CNTs) on metal foils as current collectors. We translate insights from CNT growth on silicon wafer substrates to grow CNT forests over 250 μm tall on thin metal foils (Cu) that are suitable for electrode fabrication. Thick electrodes are then created by coating CNT forests with Si thin films by low pressure chemical vapor deposition. Half-cells using monolithic and honeycomb patterned Si-CNT electrodes were cycled over a range of current densities, demonstrating the electronic connection between the deposited Si and Cu foil via the aligned CNTs. The honeycomb electrodes exhibit large gravimetric (~1750 mAh/g_{Si}) and areal (~20 mAh/cm^2) capacities, and exhibit reduced capacity fading when compared to non-patterned electrodes.

Next, the Si-CNT composites are investigated as a template for a 3D full cell design, Geometrically, compared to a planar electrode of a given energy density, the decreased diffusion distance of a 3D cell results in an improvement in power density, thereby decoupling the inherent tradeoff between the energy density and power density that is experienced by planar cells. The difficulty of producing 3D full cells comes from the need to produce high conformality electrolyte films that are pinhole free and which demonstrate sufficient ionic conductivity. To address this issue, we utilize an initiated chemical vapor deposition (iCVD) process to deposit conformal poly(hydroxyethyl methacrylate-*co*-ethylene glycol diacrylate) thin films on to the patterned Si-

CNT composites. Doping these copolymer films with lithium salts results in ionic conductivities on the order of ~10^{-5} S/cm, which is among the highest conductivities exhibited by conformal electrolyte technologies. To complete a full battery cell, a slurry-based cathode is infiltrated into the iCVD coated Si-CNT composite electrode. These cells are then soaked in a liquid electrolyte and cycled to demonstrate the first-time use of an iCVD polymer electrolyte in a full cell and a proof-of-concept CNT-based 3D full cell. Lastly, a 2D finite element simulation is presented to predict the theoretical energy and power densities of idealized interdigitated CNT-based full cells.

Thesis Supervisor: Anastasios John Hart

Title: Department Head, Professor of Mechanical Engineering; Director, Laboratory for Manufacturing and Productivity; Director, Center for Advanced Production Technologies

THIS PAGE IS LEFT INTENTIONALLY BLANK

Acknowledgements

I need to start by thanking my advisor, Professor A. John Hart, for all of his help and support over the last five years. It has been a wonderful experience to work for you and I truly appreciate all of your advice, mentorship, sports discussions and constant optimism during the difficult portions of the project. Thank you for teaching me to think big! I would also like to thank all the members of the Mechanosynthesis Lab, particularly those who were members of the CNT/Comp/Print cluster, for making my time in the lab enjoyable. It was a pleasure to work with all of you. Specifically, I would like to thank:

- Dr. Bethany Lettiere for providing me with a solid experimental foundation, always being available to trouble shoot CNT growth and that damn sputerererer and, most importantly, your friendship, the regular goodies left on my desk and understanding that batteries are hard.
- Dr. Cécile Chazot for your continuous technical advice on all things materials processing and characterization, and for performing the TGA experiments in Chapter 2. More importantly for every lunch outside Building 35, Flour coffee, softball game, turkey gang sighting, Quals fairy visit and photo of Korra.
- Dr. Kaihao Zhang for acquiring the CNT Raman spectroscopy data in Chapter 2.
- Michael Durso for our regular office chats, acquiring the Si-CNT Raman spectroscopy data in Chapter 2 and the FTIR data in Chapter 4.
- Olek Perarie for machining the shadow masks and some Swagelok cell components used in Chapter 2.
- Will Sawyer for your help in the machine shop and the always interesting discussions about CNT growth (or lack thereof).
- Michael Arnold for help keeping the 418B glovebox running.
- Ryan Penny for the Bruins talk while I was stuck in the glovebox.
- Christine Jacob for training, calibration and maintenance on Gaia.
- Ji-Hun Jeong for drastically improving the efficiency of the Cu foil patterning process utilized in Chapter 2.
- Jon-Edward Stokes and Tobi Majekodunmi for the COMSOL simulations in Chapter 5. It was a pleasure to mentor you, thank you for making my time in MICRO so rewarding.
- Dr. Ulrich Muecke for your help brainstorming in the initial phases of the project, when I knew almost nothing about batteries.
- Justin Silva for always taking care of everything that needed to be taken care of and allowing me to focus on my work.

I would like to thank my committee members for their time and support during my time at MIT. To Professor Carl Thompson for the helpful discussion when the CNTs simply would not grow and on all things CVD related. To Professor Jennifer Rupp for helping make sure the literature review in Chapter 3 was as complete as possible and to your lab members, Dr. Lingping Kong and Sara Sand, for performing and helping analyze the EIS measurements in Chapter 4. Lastly, to Professor Betar Gallant and Dr. Haining Gao, for your valuable help that started with cell assembly and went all the way to data evaluation as co-authors on the manuscript that makes

up Chapter 2; I am grateful of all of your time as project would not have been possible without your help. A second thank you to Dr. Gao for assembling the coin cells tested in Chapter 2.

I also need to thank the other MIT community members who made my time here productive and enjoyable. To my PPSM colleagues Dr. Michael Stolberg and Dr. Somesh Mohapatra, for their help preparing for the qualifying exams and for their friendship after quals were done. To Cole Fincher and Yukio Cho for valuable discussion on cell performance and for making their potentiostat available when our equipment would not suffice. To Professor Karen Gleason and Dr. Maxwell Robinson for their help with the iCVD work in Chapter 4. In particular to Dr. Robinson for his help coming up with the recipes, including running the PHEMA deposition, used in Chapter 4 and his substantial efforts in training me to ensure a smooth transition of the Altus iCVD reactor to our stewardship. I would also like to thank Amy Tatem-Bannister and Donna Johnson for their help managing the iCVD reactor space at the ISN.

A very special thank you to the MTL and MIT.nano staff for accommodating all my unusual material requests. To Dave Terry and Dennis Ward for your help with photolithography. To Gary Riggott and Kurt Broderick for your mechanical support trouble shooting the old EML Plasmatherm. To Nicole Bohn for your help with all things XRM. To Dr. Jorg Scholvin and Eric Lim, thank you for keeping the LPCVD tubes in TRL open as long as you did, and to Eric for performing the Chapter 2 LPCVD Si depositions. Your efforts greatly improved our electrode performance.

Thank you to the organizations which provided the funding that supported this work. This thesis was primarily supported by Automobili Lamborghini. Thank you to Stefan Nothdurfter for your belief in the project and interest in the fundamental science behind it. Additional funding was provided by the Natural Sciences and Engineering Research Council of Canada (NSERC), the MIT Portugal Program (MPP2030), the Advanced Research Project Agency-Energy (ARPA-E) and Alberta Student Aid.

Thank you to my support network outside of MIT. To Professor Marta Cerruti and Dr. Kaiwen Hu for your mentorship and helping me develop many of the technical and analytical skills that were put to use on this project. To Dr. Julion Marrinan for the tools to effectively manage my stress and focus on what mattered. To Brittany and Alyssa Kelley, Derek Aranguren and Jonny Craske, for your friendship and love. To Aunt Eileen for always being there to listen, providing Sophia and I with the occasional getaway, and for taking a genuine interest in my work. To Uncle Ron and Aunt Cindy for your lifelong support and interest in both my school work and hobbies.

To Great Grandma Church for understanding the importance of an education, even one from an American school, and for your support in pursuit of that education.

To Phil, Tracey, Babette and Lilith, thank you for everything that you do for me, in particular for the swift evacuation and hospitality during the COVID-19 shutdown, and making me feel like a member of your family.

Thank you, Mom and Dad, for your love, belief in me and enabling all the opportunities that led me to where I am today. Elizabeth, thank you for letting me finish my education first (despite my nearly blowing a two-and-a-half-year head start).

Finally, to Sophia, thank you for all the love.

THIS PAGE IS LEFT INTENTIONALLY BLANK

Table of Contents

Table of Figures

Table of Tables

THIS PAGE IS LEFT INTENTIONALLY BLANK

Chapter 1- Introduction

1.1 Lithium-Ion Batteries: Interest and State of the Art

Today's society faces a challenging issue in meeting the world's increasing energy demands in a sustainable and efficient manner. The current energy economy is largely dependent on fossil fuels, which are non-renewable and have significant concerns over their negative effect on environmental issues, such as climate change and air pollution [1]. While clean energy sources, such as solar and wind, have seen significant development over recent years a significant hurdle is the efficient integration of energy storage for transportation and small-scale personal devices [1], [2]. Electrochemical energy storage in rechargeable batteries has emerged as a feasible solution, and has seen significant research in the market for portable electronic devices (cell phones, laptops, tablets, etc.) and in electric vehicle (EV) development [1], [2]. Similarly, the developmental surge in microelectromechanical (MEMS) circuits has created a niche for thin film micro batteries that are < 10 μm thick to power these autonomous microsystems, with applications ranging from medical implants to sensing and communication [3], [4].

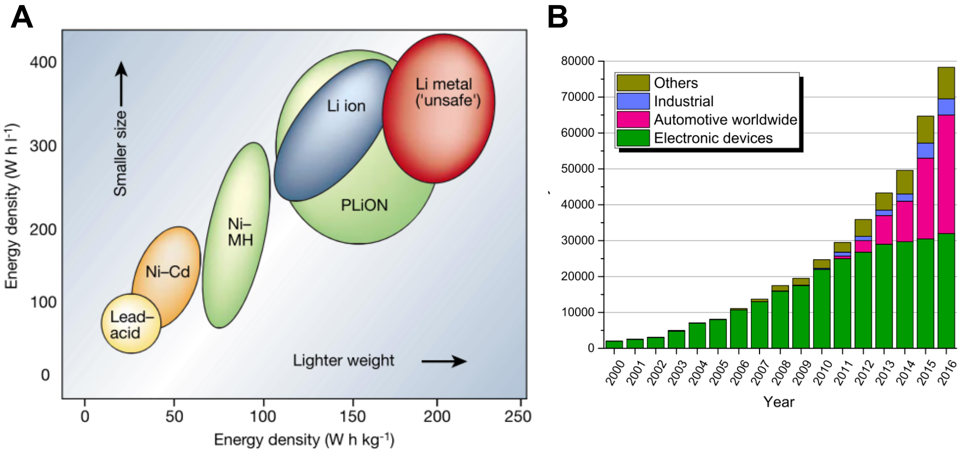

Figure 1.1: A) Specific and volumetric energy density comparisons for various battery technologies. Reproduced with permission [2]. Copyright 2001, Springer Nature. B) LiB cell level sales from 2000 to 2016. Reproduced with permission [1]. Copyright 2017, Springer Nature.

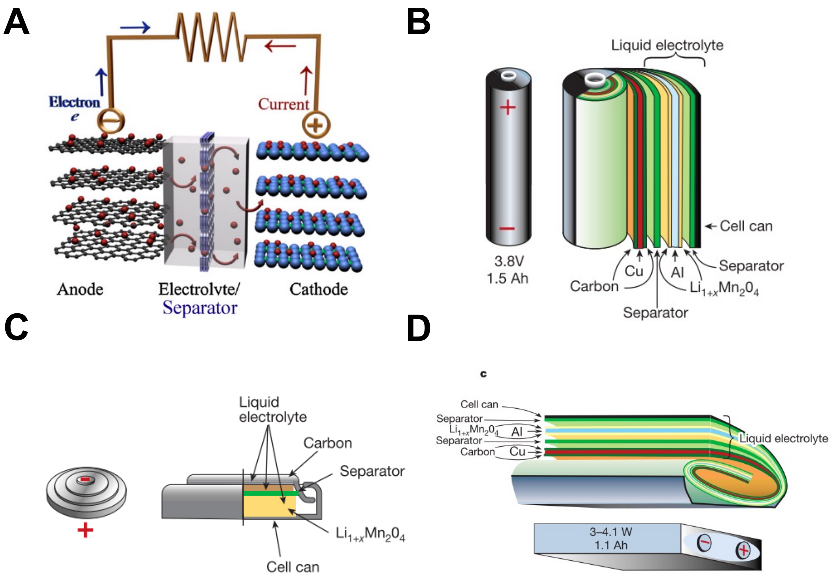

Figure 1.2: A) Schematic representation of a LiB cell with graphite anode and $LiCoO_2$ cathode. Reproduced with permission [5]. Copyright 2011, Elsevier. Schematics showing various LiB configurations such as B) cylindrical, C) coin and D) prismatic. Reproduced with permission [2]. Copyright 2001, Springer Nature.

The amount of electrical energy per unit weight (specific energy density, Wh kg^{-1}) or per unit volume (volumetric energy density, Wh L^{-1}) is an important characteristic in determining battery suitability for powering devices and is determined by the cell potential (V), active material capacity (mAh kg^{-1}) and active material amount [2]. Figure 1.1A compares the energy densities of various electrochemical storage chemistries that were available as the global society started to become more mobile and information-rich in 2001. In the 20 years since, the development and implementation of these different chemistries has been a product of their associated energy densities, with one technology emerging as a favorite. Of the technologies in Figure 1.1A, Pb-acid (20-40 Wh kg^{-1}), Ni-Cd (20-50 Wh kg^{-1}) and Ni-Metal Hydride (Ni-MH, 70-100 Wh kg^{-1}) see limited use [1], [2]. For example Pb-acid systems are restricted mainly to ignition in automobiles and Ni-Cd are used in high-power applications like power tools [2]. Due to their high energy density Li-based batteries are seen as superior to these other electrochemical systems, Figure 1.1B shows the significant increase in LiB sale between 2000 and 2016 that resulted from the creation of additional markets in personal electronics and EV [1]. Today LiB account for ~63% of worldwide battery sales and have an estimated $213.5 billion global market [6].

Table 1.1: Components and approximate make-up for commercially available LiB cell.

Active Battery Components	**Thickness (µm)**	
Positive electrode	~20-85	
Material	**Charge Capacity (mAh g^{-1})**	**Electrode Weight Percent (%)**
Transition metal oxide (e.g., LCO, NCA or NMC)	~125-225	~80-90
Conductive additive (e.g., carbon black) and binder (e.g., polyvinylidene fluoride (PVDF))	0	~10-20
Negative electrode	~20-65	
Material	**Charge Capacity (mAh g^{-1})**	**Electrode Weight Percent (%)**
Graphite	372	~90-95
Si	3600	~0-5
Binder (e.g., PVDF)	0	~5
Inactive Battery Components		
Material	**Charge Capacity (mAh g^{-1})**	**Thickness (µm)**
Organic solvent electrolyte (e.g., 1 M LiPF$_6$ in 1:1 ethylene carbonate:dimethyl carbonate)	0	-
Separator (e.g., polyethylene or polypropylene)	0	25
Negative electrode current collector (Cu)	0	9
Positive electrode current collector (Al)	0	15

A typical LiB cell (Figure 1.2A), is comprised of a porous graphite negative electrode and porous $LiCoO_2$ (LCO), or other transition metal oxide ($LiNi_xCo_yAl_zO_2$-NCA or $LiNi_xMn_yCo_zO_2$-NMC), positive electrode infiltrated by a liquid organic electrolyte and separated by a separator membrane [1], [5], [7], [8]. In order to maintain electrical and mechanical integrity the active materials in each electrode are supplemented with conductive additives and organic binders. The negative and positive electrodes are connected to current collectors to complete the circuit [7]. A breakdown of typical LiB composition and dimensions are available in Table 1.1. During discharge electrical power is generated when Li^+ ions, via the electrolyte, and electrons, via the external circuit, spontaneously move from the negative to positive electrode. During charging, this process is reversed by an applied external voltage. The voltage across the cell is determined by the active materials used and is typically in the ~3.5-3.8 V range for commercial LiB [1], [2], [6], [8]. Typical commercial LiB cells (Figure 1.2B through D) are made by slurry casting the active materials onto metal foils and then rolling or folding the layers into the desired geometry [2], [7]. These designs are inexpensive to manufacture and a state-of the art cell (Samsung ICR18650-32A $LiCoO_2$) has an energy density of approximately 270 Wh kg^{-1} (~720 Wh L^{-1}) at the cellular level and is rated for 300 cycles [7], [9].

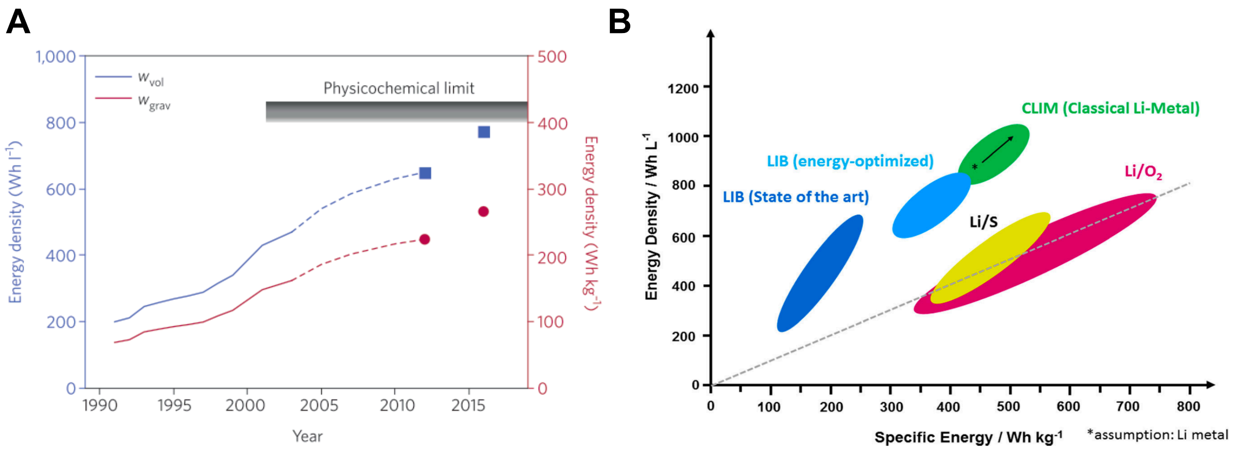

Figure 1.3: A) Energy density of standard LiB from 1990 to 2015. Reproduced with permission [10]. Copyright 2016, Springer Nature. B) Updated 2017 comparison of volumetric and specific energy densities for various Li-based battery technologies. Reproduced with permission [1]. Copyright 2017, Springer Nature.

1.2 Issues Limiting LiB Implementation and Performance

Due in large part to materials development and innovation, the specific (~80 → ~300 Wh kg^{-1}) and volumetric (~200 → ~700 Wh L^{-1}) LiB energy densities have tripled since the initial LiB production by Sony in the early 1990's [1]. Despite this impressive improvement, the current LiB configuration is close to reaching its theoretical maximum energy densities (Figure 1.3A) [1], [6], [7]. Despite having a larger capacity compared to other electrochemical systems, LiB have historically had difficulty keep up with the increased energy demands in both the EV and microbattery fields. While modern EVs have mostly overcome the "range anxiety" of previous models, and there numerous EVs with a range over 200 miles on a single charge, the energy density of LiB still lacks far behind conventional fossil fuel sources [7], [11]–[13]. To address these problems the United States Advanced Battery Consortium set a goal to achieve 350 Wh kg^{-1} specific energy density and 300 W kg^{-1} peak specific power at the cellular level by 2020 [14]. It should be noted that this goal does not include other aspects required for system level integration, such as packaging, controls and thermal management. Outside of EV, LiB also have difficulty meeting applications that require high energy and power storage density due to their small size. This includes medical implants, microsensors and micro-electromechanical systems (MEMS) [3], [4]. These devices require rechargeable batteries where all components are compacted into a 1-10 mm^3 volume [4]. In fact, it is not uncommon in MEMS systems for the battery to be several times larger than that of the device [3]. In both EV and MEMS applications it is necessary to find ways to increase the energy and power density of the devices that power them, thereby decreasing battery's the mass, volume and surface area contribution to the system.

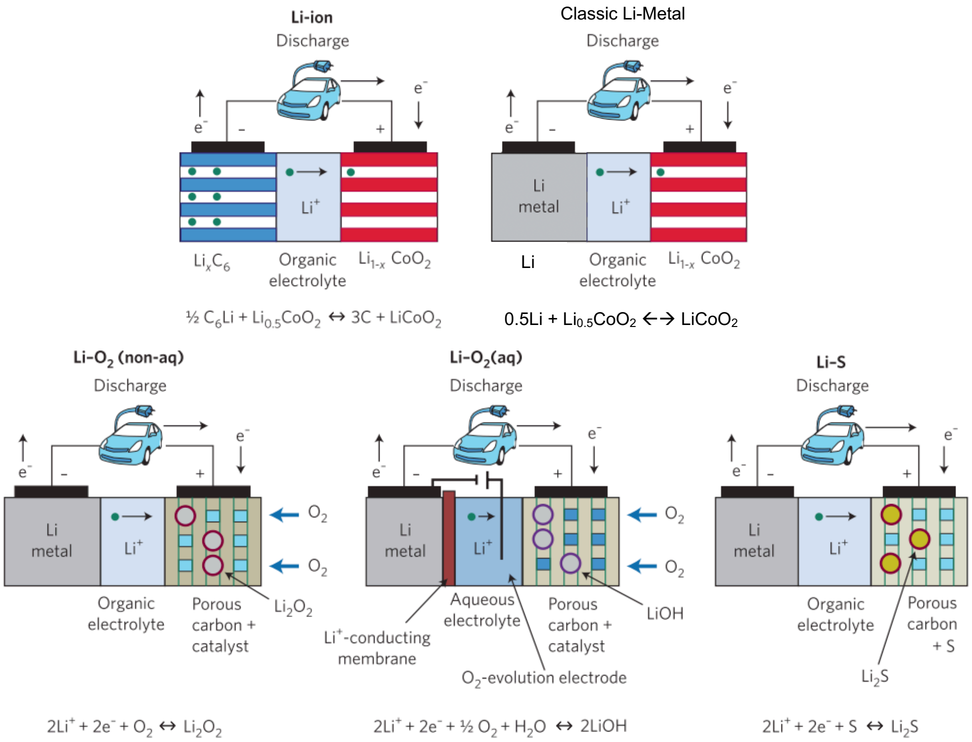

Figure 1.4: Schematic representations of cells for various Li-based electrochemical cells. Modified with permission [15]. Copyright 2012, Springer Nature.

In the quest to improve cellular energy density, a significant amount of research is devoted towards developing systems with Li-metal as the negative electrode. Li-metal regarded as the "Holy Grail" negative electrode, as it has a large charge capacity (~3860 mAh g^{-1}) and low electrochemical potential (-3.040 V vs. the standard hydrogen electrode) [1], [6], [16]. Several potential Li-metal systems are under development and may exhibit superior energy densities compared to current LiB (Figure 1.1A and Figure 1.3B) [1], [15]. These include the classic Li-metal system, where the LiB's graphitic negative electrode is replaced with Li-metal, and Li-O_2 and Li-S systems where the transition metal oxide active material in the cathode is replaced with O_2 or S respectively (Figure 1.4) [1], [15]. Despite intensive research these technologies are still several years away from commercialization, as several issues plague Li-metal anode implementation (Figure 1.5A).

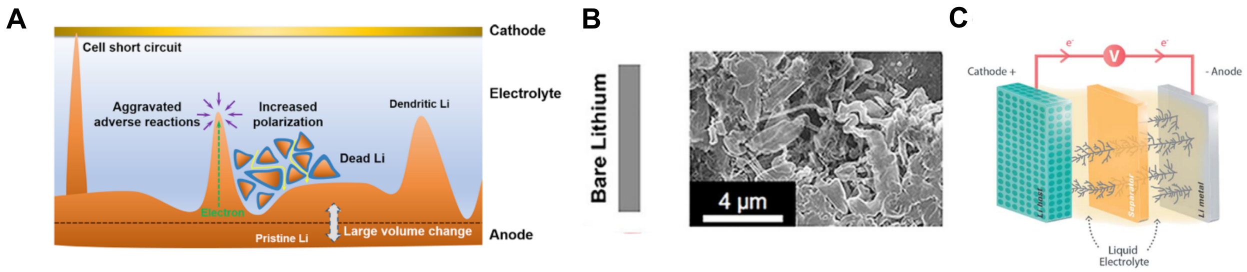

Figure 1.5: A) Schematic of difficulties facing Li-metal battery operation. Reproduced with permission [6]. Copyright 2017, American Chemical Society B) Dendrite formation on bare Li foil after cycling observed using SEM. Reproduced with permission [17]. Copyright 2018, Elsevier. C) Schematic of Li dendrite growth in Li-metal battery causing short circuit. Reproduced with permission [16]. Copyright 2016, Royal Society of Chemistry.

The most dangerous obstacle is the potential for short circuiting due to dendrite formation and growth. During repeated cycling scanning electron microscopy (SEM) images show the Li dendritic fingers grow away from the negative electrode (Figure 1.5B), easily penetrating through the liquid electrolyte and porous polymeric separator. Eventually some dendrites will make physical contact with the positive electrode, forming an electrical contact between the cell's two electrodes (Figure 1.5C). This provides a low resistance path for electron transport, eliminating electron flow through the external circuit, and leads to high self-discharge currents. This self-discharge is typically accompanied by thermal runaway, which ignites the flammable organic liquid electrolyte, causing dangerous fires and explosions [6], [7], [16]. In fact the volatility of traditional Li-metal batteries due to dendrite formation was a significant reason research originally moved away from Li-metal systems and towards intercalation based LiBs [1], [7]. Until a solution to the dendrite problem is achieved, Li-metal batteries remain too dangerous for wide scale implementation and consumer use.

1.3 Optimizing LiB Energy Density, Safety and Performance

1.3.1 Higher Capacity Active Materials

Another pathway, and one that avoids Li-metal anodes, towards high energy density cells is to further improve and optimize the geometry and materials selection for LiB systems (Figure 1.3B). The simplest way to do this is to introduce active materials that either increase the LiB's operating voltage or have increased specific charge capacities [1], [8]. For increased operating voltage, research has been performed on using high voltage intercalation positive electrode materials, such as $LiMn_2O_4$ or $LiCo_2O_4$, that increase the operating to > 4.0 V (Figure 1.6A). For increased capacity significant work has focused on introducing conversion positive and negative electrodes. For example, negative conversion electrodes (Figure 1.6B), have large specific capacities when compared to graphite (~372 mAh g^{-1}). Of the conversion electrodes Si is readily abundant, cheap and exhibits an impressive~3600-4200 mAh g^{-1} specific capacity. However, during cycling Si suffers from a 250-300% volume changes [8], [18]. As a result, Si electrodes suffer a significant capacity fading issue, as particle pulverization or thin film delamination leads to active material loss upon repeated cycling (Figure 1.6C) [18], [19]. Finding ways to integrate these high-capacity materials, such as Si, will be integral to improving cell level energy density.

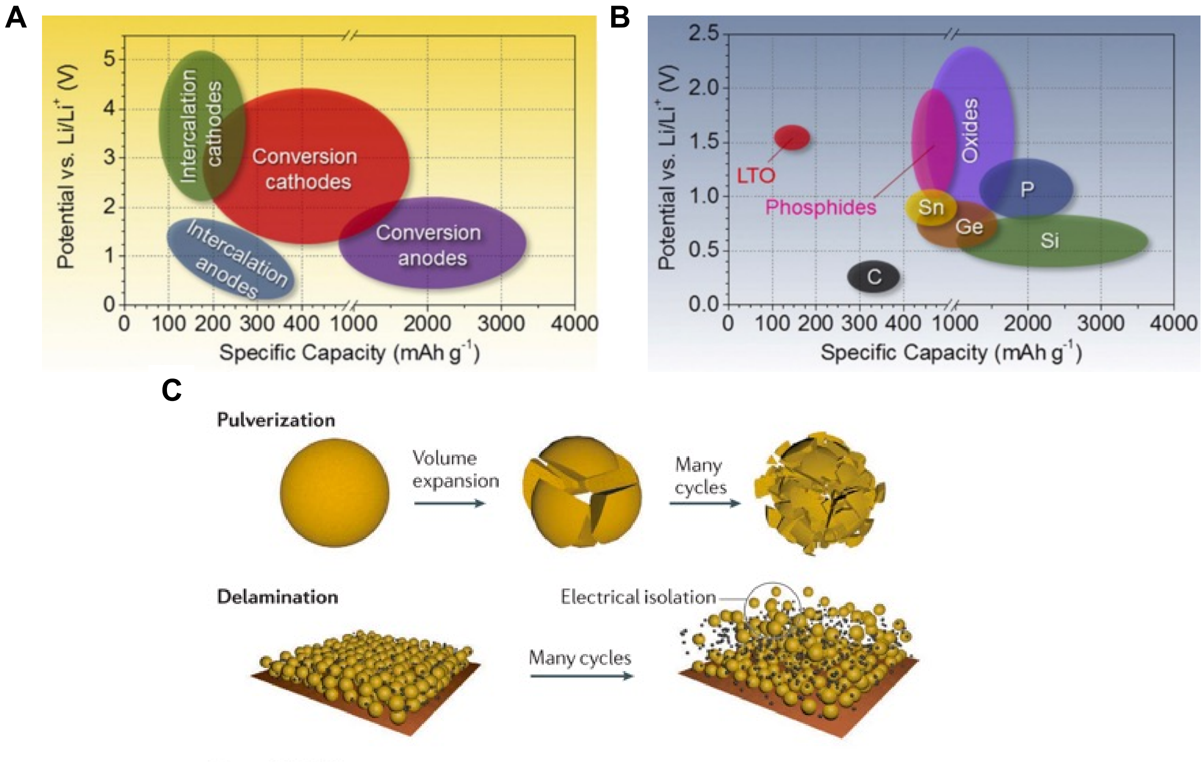

Figure 1.6: A) Voltage and specific capacity plot for various types of active materials and B) voltage a specific capacity for anode materials. Reproduced with permission [8]. Copyright 2015, Elsevier. C) Failure mechanisms plaguing Si-based electrodes. Reproduced with permission [19]. Copyright 2016, Springer Nature.

1.3.2 Solid State Electrolytes

Another method to improve cell level energy density is to eliminate or minimize the number of inactive components in the cell [7]. One avenue is to introduce a solid state electrolyte (SSE), that eliminates the need for the liquid electrolyte and separator combination found in a conventional LiB and creates a solid state battery (SSB) [1], [20]. Generally, SSEs can be grouped into oxides and nitrides, sulfides or solid polymers by their representative composition. Due to the inclusion of a liquid organic phase gel polymer electrolytes are not considered to be SSEs but offer an intermediary between SSEs and liquid electrolytes. Table 1.2 outlines some common electrolytes types that belong to each SSE class and gives a representative composition for each [21]–[25]. As previously mentioned, the organic solvents used in LiB are highly flammable, and thermal runaway leads to rapidly developing fires and eventually explosions [6], [7], [16]. This makes building large volume cells difficult, as it increases the combustible material volume and lowers heat dissipation [20]. Using an inert, non-flammable SSE will allow for the fabrication of safer batteries on a larger scale. One potential drawback to SSE implementation is that certain oxide and sulfide SSE, such as garnet (LLZO), LPS and LATP in Figure 1.7A, have larger densities than conventional liquid electrolytes. In these cases the electrolyte layer must be fabricated beneath a certain “break even” thickness to prevent any loss in specific energy density [26].

Table 1.2: Common SSEs by designation as oxide/nitride, sulfide or solid polymer and representative compositions.

Oxides		
Classification	**Abbreviation**	**Representative Composition**
Perovskite-type	LLTO	$Li_{3x}La_{2/3-x}TiO_3$
Anti-perovskites	LiRAP	Li_3OX X=Cl, Br, I
Lithium super ionic conductor	LISICON	$Li_{2+2x}Zn_{1-x}GeO_4$
Sodium super ionic conductor-like	NASICON-like	LATP: $Li_{1+x}Al_xTi_{2-x}(PO_4)_3$ LAGP: $Li_{1+x}Al_xGe_{2-x}(PO_4)_3$
Garnet-type	LLZO	$Li_3Ln_3M_2O_{12}$ M= Te, W Ln=Y, Pr, Nd, Sm, Eu, Gd, Tb, Dy, Ho, Er, Tm, Yb, Lu
Lithium phosphorous oxynitride	LiPON	$Li_xPO_yN_z$
LiN_3-type	LiN_3	LiN_3
Sulfides		
Classification	**Abbreviation**	**Representative Composition**
Thiolated lithium super ionic conductor	Thio- LISICON	$Li_{4-x}Ge_{1-x}P_xS_4$
-	LPS/LGPS	$Li_{10}MP_2S_{12}$ M=Ge, Si, Sn, Al, P
Argryodites	-	$LiPS_5X$ X= Cl, Br, I
Solid Polymers		
Classification	**Common Example**	**Repeat Unit**
Polyethers	Poly(ethylene oxide) (PEO)	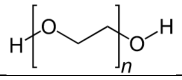

In addition to offering improved cell safety and removing the separator material, SSB may operate at power densities higher than traditional LiB. LiB power density is limited by a number of factors during operation. In addition to Li^+ ions, anions are also mobile in liquid electrolyte (most liquid electrolytes have a transference number under 0.5) and operation at high current density leads to diffusion limitations resulting concentration gradient formation in the electrolyte.

Liquid electrolytes are also limited due to desolvation steps that occur before Li^+ can be intercalated into the electrode. These desolvation steps have high activation energies and limit the electrode reaction kinetics [20]. Some SSE are free from these limitations as negative charges are immobilized within the solid framework, which is also free from solvation.

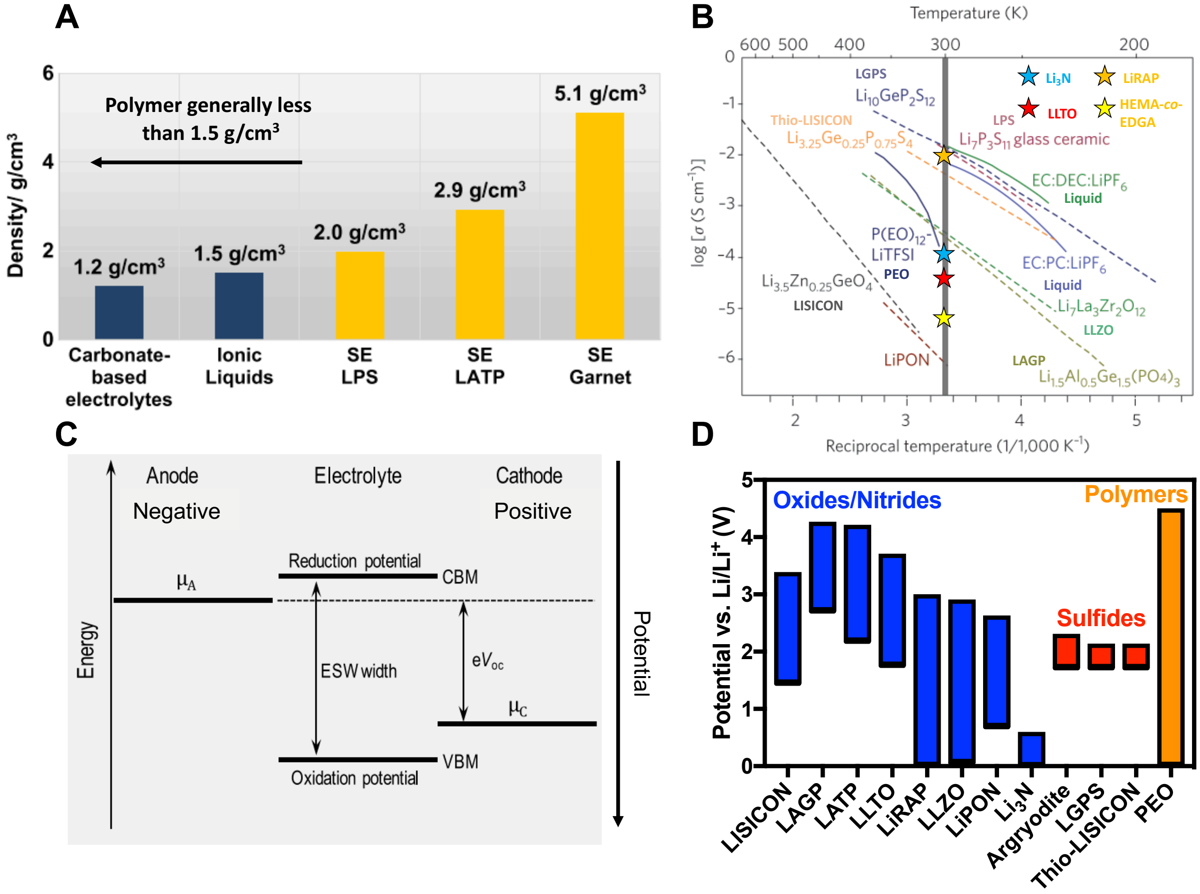

Figure 1.7: A) Densities of several liquid electrolytes and SSEs. Reproduced with permission [1]. Copyright 2017, Springer Nature. B) Ionic conductivity as a function of temperature for potential SSE. Reproduced plot and data taken with permission from [10], [24], [27]. Plot copyright 2016, Springer Nature. C) Energy diagram of the electrolyte interface with the positive and negative electrodes. Reproduced with permission [28]. Copyright 2019, American Chemical Society. D) ESW for various SSEs.

$$R\ (\Omega) = \frac{L}{\sigma\ (S\ m^{-1}) \cdot A}\ (Eq. 1.1)$$

$$\sigma\ (S\ m^{-1}) = \frac{\sigma_o}{T} e^{\frac{-E_A}{k_B \cdot T}}\ (Eq. 1.2)$$

$$\sigma\ (S\ m^{-1}) = \sigma_o \cdot T^{0.5} e^{\frac{-B}{T-T_0}}\ (Eq. 1.3)$$

In order for this potential to be met SSE should possess ionic conductivities on par with liquid electrolytes. In *Eq. 1.1* the ionic resistance (R) is a function of electrolyte thickness (L), electrode-electrolyte contact area (A) and the ionic conductivity (σ) [29]. The ionic resistance is inversely proportional to ionic conductivity so, assuming cell geometry and SSE thickness remain constant, the Ohmic losses are mitigated by increasing ionic conductivity. Organic electrolytes containing Li-salts exhibit conductivities on the order of 10^{-3} to 10^{-2} S cm^{-1}. Due to their larger transference number, at a minimum, SSE should exhibit ionic conductivities on the order 10^{-5} to 10^{-3} S cm^{-1} to be considered for study in a SSB [20], [25]. Achieving this level of conductivity has been a challenge for SSEs of all types, and it is not uncommon for ionic conductivity to vary by orders of magnitude as ion valency and size, conduction mechanism, electrolyte composition, crystal structure and operating temperature are varied [24].

Ion conduction in crystalline ceramic electrolytes is governed by Arrhenius-type behavior (*Eq. 1.2*), where the pre-exponential factor (σ_o) represents the number of charge carriers and temperature (T). The Boltzmann constant (k_B) and the diffusion activation energy (E_A) also influence conductivity [24]. The most straightforward way to improve ionic conductivity of a ceramic electrolyte is to increase temperature or to decrease the activation energy, which is associated with ion-hopping between lattice sites. However, glass ceramics and solid polymer electrolytes do not exhibit this Arrhenius behavior above their glass transition temperature, as ion motion is more closely linked to long-range motions in the SSE matrix. Instead, conductivity is better described using the glass transition temperature (T_g) via the Vogel-Tammann-Fulcher (VTF) equation (*Eq. 1.3*). Here the ionic conductivity is expressed a function of temperature (T), a pseduoactivation energy for conductivity (B) and a reference temperature (T_o) that is 10-50 K below the glass transition temperature [24]. It is worth nothing that liquid electrolytes follow the same behavior. Similar to crystal ceramics, the ionic conductivity for glass electrolytes can be increased by increasing temperature or by decreasing the glass transition temperature. The Arrhenius (straight lines) and VTF (curved lines) behavior for various electrolytes is observable in Figure 1.7B, with the conductivity of each material changing by several orders of magnitude as temperature is varied. As ionic conductivity is strongly influenced by temperature it is important to compare the ionic conductivity of the materials at the cell operating temperature. This is usually taken to be at ambient temperature (~298-300 K).

Table 1.3: Summary of important properties for various SSE classes.

	Oxides	**Sulfides**	**Solid Polymers**
Ionic Conductivity (S cm^{-1})	10^{-7} to 10^{-3}	10^{-3} to 10^{-2}	10^{-8} to 10^{-4}
ESW	Varies, typically stable against Li-metal OR positive electrode	Poor, not stable against Li-metal or positive electrode	Stable against both Li-metal and most positive electrodes
Density (g cm^{-3})	3-5	2-3	1-1.5
Modulus (GPa)	> 100	~20	< 0.2
Chemical Stability	Degrades with moisture or CO_2 contact	Unstable in contact with moisture, H_2S production	Stable and safe
Cost and Processability	Expensive and difficult to produce at required thickness	Expensive and requires inert atmosphere production	Already industrially produced in other industries and cheaper than liquid alternative

While ionic conductivity is important it is not the only parameter that defines a material's ability to be utilized as a solid electrolyte. The electrochemical stability window (ESW) is an important parameter in determining whether an SSE is stable against the negative and positive electrodes. As shown in Figure 1.7C, the ESW is determined by the SSE's reduction and oxidation potentials. These are respectively governed by the conduction band maximum (CBM) and valence band minimum (VBM) energy levels. Promising SSEs should have a large ESW. To meet this criteria the energy gap between the CBM and VBM must exceed the energy difference between the negative (μ_A) and positive (μ_C) electrodes, the CBM should be greater than μ_A and the VBM should be lower than μ_C [28], [30]. If the CBM energy level drops below μ_A then the SSE at the negative electrode will be reduced by the active material. Similarly, if the VBM maximum rises above μ_C then the SSE at the positive electrode will be oxidized by the active material. These unwanted, parasitic reactions result in the formation of solid electrolyte interphase (SEI) layers that consume active material and may be impassible to Li transport, significantly lowering cell lifetime and capacity. For operation in a LiB an ideal SSE possess an ESW that stretches from just above 0 V vs. Li/Li$^+$ to ~ 4.3 V vs. Li/Li$^+$. This would ensure the SSE is stable and does not react with either the positive or negative electrode. The electrochemical stability windows for a variety of SSE are plotted in Figure 1.7D. The values in Figure 1.7D have been compiled from a variety of experimental results and first principal calculations [25], [28], [30]–[32].

A comparison between the oxide and nitride, sulfide and polymer SSE for the properties discussed above and several other important parameters is summarized in Table 1.3. Oxides, such as LLZO, generally have sufficient ionic conductivity, relatively large ESW and a high Young's modulus but have high densities, contain expensive elements and are difficult to process with conventional techniques. Sulfides have the best ionic conductivity and acceptable mechanical properties, but H_2S off gassing and low ESW present a large challenge. Both oxides and sulfides face uncertain financial situations, as the production cost far exceeds the cost of state of the art LIB [26], [33]. Certain polymers have high stability windows are arguably most compatible with industrial scale processing, but are limited by their low ionic conductivity and mechanical properties. In general, SSEs suffer from poor interfacial adhesion at the electrodes during cycling, and surface engineering of this interface is an active research field. The discovery of a easily processible oxide, stable sulfide or polymer with improved ionic conductivity would become an immediate front runner in the race for a commercially viable SSE [7], [26].

1.3.3 Thick Electrodes and 3D Full Cells

As previously mentioned, and shown in Figure 1.2, LiB are fabricated with a 2D geometry consisting of planar electrodes on either side of a separator membrane. A simple strategy to increase a cell's energy density is to try and minimize inactive material content [7]. These inactive materials do not directly contribute to the device's charge capacity and include current collectors, electrolyte, separator and other additives Figure 1.2. Short of removing these inactive components the simplest way to minimize their contribution is to increase electrode thickness (*Eq. 1.4,* Figure 1.8), indicating that energy density (E_D) is proportional to electrode thickness (L_E) [4].

$$E_D \propto L_E \; (Eq. 1.4)$$

$$P_D \propto E_D \cdot \tau \; \propto \frac{E_D \cdot D_{Li}}{L_E^2} \; (Eq. 1.5)$$

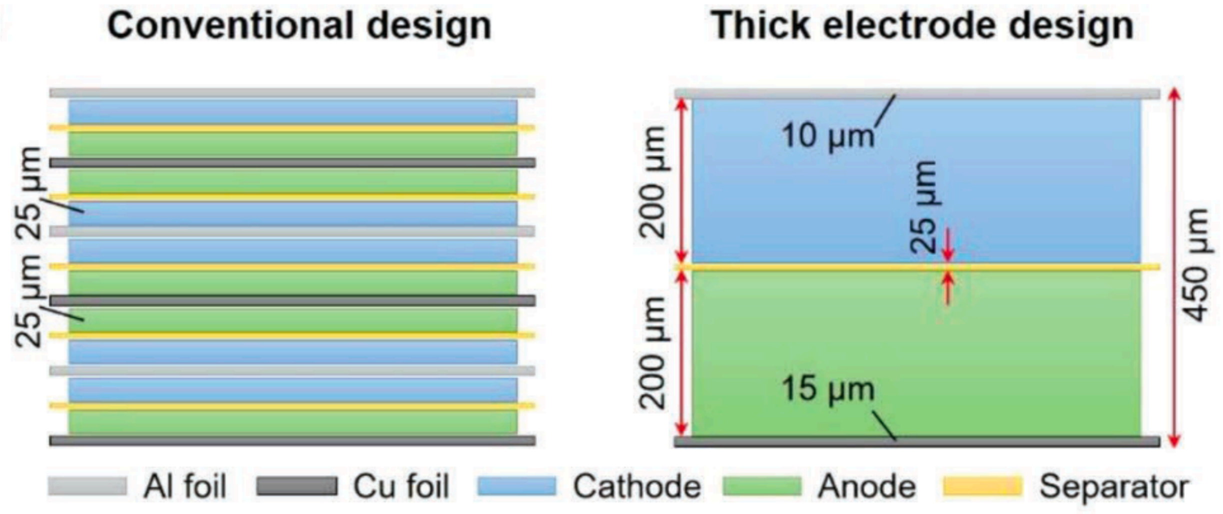

Figure 1.8: Schematic demonstrating how thick electrode cells minimize the contributions of inactive components (current collectors and separators) when compared to conventional designs. Reproduced with permission [34]. Copyright 2019, Wiley-VCH.

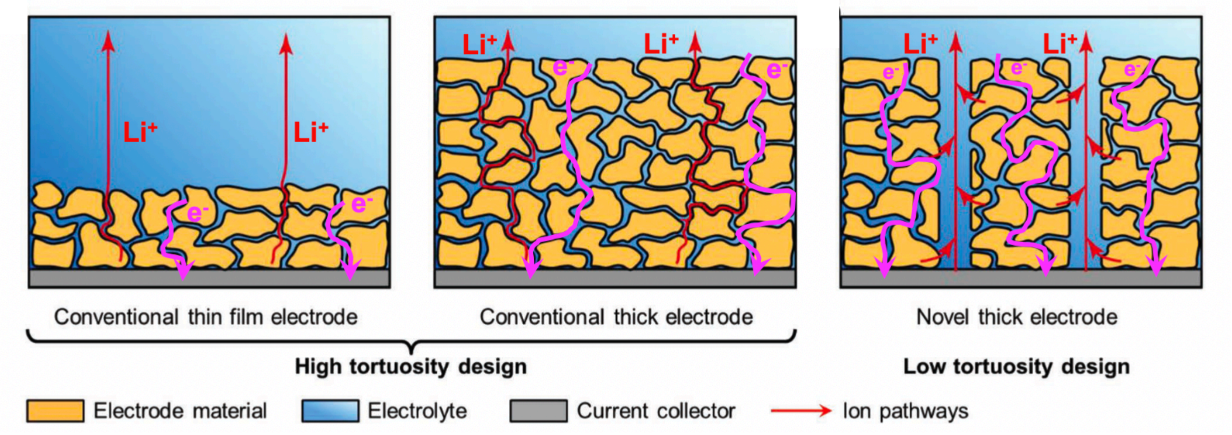

Figure 1.9: Schematic showing how slurry-based thick electrodes suffer from increased diffusion lengths due to their high tortuosity and how 3D structing can mitigate this issue by providing Li-ion diffusion channels. Reproduced with permission [34]. Copyright 2019, Wiley-VCH.

While increasing electrode thickness seems like a simple solution, it comes with a significant limitation for both slurry-based and thin film electrodes. The high tortuosity of slurry-based electrodes results in significant increases in the distance Li-ions must travel as the electrode thickness is increased (Figure 1.9), which often results in inefficient active material utilization and rate limitations [34]. Thin film planar batteries experience a similar issue, as the electrode thickness increases power limitations will occur due to slow Li ion diffusion in solid materials ($< 10^{-10}$ cm^2 s^{-1}). The cell's discharge time constant (τ) can be estimated by using the Li^+ diffusion coefficient (D_{Li}), electrode thickness and Fick's laws. The result, *Eq. 1.5*, is that power density (P_D) is inversely proportional to the square of electrode thickness [4]. While increasing electrode thickness does indeed increase energy density, it also results in an inherent trade-off between energy and power densities. Furthermore, increasing electrode thickness compromises the electrodes' mechanical integrity, as the active materials experience significant volumetric changes during cycling; introducing mechanical fatigue that is a significant barrier to long-life operation [3], [5]. As a result, thick electrodes often incorporate some degree of 3D patterning to provide channels for Li-ion diffusion and to accommodate active material expansion in the electrode (Figure 1.9) [34], [35].

Despite these potential improvements 3D electrodes in a planar configuration still suffer from increased diffusion distances as well as a reduction in active material due to increased electrode porosity. One strategy is to abandon the planar designs of a standard LiB in Figure 1.2 and move towards batteries with 3D architectures, where the electrodes have active surface areas exposed in three dimensions [4]. There are many possible 3D architectures, and some examples from literature are presented in Figure 1.10A through Figure 1.10D. In all designs the two electrodes are separated by a conformal thin film electrolyte.

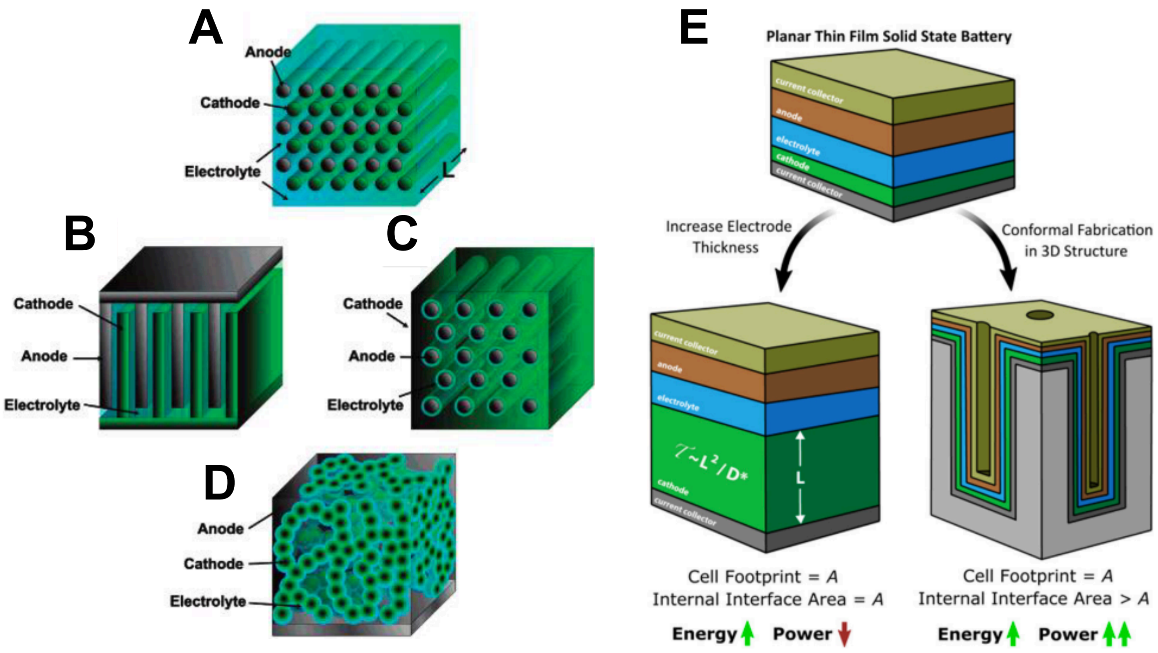

Figure 1.10: Schematics for A) variations in 3D battery architectures including: B) interdigitated anode and cathode rods, C) interdigitated anode and cathode plates, D) anode array surrounded by infiltrated cathode material and E) gyroidal structure. All designs feature a conformal thin film electrolyte between the two active materials. Reproduced with permission [36]. Copyright 2004, American Chemical Society. F) Shows the increase in interfacial area obtained through a 3D design. Reproduced with permission [37]. Copyright 2018, American Chemical Society.

These 3D architectures allow for a higher surface area for the same volume and footprint as the 2D electrode. As a result, a given active material volume can be distributed with a lower electrode feature thickness (Figure 1.10E). This increased surface area enables shorter Li$^+$ diffusion distances for a given amount of active material and decouples the trade-off between energy and power density inherent to planar designs [3], [4], [36], [38].

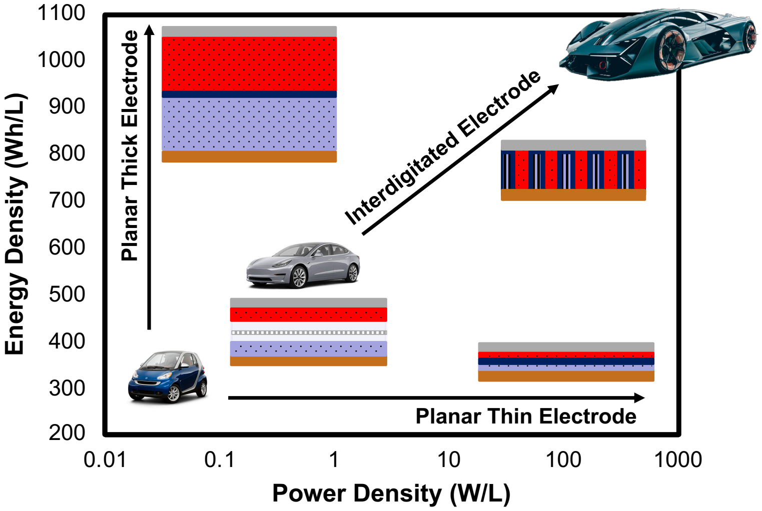

Figure 1.11: Illustration of power and energy density trade-off experienced by planar battery structures. A well-built interdigitated structure should overcome this trade-off and allow devices with high energy and power densities.

In their initial analysis for 3D battery structures Hart *et al.* compared a 2D planar battery to a 3D interdigitated cylindrical array battery (Figure 1.10) of equal volume. Compared to the 3D design the 2D battery has 70% lower surface area, a 350% larger diffusion distance and to achieve an equal power density the 2D battery's areal footprint would increase by over 300% [39]. These significant size savings make 3D battery architectures a viable option for applications, such as EV and MEMS, where minimizing battery size is required for optimized integration and high-level performance. Furthermore, increasing interdigitated electrode length minimizes the mass and volumetric contribution from dead materials (i.e. current collectors), and the decreased Ohmic drop across thinner films allows 3D devices to truly achieve high energy and power density, overcoming the energy-power trade-off illustrated in Figure 1.11 for planar batteries [38], [39]. It should be noted that increasing the interdigitated electrode length will increase the electrode's Ohmic resistance to a point where it offsets the increased capacity, making the ideal electrode thickness a function of geometry and conductivity [39].

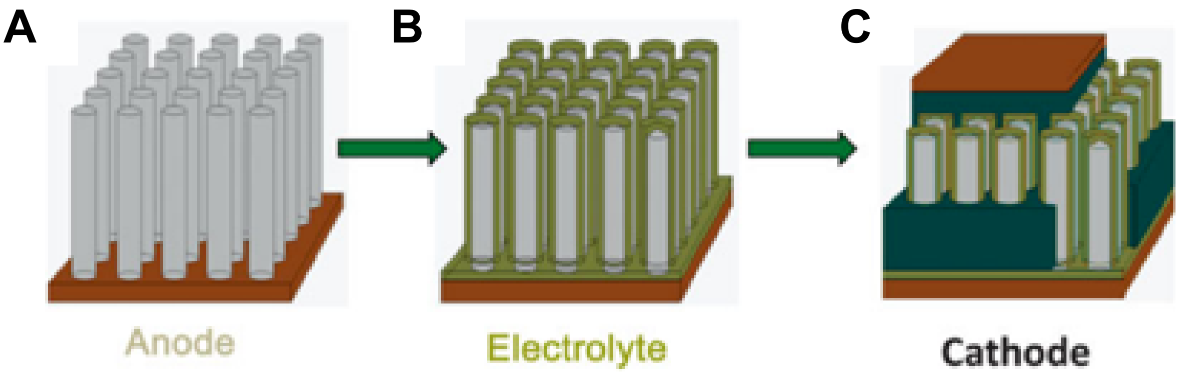

Figure 1.12: Sample fabrication process for interdigitated 3D battery starting with A) nano-rod/nano-tube fabrication followed by B) conformal electrolyte coating and C) bulk cathode infiltration. Reproduced with permission [3]. Copyright 2011, The Society.

Table 1.4: Make-up and performance of full-cell 3D batteries.

3D Design	Positive Electrode	Electrolyte	Negative Electrode	Cycles	Capacity (mAh cm^{-2})
Column array in glass microchannels	Electrodeposited MoO_yS_z	Spin-coated polymer gel electrolyte	Mesocarbon microbead slurry	200	2
Column array in etched Si wafer	Thin film LiV_2O_5	Thin film Li_2PO_2N	Thin film SnN_x	100	2.6 x 10^{-3}
Interdigitated electrodes on honeycomb electrolyte	LCO slurry	Solid honeycomb $Li_{0.35}La_{0.55}TiO_3$	$Li_4Mn_5O_{12}$ slurry	3	7.3 x 10^{-3}
Interdigitated electrodes on Si pillars	NCA slurry	Spin coated polymer gel electrolyte	Si pillars	100	0.5
Gyroid on block co-polymer	Vapor/liquid infiltrated S	Electropolymerized solid polymer	Amorphous carbon	20	0.2

While 3D batteries offer promising electrochemical properties their complex geometries require an involved fabrication process. Fabrication often begins with producing a single arrayed electrode, Figure 1.12A. A majority of the literature has focused on such half-cell fabrication [3]. Traditional lithographic and thin film fabrication technologies offer the ability to synthesize many geometries based on those presented in Figure 1.10 [39]. In addition to maintaining short diffusion distances, there are several other advantages to patterning electrodes with nano or microscale features. These include increased number of active sites for electrode reactions resulting from increased electrode-electrolyte contact area, improved mechanical properties; as low-dimensional materials (such as nano-wires or nanotubes) have high mechanical strengths, and easily controlled electrode porosities that can be designed to accommodate volumetric expansion in certain dimensions [5]. Previous 3D half-cell configurations have been fabricated from Si nanowires [40], ion etched Si trenches [41], active material coatings on metallic nanowires [42]–[46] and pyrolyzed carbon posts [47], [48].

While half-cell capabilities have been well demonstrated there have been fewer attempts to fabricate full-cell 3D batteries. The final two steps in Figure 1.12B and 1.12C pose significant challenges. For example, the electrolyte coating must be conformal and pinhole free and allow for sufficient Li^+ transport [3]. Lastly, active material needs to be infiltrated into the electrolyte coated structure. This can be done by infiltrating a traditional slurry or through an additional thin film coating step. A slurry should consist of an active material, electrolyte particles, conductive additives and binder, and must wet, but not damage or dissolve, the electrolyte during infiltration. In addition, the cast electrode packing density must be high to avoid any major voids in the 3D structure. Slurry's have successfully been infiltrated into 3D battery geometries with features sizes of ~100 μm [3], [49], [50] while thin film 3D batteries have been deposited with features of ~100 nm [37], [51], [52]. The fabrication steps and performance of several Li-based 3D full-cells are summarized in Table 1.4, with many outperforming their equivalent 2D planar battery [37], [49]–[51], [53].

1.4 Thesis Outline

1.4.1 Overview: Interdigitated 3D CNT Battery

As outlined above, the ideal material to template an interdigitated design should be mechanically robust, electrically conductive, easily patterned at the microscale level, and porous enough to support active material expansion and enable rapid transport kinetics. This thesis aims to design, analyze, and fabricate a 3D full-cell by using patterned vertically aligned carbon nanotube (CNT) forests with microscale features as the scaffold for full-cell development.

CNTs are known to have high thermal (3500 W m^{-1} K^{-1}) and electrical conductivities (10^5 S m^{-1}) and can carry currents up to 10^9 A cm^{-2} [54], [55]. In addition to their excellent electrical conductivity CNT forests exhibit high mechanical strength and flexibility [54], [56], [57]. These mechanical properties, coupled with their inherent high porosity, make vertically aligned CNTs an ideal scaffold to support the large volumetric changes experienced by high energy density active materials during cycling. Lasty, while wafer scale CNT growth is well understood and optimized, works have demonstrated potential for roll-to-roll catalyst patterning [58] and CNT synthesis [57], allowing for eventual integration into an industrial process; something that would be difficult for the batch processes outlined in Table 1.4.

Importantly, CNT forests can be patterned via photolithography and grown using chemical vapor deposition (CVD) [59]–[61], enabling precise definition of the electrode architecture in this research. The proposed fabrication process for a structurally integrated micro-honeycomb CNT battery is presented in Figure 1.13. Cell level fabrication is outlined in Steps 1 through 5. First, (Step 1) Cu foils will be coated with a patterned catalyst stack that allows for vertically aligned CNT growth. Then, (Step 2) tall and patterned CNT forests will be grown directly on Cu foil substrates. These CNTs will serve as a scaffold to support the battery active material and facilitate electron transport from the active material to the current collector. Step 3 will utilize conventional CVD processes to conformally coat the CNTs with silicon negative electrode material. This will be followed by another coating step, where uniform polymer electrolyte will conformally coat the Si-CNT forest composite (Step 4). The second electrode is then inserted (Step 5) by infiltrating a cathode slurry, similar to the one used in a LiB, into the honeycomb's holes. The cell is then completed by capping the cast slurry with the appropriate Al current collector (Step 5).

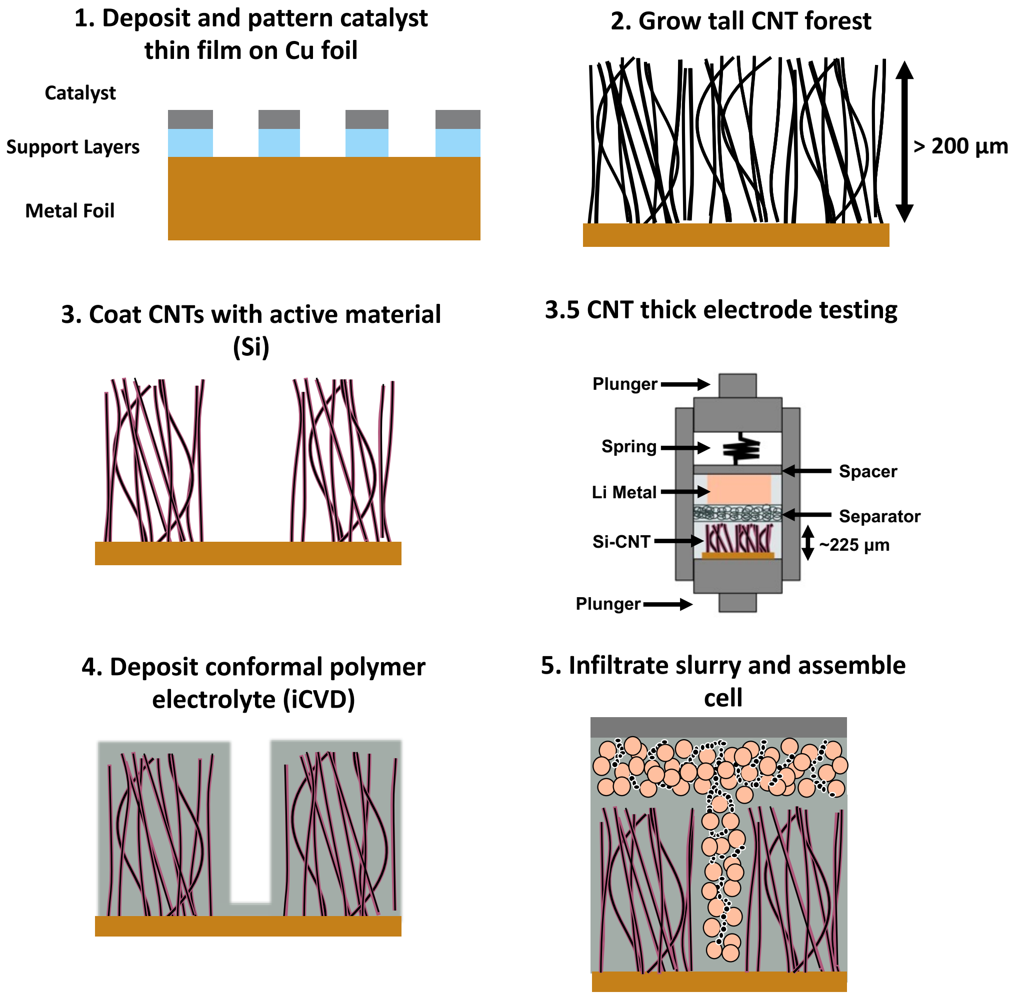

Figure 1.13: Schematic for interdigitated CNT battery fabrication.

1.4.2 CNT Growth on Metal Foils

First synthesized in the 1980's CNTs are cylinders consisting of one (single-wall, SWCNT) or more (double to multi-wall, MWCNT) layers of rolled graphene with a length ranging from 100 nm to several cm. The ideal CNT sheet consists of a hexagonal lattice of carbon atoms and CNTs exhibit many of the superior mechanical and electrical properties exhibited by planar graphene. Mechanically CNTs can exhibit an elastic modulus of ~1 TPa and a 100 GPa tensile strength. The electronic properties depend on the angle between the tube axis edge and graphene lattice, and as a result SWCNTs can be either metallic or semi-conducting. Metallic SWCNTs and MWCNTs are capable of carrying currents up to 10^9 A cm^{-2} and exhibit high thermal conductivity (3500 W m^{-1} K^{-1}) [62], [63].

Despite their exceptional potential properties, there is significant difficulty in producing CNTs with either sufficient lengths or in sufficient masses for practical applications on an industrial scale. Important methods of producing CNTs include utilization of floating-catalyst CVD systems, whereby the CNTs are produced in a plasma phase before being collected into solid structures such as sheets and yarns, and the CVD ("growth") of vertically aligned CNTs, known as forests, directly on a solid substrate (Figure 1.14A) [62], [63]. Their high degree of alignment coupled with excellent electrical, mechanical and thermal properties makes aligned CNTs an intriguing option to fabricate thermal interface materials, electronic interconnects, nanoporous stamps, supercapacitor electrodes, and, as studied in this work, battery current collectors or electrodes [59], [62]–[67].

While many substrates (such as a quartz wafer) and catalyst (Ni, Co) combinations have been used for CNT forest growth a common combination is a thin film stack consisting of Fe catalyst on a Al_2O_3 support layer on top of a Si/SiO_2 wafer substrate [61], [64], [68], [69]. Upon exposure to hydrogen and high temperature this Fe film dewets to form a layer or Fe nanoparticles. The substrate is the exposed to a carbon precursor (typically methane, acetylene or ethylene) which breaks down in the furnace and nucleates CNTs at the Fe nanoparticles. The spacing of the CNTs is dependent on the density and size of these particles, with typical CNT spacing on the order of 10-100 nm (Figure 1.14B). The height of the aligned CNTs can be controlled by manipulating the amount of time the substrate is exposed to the precursor and can result in CNTs with heights on the millimeter scale (Figure 1.14C) [64], [70]. However, CNT growth is complex process with many interconnected parameters, such as ambient lab conditions [69], moisture content [61], furnace carbon content (Figure 1.14C) [64] and catalyst thickness [71], affecting the overall CNT density and height. Once a growth process has been established the location of the catalyst stack can be controlled through traditional photolithography processes, enabling an additional level of control over the CNT structure's geometry in the formation of pillars, fins or honeycomb structures (Figure 1.14D) [59], [68], [72].

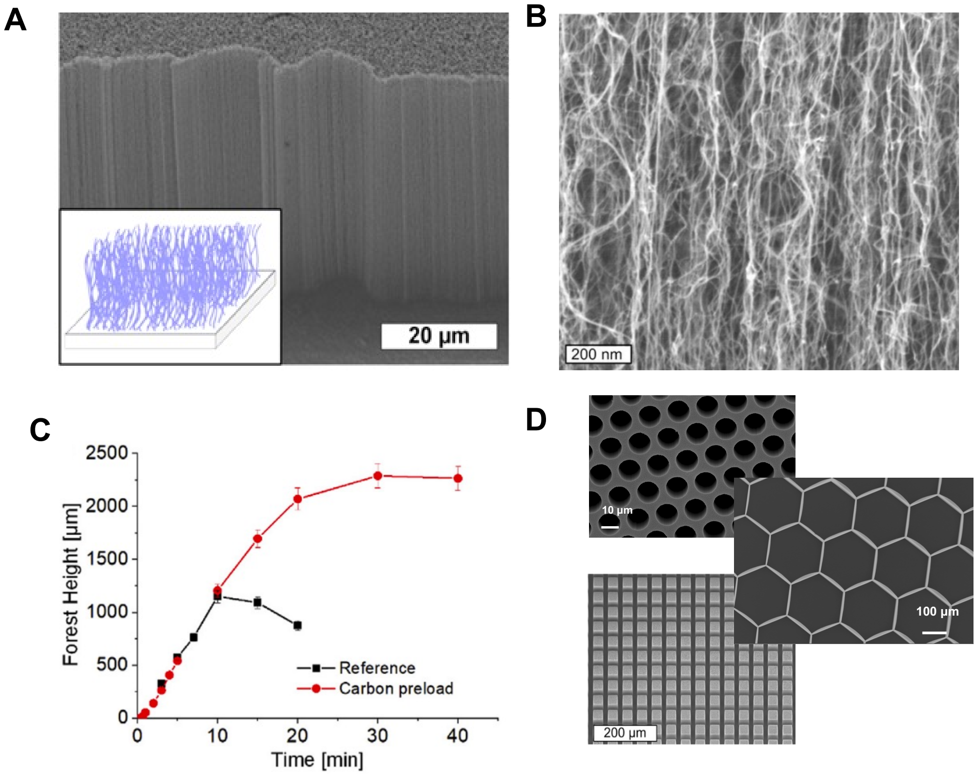

Figure 1.14: A) Vertically aligned CNTs grown on a Si wafer. Reproduced with permission [65]. Copyright 2016, American Chemical Society. B) Zoomed in view showing the aligned nature and inherent nanoporosity of a CNT forest. Reproduced with permission [59]. Copyright 2016, The Authors. C) CNT forest heigh as a function of growth time and carbon conditioning. Reproduced with permission [64]. Copyright 2019, Elsevier. D) CNTs patterned into honeycomb, fin and pillar structures. Reproduced with permission [59]. Copyright 2016, The Authors.

Their inherent nanoporosity and high electronic conductivity, coupled with the ability to precisely control the height and microstructure, makes aligned CNTs a unique starting point for the fabrication of the thick 3D battery electrodes in Figure 1.8 and 3D full cells in Figure 1.9. However, most CNT growth processes are optimized using non-conductive and rigid quartz or silicon substrates, which are unsuitable to replace the Al or Cu foils utilized in state-of-the art LiB. This necessitates a transfer method from Si wafer to metal foil, a process that can damage the interfacial CNTs and causes increased electrical and thermal resistance [71], [73]–[76]. As a result, there has been interest in developing methods to grow CNTs directly on metallic foils for implementation as 3D current collectors in lithium-ion cells.

One strategy for growing CNTs directly on metallic substrates is to select substrates that contain a known CNT catalyst, such as Fe or Ni, that will not interfere with the growth process. CNT growth using conventional CVD processes have been demonstrated on Ni foil [77]–[79], Inconel foil [80], [81] and stainless steel substrates [82]–[85]. However, it would be preferable to transition CNT growth to Cu or Al that are the industry standard in LiB due to their electrochemical stability in the operating voltage range. Growth on Al is challenging, as the temperatures optimal for aligned CNT growth are generally above the melting temperature of Al, but low temperature processes have been developed for growth of CNTs on Al foils [86], [87].

CNT growth on Cu substrates have received significant interest for implementation in LiB anodes. The difficulty in growing CNTs directly on a Cu substrate is two-fold. First, Cu exhibits a low bulk carbon solubility (0.0008 at.%) compared to Fe (0.4 at.%) or Ni (0.2 at.%). CNT growth on Cu necessitates the deposition of a thin Fe or Ni catalyst layer, which is supported by an insulating oxide, generally Al_2O_3, layer [71]. Furthermore, during growth Cu atoms diffuse through cracks in the support layer and poison the catalyst. This poisoning results in CNTs grown on Cu using a standard catalyst stack (Figure 1.15A) often being unaligned or very short (< 10 µm, Figure 1.15C) [71], [88]–[90].

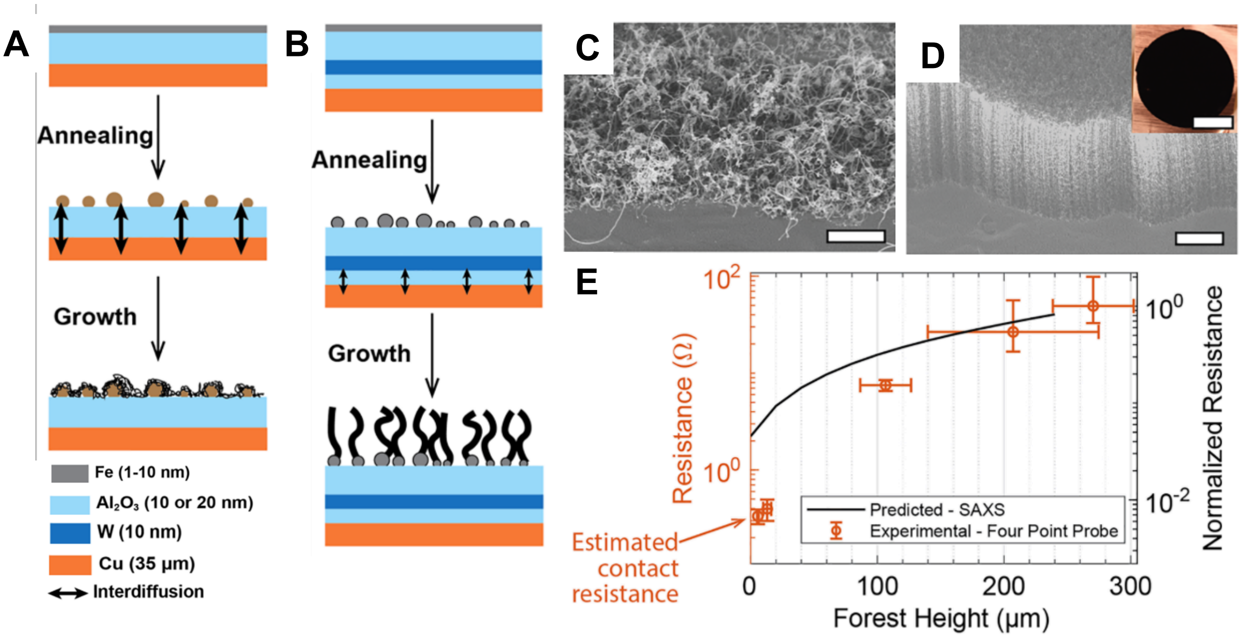

Figure 1.15: Schematics for CNT growth on Cu without A) and with B) a W diffusion barrier resulting in C) disordered and D) vertically aligned growth respectively. Insert in D) shows a macroscale top view of CNT forest. E) Measured and normalized resistance as a function of forest height. Scale bars at 3 µm in C), 10 µm in D) and 5 mm in D) insert. Reproduced with permission [71]. Copyright 2020, American Chemical Society.

Two strategies exist to prevent the Fe catalyst from being poisoned by the Cu substrate. The first is to allow for Cu diffusion through the Al_2O_3 layer but manipulate the stack by increasing Al_2O_3 thickness [91] or strictly controlling annealing time [92] to prevent the Cu from reaching the Fe layer. Another strategy is to utilize a diffusion barrier, such as W or TiO_2, to provide an additional layer of protection from Cu diffusion [71], [93]. Lettiere *et al.* utilized a sputtered W layer (Figure 1.15B) to prevent Fe catalyst poisoning and, using a growth recipe containing optimized catalyst thickness, carbon preconditioning and moisture content, grew 50-270 µm tall vertically aligned CNTs Figure 1.15D) [64], [71]. These vertically aligned CNT forests exhibited much lower bulk resistances (< 50 Ω, Figure 1.15E) than forests grown without diffusion barriers

(> 325 kΩ for 1 mm tall forest) [92]. This low resistance was attributed to cracks forming in the Al_2O_3 support layers and high CNT density and quality [71].

Building upon initial success growing non-patterned CNT forests on Cu foil, Chapter 2 of this thesis contains work on improving the growth processes first outlined by Dee *et al.* [64] and Lettiere *et al.* [71]. Here, sample positioning and furnace moisture content are demonstrated to critical processes parameters in consistently producing tall (> 200 μm) CNT forests directly on Cu foils for integration as current collectors in LiB cells. Chapter 2 also contains methodology for patterning the catalyst to produce patterned CNT forests with increased porosity increased for active material loading and more efficient lithium-ion transport through the open pathways in the structure.

1.4.3 Aligned-CNT Electrodes

Despite their excellent electrical conductivity, porosity and mechanical strength unmodified CNTs are generally seen as an unsuitable active material due to a high irreversible lithium uptake, that results in an inconsistent reversible specific capacity. Despite this inconsistency CNTs can have a larger specific capacity than graphite (~350-900 mAh g^{-1}), with higher capacities being attributed to increased defect concentrations in the CNT structure [55], [67], [79], [94], [95]. As a result, this upgraded capacity comes at the cost of reduced mechanical and electrical properties [55]. Most research into CNT inclusion in LiB batteries has focused on pairing CNTs with more conventional active materials, thus taking advantage of the CNTs ability to increase electrode conductivity, porosity, and flexibility while utilizing the active material to increase capacity. Common strategies have included chemical vapor deposition onto CNT films/fabrics [96]–[100], carbon sponges [101], [102], aligned CNT sheets [103], and mixing CNTs with active material micro- or nanoparticles [104]–[110].

Active material deposition on CNT forests has certain distinct advantages, such as direct electrical connection from the active material to the current collector through CNTs and faster discharge rates due the forest's high porosity. Successfully deposited active materials on vertically aligned CNT forests include $FePO_4$ [111], Fe_2O_3 [75], [112], $LiMn_2O_4$ [77], $Li_4Ti_5O_{12}$ [77], S [78], V_2O_5 [79] and Si [76], [91].

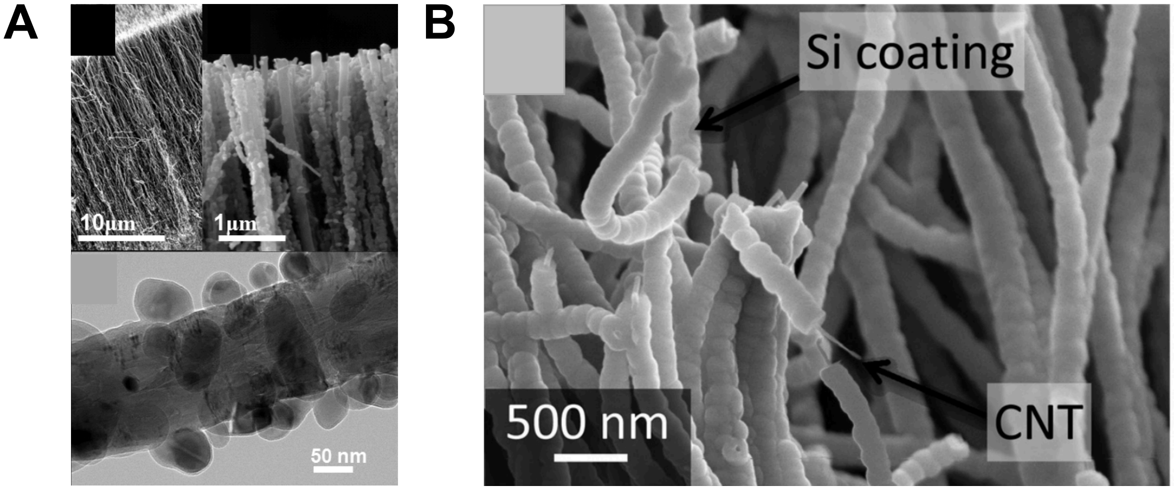

Figure 1.16: SEM and TEM of vertically aligned CNTs coated by Si using A) thermal decomposition. Reproduced with permission [110]. Copyright 2010, American Chemical Society. B) Using ultrahigh vacuum CVD. Reproduced with permission [76]. Copyright 2012, Wiley-VCH.

Of the active materials deposited CNT forests offer a unique potential to serve as scaffolds for conversion anode materials such as Si. Si has a low delithiation potential, exceptionally high specific (~4200 mAh g^{-1}) and (~9790 mAh cm^{-3}) volumetric capacities and is a readily abundant, non-toxic material [8], [113]. However, Si experiences a ~300% volume change upon complete lithiation. This volume change can cause material pulverization, electrode peel-off and continuous growth of the SEI; all of which contribute to significant decreases in electrode capacity, electrical conductivity and lifetime [113]. The porous and aligned nature of CNT forests can be utilized to address some of these issues if the CNTs are coated with Si thin films (<100 nm thick) as the porous spacing between CNTs accommodates the expansion occurs during Si lithiation and delithiation. Furthermore, each CNT is electrically connected to the current collector, ensuring continuous electrical contact with the Si coatings [76], [110], [113]. SEM and transmission electron microscopy (TEM) images of vertically aligned CNTs conformally coated in Si are presented in Figure 1.16.

Chapter 2 includes work in coating patterned and non-patterned CNT forests with Si thin films via a low-pressure CVD (LPCVD) process and the implementation of the resulting Si-CNT in Li-ion half-cells to demonstrate their potential as thick electrodes.

1.4.4 Conformal Electrolyte Technologies and Initiated Chemical Vapor Deposition

Once the patterned CNTs are coated with Si the next step is to deposit an electrolyte layer. It is crucial that this layer be pinhole free to prevent short circuiting, ionically conductive and electrically insulating. Since conventional electrolyte materials lack suitable processing techniques to deposit thin films over high aspect ratio micro or nanoscale features, conformal electrolyte deposition has posed a significant challenge in 3D battery development. As a result, several non-conventional electrolyte materials and fabrication techniques have been investigated to produce thin film conformal electrolyte coatings. The primary issue with these unconventional materials is their low ionic conductivities, which can result in a significant voltage drop across the electrolyte layer (*Eq. 1.1*). However, this drop can be slightly mitigated by using thin electrolytes with large surface areas.

Initially, electropolymerization (EP) seemed like a promising technique to produce thin film solid polymer electrolytes due to its self-limiting nature. The electrode becoming electrically insulated as the redox initiated polymerization occurs. The result is that polymerization occurs more rapidly over the bare electrode regions, resulting in a uniform pinhole free coating over the electrode surface and preventing over deposition on corners or edges [3]. Depositing poly(phenylene oxide) (PPO), and its variants by EP has been extensively investigated. However, these films have exceptionally low ionic conductivity, ranging from 10^{-12} to 10^{-9} S cm^{-1} and their self-limiting nature makes producing films thicker than 50 nm difficult [51], [114]–[116]. More recently works have deposited ceramic oxide electrolytes on high aspect ratio features by atomic layer deposition (ALD), but these also suffer from low ionic conductivity ($< 10^{-7}$ S cm^{-1}) and their high densities, brittleness and slow deposition rates make them difficult to integrate at scale [37], [111], [117], [118].

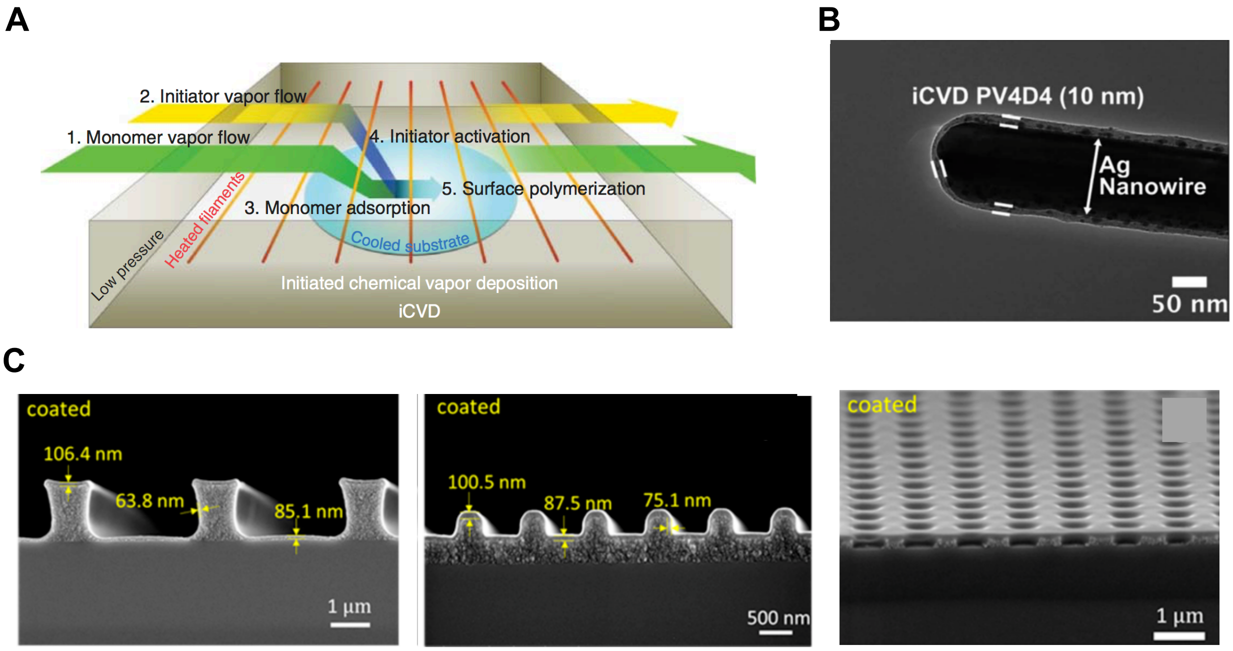

Figure 1.17: A) Generalized schematic for iCVD of polymer systems. Reproduced with permission [119]. Copyright 2015, Wiley-VCH. B) Polysiloxane on Ag nanowire. Reproduced with Permission [29]. Copyright 2015, Royal Society of Chemistry. C) HEMA-co-EGDA on TiO_2 nanopores, microline arrays and nanoline arrays. Reproduced with permission [27]. Copyright 2019, American Chemical Society.

Polymer electrolytes deposited by solution infiltration [120] and spin coating [50] have been utilized in 3D microbatteries. However, initiated chemical vapor deposition (iCVD) is a promising option for conformal electrolyte coatings in 3D microbatteries. iCVD is a modification of conventional CVD targeted at creating high quality polymer coatings. A generalized iCVD process is outlined in Figure 1.17A. First monomer and initiator vapor are delivered into the reaction chamber (Steps 1 and 2), the monomer then adsorbs on the substrate surface (Step 3). While the monomer vapor is adsorbing the initiator vapor is activated by heated wires suspended throughout the reaction chamber (Step 4). The activated initiator then adsorbs on the surface where it initiates surface polymerization by reacting with an adsorbed monomer (Step 5). The activated chain will continue to propagate by reacting with more adsorbed monomer until chain growth is terminated by capping the activated chain ends. By controlling processing parameters (substrate temperature, filament temperature, gas flow rates) film growth rates can be tuned from 10 nm per minute to 1 μm per minute [121], [122].

The Gleason Group at MIT first used iCVD to produce polysiloxane thin films over high aspect ratio Ag nanowires that are pinhole free at thicknesses as small as 10 nm (Figure 1.17B) [29]. Following lithiation these polysiloxane films exhibit a modest conductivity of ~10^{-8} S cm^{-1} [29], [123], [124]. Despite the modest conductivity Chen *et al.* proposed that the modest conductivity is compensated by the lower ionic diffusion time constant (τ in *Eq. 1.5*) resulting from the iCVD siloxane's thickness (L_E in *Eq. 1.5*) being three to four orders of magnitude lower than a conventional solid electrolyte [29].

Li *et al.* built off the polysiloxane works and were able to produce solid copolymer electrolytes using iCVD. Hydroxyethyl methacrylate (HEMA) was crosslinked with ethylene glycol diacrylate (EGDA) to coat numerous high aspect ratio substrates (Figure 1.17C) with HEMA-*co*-EGDA films [27]. After doping with Li-containing salts (LiTFSI), these films exhibit a 6.1 x 10^{-6} S cm^{-1} ionic conductivity, the highest value reported for a nanoscale conformal electrolyte [27]. Another unique feature of the iCVD films is that the conductivity and mechanical properties are easily changed by manipulating the monomer precursor concentrations, allowing design of an electrolyte suitable for electrochemical performance and mechanical integration [27], [125].

Chapter 3 of this thesis contains an extensive literature review of conformal 3D electrolyte fabrication techniques, materials systems and their associated ionic conductivities to identify the top candidates to make 3D batteries a commonplace reality. Chapter 4 contains a breakdown of the theory behind obtaining conformal iCVD coatings on high aspect ratio substrates, such as aligned CNTs, and the resulting experiments to produce and characterize iCVD coated CNT structures and the ionic conductivity of the resulting films.

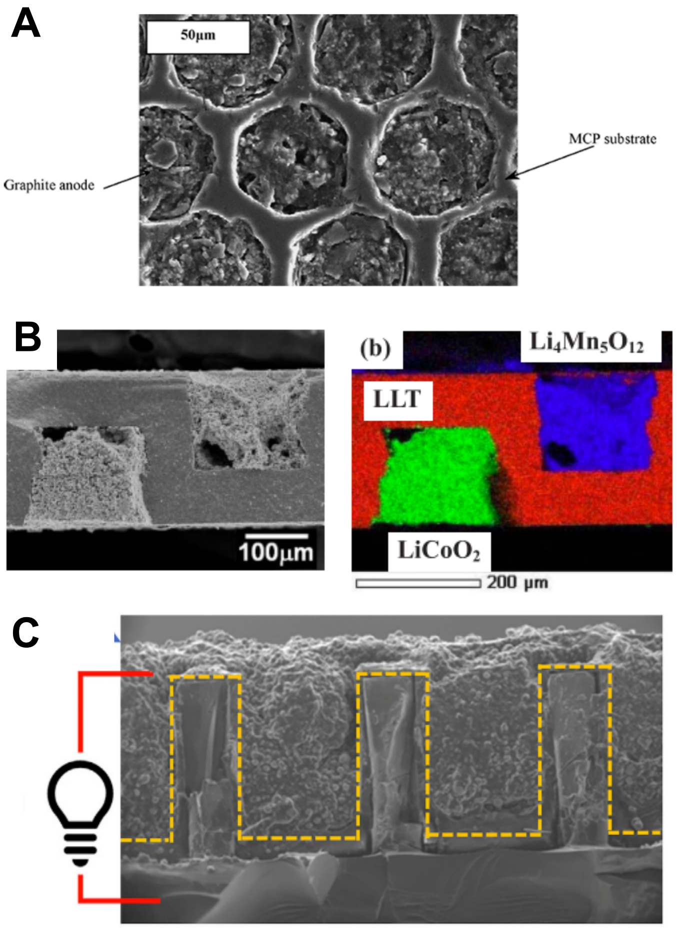

Figure 1.18: Examples of infiltrated electrode slurries in 3D micro-batteries. A) graphite slurry in microchannel glass plate. Reproduced with permission [53]. Copyright 2005, IEEE. B) LCO and LMO slurry in honeycomb SSE. Reproduced with permission [49]. Copyright 2010, IOP. C) NCA slurry between Si micropillars. Reproduced with permission [50]. Copyright 2018, Elsevier.

1.4.5 Full Cell Fabrication and Modeling

The final step in micro-honeycomb CNT battery fabrication is infiltrating a slurry containing positive electrode active material into the spacing between the CNTs pores. The infiltrated slurry will be similar to those in traditional LiB containing 80-90 wt.% (~45-50 vol.%) active material (NMC, NCA or LCO, 100-500 nm diameter) with the balance containing binder, electrolyte and conductive carbon additives [5], [7]. Several works in Table 1.4 have infiltrated electrode slurry's using vacuum infiltration and SEM for these are shown in Figure 1.18 [49], [50], [53].

While the previously mentioned works have infiltrated active material particles into micron sized pores, one significant challenge is infiltrating maintaining ionic conductivity throughout the electrode cross section. Generally, this issue is addressed by soaking or injecting the electrodes in a traditional liquid electrolyte [50], [53], and this strategy will be utilized here to enable Li-ion diffusion through the Si-CNT composite and the slurry-cast electrode. Once the slurry is infiltrated the Al positive electrode current collector is attached to the infiltrated slurry to complete the cell. Chapter 5 contains work on infiltrating slurry into patterned CNT structures, including the impact of cross-linking on iCVD electrolyte stability and a proof-of-concept CNT-based full cell.

In conjunction with the fabrication process Chapter 5 also contains finite element analysis (FEA) simulations used to identify limiting factors and predict 3D CNT-battery performance. The schematic in Figure 1.19A outlines the notation used for the micro-honeycomb geometries discussed in this section. A *d*-*a* honeycomb describes a hexagonal unit cell with hole diameter *d* and center-to-center distance *a* in μm. The primary goal in the materials and honeycomb structure selection is to increase the cell level energy density and power density with respect to a conventional LiB. One important consideration already mentioned was the Ohmic resistivity across the electrolyte, as the iCVD poly(HEMA-*co*-EGDA) has an ionic conductivity three orders of magnitude lower than the those of conventional electrolytes. In order for poly(HEMA-*co*-EGDA) to be competitive at thicknesses between 0.1 and 1 µm, the contact area between electrode and electrolyte needed to increase by a factor of 10 to 100 compared to a conventional SSB. Figure 1.19B shows the surface area ratio (SA_r) for numerous honeycomb spacings. The SA_r is the ratio of electrode surface area in the honeycomb design to a planar design of equal footprint area. Honeycomb geometries with features sizes in the 5-20 µm range meet this requirement at forest heights in the 100-300 µm range, indicating that these feature sizes are a good place to start for honeycomb patterning and CNT growth.

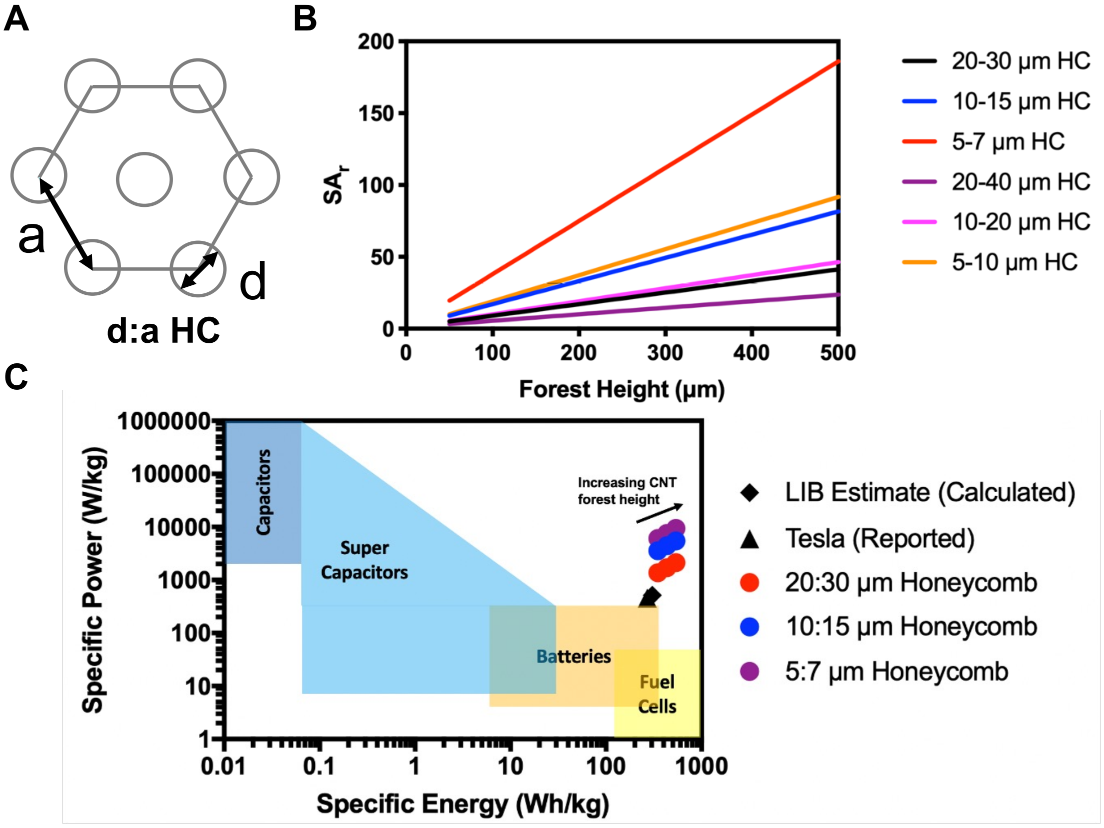

Figure 1.19: A) schematic demonstrating notation for honeycomb geometries, a is the center-to-center spacing and d is the hole diameter. B) comparison of surface area ratio between micro-honeycomb scaffold and planar batter with same footprint. C) Plot comparing energy and power density between conventional LiB and micro-honeycomb CNT battery at the cellular level. Performance ranges in C) taken from [35].

Estimated ideal specific energy and specific power densities for micro-honeycomb CNT batteries with features in the 5-40 µm range are compared with a LiB Figure 1.19C [7]. These calculations are performed at the cellular level, including current collectors. The specific energy density is calculated by multiplying the total charge within the cell by the average operating voltage. The specific power density is estimated by multiplying the cell's energy density by the cells discharge time constant, estimated using *Eq. 1.5*. At forest heights above 100 µm the micro-honeycomb CNT batteries begin to show superior energy and power performance compared to traditional LiB. The improvement in energy density is due inactive component removal (binder in negative electrode and separator), minimized contribution of inactive components (current collectors by tall forests), thin poly(HEMA-*co*-EGDA electrolyte) and the high-capacity Si used in the negative electrode. The increased power density is controlled by the decreased diffusion distances in the honeycomb's thin electrodes and electrolyte compared to the LiBs separator and thicker electrodes.

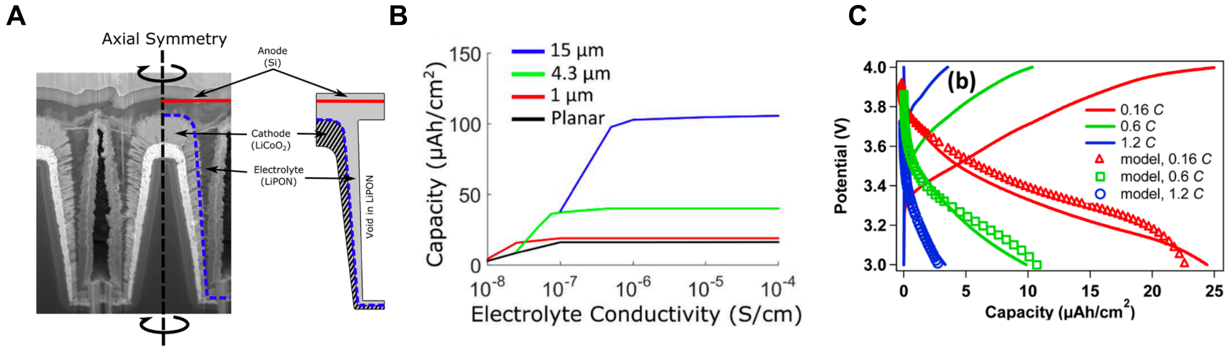

Figure 1.20: A) Schematic for 2.5D SSB. Reproduced with permission [126]. Copyright 2016, American Chemical Society. B) 2.5D SSB discharge capacity as a function of electrode height and SSE ionic conductivity. Reproduced with permission [127]. Copyright 2017, The Authors. C) Comparison between experimental and modeled discharge curves. Reproduced with permission [126]. Copyright 2016, American Chemical Society.

However, the specific energy densities presented in Figure 1.19C are calculated assuming no Ohmic, kinetic or mass transport losses. Finite Element Analysis (FEA) tools, such as COMSOL, allow for an in depth look at how material properties and cell geometries affect important electrochemical processes that affect cell behavior and performance. These simulations can used to understand limitations in cell behavior and improve cell materials selection and design. For example, McKelvey *et al.* and Talin *et al.* used FEA to understand the limitations of their thin film 2.5D battery (Figure 1.20A) [126], [127]. The simulations showed how pillar height and SSE ionic conductivity influenced cellular capacity (Figure 1.20B), and noted that an ionic conductivity of at least 10^{-6} S cm^{-1} was required to prevent any unwanted capacity loss. These simulations matched well with experimental data (Figure 1.20C), and the authors predicted the discharge capacity could be improved if the conductivity of their electrolyte could be improved from 10^{-7} S cm^{-1} to the 10^{-6} S cm^{-1} threshold and be deposited to have uniform thickness [126], [127].

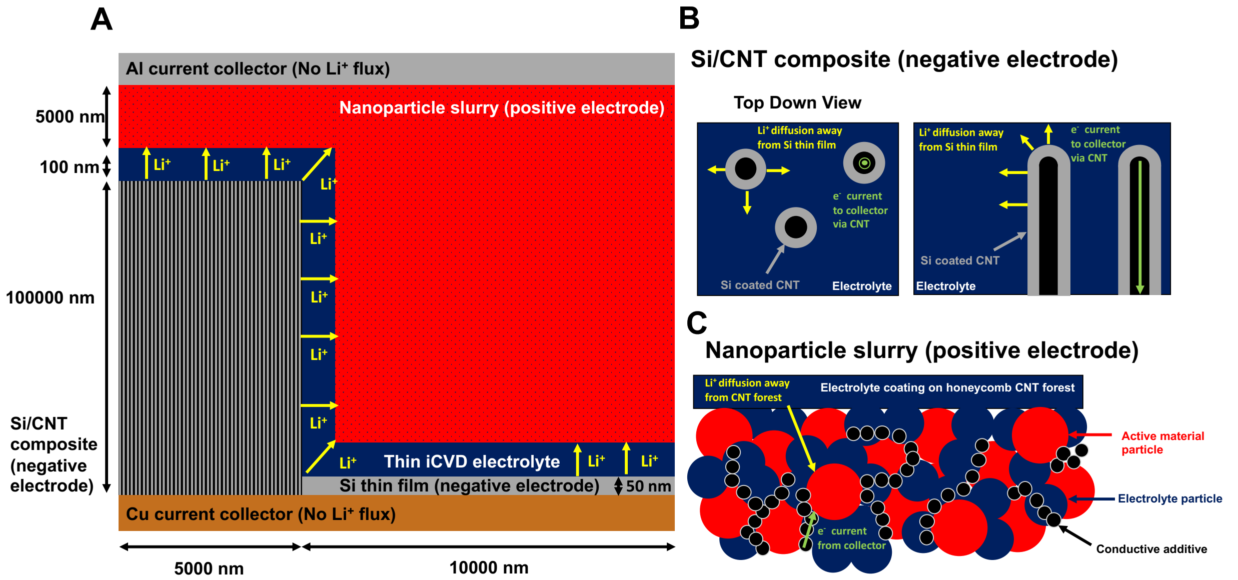

Figure 1.21: A) Schematic cross section for micro-honeycomb CNT battery along with Li^+ diffusion and e^- current directions and paths in the B) Si/CNT composite and C) nanoparticle slurry electrodes during discharge.

Generally, FEA analysis for 3D batteries has considered Li^+ diffusion and migration in the electrolyte (Nernst-Plank equation), Li^+ transport in the active material (Fick's laws) and Li^+ transfer across the electrode-electrolyte boundary (Butler-Volmer kinetics) [126]–[128]. In Chapter 5 a similar approach is taken in COMSOL to model and predict the optimal behavior of 3D CNT batteries. This allows for insight into how the unique geometric and material features affect micro-honeycomb CNT battery performance, including the CNT forest height, honeycomb pore diameter, honeycomb wall thickness, electrolyte thickness and nanoparticle slurry thickness. An important focus is placed on how electrolyte ionic conductivity influence battery performance, as this was a limiting factor in pervious 3D battery performance [126], [127].

In addition to the cell level features from Figure 1.21A, the modeling will also be used to understand how the material properties and orientation in the negative and positive electrodes influence performance. The negative electrode (Figure 1.21B) consists of vertically aligned CNTs coated with Si and then poly(HEMA-*co*-EGDA) electrolyte. This results in a unique geometry, where the Li^+ ions will diffuse away from the Si thin films and the e^- will have a straight path to the current collector through the vertical CNTs. Here, properties of the CNTs, such as density, alignment and electronic conductivity, and Si thin films, like thickness, can be considered in the electrode model. The Li^+ and e^- transport pathways are vastly different in the infiltrated slurry positive electrode (Figure 1.21C), where the Li^+ and e^- are transported to meet at the active material particles via a winding, continuous pathway of solid electrolyte or conductive additive particles. In this electrode model material parameters such as particle size, volume fraction, diffusion or conduction path tortuosity and additive electronic conductivity are implemented to understand their effect on battery behavior.

1.4.6 Conclusions and Outlook

Chapter 6 consists of a summary of this work, including the relevant contributions to the field, and comments on potential future works.

THIS PAGE IS LEFT INTENTIONALLY BLANK

Chapter 2- Thick Architected Silicon Composite Battery Electrodes Using Honeycomb Patterned Carbon Nanotube Forests

2.1 Abstract

The immediate and ever-increasing energy demands for personal electronic and electric vehicle performance can be met by increasing the energy density of lithium-ion batteries, which can be achieved by incorporating thick electrodes. However, increasing electrode thickness requires new architectures to maintain mechanical integrity and adequate conductivity. We present thick architected "honeycomb" battery electrodes using patterned, vertically aligned carbon nanotubes (VA-CNTs) as current collectors. VA-CNT forests are grown by atmospheric pressure CVD on Cu foils coated by a patterned thin film catalyst. The CNT forests reach ~400 μm thickness with uniform vertical hole arrays (aspect ratios up to 20:1). Thick composite electrodes are created by LPCVD deposition of Si on individual CNTs, enabled by the inherent nanoporosity of the CNT forests (> 95%). These Si-CNT electrodes are cycled in half-cells and electrodes with 3.5-4.3 mg/cm^2 Si loadings achieve ~4.7 mAh/cm^2 areal capacities, demonstrating electronic connection between the Si and Cu foil via the aligned CNTs. The honeycomb patterning significantly improves capacity retention (78%) over the first 30 cycles compared to non-patterned electrodes (58%). We attribute this retention improvement to the honeycomb's ability to accommodate Si expansion, thereby reducing cracking that might cause active material loss and SEI instability. The Si-CNT electrode capacity can be increased to 20 mAh/cm^2 by increasing the Si loading. Finally, a fluoroethylene carbonate containing electrolyte is used to increase cell

lifetime. Here, the honeycomb electrodes have a higher areal capacity (~10.2 mAh/cm^2) and retained (74%) capacity over 105 cycles, with currents ranging from 100 mA/g to 400 mA/g, than their non-patterned counterparts. Our work here demonstrates the role that patterning plays in enabling aligned CNT electrodes with high areal capacity and extended lifetimes. These Si-CNT electrodes serve as a robust template for thick electrode development and with potential further improvement through CNT height and honeycomb dimension optimizations.

2.2 Introduction

The growing demand for electric vehicles and portable electronics has created a significant interest in the scalability, recyclability, and economics of both traditional and emerging battery technologies. Despite their commercial dominance, lithium-ion batteries are approaching the maximum theoretical energy density achievable under their current configuration, making it difficult to keep up with consumer demands and industry targets [1], [10], [34], [35]. One strategy for increasing cell level energy density is to incorporate thicker electrodes which reduce the volume and mass contributions of inactive components, such as the current collectors and separators. Current lithium ion cells utilize slurry cast electrodes with < 60 μm thickness that have areal capacities on the order of 2-4 mAh/cm^2 [101], [129] and significant energy density gains can be achieved by increasing electrode thickness to > 100 μm [34], [35], [76]. For example, in their review Kuang *et al.* calculated that increasing the electrode thickness from 25 μm to 200 μm reduced the inactive volume component from 44 wt.% to 12 wt.%, which corresponded to a 30 wt.% increase in active material loading [34].

Several considerations arise when designing thick electrodes, which do not favor slurry-cast designs. Foremost is the significantly larger diffusion distance encountered by Li-ions as the tortuous slurries are made thicker, along with increased mechanical fatigue which degrades the electronic connection between the active material and the current collector [34], [35], [76]. Three-dimensionally (3D) structured electrode designs can overcome these issues by providing micro-scale channels to enable rapid charge transport and accommodate active material expansion. To meet these criteria, the materials used in 3D electrodes must be mechanically robust, electrically conductive, and processable in a manner enabling precise control over geometry and thickness [34].

Previous works have produced 3D structured electrodes by utilizing Si nanowires [40], ion etched Si trenches [41] and active material coatings on metallic nanowires [42]–[46]. However, these electrodes are difficult to produce at the required thicknesses and at scale. Carbon-based 3D structures are promising scaffolds to fabricate thick electrodes, due to their electrical conductivity, ability to be fabricated over a wide range of length scales, and porosity that allows for active material incorporation and volume expansion [35]. For instance, compared to the 2–4 mAh/cm^2 exhibited by commercial lithium-ion systems [101], [129], Narita *et al.* achieved 4 to 10 mAh/cm^2 capacity with ~1 mm thick pyrolyzed 3D polymer electrodes [130]; Zheng *et al.* utilized aligned carbon fiber frameworks loaded with $LiFePO_4$ to produce electrodes with 20 mAh/cm^2 capacity [131]; and Hu *et al.* and Luo *et al.* coated thick carbon nanotube sponges with Si [101] or SnO_2 [102], and demonstrated 20 mAh/cm^2 and 7.4 mAh/cm^2 performance respectively.

Carbon nanotube powders (CNTs) are commonly included in slurry based electrodes to provide enhanced electronic conductivity and mechanical resilience [55], [66], [109], [110], [132]. Vertically aligned carbon nanotubes (VA-CNTs or "forests") offer a means to translate these advantages to 3D electrodes. CNT forests form by self-organization during chemical vapor deposition (CVD) of common hydrocarbon sources (e.g., C_2H_2, C_2H_4) on catalyst coated substrates. The CNT forest height and geometry can be respectively tailored by controlling the growth (deposition) time [61], [64] and catalyst layer patterning [59], [133]. In an ideal 3D electrode these aligned CNTs serve as highways to move electrons from the current collector substrate to active material at the electrode extremes. However, well-established CNT growth techniques utilize rigid, non-conductive substrates, such as silicon or quartz wafers, which adds an extra layer of difficulty when incorporating VA-CNTs into electrochemical devices.

One route for enabling aligned CNT electrodes is to transfer the CNTs to a conductive substrate. Evanoff *et al.* grew ~1 mm long CNTs using an aerosol-based CVD process and thermally transferred them to a Cu foil to create a thick electrode that offered exemplary specific capacity when coated with Si [76]. Jessl *et al.* [75] and Ahmad *et al.* [112] produced patterned VA-CNTs on Si wafers before transferring them to poly(vinylidene difluoride) substrates doped with conductive additives and produced battery electrodes by adding Fe_2O_3 active material. Pawlitzek *et al.* grew aligned CNTs on Ni foil and coated them with $LiMn_2O_4$ and $Li_4Ti_5O_{12}$ particles before transferring them to Al foils for use in half and full cell experiments [77]. While all these works produced functional VA-CNT based lithium-ion electrodes, the ideal VA-CNT electrode fabrication process involves CNT growth directly onto a conductive substrate suitable for incorporation into a lithium-ion cell.

Although VA-CNTs have been grown on Ni [77], [79], [134], Inconel [80] or stainless steel [82], [83] foils, direct VA-CNT growth on metals typically used in lithium-ion batteries, such as Cu [12], is difficult. Cu exhibits a low bulk carbon solubility (0.0008 at.%) compared to Fe (0.4 at.%) or Ni (0.2 at.%), and therefore Cu cannot serve as the native catalyst for CNT growth. CNT growth on Cu necessitates the deposition of a thin catalyst layer (e.g., Fe or Ni), which must be supported by an insulating oxide layer (most commonly Al_2O_3) [71]. Yet, in this configuration Cu atoms diffuse through the support layer and poison the catalyst layer, compromising CNT yield

[71], [92]. CNTs can be grown directly on Cu foil by using thicker Al_2O_3 layers and carefully controlling annealing time [91], [92]. Ezzedine *et al.* fabricated a 50 nm thick Al_2O_3 film beneath their Fe catalyst layer to grow CNTs with heights up to 145 μm and then utilized 30 to 60 μm tall Si coated forests as electrodes [91]. These non-patterned forests demonstrated respectable areal capacities up to 8.5 mAh/cm^2 but suffered poor capacity retention at higher Si loadings, as ~40% of the starting capacity had been lost after 40 cycles. The authors attributed these losses to Si and solid electrolyte interphase (SEI) cracking and pulverization during cycling [91].

More flexibility in the growth process and taller CNTs can be obtained by utilizing a thin, electrically conductive diffusion barrier between the metallic substrate and oxide support layer [71], [93]. Recently, Lettiere et al. demonstrated that a thin W layer, deposited in the middle of the Al_2O_3 layer between the Cu and Fe, prevented Fe catalyst poisoning and, by tailoring of the CVD recipe, grew tall (~270 μm) CNTs directly on Cu foils. The obtained CNT forests were found to have low resistance (< 50 Ω) when measured through the thickness of the CNT forest and foil. This low resistance was attributed to cracks forming in the Al_2O_3 support layers and high CNT density and quality [64], [71].

Here, we build off Lettiere *et al.*'s work by utilizing their catalyst stack to develop architected 3D Si-based battery electrodes using honeycomb-patterned CNT forests grown directly on Cu foils. Using our growth process these forests consistently reach heights over 250 μm and can approach thicknesses of 400 μm. The role of these honeycomb patterns is twofold. First, they provide ease of diffusion for precursor materials to allow for uniform active material coatings deep inside the forest. In our case we utilized low pressure chemical vapor deposition (LPCVD) Si. LPCVD allows for active material incorporation by conformal coating the individual CNTs while Si has a high specific capacity that will allow for further capacity gains when paired with a thick electrode design. Second, during cycling of these Si-CNT electrodes the honeycomb accommodates active material expansion to reduce capacity fading upon repeated cycling. The honeycomb patterned Si-CNT electrodes exhibit capacities up to ~20 mAh/cm^2 and ~1750 mAh/g$_{Si}$ upon cycling and demonstrates the role patterning plays in enabling thick Si-CNT electrodes by allowing for high areal Si loadings and improved capacity retention upon repeated cycling.

2.3 Results and Discussion

To realize architected Si-CNT electrodes, we first developed a robust protocol for tall VA-CNT growth on Cu foils, adapted from the Fe/Al_2O_3/W/Al_2O_3 film stack first demonstrated by Lettiere *et al*. [71] To grow the VA-CNTs we utilized a homebuilt CVD furnace containing a transfer arm to allow samples to be moved in and out of the furnace during the growth process (Figure 2S.1A and Figure 2S.1B). We utilized a growth recipe similar to our previous works [64], [71], with the catalyst coated Cu foils starting outside the furnace as the furnace temperature increases to 775 °C. The foils are inserted into the furnace and annealed under He and H_2 before being removed. With the samples outside the H_2O content inside the tube was then increased to ~2350 ppm before reinserting the samples to grow VA-CNTs in a mixture of He, H_2, H_2O and C_2H_4 at 775 °C. Detailed information on catalyst preparation and the CNT growth process can be found in the experimental information section and supporting information.

To consistently achieve tall VA-CNTs (150–250 μm) suitable for thick electrode development we performed a parametric study of growth time and sample position on the transfer arm. For each growth the transfer arm was loaded with four samples (Figure 2S.1B). Growth times ranged from 1 to 20 min and VA-CNT height was determined by averaging post-growth scanning electron microscopy (SEM) measurements at five points along the forest sidewall. SEM images show the well aligned and tall nature (Figure 2.1A, Figure 2S.1C and Figure 2S.1D), along with the inherent nanoporosity (Figure 2.1B), of the VA-CNT forests on Cu foils. These growths are similar to VA-CNTs on Si wafers, and should act as an excellent scaffold for active material deposition [59].

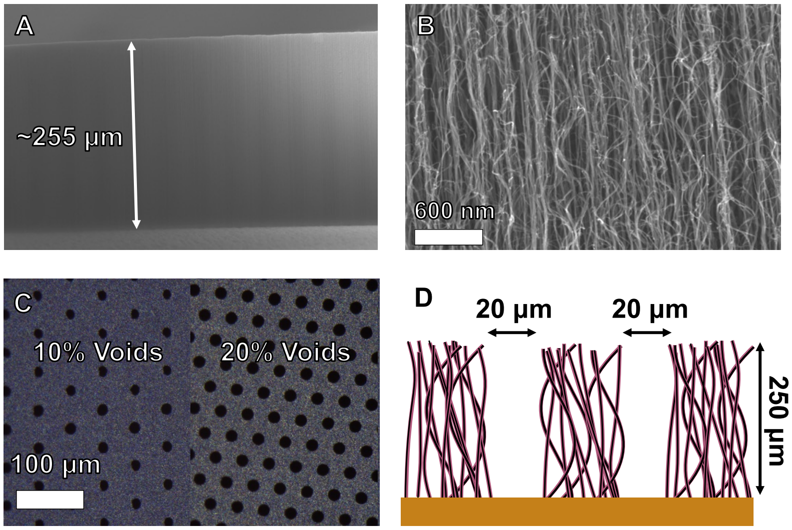

Figure 2.1: A) SEM image of a 20% VA-CNT forest sidewall. B) SEM image showing the inherent nanoporostiy of VA-CNTs. C) Optical microscopy image of honeycomb patterned CNTs with 20 μm diameter holes. The spacing of the holes can be modified to change the electrode void fraction. D) Schematic of honeycomb patterned VA-CNTs electrodes (gold-Cu, black-CNT) with active material coating (pink-Si).

Figure 2S.1E shows that boat position significantly influences VA-CNT height for growth times longer than 5 min; with VA-CNT height being lowest at the most upstream position, increasing at the middle two positions and decreasing for the most downstream position. We speculate that the increase in height at the middle two positions is enabled by C_2H_4 breakdown over the most upstream sample, while attributing the lower height of the final downstream sample to carbon precursor depletion. From Figure 2S.1F we utilize samples in the second position after a 20 min growth (~250 μm tall) as an optimal starting point for our thick electrode fabrication.

Raman analysis (Figure 2S.2A) indicates the forests are comprised of multiwall CNTs, as evidenced by the strong D-band at ~1330 cm^{-1} and G-band at ~1580 cm^{-1} which are respectively attributed to the sp^2 lattice vibrations and defects in this lattice [135], [136]. The VA-CNTs have a high decomposition temperature (~710 ^{o}C) when characterized by thermogravimetric analysis (TGA) under air. Unlike our previous growths at ~220 ppm H_2O, the TGA data in Figure 2S.2B does not show any mass loss at ~200 ^{o}C, suggesting that the higher moisture (~2350 ppm) during the atmospheric CVD growth process removed amorphous carbon *in situ* [69], [71], [137]. This is advantageous for tall VA-CNT growth, as unchecked amorphous carbon deposition rapidly forms a coating that kills catalyst activity [137].

Patterned VA-CNTs are similarly produced on Cu foils by lithographic patterning of the catalyst film prior to CNT growth. Using a direct-write maskless patterning procedure, which allows us to rapidly change the hole spacing and diameter, and conventional photolithography techniques we produced a variety of catalyst honeycomb patterns (Figure 2S.3A and Figure 2S.3B). For electrode development we produced honeycomb patterns with controlled void percentages by varying the 20 μm diameter hole spacing (Figure 2.1C). Under identical growth conditions, the honeycomb VA-CNTs with 20% voids are a similar height as the nonpatterned samples (Figure 2.1A). The tall and uniform growth was consistent for a variety of honeycomb patterns (Figure 2S.3C and Figure 2S.3D), demonstrating that our patterning and growth process provides exceptional control over electrode thickness and porosity distribution.

While VA-CNTs on Cu can be an excellent 3D current collector due to their high electrical conductivity, CNTs are an inherently poor active material due to their tendency to lithiate largely irreversibly [55], [66]. Therefore, it is necessary to incorporate an active material onto the CNTs to increase the electrode's reversible capacity. Si emerged as an attractive active material coating as it is readily abundant and has a high specific capacity (~3600 mAh/g), which makes it an attractive replacement for the conventional graphite anode (~372 mAh/g) when designing high energy density cells. Furthermore, conformal, Si coatings have been achieved on a number of high aspect ratio structures using CVD deposition methods from conventional semiconductor processing [76], [83], [91], [96], [97], [101], [107], [110], [138]. Figure 2.1D shows a schematic of a honeycomb VA-CNT electrode with a conformal Si coating to enable high capacity.

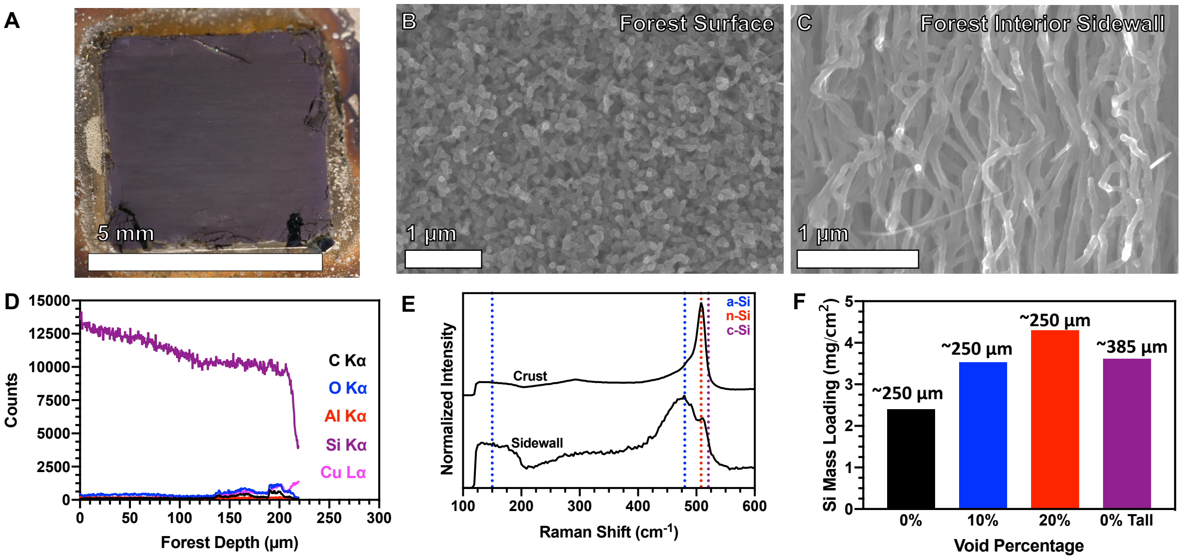

Figure 2.2: A) Si-CNT composite electrode on Cu foil. Characterization of Si coated VA-CNTS including SEM images of B) surface and C) interior sidewalls, D) interior EDS linescan and E) Raman spectroscopy. F) Si mass loading for VA-CNT architectures following a 36 min deposition. Electrodes are ~250 μm tall except for the 0% Tall sample, which is ~385 μm tall.

Despite having a high specific capacity, Si electrodes suffer from significant capacity fading as Si undergoes a ~300% volume change during cycling [11], [91]. This expansion and contraction process, as experienced in the work of Ezzedine *et al.*, causes active material loss through delamination or pulverization, and repeatedly destroys the protective SEI layer that forms during cycling [91]. This continual SEI reformation not only depletes active material but also consumes electrolyte and leads to increased cell impedance [8], [19]. These losses can be mitigated by the large porosity and hierarchal structure of 3D carbon scaffolds, such as our honeycomb VA-CNTs.

We used a low-pressure chemical vapor deposition (LPCVD) process to deposit amorphous Si (a-Si) on our VA-CNTs and produce Si-CNT composites (Figure 2.2A). SEM images show that conformal Si coatings are obtained on top surface (Figure 2.2B) and interior (Figure 2.2C) of the forests. Energy dispersive X-ray spectroscopy (EDS, Figure 2.2D) shows a consistent Si signal from the forest surface to base. The results in Figure 2.2B through Figure 2.2D indicate that the LPCVD process conformally coats the CNTs from top to bottom throughout the entire forest, enabling high theoretical capacity by large Si loading. We further analyzed the Si coatings through Raman spectroscopy (Figure 2.2E). Both the top and sidewall measurements show a broad band centered at ~480 cm^{-1} indicative of amorphous Si (a-Si). The absence of a sharp, symmetric peak at ~520 cm^{-1} indicates no bulk crystalline Si (c-Si) is formed during deposition. However, the top measurement shows a sharp, asymmetric peak at ~508 cm^{-1}. This peak is also present, albeit to a lesser degree, in the sidewall measurement and is attributed to nanocrystalline Si (n-Si) formation within the amorphous phase [139], [140].

These Si-CNT electrodes offer areal mass loadings (Figure 2.2F) competitive with existing commercial electrodes [141]. For a set ~250 μm height, honeycomb pattern VA-CNTs achieve higher mass loadings, likely due to honeycomb voids enabling the greater penetration of the precursor gases into the bulk of the forest. In fact, for a non-patterned (0%) forest to reach a similar areal loading as the honeycomb VA-CNTs in Figure 2.2F the forest height (0% Tall) must be increased to ~385 μm (Figure 2S.4).

We evaluate the electrochemical performance of the Si-CNT composite electrodes shown in Figure 2.2 by performing half-cell measurements against Li-metal foil. These Si-CNT electrodes are galvanostatically cycled (0.5 mA/cm^2) in a 1 M LiTFSI-0.1 M $LiNO_3$ 1,3 Dioxolane (DOL) electrolyte between 1 V and 0.05 V vs. Li/Li^+ with a constant voltage hold at 0.05 V on discharge (Si lithiation step). As shown in Figure 2.3A, the 10% and 20% honeycomb Si-CNT electrodes, as well as the taller non-patterned sample, achieve ~5 mAh/cm^2 areal capacities over their first few cycles, which is on par with commercial lithium-ion anodes (2–4 mAh/cm^2) [101], [108], [129]. Due to the lower mass loading of Si (Figure 2.2F), the ~250 µm tall non-patterned sample shows a lower areal capacity.

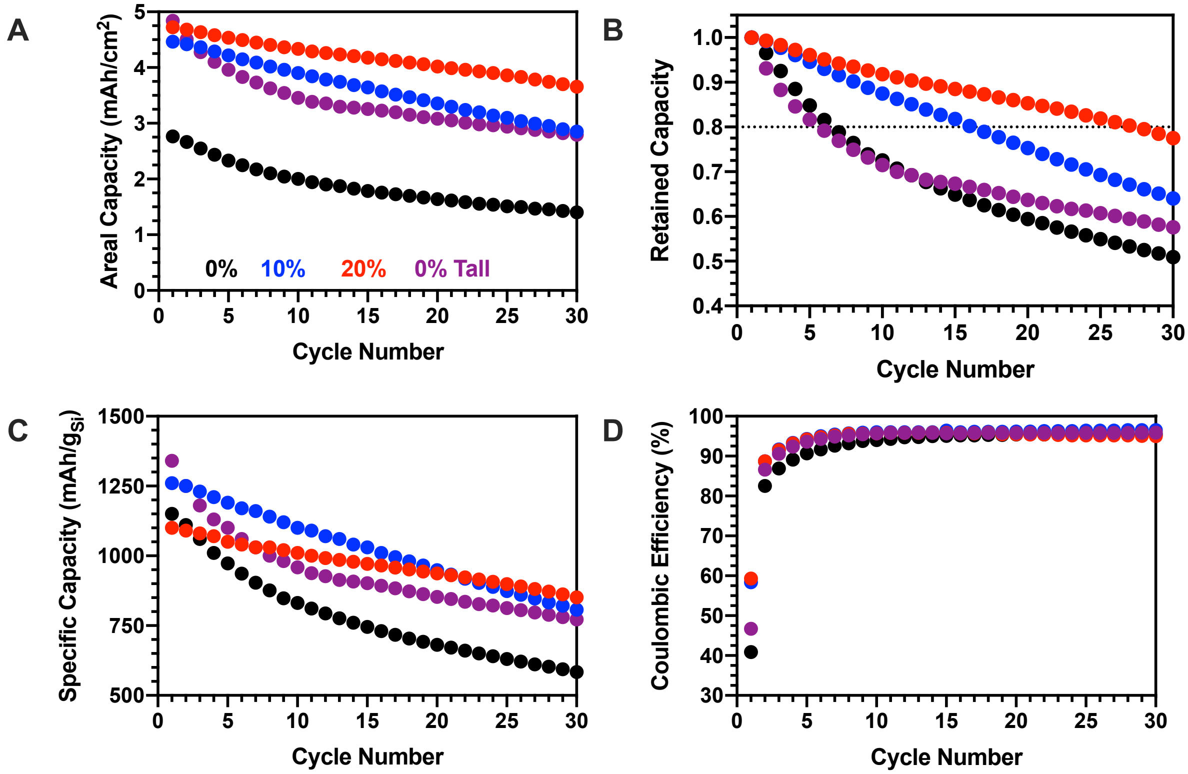

Figure 2.3: A) Areal capacity, B) retained capacity, C) specific capacity and D) coulombic efficiency for Si-CNT electrodes with various degrees of porosity. The Si-CNT electrodes were cycled in 1 M LiTFSI-0.1M $LiNO_3$ in DOL between 1 V and 0.05 V vs Li/Li$^+$ at 0.5 mA/cm^2. A voltage hold was applied at 0.05 V during the discharge (Si lithiation) until the current reached 20% of its starting value.

However, on repeated cycling the non-patterned samples' capacity fades rapidly, while the 10% and, especially, 20% honeycombs show much higher capacity retention. Figure 2.3B shows how the honeycomb structure influences capacity fading in our Si-CNT electrodes. Both the non-patterned samples show significant capacity loss over their first few cycles. In fact, both these non-patterned samples drop beneath 80% of their starting capacity, a criteria often used to define cell lifetime, after only the 7th cycle [142]. Honeycomb patterning mitigates this capacity fading as the 10% and 20% honeycomb electrodes drop beneath the 80% threshold in Figure 2.3B on their 17th and 28th cycle respectively. In addition, the honeycomb electrodes exhibit improved performance over the non-patterned samples by several other metrics. While all of Si-CNT electrodes obtain specific capacities that are on par with other nano-structured Si electrodes [101], [108], [132], [138], [141], the honeycomb electrodes offer a more stable specific capacity (Figure 2.3C) and higher coulombic efficiencies over the first five cycles (Figure 2.3D).

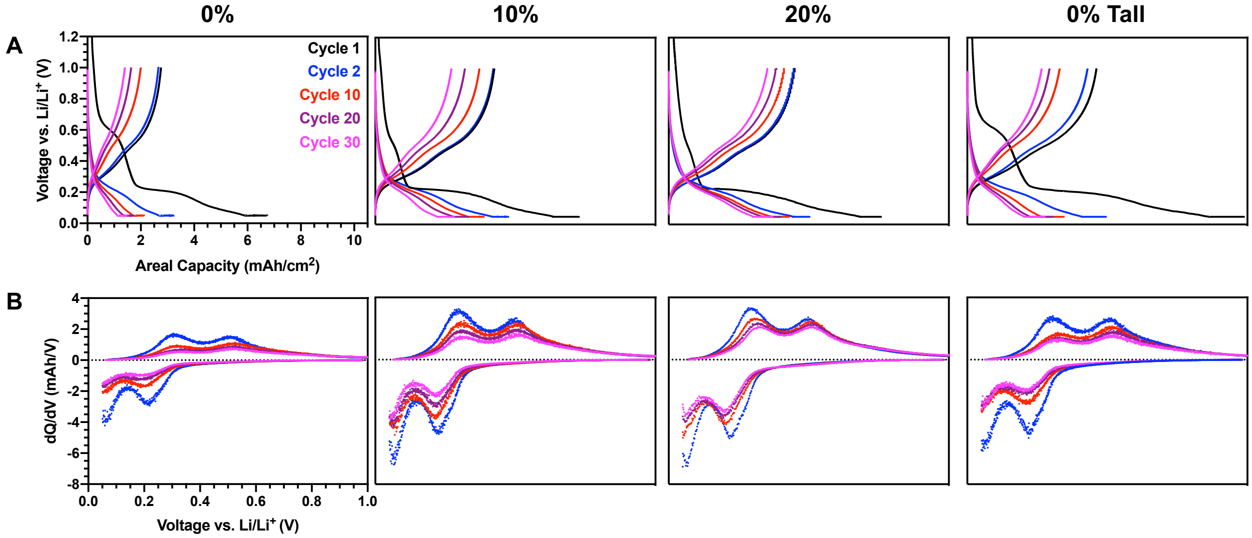

Figure 2.4: A) Voltage profiles and associated B) dQ/dV plots for Si-CNT electrodes with different honeycomb patterns. The Si-CNT electrodes were cycled in 1 M LiTFSI-0.1M $LiNO_3$ in DOL between 1 V and 0.05 V vs Li/Li^+ at 0.5 mA/cm^2. A voltage hold was applied at 0.05 V during the discharge (Si lithiation) until the current reached 20% of its starting value. The x- and y-axis are the same for all plots.

The charge-discharge profiles (Figure 2.4A) re-iterate the significant capacity fading of the non-patterned samples over the early cycles as well as the low coulombic efficiency on the first cycle. On first discharge both non-patterned samples exhibit a small plateau beginning at ~0.6 that results in a peak in the associated dQ/dV plots (Figure 2S.5). This peak likely corresponds to a SEI formation and electrolyte decomposition [143], [144]. This plateau is much shortened (Figure 2.4) and the associated peak much smaller (Figure 2S.5), almost to the point of absence, in the 10% and 20% honeycomb samples. We attribute this to more efficient SEI formation due to accommodation of Si expansion by the honeycomb voids that prevents cracking. This also explains why the non-patterned samples have a lower first cycle coulombic efficiencies than their honeycomb counterparts (Figure 2.3D).

The dQ/dV plots after the first cycle (Figure 2.4B) are typical for Si electrodes. During the second discharge, peaks are observed at ~0.22 V, corresponding to the formation of a-Li_2Si, and at ~0.06 V, corresponding to the formation of a-$Li_{3.5}Si$. Upon charging there are peaks at ~0.3 V and ~0.49 V that represent the delithiation of a-$Li_{3.5}Si$ to a-Li_2Si and then a-Li_2Si to a-Si [110], [145], [146]. As cycle number increases the lithiation and delithiation peak behavior for the 10% and 20% honeycomb electrodes is different when compared to the non-patterned electrodes. As cycle number increases, the non-patterned electrodes show a rapid drop-off in the intensity of the lithiation peaks at ~0.22 V, while the peak at ~0.06 V shifts outside of the 0.05 V voltage cutoff. A similar decrease is visible during half-cell charging, where the intensity of both delithiation peaks drop substantially for the non-patterned samples. The decrease in these peaks, in particular at ~0.06 V, correlates with the capacity fade exhibited during cycling. In the honeycomb electrodes, the intensity of the lithiation and delithiation peaks is reduced, with the 20% electrode exhibiting less peak intensity loss than the 10% electrode, and the ~0.06 V peak remains inside the voltage cutoff range, indicating a higher degree of Si lithiation for the honeycomb samples. From the second cycle onward, we do not see any significant peaks in the dQ/dV plots that might correspond to lithiation or delithiation of CNTs. The absence of these peaks is likely due to the lower specific capacity (~200 mAh g^{-1} vs. ~3600 mAh g^{-1}) and areal mass loading (< 0.5 mg/cm^2 vs. > 1.5 mg/cm^2) of the CNTs when compared to the deposited Si coatings.

We look to the nature of Si lithiation to explain why the honeycomb electrodes offer improved capacity retention over the first 30 cycles. The significant volume change upon lithiation of Si underscores two mechanisms that lead to capacity fade: formation of electrically isolated Si through delamination or pulverization, and the consumption of electrochemically active Si, electrolyte salt and electrolyte solvent through SEI destruction and reformation [8], [19]. The Si coating on the top surface of the forest is quite dense, allowing little room to accommodate Si expansion and contraction. The constrained Si expansion on the surface likely results in cracking that causes constant SEI reformation, a process that continually consumes electrolyte components and creates a thick SEI that clogs the electrode. As a result Li-ion transport and cell resistance increase, causing the lithiation and delithiation overpotentials to increase [146], [147]. This is evident in the dQ/dV (Figure 2.4B) plots for both non-patterned electrodes, where the increased overpotential shifts the a-$Li_{3.5}Si$ formation below the 0.05 V cutoff. In addition to the electrode structural differences (non-patterned vs. honeycomb), the deposited Si's structure also influences electrode performance. The Raman analysis (Figure 2.2E) shows that the top surface of the electrode contains a significant amount of n-Si whereas the sidewalls contain more a-Si. Therefore, the non-patterned samples experience additional losses due to their increased crust surface area, as crystalline forms of Si are known to experience increased densification that lead to a loss of ionic conductivity in the electrode [147], [148]. This is not the case in the honeycomb samples, where the patterned 20 μm holes provide room to accommodate Si expansion and allow a pathway for Li-ions to penetrate deeper into the electrode once the SEI forms on the top surface.

This hypothesis is validated upon further cycling. The capacities, charge-discharge profiles and dQ/dV plots for the Si-CNT electrodes after 100 cycles are presented in Figure 2S.6, Figure 2S.7 and Figure 2S.8, respectively. As cycling progresses the areal, specific and retained capacities (Figure 2S.6) for all Si-CNT samples converge to the same value. The 20% honeycomb sample takes longer (~50 cycles) to converge with the behavior of the other samples, and does so only after a significant drop-off around cycle 37. In the Figure 2S.8 dQ/dV plots, the 10% and 20% honeycomb electrodes eventually suffer the same shift in lithiation and delithiation potential experienced by the non-patterned electrodes earlier in their cycle life. After 100 cycles, the electrodes (Figure 2S.9) were removed from the cells, washed and taken for SEM analysis (Figure 2S.10). The SEM analysis shows that the once pristine 10% and 20% honeycomb structures (Figure 2.1C) are now covered with a thick, polymer-like SEI layer that clogs the honeycomb structure. This film is likely formed by the $LiNO_3$-initiated polymerization of DOL, as is commonly observed on Si electrodes [149], [150]. At low cycle numbers this SEI layer has yet to fill the honeycomb holes, allowing easier Li-ion penetration into the electrode and higher areal capacities. As cycling continues this film fills up the honeycomb holes, resulting in degraded performance that eventually matches the non-patterned electrode. Some performance degradation should also be contributed to the formation of SEI on the Li-metal counter electrode, as DOL-based electrolytes are known to have low room temperature coulombic efficiencies when cycled with Li-metal. We find the coulombic efficiency on Li-metal to be ~85% (Figure 2S.11), indicating that issues, such as unstable SEI or unreacted Li formation, at the Li-metal electrode may contribute to eventual cell decline in tandem with the SEI issues on the Si-CNT electrodes. This could be mitigated in future works by cycling at elevated temperature [149], [151], [152]. Since all cells in Figure 2.3 were fabricated under identical conditions we attribute the increased performance of the honeycomb electrodes to their more porous structure. Altogether, our results show that the honeycomb patterning plays a crucial role controlling capacity retention in our Si-CNT electrodes.

In addition to cycling Si-CNT electrodes at 0.5 mA/cm^2 we also cycled a 40% honeycomb and a non-patterned electrode in a 1 M LiTFSI-DOL electrolyte at 2 mA/cm^2 for 150 cycles before dropping the current to 1 mA/cm^2 for an additional 150 cycles. The 40% honeycomb electrode exhibits superior areal Si loading (Figure 2S.12A), areal capacity (Figure 2.5A), specific capacity (Figure 2S.12B) and retained capacity (Figure 2S.12C) over these 300 cycles. The small bump in capacity over the first few cycles is attributed to cracking in the Si film that exposes additional Si material, enabling it to lithiate on future cycles [153]. While the non-patterned electrode has a higher starting specific capacity (Figure 2S.12B) it is overtaken by the 40% honeycomb electrode. Here we hypothesize that the higher current density limits the honeycomb's ability to utilize the additional Si located deeper inside the honeycomb structure, with the non-patterned electrode's higher external Si content allowing for more effective Si utilization at earlier cycles. However, due to previously mentioned failure mechanisms, the 40% honeycomb electrode does not experience the same degree of capacity fading as the non-patterned electrode, which enables it to achieve a higher specific capacity upon repeated cycling.

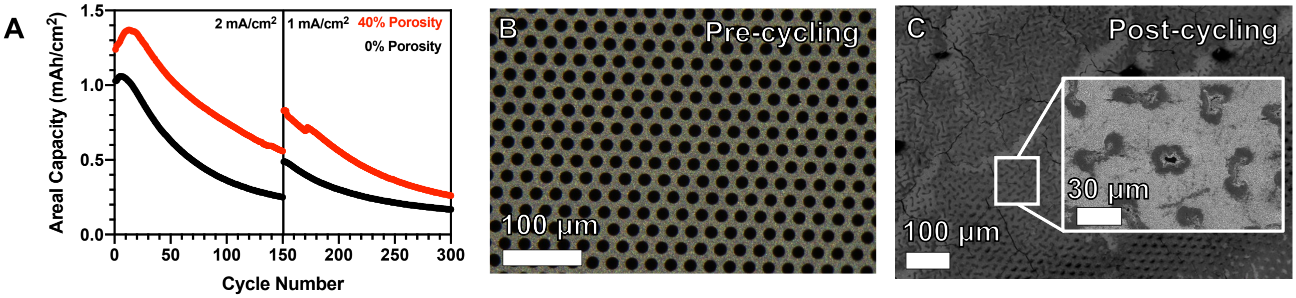

Figure 2.5: A) Areal capacity for 40% and 0% Si-CNT electrodes 2 mA/cm^2 and then 1 mA/cm^2 for 150 cycles at each current density in 1 M LiTFSI in DOL between 1 V and 0.05 V vs. Li/Li$^+$. B) Pre-cycling optical microscopy image and C) post cycling SEM image for the 40% honeycomb electrode.

In Figure 2.5B we show an optical microscopy image of the 40% honeycomb structure prior to cycling, and in Figure 2.5C we see the same electrode by SEM after completing 300 cycles. Since there is no $LiNO_3$ present in this electrolyte, the post cycling image does not exhibit the polymeric film seen previously (Figure 2S.10). The lack of polymeric film allows us to observe that the combination of SEI formation and Si expansion fill up honeycomb over the 300 cycles. This also explains the cycling behavior in Figure 2.5A and Figure 2S.12, where the capacities of the 40% honeycomb and non-patterned electrode converge at high cycle number. At low cycle numbers the pores allow enhanced Li-ion diffusion into the electrode, enabling higher capacity, but once the pores close off the 40% honeycomb behaves similarly to the non-patterned electrode.

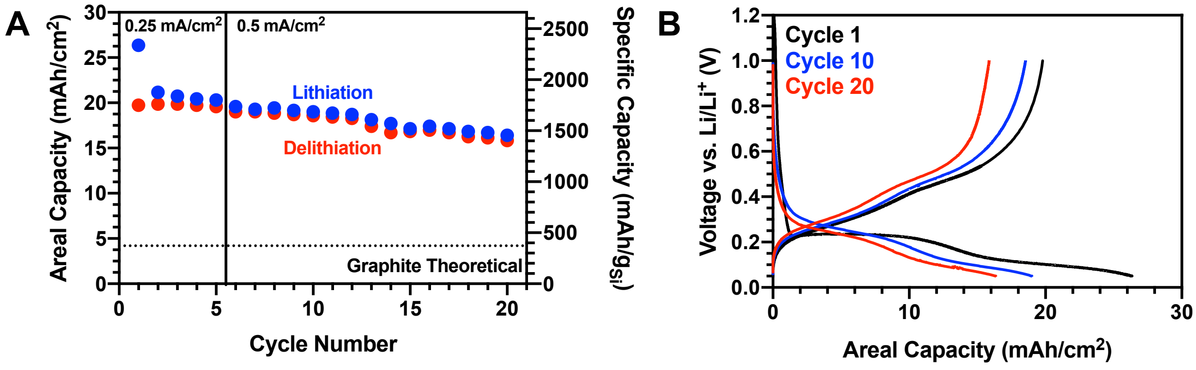

Figure 2.6: A) Capacities and B) voltage profiles for a 20% honeycomb Si-CNT with 11.3 mg /cm^2 Si loading electrode cycled in 1 M LiTFSI in DOL between 1 V and 0.05 V vs. Li/Li$^+$.

Next, we increase the Si loading to determine the honeycomb Si-CNT electrodes ability to function as a thick electrode with high areal capacity. Figure 2.6 shows the results of a 20% honeycomb electrode, with a ~11.3 mg/cm^2 Si loading, cycled between 1.0 V and 0.05 V vs. Li/Li$^+$ in 1 M LiTFSI-DOL. Over 20 cycles this high Si loading 20% honeycomb electrode exhibits an initial a capacity of ~19.7 mAh/cm^2 and with >15.8 mAh/cm^2 retained after 20 cycles, approximately 3–5 times higher than existing slurry cast lithium-ion electrodes [101], [129]. On the 21st cycle the electrode fails to reach the charge voltage (Figure 2S.13A). A similar phenomena was observed by Park *et al.* for their segregated Si-CNT electrodes when the areal capacity was increased to ~30 mAh/cm^2 [109]. We attribute this to micro-shorts due to dendrites that arise from the overstressed Li-metal foil [154] and serious electrolyte depletion [109], [155], rather than failure of the Si-CNT electrode itself. Dendrite formation in Si-Li cells is strongly related to the applied pressure, which could be optimized in future work [156]. The dQ/dV plots show stable Si lithiation and delitiation on previous cycles (Figure 2S.13B) and a post failure photograph shows significant structural damage to the electrode (Figure 2S.13C) that we attribute to increased stresses from Si expansion due to the higher loading. We found that non-patterned Si-CNT electrodes with higher Si loading (> 3.8 mg /cm^2) tend to short on their first discharge (Figure 2S.14), again demonstrating the superiority of the honeycomb patterned electrodes.

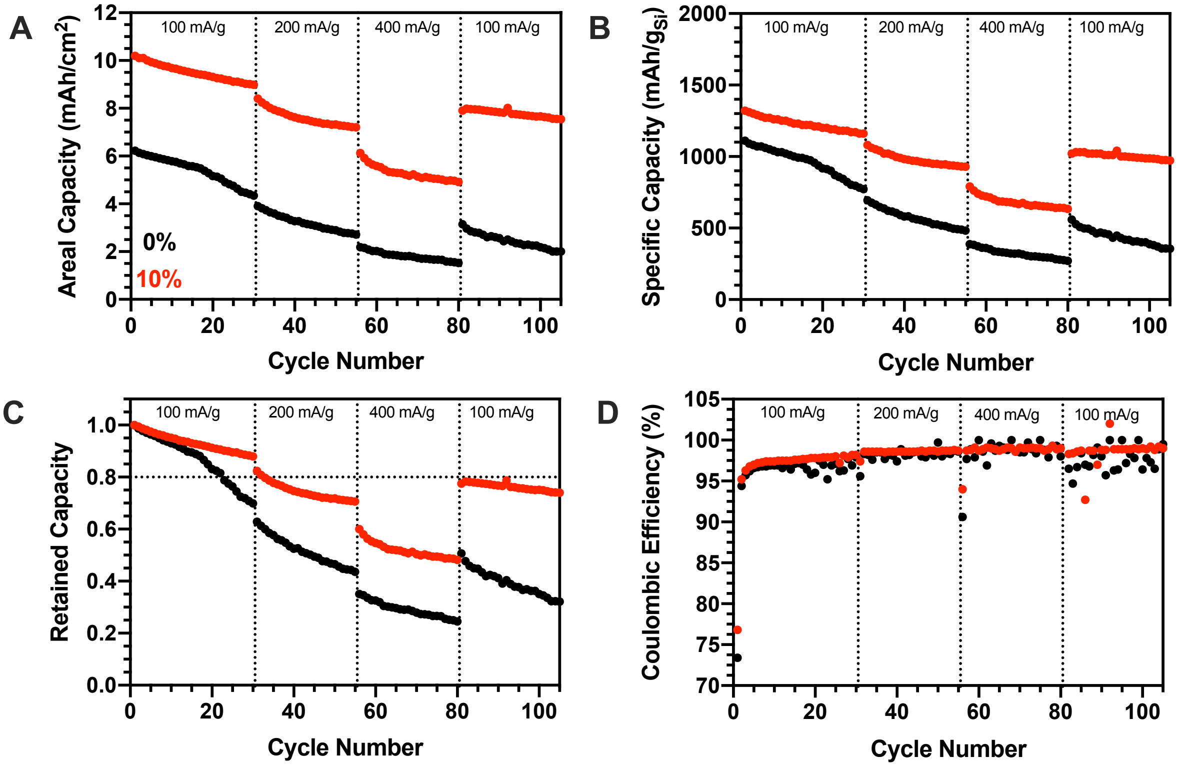

Figure 2.7: A) Areal capacity, B) specific capacity, C) retained capacity and D) coulombic efficiency for Si-CNT electrodes with various degrees of porosity. The Si-CNT electrodes were cycled in 1 M $LiPF_6$ EC/DEC (1:1 v/v) with 10% FEC additive between 1 V and 0.05 V vs Li/Li$^+$. A voltage hold was applied at 0.05 V during the discharge (Si lithiation) until the current reached 20% of its starting value.

While our previously tested honeycomb Si-CNT electrodes exhibit high areal capacity, their long-term cycling performance still requires optimization. While the Swagelok cells we have utilized are convenient for their reusability and ability to easily harvest electrodes for post-cycling analysis, it can often be difficult to ensure uniform and consistent pressure is applied from cell to cell. Further, for Si electrodes the quantity of applied pressure has been shown to influence both capacity retention and cell lifetime [156]. This, coupled with the room temperature performance of our DOL-based electrolyte, contributes to the significant long term performance degradation or failure experienced by our Si-CNT electrodes (Figure 2S.6, Figure 2S.7, Figure 2S.8 and Figure 2S.13).

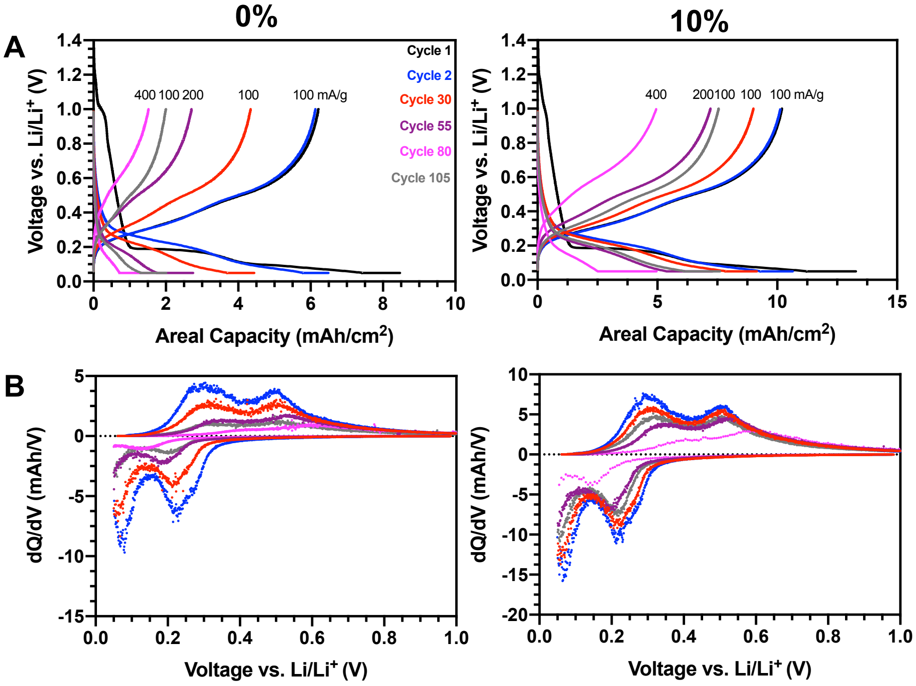

Figure 2.8: A) Voltage profiles and associated B) dQ/dV plots for Si-CNT electrodes cycled in 1 M $LiPF_6$ EC/DEC (1:1 v/v) with 10% FEC additive between 1 V and 0.05 V vs Li/Li^+. A voltage hold was applied at 0.05 V during the discharge (Si lithiation) until the current reached 20% of its starting value.

To improve their long-term cycling performance, we fabricated additional Si-CNT half-cells using 2032-coin cells, a 1 M $LiPF_6$ 1:1:0.1 ethylene carbonate:diethyl carobonate:fluroroethylene carbonate (EC:DEC:FEC) electrolyte and cycled these electrodes at 100 to 400 mA/g_{Si}. Figure 2.7 and Figure 2.8 show that, for a standardized forest height and Si deposition time, a 100 µm tall 10% honeycomb electrode exhibits significantly better areal capacity, specific capacity, retained capacity and coulombic efficiency than a non-patterned electrode. In particular the 10% electrode exhibits a > 8 mAh/cm^2 areal capacity when cycled at 100 mA/g_{Si}. Further, use of the carbonate-based electrolyte containing fluoroethylene carbonate with the 10% honeycomb structure achieves a higher first cycle coulombic efficiency (75% vs 60%) and prevents the significant drop-off in performance experienced using DOL-based electrolytes upon repeated cycling. These improvements in performance are attributed to FEC's ability to form a more stable SEI on the Si-CNT electrode, as previously been observed for Si powder electrodes, and on the Li-metal reference electrode [146], [152].

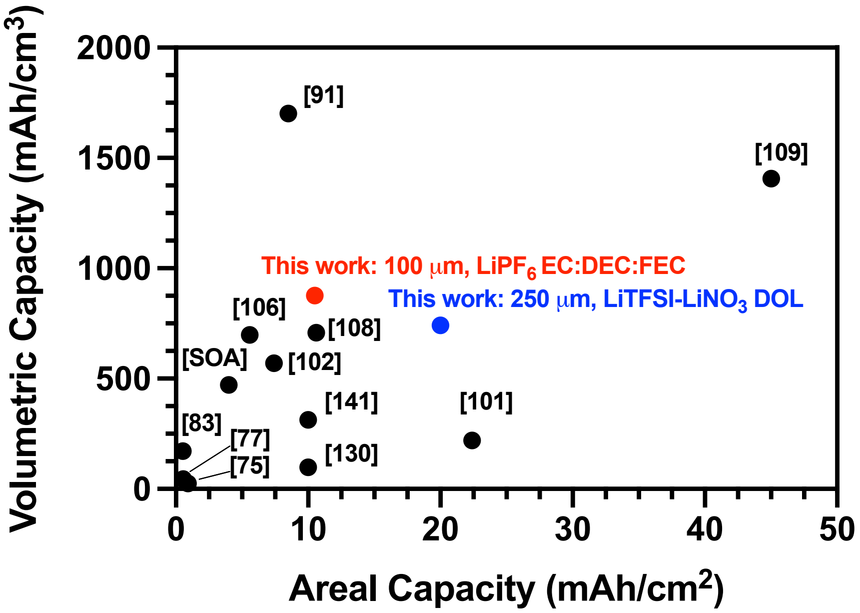

Figure 2.9: Comparison of areal and volumetric capacities for a selection of structured thick lithium-ion anodes.

In Figure 2.9 we compare the areal and volumetric capacity of honeycomb Si-CNT electrodes with published values for a commercial lithium ion anodes [101], [129] along with several structured and thick lithium-ion anodes [75], [77], [83], [91], [101], [102], [106], [108], [109], [130], [141]. Here, the electrode volumetric capacity is calculated by dividing the areal capacity by the electrode thickness plus an additional 20 μm. The additional 20 μm corresponds to a 10 μm thickness current collector and 10 μm accounting for half the separator membrane thickness. Including these components helps account for the fact that thicker electrodes minimize inactive material content [12]. A full breakdown of the electrode properties and performance metrics can be found in Table 2S.1.

Figure 2.9 also shows that our honeycomb Si-CNT electrodes exhibit high areal and volumetric capacity. Among structured and thick electrodes the honeycomb Si-CNT forests trail only the Si-CNT sponge of Hu *et al.* [101] and the segregated Si-CNT films of Park *et al.* [109]. However, despite their similar areal capacity, the honeycomb Si-CNTs exhibit much greater volumetric energy densities than the Si-CNT sponges, as (due to their higher packing density) the honeycombs achieve comparable areal loadings of Si at only one tenth to one quarter the thickness required for the sponges (100–250 μm versus >1 mm) [101]. In terms of volumetric capacity our the work trails only Park *et al.*[109] and, despite our increased areal loading, the aligned Si-CNTs of Ezzedine *et al.* [91]. It is possible that Ezzedine *et al.* are able to achieve increased capacity at lower heights via a more optimized Si LPCVD process to achieve more uniform depositions, which can be addressed in future work. However, Ezzedine *et al.* experience a 35% capacity loss, in their high loading Si-CNT electrodes over the first six cycles [91]. This is in strong contrast to our 250 μm tall 20% honeycomb Si-CNT electrodes which retain ~78% capacity after 30 cycles (Figure 2.3B) and the 100 μm tall 10% honeycomb Si-CNT electrode which operates at ~88% capacity after 30 cycles (Figure 2.7C). This demonstrates the importance of the honeycomb patterning in enabling high areal capacity and capacity retention. The areal capacity of the Si-CNT honeycombs is expected to be directly proportional to the electrode thickness, and can be improved as such, and further improvements in volumetric capacity are likely possible by optimizing the honeycomb structure and Si deposition process to maximize Si loading while accommodating reversible expansion during cycling.

2.4 Conclusions

We have demonstrated the fabrication and half-cell properties of thick architected Si-CNT electrodes based on a honeycomb pattern. The VA-CNTs were grown directly on copper foil, precisely controlling the height and porosity of the CNTs through the growth time and catalyst patterning respectively. We then coated the VA-CNTs on Cu foil with Si by an LPCVD process, observing that the CNT forests with honeycomb patterning achieved higher Si loadings for a set forest height and deposition time due to improved precursor diffusion into the forest. The honeycomb patterned Si-CNT composites were utilized as thick electrodes, with the patterning playing a crucial role in reducing capacity fading upon repeated cycling over current densities ranging from 0.5 mA/cm^2 to 2 mA/cm^2. By increasing the Si loading on the forests our electrodes demonstrated areal capacities of ~19.7 mAh/cm^2, almost 5 times higher than existing slurry cast Li-ion electrodes and competitive, both in terms of areal and volumetric capacity, with other carbon-based thick 3D electrodes. We were able to obtain improved cyclability and lifetime by utilizing a FEC containing electrolyte and better controlling the applied stack pressure. This work demonstrates the potential VA-CNTs to serve as a scaffold for thick electrode development to enable high areal capacity performance. Future works will look to further enhance electrode performance by optimizing the VA-CNT patterning and height, as well as improve the Si deposition parameters to better control the active material loading and distribution.

2.5 Experimental Methods

2.5.1 VA-CNT Patterning and Growth

35 μm thick Cu foil (JX Nippon Mining and Metals) was cleaned with isopropyl alcohol (VWR) and attached to a Si wafer for mechanical support using Kapton tape. These Cu foils were then coated with AZ 3312 positive photoresist (AZ Electronic Materials) spin coated using a three-step coating process of 500 rpm for 6 s, 750 rpm for 6 s and 3000 rpm for 30 s. The coated Cu foils were baked on hotplate at 110 °C for 90 s. The AZ 3312 coated foils were then patterned using a 405 nm laser with a 130 mJ/cm^2 dose in a Heidelberg MLA-150 maskless aligner. Following exposure, the Cu foils were removed from the Si support wafer and developed in AZ 300 for 90 s. The develop foils were cleaned with deionized water and dried with compressed air. The patterning

produced square electrodes with a 25 mm^2 area for catalyst deposition. Some squares were patterned to include a honeycomb features.

The foils are then coated with a 10 nm Al_2O_3/10 nm W/20 nm Al_2O_3/3 nm Fe catalyst stack using a sputtering system (Angstrom Engineering) utilized in our previous work [71]. In preparation for CNT growth the Cu foil was cut into pieces each containing one 25 mm^2 electrode. These pieces were attached to a Si support wafer and subjected to a three-step liftoff process to remove the developed photoresist. The foils were sonicated (Crest 1100D) for 2 min in acetone (VWR), then 2 min in dimethyl sulfoxide (Sigma) and then another 2 min in acetone. The sonicated foils were dunked twice in isopropyl alcohol and dried with compressed air.

CNT growth was performed using a homebuilt CVD 1” tube furnace (Lindberg, Figure 2S.1A) similar to the one utilized in our previous works [64], [71]. The samples were held within the tube on a quartz boat (Figure 2S.1B) and outside of the heated zone while the furnace is heated to 775 ^{o}C and the tube is prepped for annealing. Once the tube was ready for annealing the samples was inserted into the heated furnace using a magnetically coupled quartz transfer arm and held in place for 10 min. After 10 min had elapsed, the sample was returned to its position outside of the heated zone and a He flow was bubbled through a water reservoir (nebulizer) for 30 min to increase the amount of moisture in the furnace. Next, the sample was placed back inside the furnace for the CNT growth step of variable time at 775 °C. After the desired growth time the He flow through the nebulizer was terminated, and the sample was transferred to an external position outside the furnace and rapidly cooled. An external fan was directed at the cool zone to further increase the cooling speed. Full details of the growth recipe are presented in Table 2S.2 and representative gas flows and furnace conditions for a 20 min growth are presented in Figure 2S.15.

Following growth, the porosity of the sample surface ("crust") was increased by plasma etching. The samples were plasma etched (Diener) under vacuum (~0.075 mTorr) while 2 sccm O_2 (Airgas) and 8 sccm Ar (Airgas) flowed through the chamber. The etch was carried out at 30 W for 5 min. Pre- and post-etch images of the crust are presented in Figure 2S.16.

2.5.2 Si-CNT Composite Electrode Fabrication

The VA-CNT samples on Cu foil were then trimmed into squares with an area of ~ 36 mm^2 to leave a thin layer of Cu foil around the 25 mm^2 CNT forests. The samples were then weighed in a quartz microbalance (Sartorius ME36S) to determine the starting mass. In preparation for Si depositions these samples were placed in a homemade quartz shadow mask to minimize Si deposition on the foil's backside. The VA-CNT samples were placed on a 1" diameter quartz plate (Thorlabs) and were then covered by a second quartz plate containing square window (~29.5 mm^2) to expose the CNTs while covering the exposed Cu foil. The bottom and edges of the quartz plates were double wrapped in Cu foil. A schematic of the shadow mask assembly process can be found in Figure 2S.17A through Figure 2S.17D.

For Si deposition the masked VA-CNT samples were placed on a 6" support wafer (Figure 2S.17E) and loaded into a LPCVD tube furnace at 525 ^{o}C. After purging with inert gas, 110 sccm of 100% SiH_4 (Airgas) flowed through the furnace at a constant pressure of 200 mTorr and the deposition time was used to control the mass of deposited Si. After deposition the Si coated samples were removed from the furnace (Figure 2S.17F) and allowed to cool to room temperature under ambient conditions. The samples were then removed from the mask and weighed a second time to determine the deposited Si mass. After weighing the electrodes were stored under vacuum in a desiccator.

2.5.3 Electrochemical Testing and Characterization

Si-CNT electrodes were dried under active vacuum at 90 ^{o}C (BUCHI) for 24 h before being moved under vacuum into an Ar filled glovebox (Airgas, MBraun Labstar) with O_2 and H_2O levels < 5 ppm. Lithium bis(trifluoromethanesulfonyl)imide (LiTFSI, Sigma) and $LiNO_3$ (Sigma) were dried under vacuum at 120 ^{o}C for 24 h in the BUCHI oven before being moved under vacuum into the glovebox. Two separate electrolytes, 1 M LiFTSI-0.1 M $LiNO_3$ or 1 M LiTFSI, were mixed using anhydrous 1,3-dioxolane (DOL, Sigma) inside the glove box. Inside the glovebox the Si-CNT electrodes were placed inside 0.5" diameter Swagelok cells (Figure 2S.18). The Swagelok components were dried at 90 ^{o}C for 12 h before being placed under vacuum in the antechamber for another 12 h. Li-metal foil (Alfa Aesar) was used as the reference and counter electrode in all cells.

Cell fabrication followed one of two routes. One set of Si-CNT electrodes were covered with 50 μL of 1 M LiFTSI-0.1 M $LiNO_3$ in DOL electrolyte, three 12 mm diameter Celgard 2500 separators, another 50 μL of that same electrolyte and finally a 9 mm diameter Li-metal foil. A stainless-steel spacer was placed on top of the Li-metal foil and the cell closed using a compression spring that applied ~155 kPa stack pressure. Two additional cells were made using this stack where the Si-CNT electrode was replaced by either a bare 12 mm diameter Cu foil (JX Nippon Mining and Metals) or a thin film analog to our Si-CNT composites. The thin film analog consisted of a 36 mm^2 square foil coated with 3-5 layers graphene and underwent an identical LPCVD process (29.5 mm^2 exposed using the shadow mask) to the Si-CNT electrodes.

Cells with 1 M LiFTSI-0.1 M $LiNO_3$ in DOL electrolyte were cycled using a BCS-805 battery cycler (Biologic) at a 0.5 mA/cm^2 current density. The cells rested for 24 h prior before being discharged at constant current to 0.05 V vs. Li/Li$^+$. This was followed by a constant voltage hold at 0.05 V vs. Li/Li$^+$ until the discharge current reached 20% of its initial value. The cells were then charged under constant current to 1 V vs. Li/Li$^+$ and the processes repeated. Finally, the cell with a bare Cu foil electrode was discharged for 1.5 mAh under constant current using a VSP-300 potentiostat (Biologic) before being charged at constant current to 1 V vs. Li/Li$^+$.

The thin film analog sample is included to determine the effect of the thin region of exposed Cu foil that surrounds the CNT forest (Figure 2.2A) on the electrode capacity. This exposed foil is utilized during electrode fabrication to minimize damage to the CNTs while handling the sample and to prevent excess Si deposition on the foil backside. During LPCVD this exposed foil is coated with a thin Si film and will contribute to the electrode's capacity. To estimate this contribution, we ran an identical LPCVD deposition on a Cu foil coated with multilayer graphene (ML-G). The multilayer graphene helps to protect the underlying Cu foil during LPCVD as we found the Si deposition process turns exposed Cu foil brittle due to metal-silicide formation. After cycling this thin film analog at 0.5 mA/cm^2 for 100 cycles (Figure 2S.19) we find that the thin film has a maximum areal capacity of ~0.2 mAh/cm^2. Using this capacity to account for the areal capacity of the exposed Cu foil we find the absolute maximum capacity contribution of Si on the Cu foil to be $<$ 2% of the total electrode capacity. Therefore, we calculate the areal capacity of our electrodes using the footprint area of the VA-CNT forests (25 mm^2). Since the mass of Si on the foil cannot be decoupled from the mass of Si on the CNTs the specific capacities are calculated using the total amount of Si deposited each sample.

Another set of Si-CNT electrodes were covered with 50 μL of 1 M LiFTSI in DOL electrolyte, one 12 mm diameter Celgard 2500 separator, another 50 μL of that same electrolyte and a 9 mm diameter Li-metal foil. A stainless-steel spacer was placed on top of the Li-metal foil and the cell closed using a compression spring applying ~ 55 kPa stack pressure. Cells with 1 M

LiFTSI in DOL electrolyte were cycled using a BCS-805 battery cycler (Biologic) at various current densities. The cells rested for 24 h prior before being cycled at constant current between 0.05 V and 1 V vs. Li/Li$^+$. dQ/dV analysis for all cells was performed using Biologic's BT-Lab software.

A final set of Si-CNT electrodes were placed inside 2032-coin cells (MTI Corp.) For the electrolyte fluoroethylene carbonate (FEC) was added to 1 M $LiPF_6$ in 1:1 v/v ethylene carbonate:diethyl carbonate (EC:DEC, Sigma) to reach a volume ratio of 10%. 100 μL were then added to the cell, along with three 16 mm diameter Celgard 2500 separators and a 15 mm diameter Li-metal foil. An electric crimper (MSK-160E, MTI Corp.) was used for coin cell assembly (constant mass loading: 0.82 tons). These coin cells were cycled using a BCS-805 battery cycler (Biologic) at various specific current densities. The cells rested for 24 h prior before being discharged at constant current to 0.05 V vs. Li/Li$^+$. This was followed by a constant voltage hold at 0.05 V vs. Li/Li$^+$ until the discharge current reached 20% of its initial value. The cells were then charged under constant current to 1 V vs. Li/Li$^+$ and the processes repeated.

2.5.4 Material Characterization

Optical microscopy was performed using a Smartzoom 5 digital microscope (ZEISS). SEM images were acquired using Gemini 450 field emission SEM (ZEISS) at a 2-10 kV accelerating voltage, a 100–500 pA current and an In-lens secondary electron detector. EDS measurements were recorded in the same SEM using a Ultim Max detector and AZtec software. For electrode SEM analysis all cells were disassembled in the glovebox under argon and rinsed with DOL before being dried and transported to the SEM under Ar.

Raman measurements were recorded using Renishaw Reflex spectrometer. CNT measurements were taken using a 532 nm laser with an integration time of 30 to 45 s. Si measurements were taken using a 532 nm laser and a 60 s integration time. TGA measurements to determine the amorphous carbon content of the VA-CNTs were performed under air using a TA Instruments Discovery TGA. After being equilibrated to 60 °C the samples were heated at a rate of 10 °C/min to 900 °C.

2.6 Supporting Information

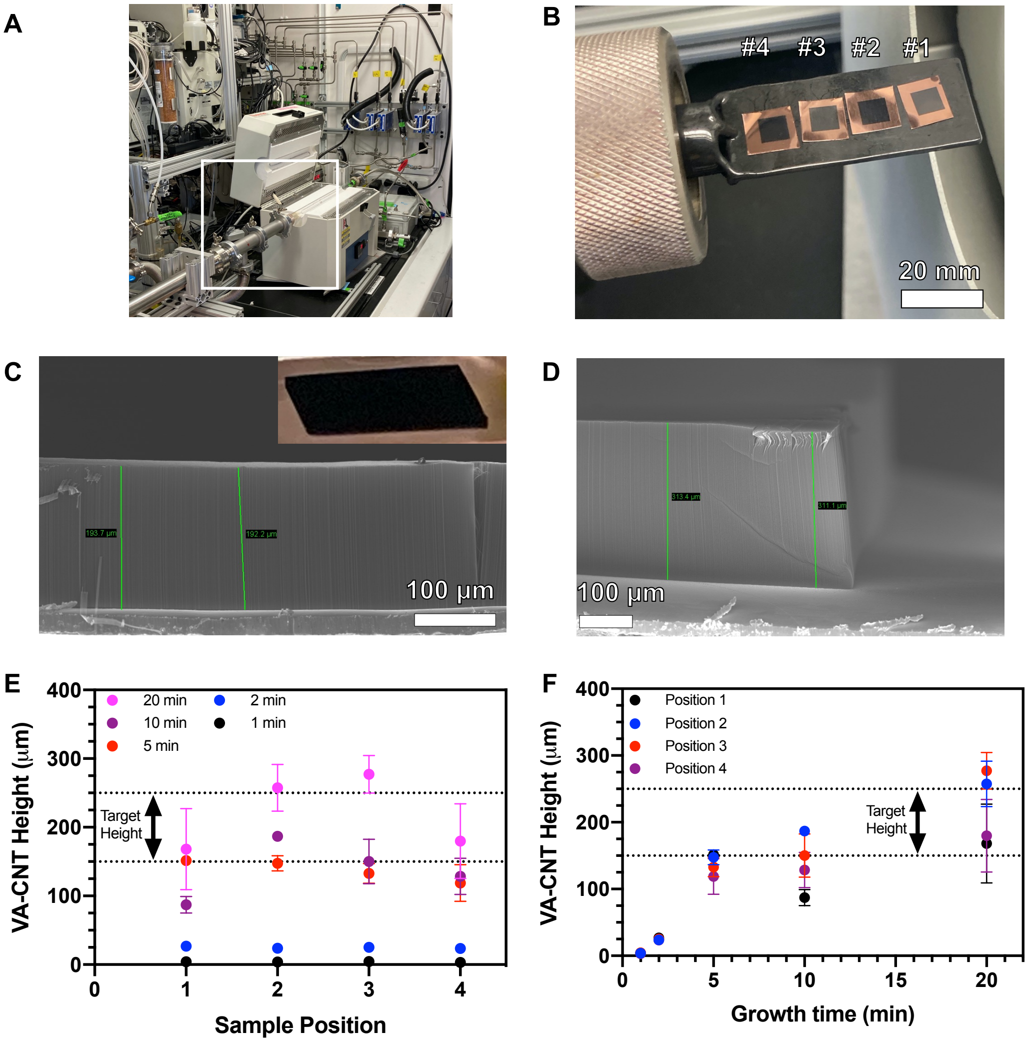

Figure 2S.1: A) Homebuilt CVD furnace for CNT growth with the transfer arm and boat highlighted by the white box, B) the boat with four electrodes prior to growth and their respective position. Non-patterned VA-CNT forests after C) 10 min growth and D) 20 min growth, E) CNT forest height as a function of sample position and F) CNT forest height as a function of growth time.

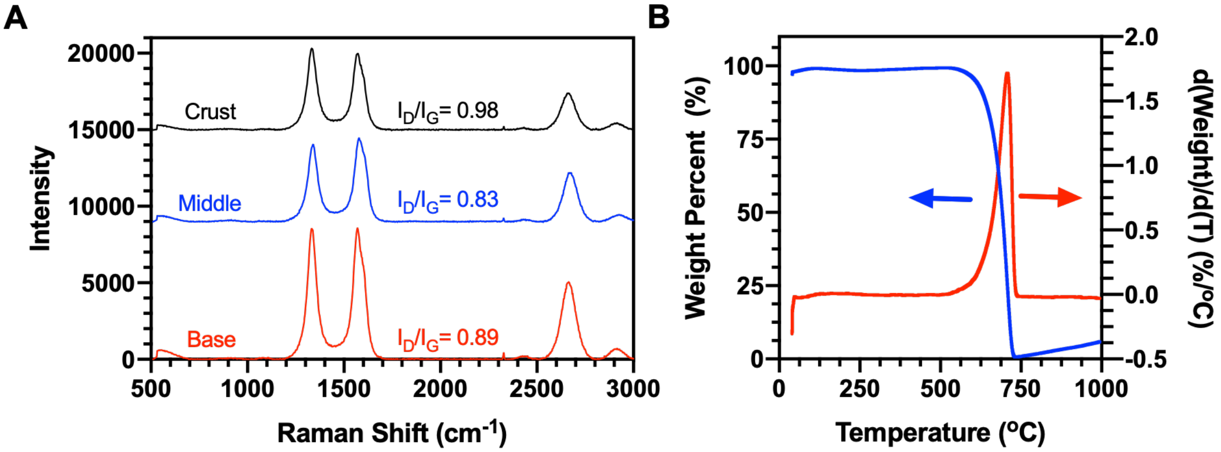

Figure 2S.2: A) Raman spectra for VA-CNT sidewalls, measurements were taken at three points from the CNT base to the surface. B) TGA analysis for VA-CNTs.

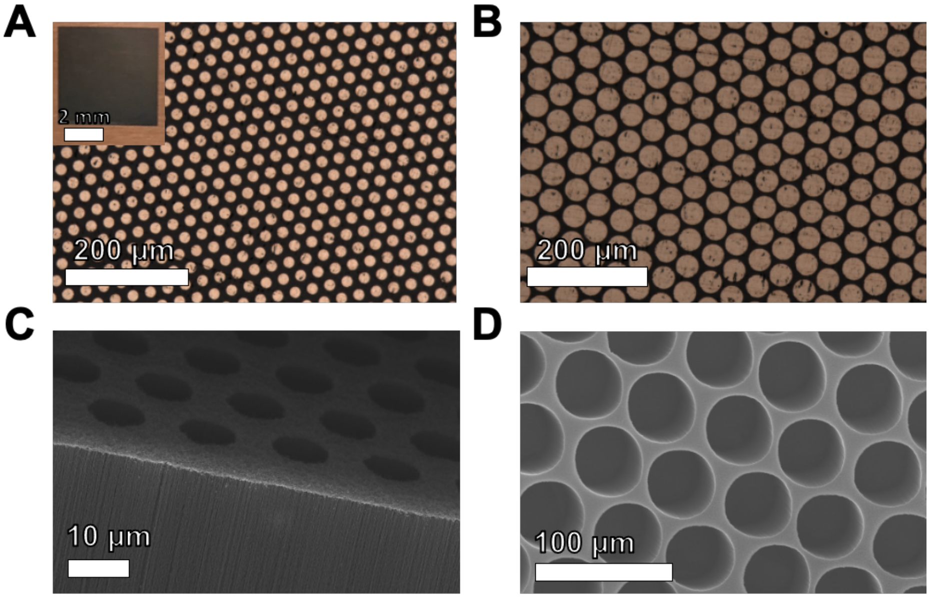

Figure 2S.3: A) Optical microscopy image for honeycomb patterned catalyst with 20 µm diameter and 40 µm spaced holes, the insert is a photograph of the entire catalyst area. B) Optical microscopy image for honeycomb patterned catalyst with 80 µm diameter and 85 µm spaced holes. C) SEM of VA-CNTs with 10 µm diameter and 15 µm spaced hole honeycomb pattern. D) SEM images of honeycomb VA-CNT forests with 80 µm diameter and 85 µm spaced holes.

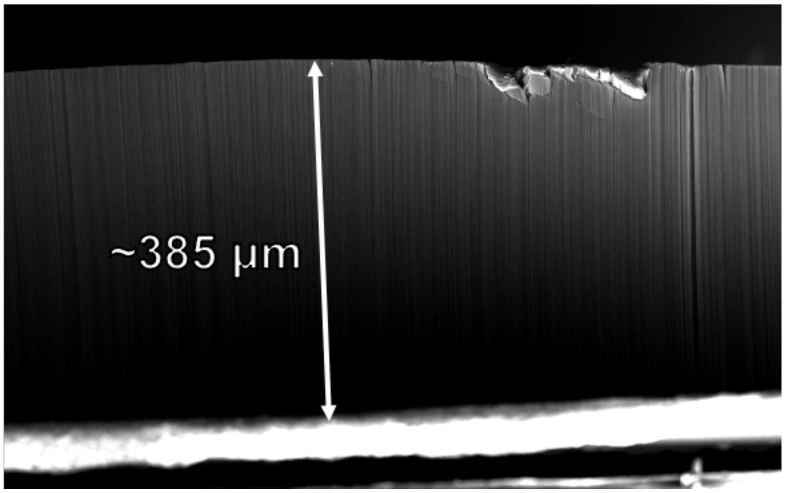

Figure 2S.4: Non-patterned CNT forest with increased height (0% Tall) to enable higher areal Si loading.

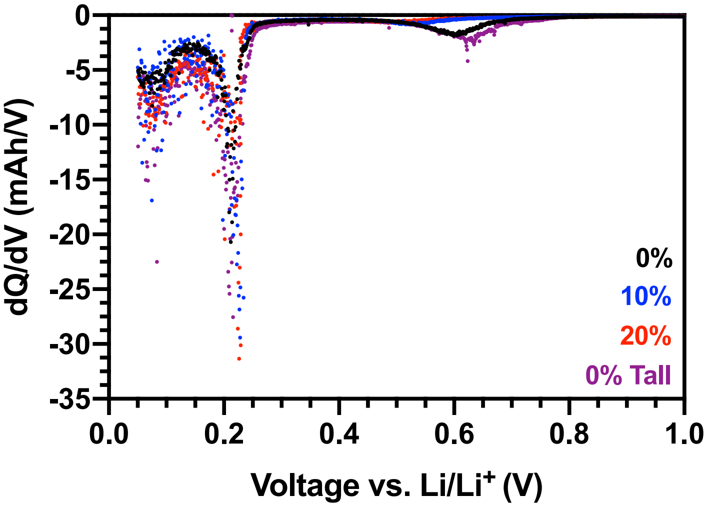

Figure 2S.5: First discharge dQ/dV plots of Si-CNT electrodes.

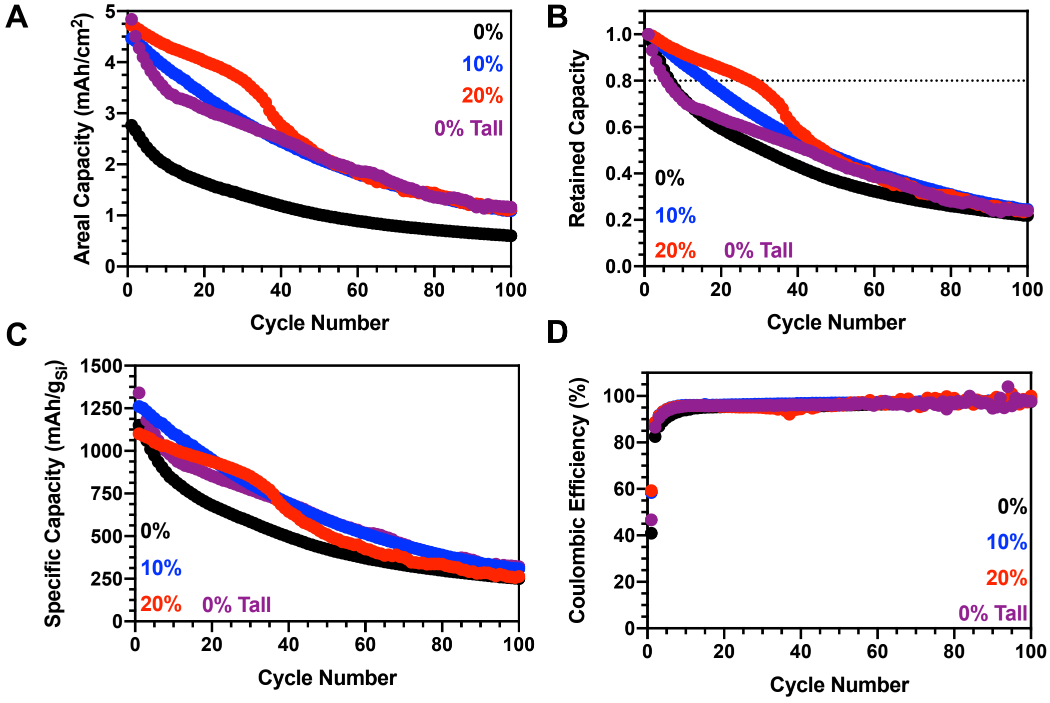

Figure 2S.6: A) Areal capacity, B) retained capacity, C) specific capacity and D) coulombic efficiency plots for Si-CNT electrodes after 100 cycles.

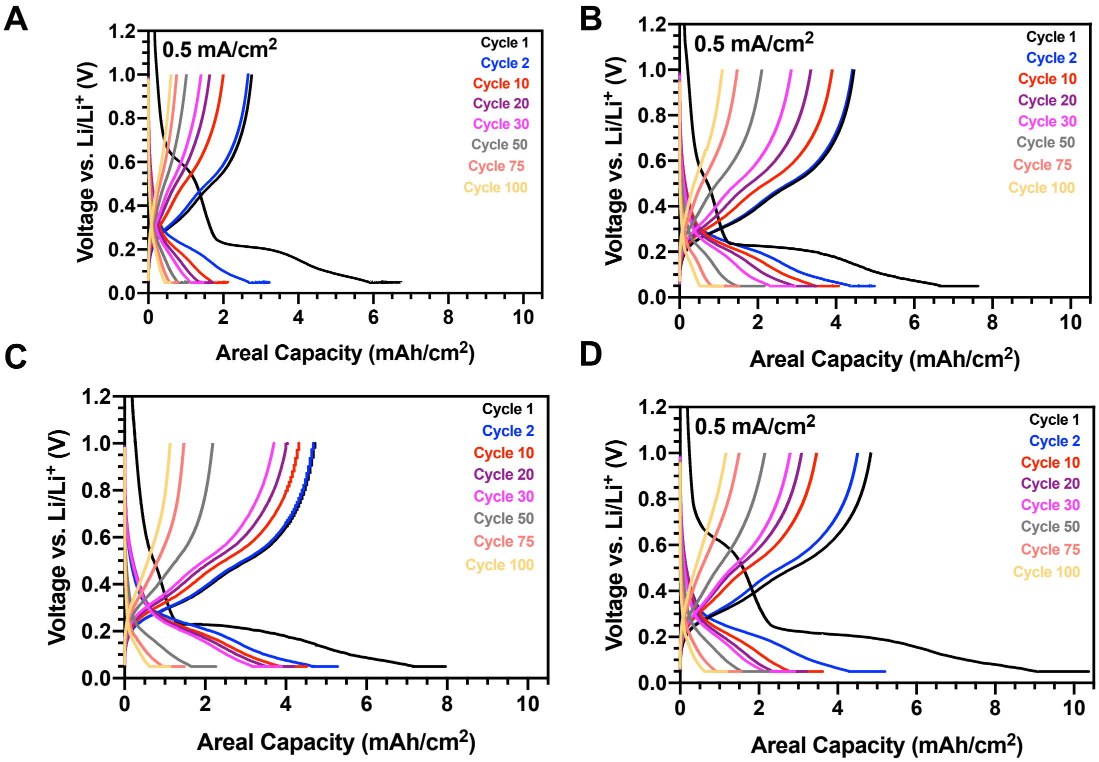

Figure 2S.7: Voltage profiles over 100 cycles for A) 0%, B) 10%, C) 20% and D) 0% tall Si-CNT electrodes.

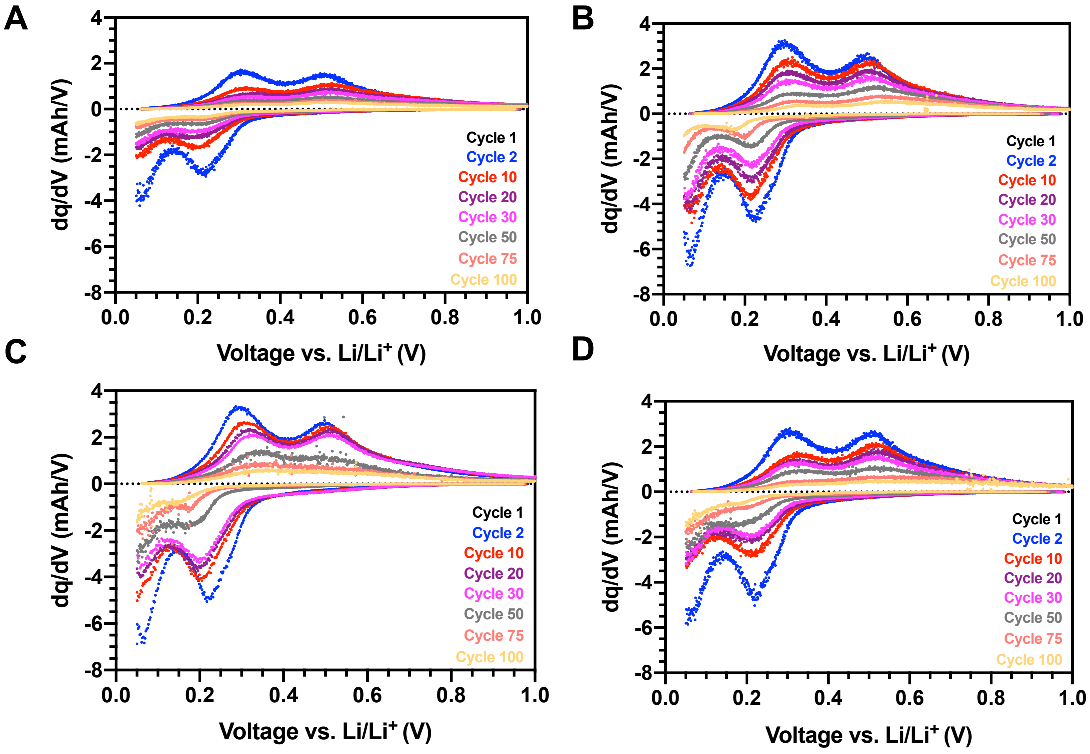

Figure 2S.8: dQ/dV profiles over 100 cycles for A) 0%, B) 10%, C) 20% and D) 0% tall Si-CNT electrodes.

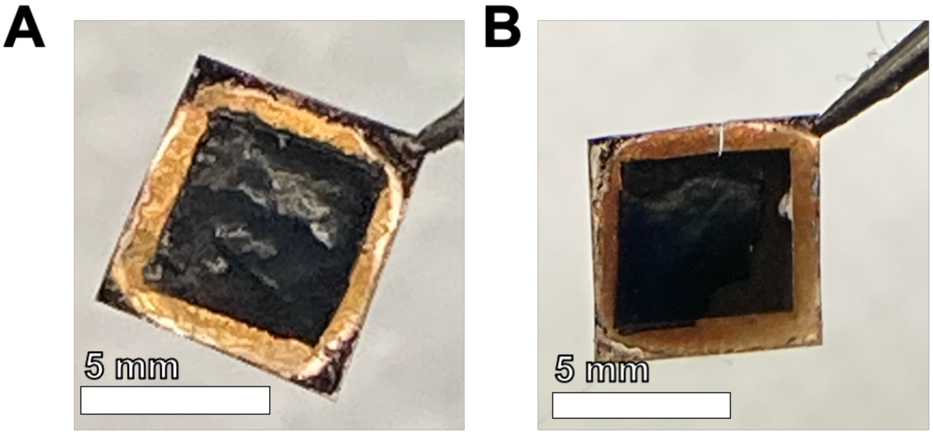

Figure 2S.9: Post 100 cycle photographs of A) 0% tall and B) 20% Si-CNT electrodes.

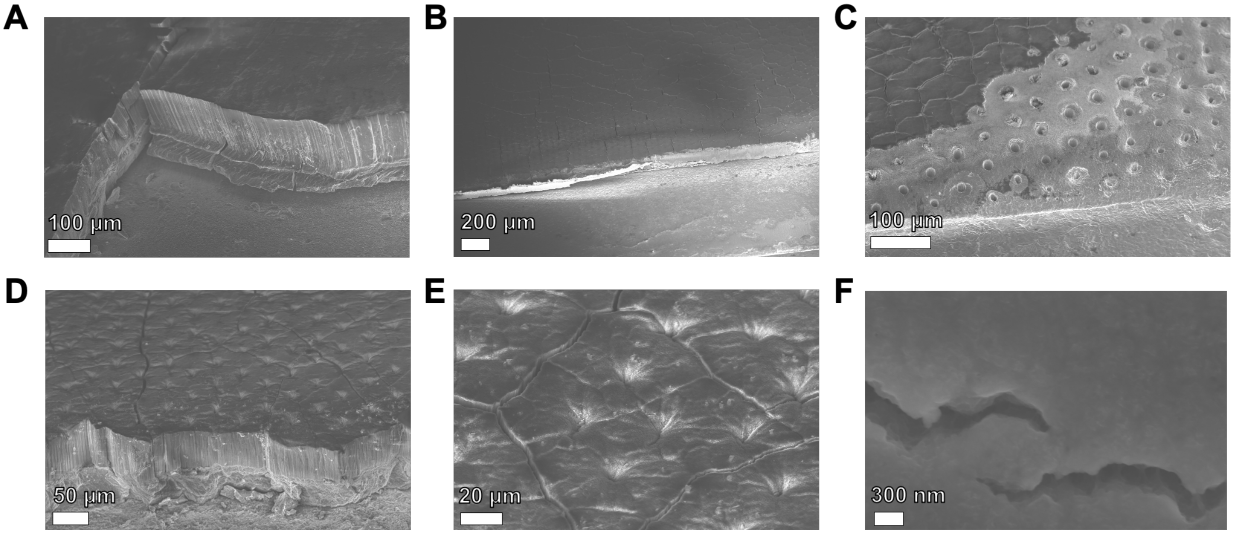

Figure 2S.10: Post cycling SEM images for A) 0% tall, B) and C) 10% and D), E) and F) 20% Si-CNT electrodes.

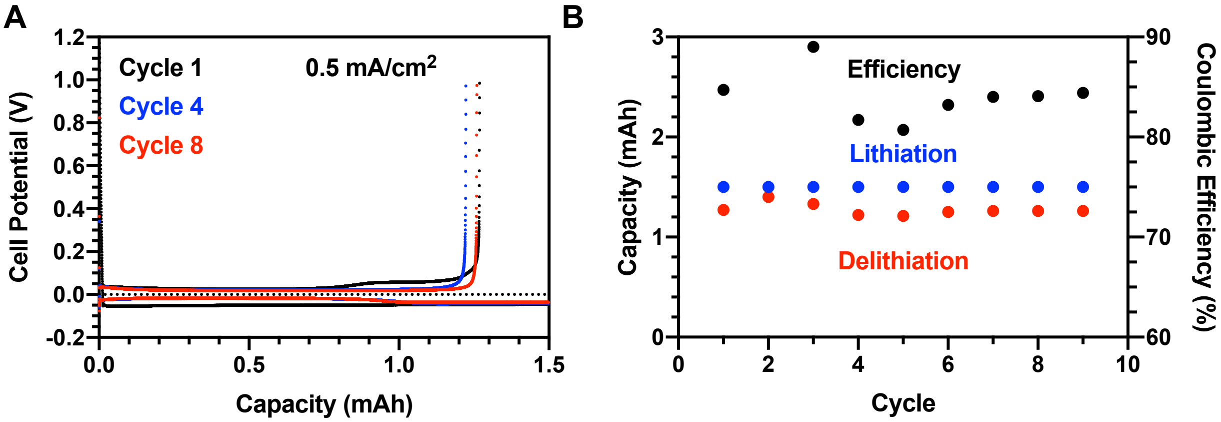

Figure 2S.11: A) Voltage profiles and B) capacity and coulombic efficiency for a Li-metal/Cu cell with 1 M LiTFSI-0.1 M $LiNO_3$ in DOL electrolyte.

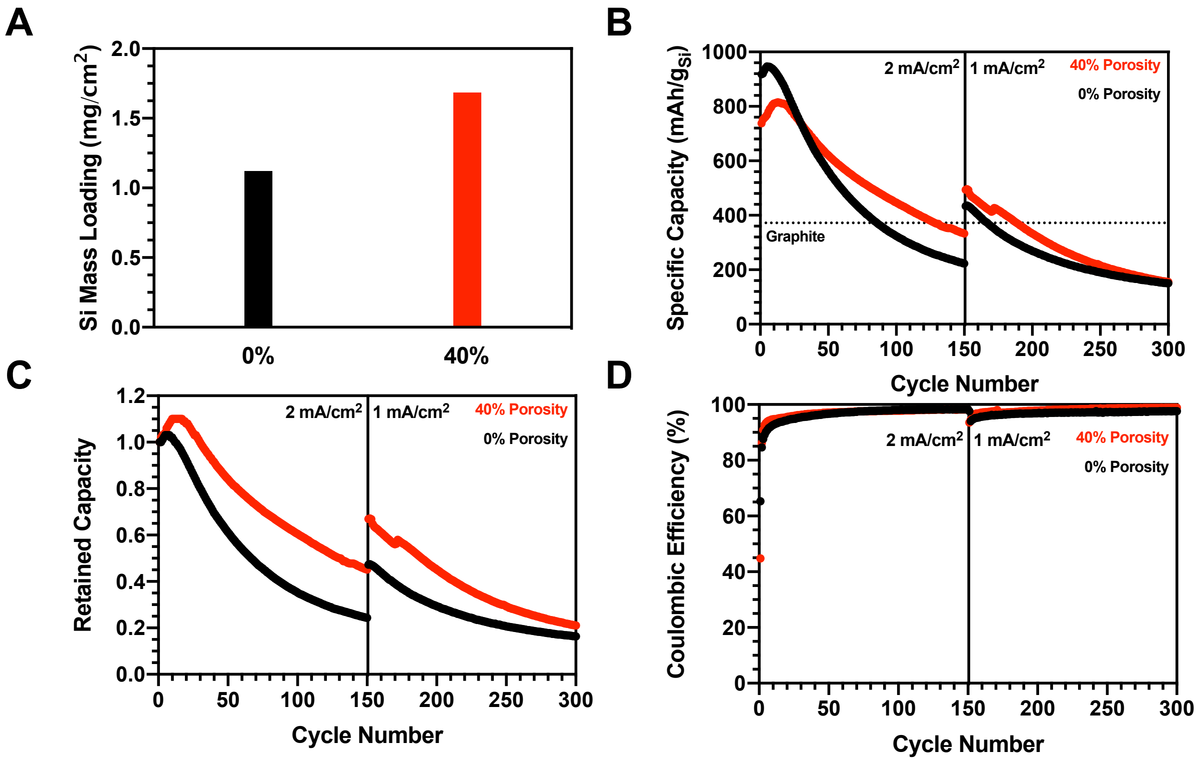

Figure 2S.12: A) Areal Si mass loading, B) specific capacity, C) retained capacity and D) coulombic efficiency for a 40% honeycomb and 0% non-patterned Si-CNT electrode.

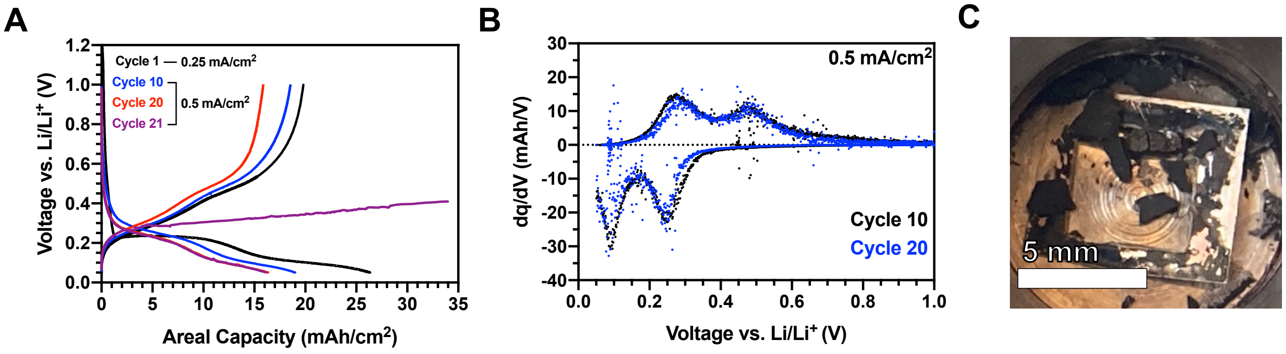

Figure 2S.13: A) Voltage profiles showing failure on cycle 21, B) dQ/dV data and C) post cycling photograph for a 20% honeycomb electrode cycled between 1 V and 0.05 V vs Li/Li$^+$.

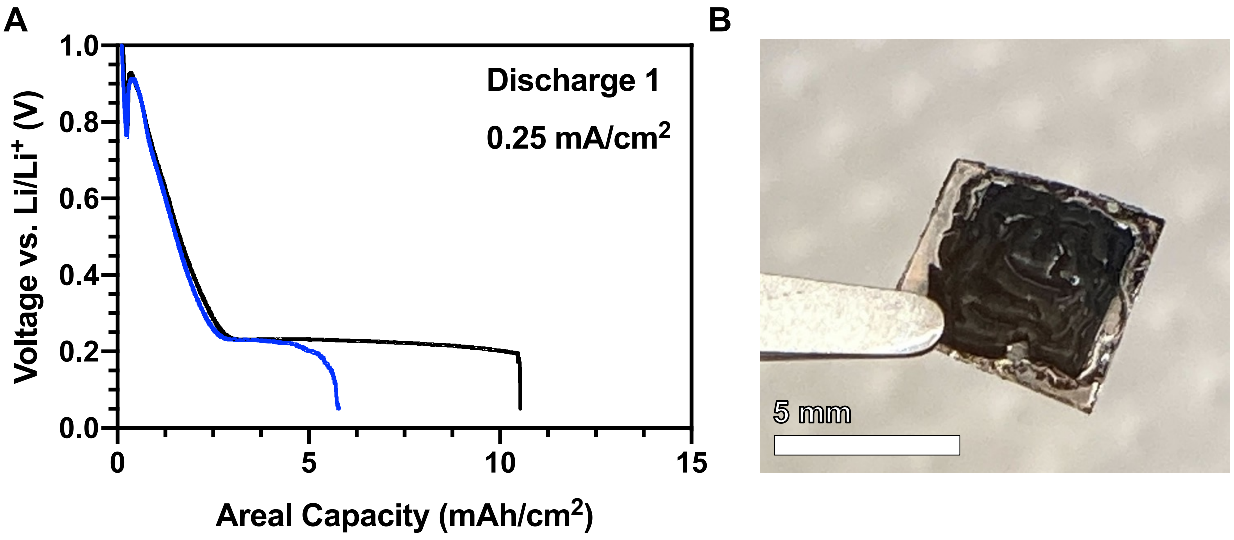

Figure 2S.14: A) First discharge profile showing short circuit and B) post failure photograph showing Si expansion for 0% non-patterned Si-CNT electrodes with >3.5 mg cm^{-2} areal loading.

Table 2S.1: Performance summary for several thick and structured lithium-ion anodes.

Description	Active Material	Thickness (µm)	Areal Capacity (mAh/cm^2)	Volumetric Capacity (mAh/cm^3)	Reference
Honeycomb CNTs on Cu	Si	250	20	741	This work
Honeycomb CNTs on Cu	Si	100	10.5	875	This work
Aligned CNTs on Cu	Si	30	8.5	1700	Batteries and Supercaps 6 (2023) 848-858 https://doi.org/10.1002/batt.202200451
Architected Carbon	C	1000	10	98	Adv. Energy Mater. 2002637 (2020) https://doi.org/10.1002/aenm.202002637
CNT Sponge	Si	1000	22.4	220	Adv. Energy Mater. 1 (2011) 523-527 https://doi.org/10.1002/aenm.201100056
CNT Sponge	SnO_2	110	7.4	569	Nanoscale 7 (2015) 20380 https://doi.org/10.1039/C5NR06613A
CNT Microscrolls	Si	60	5.58	698	Energy Environ. Sci. 13 (2020) 848 https://doi.org/10.1039/C9EE02615K
Aligned CNTs on stainless	Si	10	0.51	170	Adv. Mater. 24 (2012) 2592 https://doi.org/10.1002/adma.201104923
Cu Foam	Si	300	10	313	Adv. Energy Mater. 4 (2014) 1301718 https://doi.org/10.1002/aenm.201301718
Honeycomb CNTs on conductive polymer	Fe_2O_3	350	0.9	24	Small (2019) 1901201 https://doi.org/10.1002/smll.201901201
Aligned CNTs on Ni	$Li_4Ti_5O_{12}$	100	0.54	45	Batteries 3 (2017) 37 https://doi.org/10.3390/batteries3040037
Segregated Si-CNT composite	Si	300	45	1406	Nat. Energy 4 (2019) 560 https://doi.org/10.1038/s41560-019-0398-y
Blade coated Si-CNT composite	Si	130	10.6	707	J. Colloid Interface Sci. 625 (2022) 871 https://doi.org/10.1016/j.jcis.2022.06.082
SOA Lithium-ion	C	65	4	471	

Table 2S.2: Steps and parameters for CNT growth on Cu foils.

Step	Time (min)	He (sccm)	H_2 (sccm)	C_2H_4 (sccm)	Nebulizer (sccm)	Temperature (ºC)	Boat Position (cold/hot)
1	25	1000	0	0	0	25	Cold
2	10	400	100	0	0	775	Cold
3	3	100	400	100	0	775	Cold
4	7	100	400	0	0	775	Cold
5	10	100	400	0	0	775	Hot
6	25	450	100	0	50	775	Cold
7	5	350	100	100	50	775	Cold
8	Variable	350	100	100	50	775	Hot
9	5	400	100	100	0	25	Cold
10	20	1000	0	0	0	25	Cold

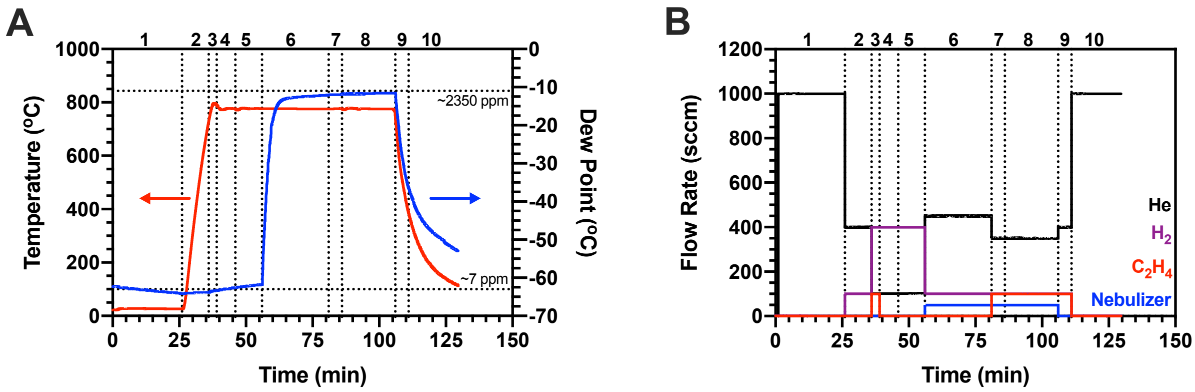

Figure 2S.15: Representative A) temperature and moisture profile, and B) gas flows for a 20 min CNT growth on Cu foil.

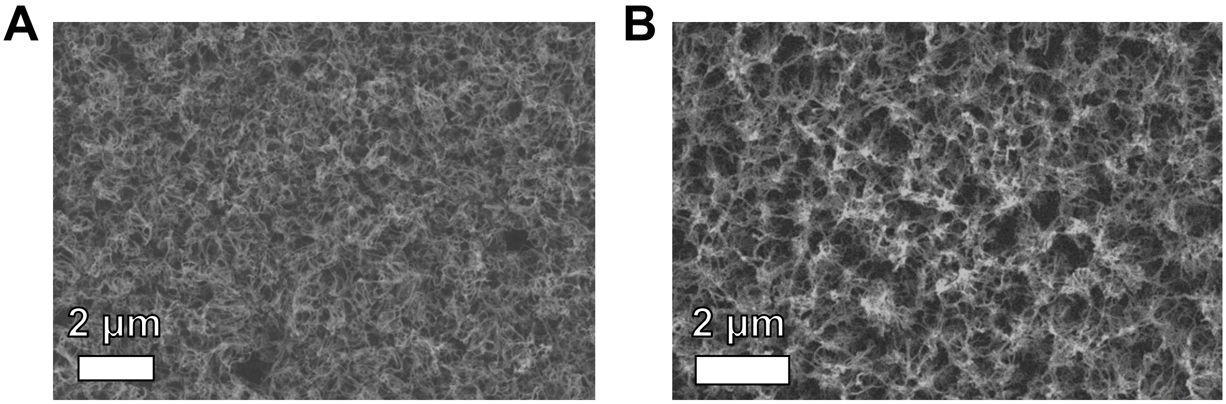

Figure 2S.16: VA-CNT forest crust A) pre- and B) post plasma etch.

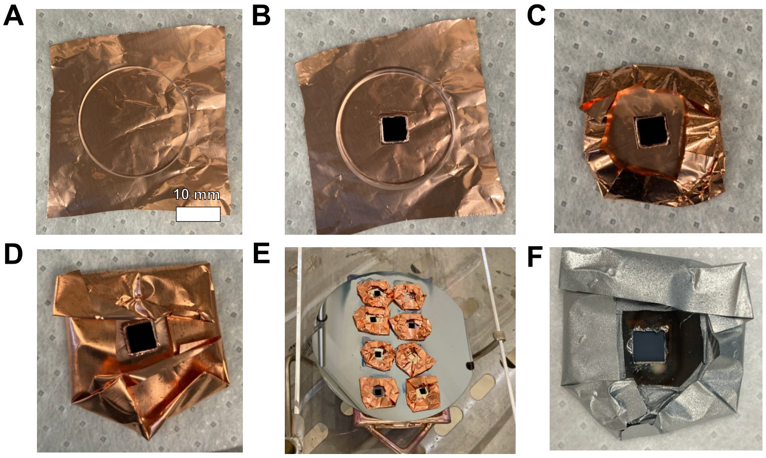

Figure 2S.17: A) Quartz plate on the first Cu foil, B) addition of VA-CNT sample with second plate containing a square window for CNT exposure, C) the first foil is wrapped around the quartz plate, D) the second foil wrap, E) masked VA-CNT on Cu samples for Si deposition, F) a sample post Si deposition.

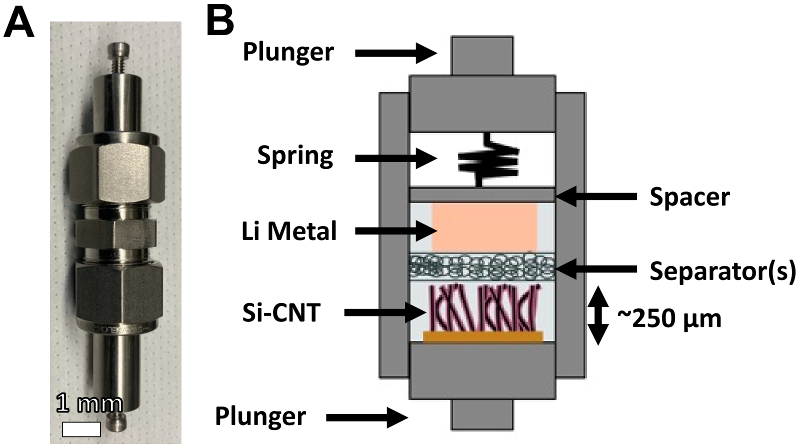

Figure 2S.18: A) Swagelok cell and B) schematic of Swagelok cell interior.

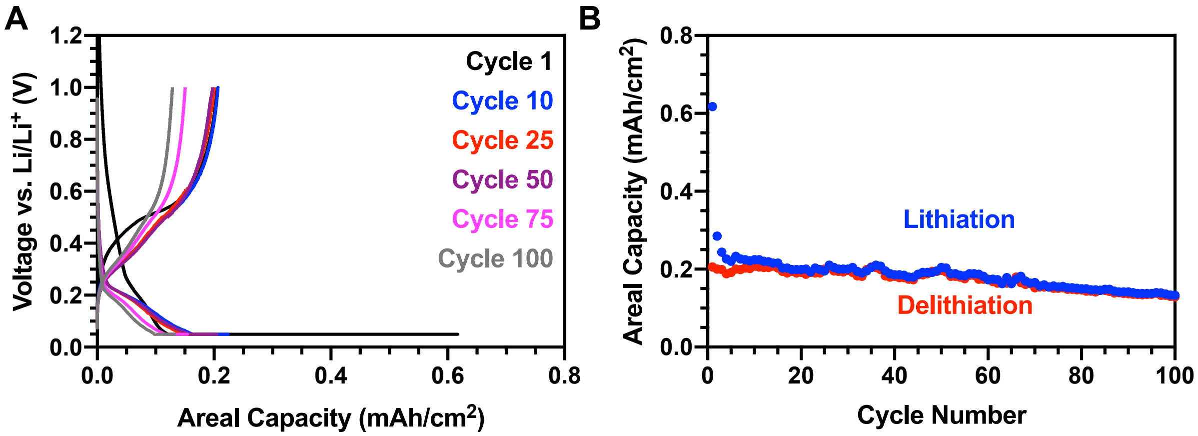

Figure 2S.19: A) Voltage profiles and B) areal capacity for a Si-MLG thin film analogue electrode cycled between 1.0 V and 0.05 V vs. Li/Li$^+$ in 1 M LiTFSI-0.1 M $LiNO_3$ in DOL.

THIS PAGE IS LEFT INTENTIONALLY BLANK

Chapter 3- A Review of Electrolyte Materials and Processing Methods Suitable for Three-dimensional Battery Architectures

3.1 Abstract

Three-dimensional (3D) battery architectures have been envisioned to enable high energy density electrodes without the associated power drop experienced by planar cells. However, the development of 3D cells has been hampered by difficulties producing conformal solid state (SSE), solid polymer (SPE) and gel polymer electrolytes (GPE) that are pinhole free, and have adequate ionic conductivities. Fortunately, 3D electrolytes are often utilized at thinner thickness, which may result in suitable performance. Here, we comprehensively review potential 3D electrolyte materials by compiling their thickness and room temperature ionic conductivity. We use area specific resistance (ASR) as a metric to compare 3D electrolytes with one another and conventional electrolytes. We find that certain process-material combinations, such as atomic layer deposition (ALD) of SSEs and initiated chemical vapor deposition (iCVD) of SPEs demonstrate ASRs beneath the interfacial impedances of Li-based systems and approach state-of-the-art thin film electrolytes. We also comment on additional factors, such as electrochemical stability, that should be further evaluated when determining suitability as a 3D electrolyte. Future research should focus on adapting known materials chemistries for vapor deposition techniques to further improve the base ionic conductivity, as they are already capable of producing the necessary conformalities and thicknesses.

3.2 Introduction

Since the initial production of lithium-ion batteries by Sony in the early 1990's[1], their commercially available specific and volumetric energy densities have more than tripled, from ~80 to ~300 Wh kg^{-1}, and ~250 to ~750 Wh L^{-1}, respectively. The predominant commercial lithium-ion cells, which have planar slurry cast intercalation electrodes, have achieved volumetric energy density greater than 95% of the theoretical maximum[1], [6], [7], [10]. Yet, there is rising demand for higher density energy and power sources in systems with applications across all length scales. For instance, implantable medical devices and small wearables (e.g., earbuds) require batteries as small as 1-10 mm^3 [3], [4]. The same issues are faced by laptop computers and electric vehicles (EVs). Despite the aforementioned improvements, significant work is required to meet the established targets for EVs, such as those of the United States Advanced Battery Consortium, which exceed 300 Wh kg^{-1} or 1000 Wh L^{-1} [7], [11], [14], [157].

One strategy to increase a lithium-ion system's energy density is to optimize the cell geometry to minimizes the content of inactive material [7], [34], [35]. Planar cell architectures dominate battery production due to their ease of industrial fabrication. This includes planar thin film lithium-ion batteries for MEMS devices [4] and, conventional pouch or cylindrical cells for portable electronics and EVs [1], [2], [12]. For planar cells the most straightforward way to minimize the inactive material content is to increase electrode thickness[4], [34], [35]. Unfortunately, while the energy density scales with electrode thickness whereas power desnity scales inversely with electrode thickness squared [4]. In thin film cells, as the electrode thickness increases, Li$^+$ diffusion ($< 10^{-10}$ cm^2 s^{-1}) through the solid active material becomes a limiting factor and results in decreasing power density despite the increased energy density [4], [5]. This trade-off between energy and power density is also experienced by cylindrical or pouch cells . Here, thick slurry cast electrodes expereince reduced rate preformance due poor charge and mass transfer kinetics resulting from high tortuosity [34], [35]. Furthermore, thick electrodes are subject to cycling stresses that can compromise mechanical integrity [158].

The issues associated with thick, planar electrodes can be avoided by moving away from these 2D designs and towards architectures where electrodes have active surface area exposed in three dimensions (3D) [4]. There are many possible 3D architectures, utilizing various types of interpenetrating rods, plates or films, as schematically shown Figure 3.1A-D [128]. For these 3D designs, a given active material volume can be distributed with a smaller electrode feature thickness Figure 3.1E). This increased surface area enables shorter Li^+ diffusion distances for a given amount of active material, and a 3D design decouples the trade-off between energy and power density inherent to planar designs [3], [4], [36]–[38].

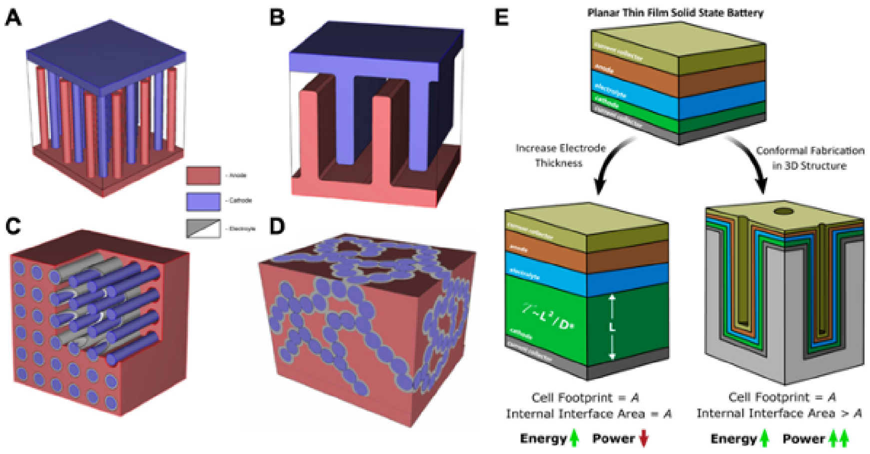

Figure 3.1: Schematics for variations in 3D battery architectures including: A) interdigitated anode and cathode rods, B) interdigitated anode and cathode plates, C) cathode array surrounded by infiltrated anode material and D) gyroidal structure. All designs feature a conformal thin film electrolyte between the two active materials. A) through D) adapted with permission [128]. Copyright 2010, Elsevier. F) shows the increase in interfacial area obtained through a 3D design to overcome the energy-power trade-off experienced by an equivalent planar cell. F) adapted with permission [37]. Copyright 2018, American Chemical Society.

While 3D batteries offer promising electrochemical properties, their complex geometries require an involved fabrication process. Lab-scale fabrication often begins by producing a single, arrayed electrode, typically using lithographic and thin film fabrication technologies. Published

3D half-cell configurations have been fabricated from, for instance, Si nanowires [40], ion etched Si trenches [41], active material coatings on metallic nanowires [42]–[46] and pyrolyzed carbon posts [47], [48].

Although half-cell capabilities are well demonstrated there have been fewer attempts to fabricate full cell 3D batteries where the solid or polymer electrolyte and two electrodes form a fully interdigitated or interpenetrating network. An intermediate configuration involves a pair of 3D electrodes separated by a conventional liquid electrolyte, with precisely controlled spacing to prevent electrode contact [48], [159], [160]. Yet, the ideal 3D battery design, as pictured in Figure 3.1E, utilizes a thin, solid conformal layer between the two interpenetrating or interdigitated electrodes. Practically, this may be a solid state (SSE), solid polymer electrolyte (SPE) or gel polymer (GPE) coating, which compared to the liquid electrolyte equivalent, allows for lower inactive material content and electrode spacing by enabling a thinner electrolyte layer. Use of an SSE or SPE also increases safety by excluding the flammable organic solvents that are commonly used in liquid electrolytes and to enhance conductivity in GPEs [1], [3], [24].

For practical use, SSEs, SPEs or GPEs must exhibit ionic conductivity that is competitive with liquid electrolytes (10^{-2} S/cm). Due to their larger transference number, SSEs for planar designs should exhibit ionic conductivities of ~10^{-5}-10^{-3} S cm^{-1} at room temperature, while SPEs and GPEs need conductivities on the order of 10^{-3} S cm^{-1} [20], [25], [161]. The ionic conductivity of solid electrolytes can span several orders of magnitude due to variation in ion valency and size, conduction mechanism, electrolyte composition, crystal structure and operating temperature [32]. Recently, planar oxide and sulfide SSEs films with thicknesses on the order of hundreds of nanometers have shown exceptional ionic conductivity of > 10^{-3} S/cm. This topic has been comprehensively reviewed by numerous works [20], [21], [24], [162]–[165]

Beyond suitable ionic conductivity, SSEs, SPEs and GPEs must satisfy several other criteria for use in 3D batteries. Notably, they must be electrically insulating, have a sufficient electrochemical stability range and be processable in manner capable of producing conformal, uniform and pinhole free films over the underlying (3D) electrode. While oxide and sulfide SSEs, SPEs and GPEs for planar cells meet these first two criteria with varying degrees of success, the employed processing methods for thin films do not generally facilitate pinhole free layers over high aspect ratio micro- or nanoscale features. As a result, advanced processing techniques have been investigated to fabricate conformal 3D electrolyte coatings with thicknesses ranging from tens of nanometers to millimeters[158], [166], [167].

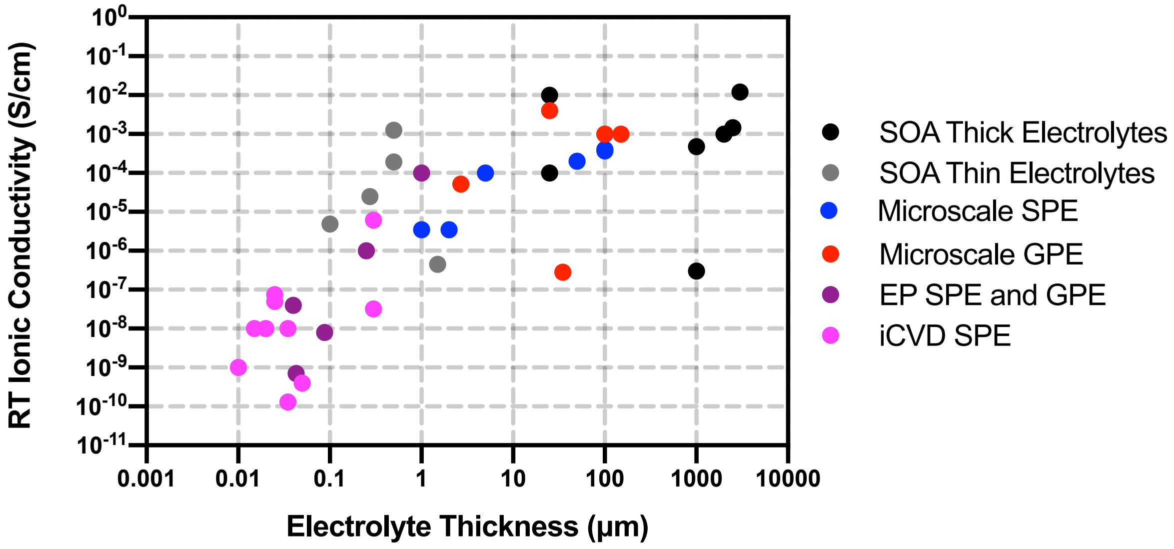

Figure 3.2: Reported values of ionic conductivity versus electrolyte thickness for SPEs and GPEs with potential for incorporation in 3D full cells. SOA planar and liquid electrolytes are included for comparison.

Yet, to date, the resulting 3D solid electrolyte materials differ significantly in composition and structure from the optimized planar SSEs and SPEs, and often have significantly reduced ionic conductivity. Therefore, a significant portion of 3D electrolyte literature is devoted to tackling the conductivity problem that has largely been solved for planar electrolytes. However, unlike their planar counterparts, the miniaturization, and decreased diffusion distances that results from 3D battery designs leads to decreased electrolyte thicknesses and an increase in electrode-electrolyte interfacial surface area. Recent reviews suggest a range of 10^{-7} S/cm to 10^{-4} S/cm as the sufficient ionic conductivity for electrolyte use in 3D microbatteries. These values are far below conventional SSEs, SPEs and GPEs but are sufficient if adequately small electrolyte thickness is achieved[4], [158], [166].

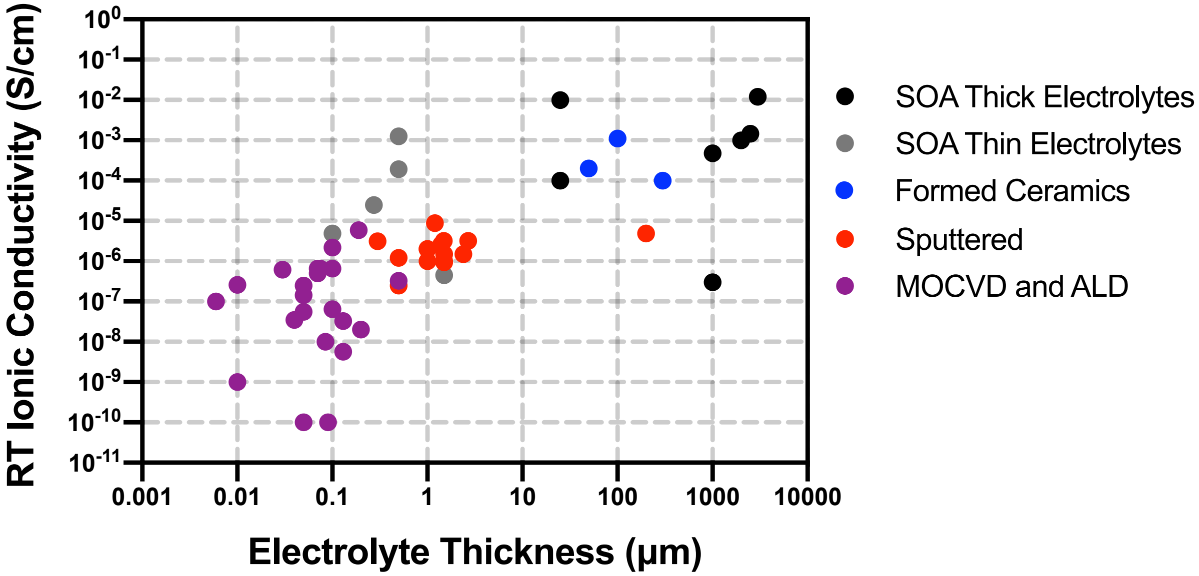

Figure 3.3: Reported values of ionic conductivity versus electrolyte thickness for SSEs with potential for incorporation in 3D full cells. SOA planar solid and liquid electrolytes are also included for comparison.

Therefore, selection of the electrolyte material, target ionic conductivity, and processing technique depend on the thickness at which the 3D features are fabricated. We have comprehensively compiled the reported room temperature (~298-303 K) ionic conductivities and thicknesses of SSEs, SPEs and GPEs used in 3D batteries, or those that may be able to do so with minor modifications. Corresponding values of ionic conductivity and thickness for all SPEs and GPEs discussed in this section are included in Figure 3.2, and all SSEs in Figure 3.3. Benchmark values for commercial planar electrolytes include state-of-the-art (SOA) carbonate liquid electrolytes[10] and poly(ethylene oxide) (PEO) based GPE/SPEs[168], [169] (Figure 3S.1A), along with both thick and thin film SSEs. The thick film SSEs included are: pellets of lithium germanium phosphorous sulfide (LGPS) [170], LLZO [171], LLTO [172], LATP [173] and LiPON [174] (Figure 3S.1A). Thin film planar SSEs include: sputtered LLZO [175], LiPON [176] and LATP[177], and pulsed laser deposition LiPO [178] and LLTO[179] (Figure 3S.1B). We then use the reported ionic conductivity and thickness values to calculate the area specific resistance (ASR) [175], [180] for each potential 3D electrolyte. The ASR enables comparison with the SOA planar equivalents to determine which deposition techniques and materials are the most promising in the pursuit of full cell 3D batteries.

3.3 Solid Polymer and Gel Polymer Electrolytes

Next, we discuss the performance of SPEs and GPEs deposited by electropolymerization (EP); individually referenced data is compiled in Figure 3S.2A. Early work towards conformal polymer electrolytes focused on EP due to its self-limiting nature when applied to electrically insulating materials, as polymerization occurs more rapidly over the bare electrode regions while stopping on the thicker areas once they become electrically insulated. This results in a uniform pinhole-free coating over the electrode surface and prevents excess deposition on corners, but does limit the film's thickness to < 100 nm [3]. Preliminary works by Rhodes *et al.* demonstrated EP of pinhole-free poly(phenylene oxide) (PPO) films over indium-tin-oxide substrates [116]. After impregnation with lithium salts and vacuum drying, the PPO films exhibited a low ionic conductivity (σ) of $7x10^{-10}$ S/cm at 43 nm thickness. Also, Rhodes *et al.* extended their EP work to poly(4-sulfonic acid-1-2-phenyelene oxide) (PSPO) and poly(2,6-dimethyl-1,4-phenylene oxide) (PDPO) films which exhibited $\sigma = 8x10^{-9}$ and $4x10^{-8}$ S/cm respectively [114]. These PPO-based EP have been used in full 3D battery cells [51], [181]. Unfortunately, the cells had low capacity and permitted leakage current possibly due to the EP film's low ionic conductivity and thinness [51].

Later EP works expanded to poly(propylene glycol) diacrylate (PPGDA) films doped with lithium bis(trifluoromethanesulfonyl)imide (LiTFSI) salts that exhibited σ ~ 10^{-6} S/cm [182]. The PPGDA EP films ranged from 0.2-2 μm thickness, the thinner of which was shown to conformally coat a Cu nano-pillar architecture (Figure 3.4A). More recently, Abdelhamid *et al.* performed ED of a polyethylene oxide-acrylate based polymer electrolyte on Si pillars. The planar version of the films acted as a GPE with σ ~10^{-4} S/cm when doped with ionic liquids[183].

More recently, initiated chemical vapor deposition (iCVD) has emerged as a candidate technique for depositing conformal SPEs for 3D batteries. Gleason and colleagues used iCVD to produce pinhole-free polysiloxane films (~10 nm thickness) over high aspect ratio Ag nanowires (Figure 3.4B) [29], [123], [124]. Poly(tetra-vinyltetramethylcyclotetrasiloxane) (PV4D4) films with 25 nm thickness exhibited σ = 7.5×10^{-8} S/cm. Yet, for 35 nm thickness, σ dropped to 1.3×10^{-10} S/cm. The authors hypothesized that this was due to increased disorder in the siloxane ring stacking that assisted in lithium transport through the film, or incomplete lithiation of the thicker film during doping [29]. The authors later investigated other polysiloxane and polysilazane SPEs, and found that PV4D4 systems exhibited the best performance with σ approaching ~10^{-7} S/cm at 25 nm film thickness[123], [124]. iCVD of hydroxyethyl methacrylate and ethylene glycol diacrylate (poly(HEMA-*co*-EGDA)) copolymers produced conformally coated thin films on a variety of structured nano surfaces, an example of which is presented in Figure 3.4C, with precise control over thicknesses from 30 to 300 nm. The ionic conductivity dropped by several orders of magnitude as the loading of cross-linker was increased and chain mobility decreased. By tuning the copolymer composition and doping with LiTFSI these poly(HEMA-*co*-EGDA) films exhibited σ = 6.1×10^{-6} S/cm, several orders of magnitude higher than previous iCVD works, for ~ 1 μm thick films [27]. Conductivity-thickness parings for all iCVD electrolytes are compiled in Figure 3S.2B.

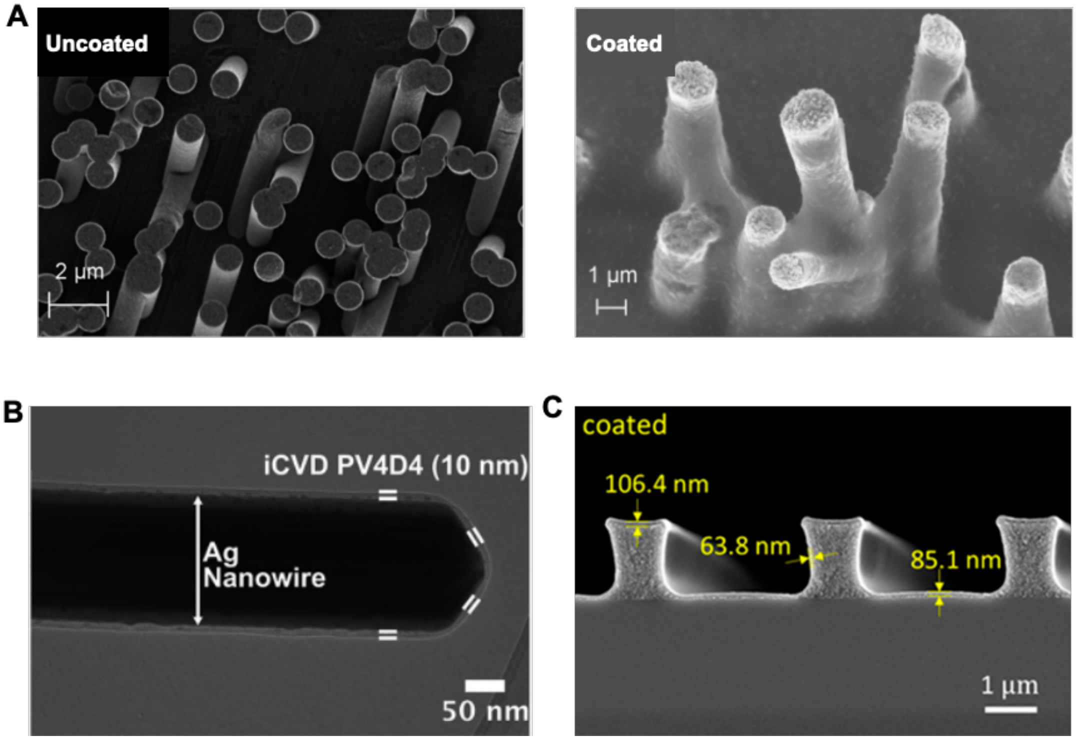

Figure 3.4: A) pre- and post EP PPGDA coating Cu nanopillars. Adapted with permission [182]. Copyright 2014, Elsevier. B) PV4D4 iCVD coating on an Ag nanowire . Reproduced with permission [29]. Copyright 2015, Royal Society of Chemistry. C) poly(HEMA-co-EGDA) iCVD coating on TiO_2 microline. Reproduced with permission [27]. Copyright 2019, American Chemical Society.

While having, generally, < 1 µm thickness makes EP and iCVD electrolytes suitable for MEMS applications there is interest in thicker 3D SPE and GPEs that enable simpler processing techniques. These coatings are more likely to be GPEs as impregnation with organic solvent improves conductivity and helps counteract the increased thickness. For example, Dokko *et al.* molded a poly(methyl methacrylate) (PMMA) sheet doped with $LiClO_4$ and various carbonates to produce a microarray battery[184]. The PMMA GPE served as a separator of ~50 µm thickness and electrolyte with σ on the order of 10^{-3} S/cm. A similar electrolyte was used with a thickness of ~10 µm by Yoshima *et al.* [185].

Fabrication of thicker 3D SPEs and GPEs can be relatively straightforward, such as by dipping 3D structures into polymer solutions or casting the polymer directly onto the 3D structure. This negates the need for the specialized reactors or electrochemical setups required for iCVD and

EP, respectively. For example, Tan *et al.* produced conformal SPEs made of a 2:1 blend of polyetheramine and poly(propylene oxide) diacrylate that contained LiTFSI salt [186]. These SPEs were successfully cast on $LiFePO_4$ electrodes (Figure 3.5A) at 2 µm thickness, giving $\sigma = 3.45 \times 10^{-6}$ S/cm at 3.1 mm thickness. Similarly, by solution casting Nakano *et al.*[187] produced ~50 µm thick PEO SPEs with $\sigma = 2 \times 10^{-4}$ S/cm. Sun *et al.* conformally cast ~1 µm thick blended poly(ether amine) (glyceryl poly(oxypropylene) and poly(propylene glyocol) diacrylate SPE coatings on conventional $LiFePO_4$ electrodes. Freestanding films (3.1 mm thickness) exhibited $\sigma = 3.5 \times 10^{-6}$ S/cm after crosslinking [188]. Sun *et al.* cast a PEO-based GPE (4×10^{-3} S/cm) into ~25 µm channels to form a full cell [189], while Ashby *et al.* infiltrated high conductivity (10^{-3} S/cm) ~100 µm thick ionogel electrolytes into their cells [190]. Last, 3D SPEs based on poly(trimethylene carbonate) (PTMC) were formed by dipping various 3D electrodes (Figure 3.5B) into solutions of PTMC that contained LiTFSI and achieved a maximum σ of 10^{-4} S/cm for ~5 µm thickness [191].

Spin coating presents another route to depositing SPEs and GPEs, which is also amenable to salt loading for suitable conductivity. Choi *et al.* produced $LiClO_4$ doped SU-8 GPEs by spin coating onto Si substrates [192]. The doped SU-8 exhibited $\sigma = 5.2 \times 10^{-5}$ S/cm at thickness of approximately 2.7 µm. Hur *et al.* used a similar approach to produce full 3D cell with a SU-8 GPE by spin coating onto Si pillars (Figure 3.5C)[50]. These films were thicker (10-50 µm) and exhibited $\sigma = 2.8 \times 10^{-7}$ S/cm, with the SU-8's conductivity being greatly influenced by the degree of crosslinking. Thicker (100 µm) methyl ether methacrylate-polyethylene glycol (MA-PEG) SPEs were spin coated by Nasreldin *et al.*, giving $\sigma = 4 \times 10^{-4}$ S/cm in a stretchable 3D microbattery [193].

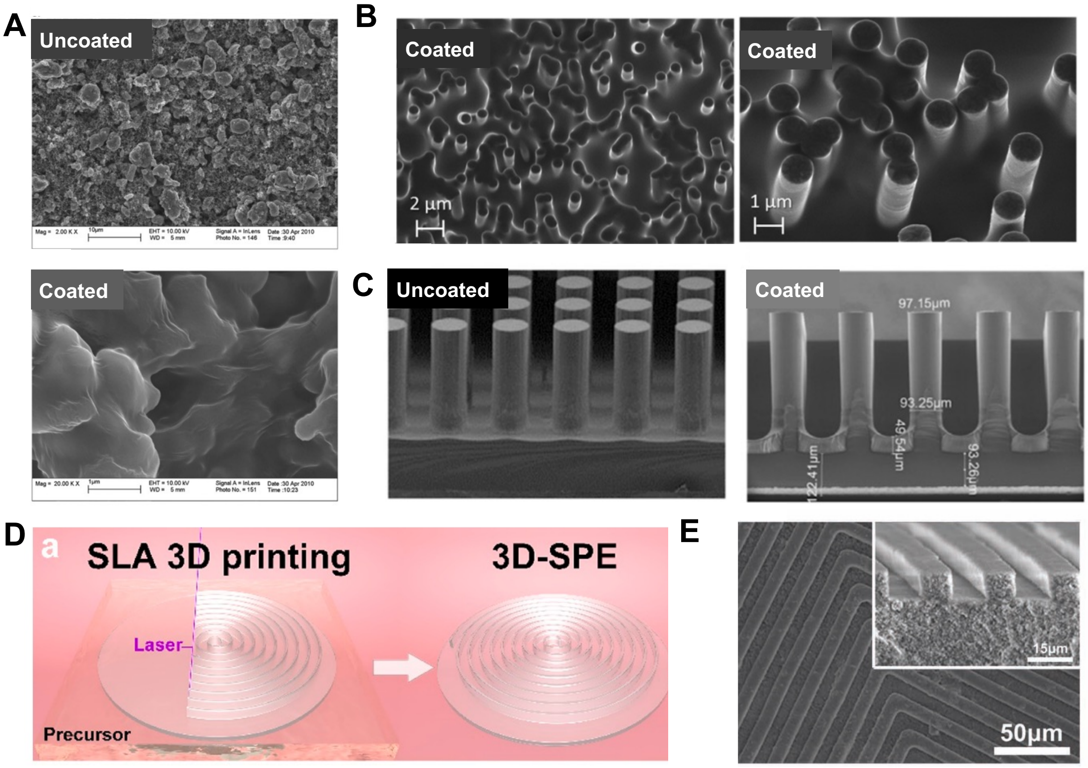

Figure 3.5: A) Pre- and post-casting of SPE onto a LiFePO$_4$ electrode. Adapted with permission [186]. Copyright 2010, Elsevier. B) dipped PTMC SPE on Cu$_2$O-Cu nanopillars. Adapted with permission [191]. Copyright 2018, American Chemical Society. C) spin coated SU-8 GPE on Si pillars. Adapted with permission [50]. Copyright 2018, Elsevier. D) SLA 3D printed SPE. Reproduced with permission [194]. Copyright 2020, American Chemical Society. E) imprint lithography GPE. Reproduced with permission [195]. Copyright 2013, Wiley-VCH.

An alternative approach to creating a conformal electrolyte coating is a structured SPE or GPE which allows incorporation of, but prevents physical contact between, two electrodes. PEO-based SPEs with ~100's of micron thickness (Figure 3.5D) have been produced using stereolithography, giving $\sigma = 3.7\text{x}10^{-4}$ S/cm [194], while imprint lithography has been utilized to create SU-8 based GPEs (Figure 3.5E) with ~150 µm thickness and $\sigma > 10^{-3}$ S/cm [195]. Conductivity-thickness parings for all microscale SPEs and GPEs are compiled in Figure 3S.2C and S2D.

3.4 Solid State Ceramic Electrolytes

Many ceramics have been investigated as SSEs for 3D battery systems. In general, ceramic based SSEs can offer higher conductivity than SPEs and are safer than GPEs. However, ceramic SSEs have high density [1], [26], are often brittle [26], and incur higher material and processing costs compared to their polymer counterparts [26], [33], [169], [196]. Despite having a modest ionic conductivity, LiPON has served as the SSE of choice for planar thin film solid state batteries; it is typically made by sputter deposition, with $\sigma \sim 10^{-6}$ S/cm [126], [176], [197]–[205]. Thicknesses are typically ~1 μm but have been reported between 0.5 to 200 μm [126], [176]. LIPONB [206], [207] and LiSiPON [208] have been produced by co-sputtering, or by incorporating the added element into the sputtering target; the same applies to sputtered lithium vanadium silicon oxide [209]. While sputtered films have been used in 3D structured cells (Figure 3.6A), sputtering does not conformally coat high aspect ratio features, and shadowing effects lead to uneven thickness and limit overall conductivity [126], [202]. Conductivity-thickness parings for all sputtered SSEs are compiled in Figure 3S.3A.

On the other hand, atomic layer deposition (ALD) has become a leading technique for conformal deposition of SSEs on 3D battery electrodes with micro- and nanoscale features. ALD produces films that are both conformal and pinhole free under appropriately controlled conditions. However, each self-limiting ALD cycle deposits a sub-nanometer film, requiring many time consuming cycles even for 10-100 nm thickness coatings, although continuous processes have been developed for non-electrolyte applications [210], [211]. Multiple comprehensive reviews have been published on use of ALD processes into 3D battery designs [158], [212].

Using sputtered SSE films as a benchmark, LiPON and LiPON-like films have been explored using ALD processes. For ALD of LiPON, Nisula *et al.* used lithium hexamethyldisilazide and diethyl phosphoramidate precursors, while Kozen *et al.* use the more common lithium *tert*-butoxide, deionized H_2O and trimethylphosphate precurors [118], [213]. Nisula *et al.* conformally coated silicon micropillars with 115 nm thickness of LiPON which exhibited a room temperature $\sigma = 6.6\text{x}10^{-7}$ S/cm (Figure 3.6B) [213]. Kozen *et al.* demonstrated $\sigma = 1.45\text{x}10^{-7}$ S/cm for films with a thickness of less than 50 nm, and deposited LiPON on individual carbon nanotubes (CNTs)[118]. More recent works studying ALD LiPON films achieved similar results, with $\sigma = 5\text{x}10^{-7}$ S/cm for a 70 nm film[214] and $3.2\text{x}10^{-7}$ S/cm for a films with thickness between 50 and 500 nm [215]. Pearse *et al.* developed unique polymorph LiPON films with $\sigma = 6.5\text{x}10^{-7}$ S/cm at 35°C for thicknesses of 70-80 nm and utilized these films in a planar thin film battery between Si and $LiCoO_2$ electrodes[52]. Pearse *et al.* later reproduced a similar electrolyte with almost identical thickness and conductivity to fabricate full 3D solid state batteries by depositing an ALD SSE on an etched Si substrate (Figure 3.6C) [37]. The LiPON coating by Put *et al.* was successfully utilized as a SSE in a planar thin film battery [214]. LiPON SSEs have also been deposited by metalorganic-chemical vapor deposition (MOCVD), with 190 nm thick MOCVD films exhibiting $\sigma = 5.9\text{x}10^{-6}$ S/cm, which is ~10-fold greater than the cited ALD LiPON works[216].

ALD lithium phosphate (LiPO) has also been investigated, with thicknesses similar to ALD LiPON but with slightly lower conductivities. In 2014 Wang *et al.* reported room temperature $\sigma = 3.3\text{x}10^{-8}$ S/cm for films with thickness of ~130 nm [217]. Liu *et al.* deposited pinhole-free, conformal LiPO films by ALD (< 10 nm thickness) on $FePO_4$ coated CNTs, though the films had a low σ, $\sim10^{-9}$ S/cm [111]. Finally, Létiche *et al.* produced full 3D cells by depositing thin films, including a LiPO electrolyte, on an etched Si wafer [218]. By varying the deposition temperature and film thickness, σ = 6.2×10^{-7} S/cm was achieved for 30 nm thickness, and σ = 2.6×10^{-7} S/cm for a 10 nm thick pinhole free-sample.

ALD chemistries for oxide-based SSEs have also been developed. The thicknesses of these films are typically tens to hundreds of nanometers, and the ionic conductivity varies by several orders of magnitude depending on the precursors, processing parameters and final film composition. For instance, Kazyak *et al.* developed an ALD route to produce garnet (LLZO) thin films with σ ~10^{-8} S/cm [219]. Investigations into lithium aluminate yielded films with σ ranging from 10^{-10} S/cm [220] to 5.6×10^{-8} S/cm [221]. A lithium silicate based oxide exhibited σ = 5.72×10^{-9} S/cm [222] just above room temperature, while a film combining lithium aluminate and silicate improved the room temperature σ to ~10^{-7} S/cm [223]. Other oxide SSEs deposited by ALD include lithium niobium oxide (6.39×10^{-8} S/cm) [224], lithium tantalate (2×10^{-8} S/cm)[117] and lithium carbonate (10^{-10} S/cm)[225]. So far the highest known ionic conductivity achieved by ALD was via a combination of lithium borate and lithium carbonate that exhibited σ = 2.2×10^{-6} S/cm at 100 nm thickness[180]. Non-oxide ALD SSEs include lithium fluoride (10^{-13} S/cm)[226], lithium aluminum fluoride (3.5×10^{-8} S/cm)[227], and lithium aluminum sulfide (2.5×10^{-7} S/cm)[228] thin films. Conductivity-thickness parings for all ALD and MOCVD SSEs are compiled in Figure 3S.3B.

It has also been shown that thicker 3D templated SSEs can serve as scaffolds for full cell fabrication. A notable example is the work by Kotobuki *et al.*, who used a honeycomb shaped perovskite-type (LLTO) structure to manufacture a 3D cell by infiltrating the shaped electrolyte with conventional slurry-based electrode materials [49]. The LLTO had a thickness on the order of 100 μm and a reported σ 1.1×10^{-3} S/cm. Similarly, Shoji *et al.* used a pressed LLZO pellet with thickness of ~500 μm and a σ ~10^{-4} S/cm to make the scaffold (Figure 3.6D) for their cell [229].

In a unique approach, Cohen *et al.* combined PEO with lithium aluminum germanium phosphate (LAGP) SSE to produce a "quasi-solid" electrolyte by electrophoretic deposition, resulting in σ = 2x10^{-4} S/cm at ~50 µm thickness [230]. Conductivity-thickness parings for all formed SSEs are compiled in Figure 3S.3C.

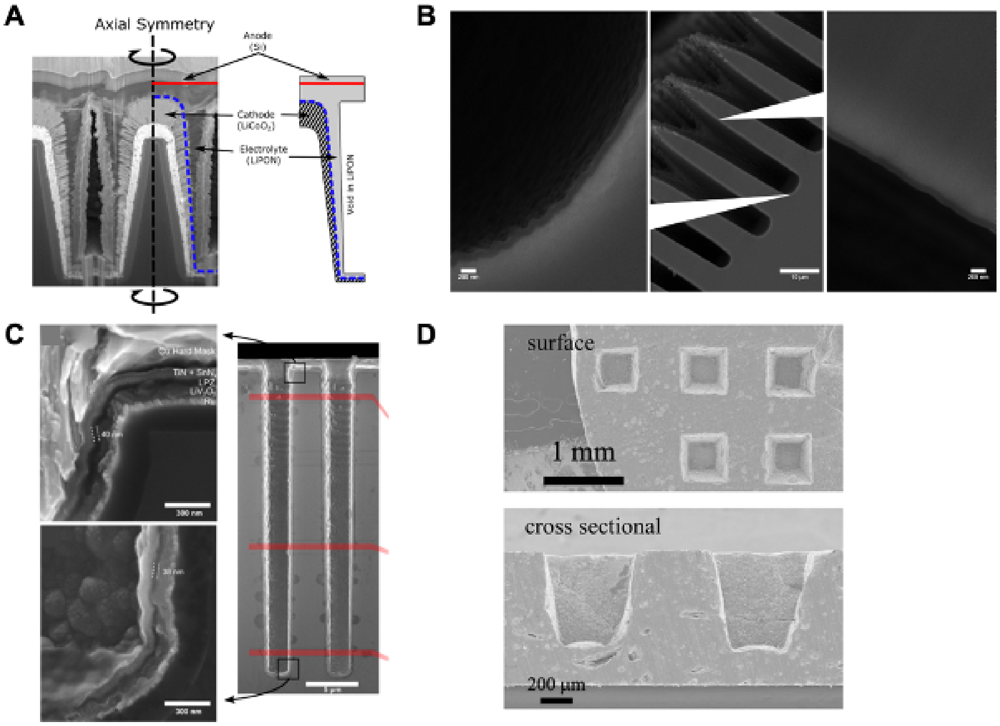

Figure 3.6: A) 3D full cell containing sputtered LiPON SSE. Reproduced with permission [126]. Copyright 2016, American Chemical Society. B) ALD LiPON SSE on 3D-microstructed Si pillars. Reproduced with permission [213]. Copyright 2015, American Chemical Society. C) full 3D cell containing LiPON like electrolyte deposited on etched Si. Reproduced with permission [2]. Copyright 2018, American Chemical Society. D) formed LLZO pellet to serve as a template for 3D full cell construction. Reproduced with permission [229]. Copyright 2016, Shoji, Munakata and Kanamura.

3.5 Ionic Conductivity Suitability and Area Specific Resistance

Ionic conductivity is perhaps the most important consideration for a material to be used as an SSE or SPE. A high ionic conductivity helps to mitigate ionic resistance losses across the electrolyte layer. In *Eq. 3.1* the ionic resistance (R) is a function of electrolyte thickness (L), electrode-electrolyte contact area (A) and the ionic conductivity (σ) [29]. As one requirement to replace liquid electrolytes in batteries, SSEs, SPEs and GPEs must exhibit ionic conductivities comparable to liquid electrolytes currently used in state-of-the-art systems (~10^{-3} to 10^{-2} S cm^{-1}). Consistently achieving this level of σ has historically been a challenge for all SSE and SPE types, and it is not uncommon for σ to vary by orders of magnitude depending on ion valency and size, conduction mechanism, electrolyte composition, crystal structure and operating temperature[24].

While recent research has produced oxide and sulfide SSEs with σ on par with liquid electrolytes[10], these high conductivity SSEs are produced for planar batteries, often at thickness > 10 µm, so their processing methods to date make them unsuitable for implementation in 3D batteries. The result is that SSEs, SPEs or GPEs used in 3D batteries are often limited to materials compatible with the limited processing techniques capable of electrolytes in a format conformal to 3D electrode structures, as highlighted by the many examples cited in the prior sections.

However, considering that 3D cells generally require a thinner electrolyte than planar designs, we can use the area specific resistance (ASR, *Eq. 3.2*) as a measure to compare 2D and 3D electrolytes. For each electrolyte there will exist a certain minimum thickness that offsets the losses from the decreased σ. While many 3D SSE or SPE works point out this trade-off, the question as to whether the conductivity and thickness combination are competitive with conventional technologies, and other 3D electrolytes, is rarely answered.

$$R\ (\Omega) = \frac{L\ (m)}{\sigma\ (S\ m^{-1}) \cdot A\ (m^2)} \qquad (Eq.\ 3.1)$$

$$ASR\ (\Omega\ m^2) = \frac{L\ (m)}{\sigma\ (S\ m^{-1})} \quad (Eq.\ 3.2)$$

In Figure 3.7, we plot the calculated area specific resistance (ASR) for each 3D SPE and GPE versus its thickness; Figure 3.8 shows the same for 3D SSEs. Additional breakdowns of ASR by electrolyte deposition or fabrication technique are found in Figure 3S.4 through Figure 3S.6. The ASR is calculated by taking the ratio L/σ (*Eq. 3.2*) [180], [218], [223]. This ASR can then be compared with the calculated ASR for conventional battery electrolytes as well as the standard interfacial impedance for conventional Li-based systems (~10 Ω m^2) [180].

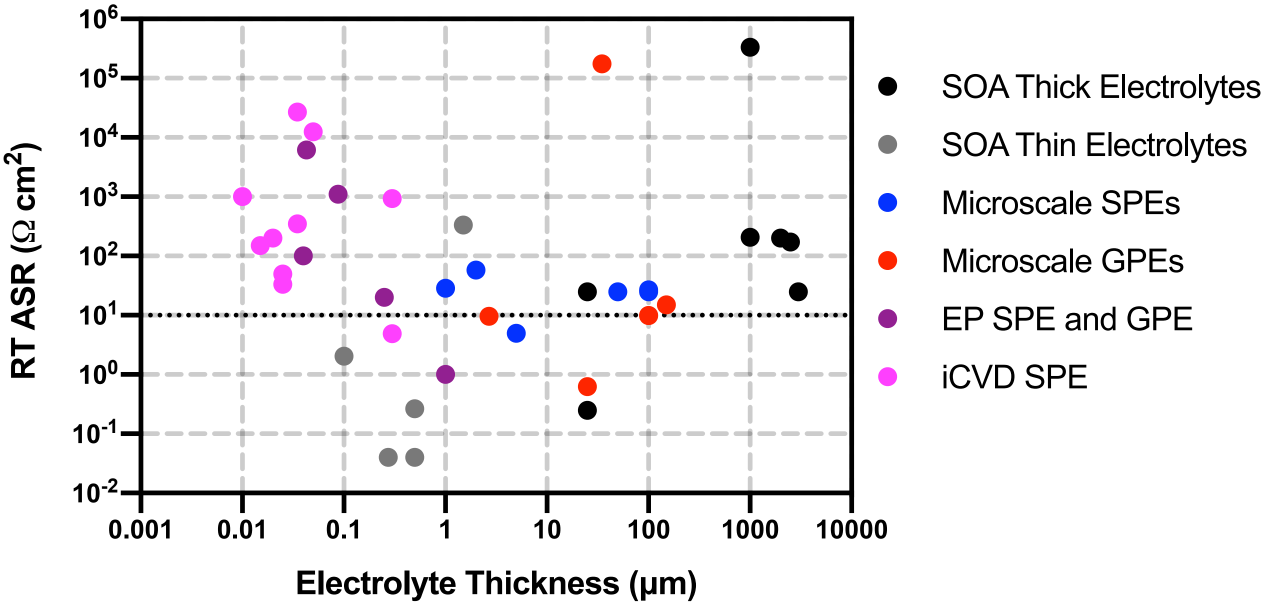

Figure 3.7: Calculated ASR for 3D SPE and GPEs, as well as SOA planar solid and liquid electrolytes.

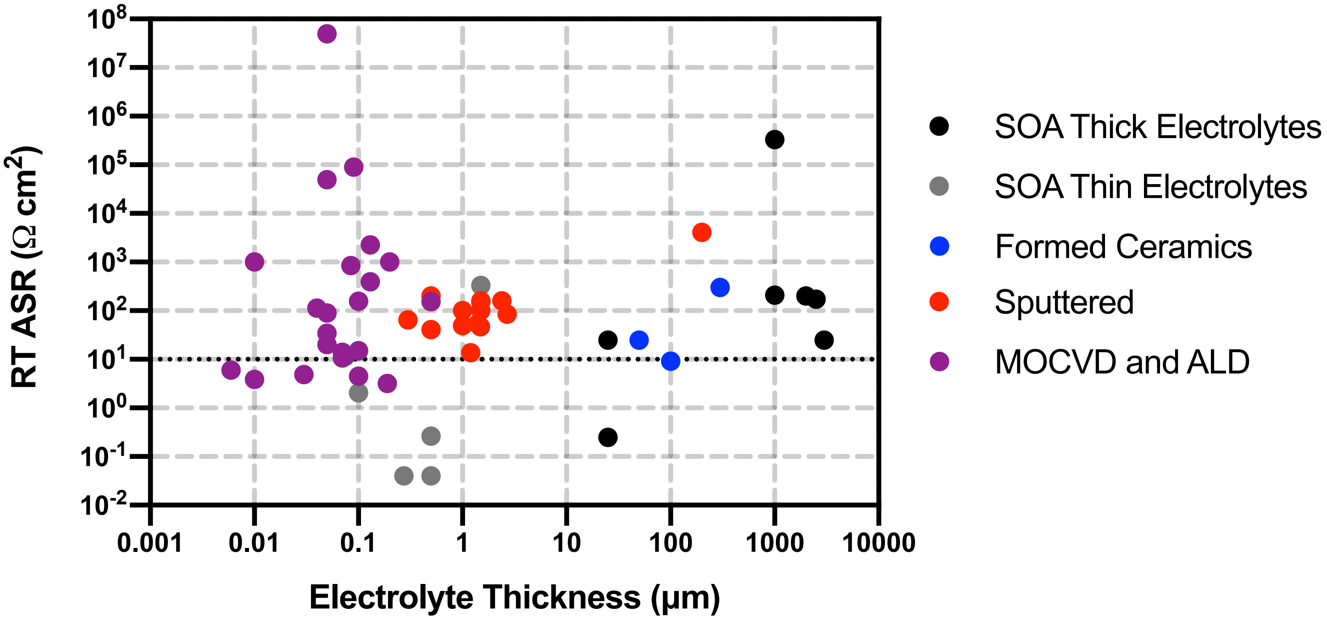

Figure 3.8: Calculated ASR for 3D SSEs, as well as SOA planar solid and liquid electrolytes.

We can draw several useful conclusions from Figure 3.7. First, the ASR of early PPO-based EP SPEs [51], [114], [116], [181] and siloxane or silazane iCVD SPEs [62–64] exceeds the

~10 Ω m^2 threshold, yet this is far surpassed by improved EP and iCVD material systems. With respect to EP, the highest ASR also corresponds to the work with the best reported conductivity; the polyethylene oxide-acrylate based GPE by Abdelhamid *et al.* gave an impressive ASR of ~1 Ω m^2, albeit by incorporating ionic liquids in the gel. A similar improvement was observed for iCVD, where recent advances in copolymerization have produced an SPE with ASR below 10 Ω m^2 [27]. Despite requiring a specialized reactor iCVD has the advantage of easily tunable thickness spanning from < 10 nm [29] to > 1 μm [119] and the ability to control mechanical properties through crosslinker composition. At $L > 1$ μm several of the SPE [191] and GPE [184], [189], [190], [192] systems also demonstrate competitive ASRs. However, these electrolytes are difficult to integrate with 3D electrodes, such as the cast SPE of Tan *et al*. (Figure 3.5A) which, despite creating a conformal exterior coating, fails to penetrate deep into the electrode. Nevertheless, even the best 3D GPEs and SPEs reported to date fall behind the ASRs of thin film planar SSEs or conventional liquid electrolytes.

Similarly, certain 3D SSE works stand out in terms of their ASR (Figure 3.8). 3D templated SSEs manufactured from conventional SSEs are competitive with their planar counterparts [49] and may provide a pathway to creating 3D SSEs using well researched materials, particularly if the forming process can achieve thinner films, as for instance Kotobuki *et al.* reached only 100 μm. Sputtered LiPON lags behind LiSiPON[208], which only approaches the ~10 Ω m^2 target. Notably, MOCVD LiPON performs far more admirably, largely in part to its thinner thickness[216]. Due to their thin thicknesses and relatively high conductivities the LiPO of Létiche *et al*. [218] and combination of lithium borate and carbonate from Kazyak *et al.*[180] are well beneath ~10 Ω m^2 threshold. Here, the lithium aluminum silicon oxide film of Perng *et al.* stands out due to the fact that its low conductivity is heavily compensated by its < 10 nm thickness [223].

While these ALD SSEs have ASRs below the target value, they still trail behind the best SOA thin film planar electrolytes and are limited in practice due to limitations in obtaining practically thick films.

3.6 Key Considerations for 3D Integration of SSE, SPE and GPEs

Several other key attributes such as stability, coating quality, and cost will also be crucial in determining the most suitable techniques and materials for future 3D battery development. These issues are also critical to planar solid state battery development, but their impact is compounded with the additional fabrication constraints of a 3D design.

3.6.1 Electrochemical Stability Window

Promising SSEs, SPEs or GPEs should have a large electrochemical stability window (ESW, Figure 3.9), which guides whether an SSE is stable against the positive and negative electrodes. The ESW is determined by the SSE's reduction and oxidation potentials, which, respectively, are governed by the conduction band maximum (CBM) and valence band minimum (VBM) energy levels. To meet this criteria the energy gap between the CBM and VBM should exceed the energy difference between the negative (μ_A) and positive (μ_C) electrodes, the CBM should be greater than μ_A and the VBM should be less than μ_C [28], [30]. If the CBM drops below μ_A then the SSE will be reduced at the negative electrode. Similarly, if the VBM rises above μ_C then the SSE will be oxidized at the positive electrode. These, often unwanted, parasitic reactions result in the formation of SEI layers that consume active material and may be impassible to Li-ion transport, significantly limiting cell lifetime and capacity.

Ideal electrolytes for integration into a Li-ion or Li-metal batteries have an ESW that stretches from ~ 0.0 to 0.1 V vs. Li/Li$^+$ to > 4 V vs. Li/Li$^+$. This is further complicated by the fact that the formation of a stable solid electrolyte interphase (SEI) may allow electrolytes to be utilized at potentials outside of their thermodynamically stable range [31]. The ESWs of planar SSE, SPEs and GPEs have been extensively researched both computationally and experimentally [25], [28], [30]–[32]. This is a significant advantage for formed ceramic SSEs, as they start from well researched materials such as LLTO [49] and LLZO [229].

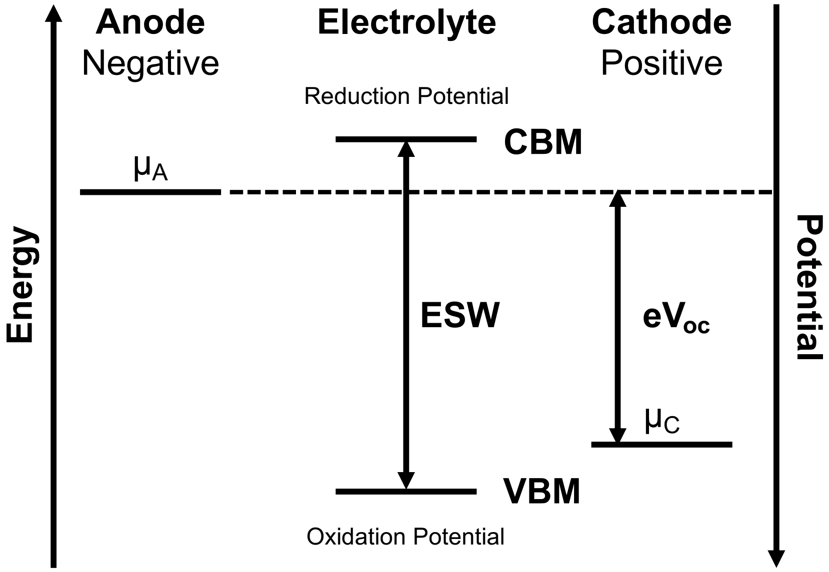

Figure 3.9: Diagram of the electrolyte interface with the positive and negative electrodes. Adapted with permission [28]. Copyright 2019, American Chemical Society.

While it is not uncommon for 3D electrolyte works to focus only on obtaining high ionic conductivity and to not include a determination of their ESW, we can draw conclusions for 3D electrolytes from research on planar electrolytes with similar chemical composition and structure. Notably, SPEs, especially those that are PEO based, have an ESW that allows for stability against Li-metal and transition metal oxide electrodes while GPEs tend to break down due to the presence of the organic solvent [34,120]. In agreement with this, Sun *et al.* reported a stability window of 0 to 5 V vs. Li/Li$^+$ for their blended poly(ether amine) (glyceryl poly(oxypropylene) and poly(propylene glyocol) diacrylate SPE coatings[188], Choi *et al.,* Hur *et al.* and Kil *et al.* all reported stability above 5 V vs. Li/Li$^+$ for their SU-8 based GPEs [50], [192], [195], He *et al.* reported a stability above 4.55 V vs. Li/Li$^+$ for their 3D printed PEO based electrolyte [194], and

Ashby *et al.* noted that their ionic liquid doped GPE had previously been determined to be stable at their $LiFePO_4$ cathode and Li-metal anode [190]. On the other hand, to our knowledge ESWs have not been reported for EP and iCVD SPEs and these ranges should be determined to ensure these electrolytes, in particular the low ASR iCVD co-polymers, can be incorporated as part of a stable full cell.

For SSEs, planar LiPON is known to be stable against negative electrodes all the way down to Li-metal due to the formation of a stable SEI phase. Despite a tendency to oxidize at ~2.6 V vs. Li/Li^+ [31], [32], certain sputtered LiPON works have reported [199], [204], but less frequently verify[176], stability up to ~ 5 V vs. Li/Li^+[176]. The addition of B or Si to sputtered LiPON has not been observed to affect stability window of the resultant SSE [206]–[208], nor does the translation to other deposition techniques such as ALD LiPON or LiPON-like SSEs [97,100] and these observations should be verified when signficant composition changes are made to the SSE.

Other 3D SSEs show ESW behavior similar to their planar counterparts, such as lithium fluoride based electrolytes [227] and Létiche *et al.* who verified that their LiPO SSE was stable up to 4.2 V vs. Li/Li^+ [218]. Reporting the ESW becomes even more important when new chemical compositions are utilized in an ALD recipe as a promising σ could be completely undone by a lack of stability. Kazyak *et al.* used density functional theory to predict that their lithium borate and lithium carbonate has a wide ESW, which, when combined their high conductivity, makes this ALD electrolyte a leading candidate for use in 3D batteries[180]. However, other ALD studies on materials typically used as electrolytes in Li-based storage systems have not reported the ESW [222]–[225]; although these ALD films are sometimes used as an artificial SEI to improve full-cell behavior, which can be seen as an alternative way to determine stability [180], [220], [221], [226].

3.6.2 Infiltration Into Porous Electrodes

Another key aspect of 3D battery fabrication is infiltration of the SSE, SPE or GPE into a micro- or nanostructured electrode, which may comprise an array of pillars and/or a porous medium. While many works demonstrate a conformal coating over the exterior of high aspect ratio features (Figure 3.10A), the practicality of such electrodes is limited when the features have a diameter/thickness greater than a few microns. In this case, (Figure 3.5C and Figure 3.10B) solid-state Li-diffusion becomes the dominating transport mechanism through the electrode and limited ion transport may result in unutilized active material. This is often the case for 3D batteries made with microscale SPE and GPE electrolytes, as the deposition techniques are limited to the exterior faces of a 3D electrode, sometimes requiring liquid electrolyte injection to maintain ionic conductivity through the electrode[50], [184], [189].

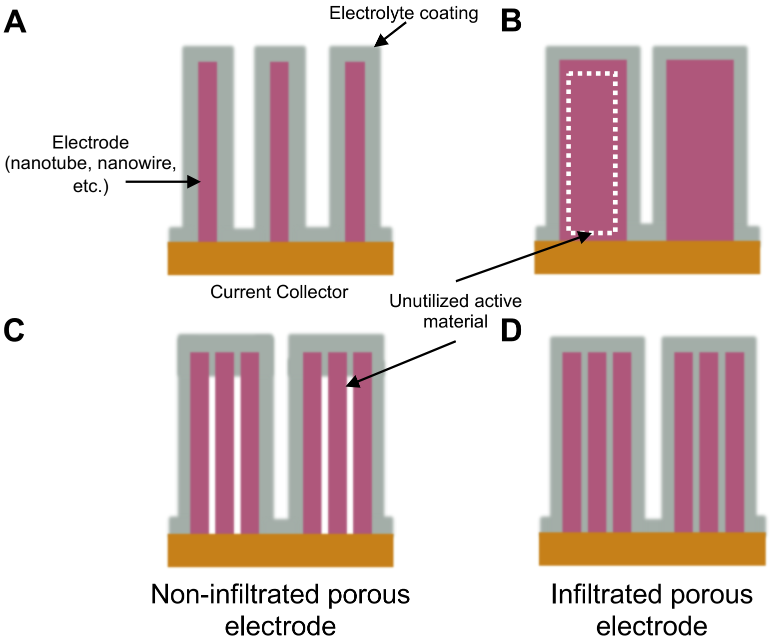

Figure 3.10: Schematic showing the importance of porosity and electrolyte infiltration into 3D electrodes as length scale and feature size increases. A) conformally coated thin non-porous electrodes, B) conformally coated thick non-porous electrodes, C) conformally coated porous electrode without electrolyte infiltration and D) conformally coated pours electrode with electrolyte infiltration.

Porosity alone does not solve this problem, as the deposited electrolyte must be able to infiltrate the pores to allow ionic transport to active material deeper in the electrode (Figure 3.10C). An example is shown in Figure 3.5A, where the SPE produced by Tan *et al*. is coating is capable of coating electrode surface but in the paper is revealed to have difficulty infiltrating further into the electrode [186], a problem that is not common to that system [193].

This issue can be mitigated by minimizing electrode feature sizes for brittle electrolytes, such as ceramic SSEs by ALD, and ensuring full penetration throughout the electrode for SPEs (Figure 3.10D). Here, conformal gas-phase deposition techniques, such as ALD or iCVD, and EP processes have a considerable advantage over the dipping, infiltration, etching and spin coating methods due to the numerous process parameters that can be tuned to ensure a controlled and uniform deposition with sufficient infiltration.

3.7 Outlook

The development of SPEs, GPEs, and SSEs with conformal deposition and high ionic conductivity has represented a significant challenge in the development of 3D batteries. While SSEs and SPEs are now reaching suitable ionic conductivities for planar battery designs, the considerations required to adapt such materials to processing techniques capable of high conformality and pinhole free films results in a significant decrease in obtainable ionic conductivity. While this is somewhat compensated by the thinner electrolyte thickness of many 3D designs, most 3D electrolytes do not have ASRs that are competitive with conventional SOA planar electrolytes. Therefore, new material chemistries need to be developed for fabrication techniques such as iCVD and ALD, to improve ASR and ionic conductivity. Despite these inadequacies certain ALD and iCVD based SSE and SPEs have achieved ASR below the ~10 Ω m^2 threshold defined as competitive in this analysis, and approaching that of thin film planar solid electrolytes. Further improvement of these materials should open the door for improved 3D battery performance and development. Additionally, to be considered as a valid replacement for planar batteries, any 3D batteries will need to be competitive on a cost level. This will be difficult, as innovations in cell chemistry, manufacturing learning rates and economies of scale have significantly reduced the \$ kWh^{-1} for planar lithium-ion batteries. This will be a significant challenge for 3D batteries, as vapor deposition processes require specialized reactors with vacuum pumps and conventional cleanroom techniques are limited to batch processes. One crucial metric in solid 3D battery development will be whether the improved performance from decoupling energy and power density justifies the increase in cost, making it likely that the entry point for 3D batteries will applications where high performance is a necessity and footprint area is at a premium such as MEMS, wearable electronics and systems for aeronautical applications.

3.8 Supporting Information

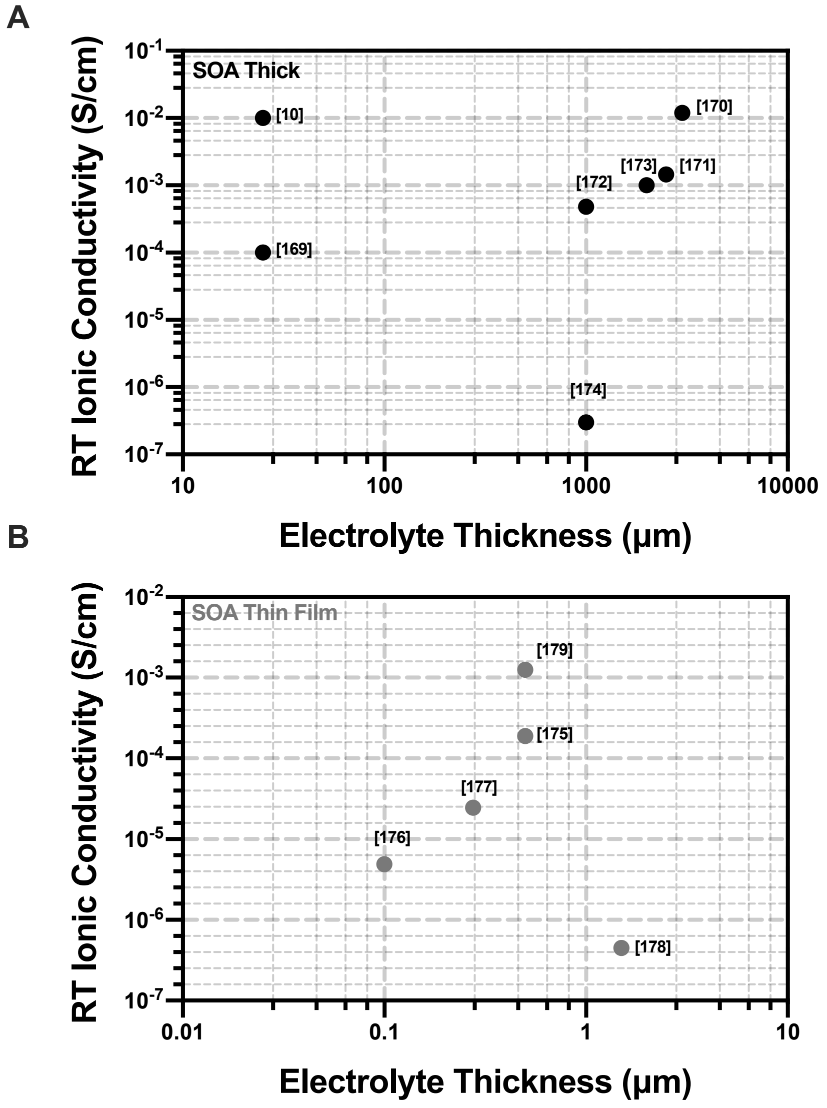

Figure 3S.1: Reported values of ionic conductivity versus electrolyte thickness for SOA A) thick SSEs, polymer and liquid electrolytes, and B) thin film SSEs.

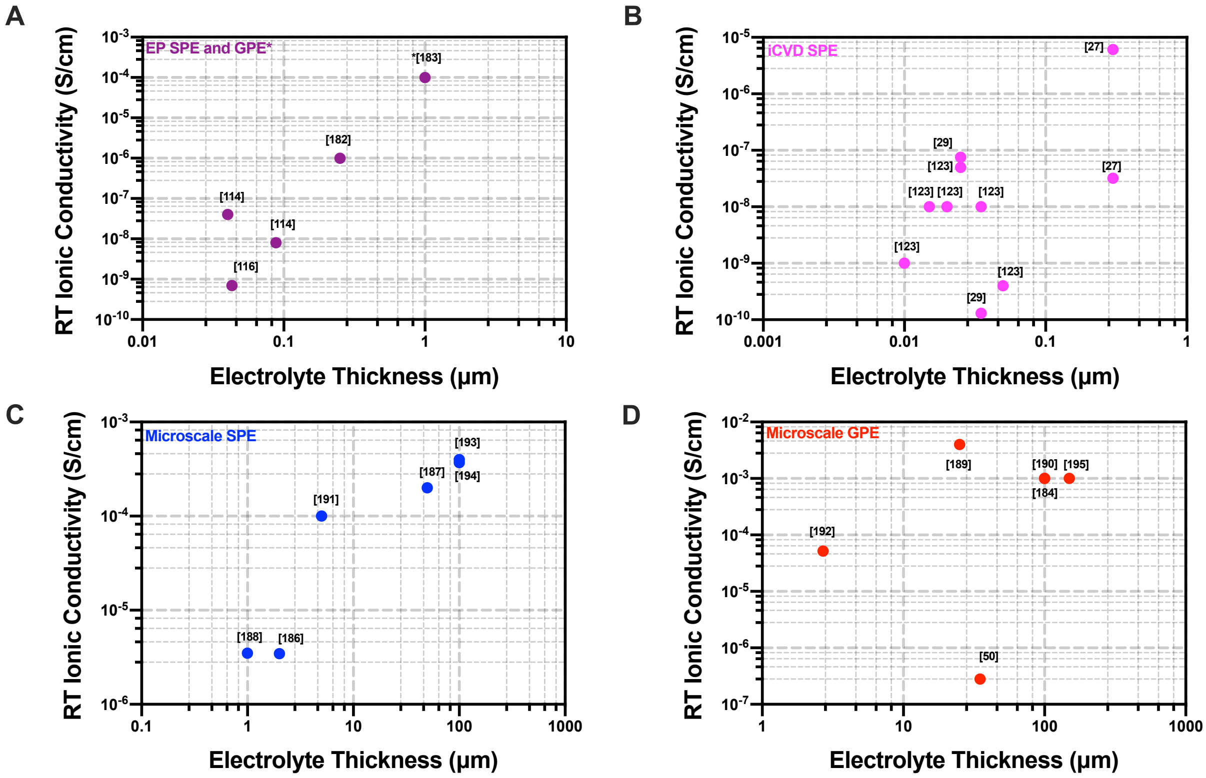

Figure 3S.2: Reported values of ionic conductivity versus electrolyte thickness for A) EP SSE and GPE, B) iCVD SSE, C) microscale SPE and D) microscale GPE

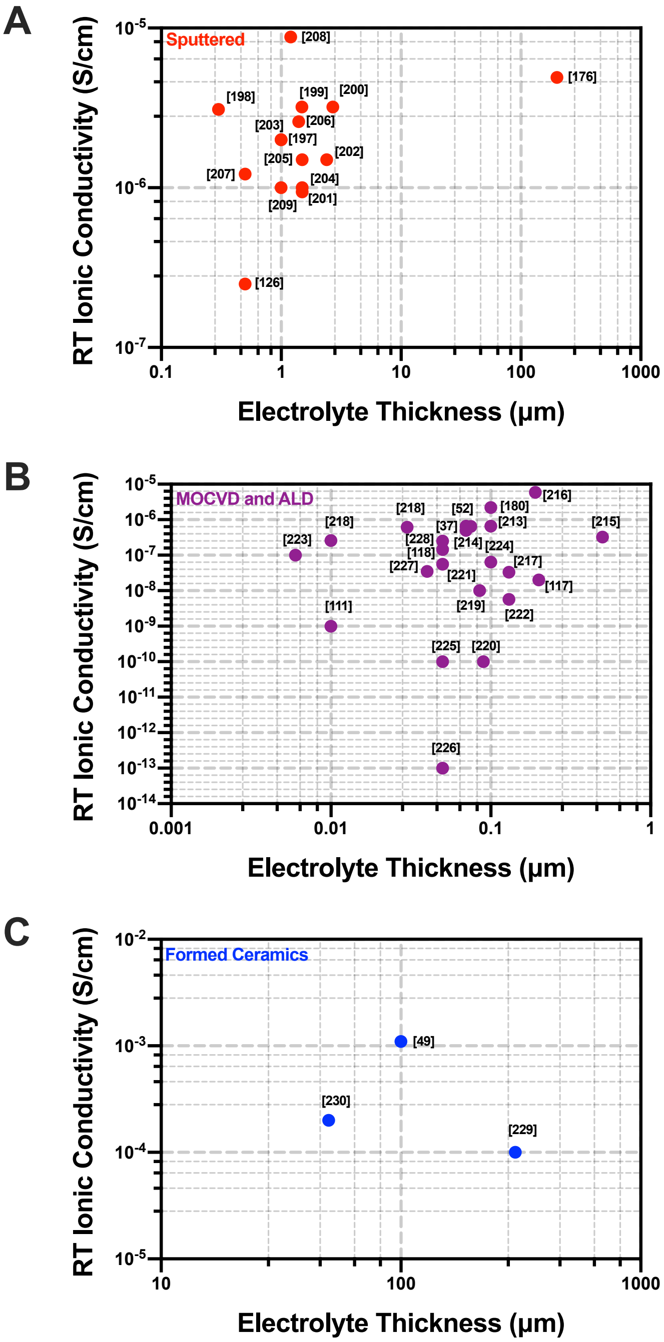

Figure 3S.3: Reported values of ionic conductivity versus electrolyte thickness for A) sputtered, B) ALD and MOCVD and C) formed ceramic SSEs.

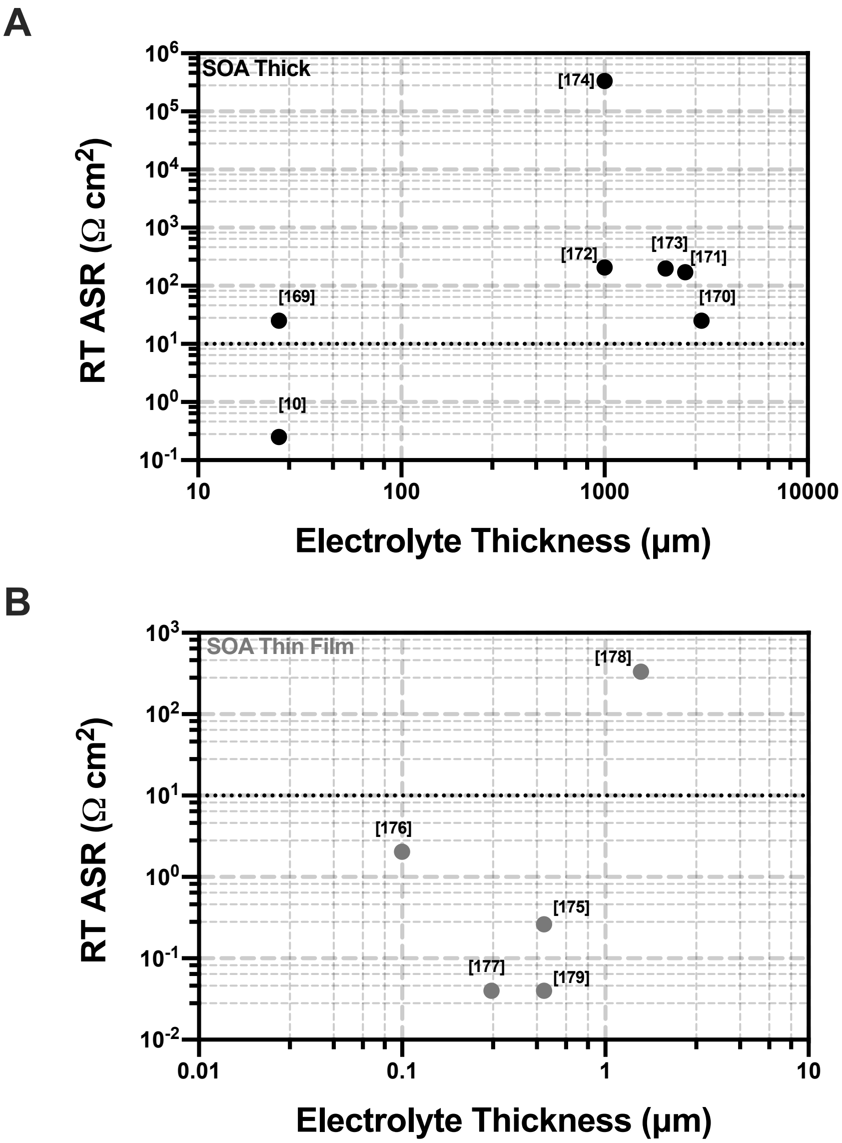

Figure 3S.4: Calculated values of ASR versus electrolyte thickness for SOA A) thick SSEs, polymer and liquid electrolytes, and B) thin film SSEs.

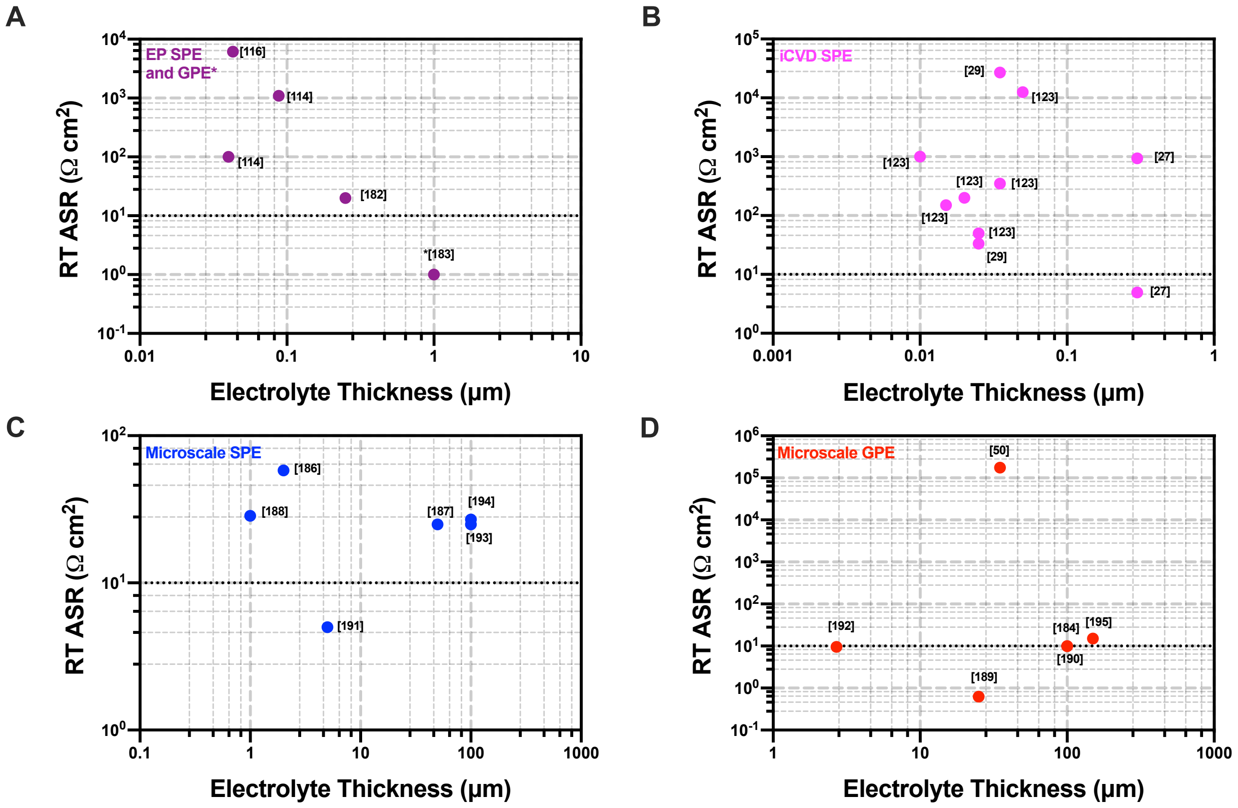

Figure 3S.5: Calculated values of ASR versus electrolyte thickness for A) EP SSE and GPE, B) iCVD SSE, C) microscale SPE and D) microscale GPE.

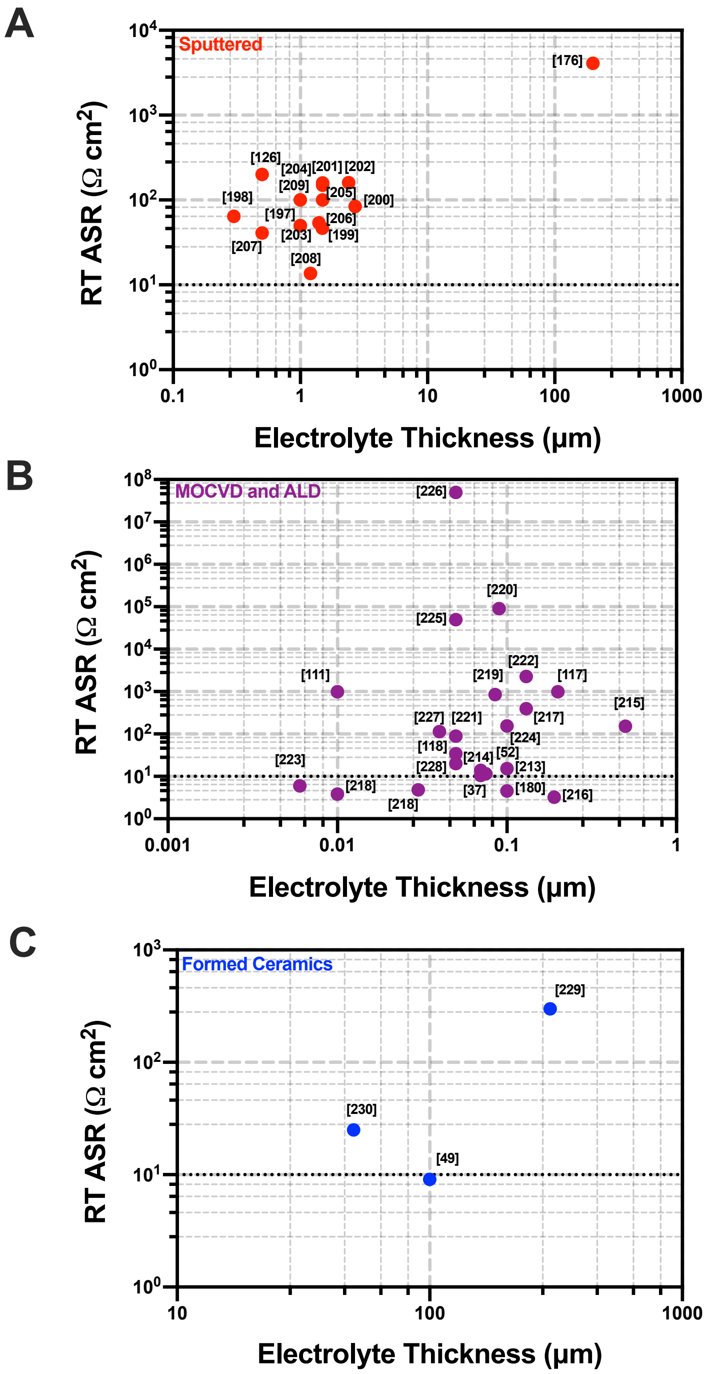

Figure 3S.6: Calculated values of ASR versus electrolyte thickness for A) sputtered, B) ALD and MOCVD and C) formed ceramic SSEs.

THIS PAGE IS LEFT INTENTIONALLY BLANK

Chapter 4- Conformal Electrolytes by Initiated Chemical Vapor Deposition

4.1 Introduction to Initiated Chemical Vapor Deposition

Chemical vapor deposition (CVD) techniques are prominent in the semi-conductor industry for depositing inorganic thin films. More recently, CVD methods have expanded to include engineering organic surfaces through polymer thin film deposition [122]. CVD's gaseous nature offers several advantages for processing polymer films compared to conventional solution-based processing methods. Foremost among these is high film quality, as potential contaminants such as salts or surfactants are not required for vapor phase polymerization. The absence of solvent also makes CVD polymerization an attractive alternative for polymer coatings on substrates that are flexible, fragile or difficult to wet, while eliminating post-polymerization curing steps [122], [231].

Furthermore, polymer CVD techniques can conformally coat high aspect ratio features. In solution-based polymerizations tension effects form liquid bridges that prevent precursor penetration to the bottom of surface features, leaving voids in the deposited material, and show thinning behavior on side walls due to meniscus formation. However, in vapor-phase processing the reactants diffuse into pores or trenches via intermolecular collisions. The reactive species then impinge on all surfaces evenly, allowing vapor-phase deposition to conformally coat high aspect ratio features (Figure 4.1) [231], [232]. These properties make CVD polymer films desirable for applications ranging from microelectronics and energy storage to antifouling and biocompatibility, where smooth, conformal and pinhole-free coatings are required [122], [233].

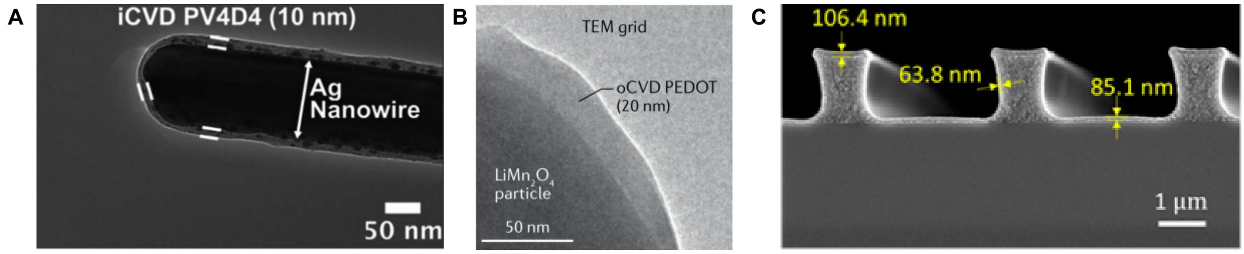

Figure 4.1: Conformal coatings of A) iCVD poly(tetravinyltetramethylcyclotetrasiloxane). Reproduced with permission [29]. Copyright 2015, Royal Society of Chemistry. B) oCVD poly(3,4,-ethylenedioxythiophene). Reproduced with permission [233]. Copyright 2020, Springer Nature. C) iCVD poly(hydroxyethyl methacrylate-*co*-ethylene glycol diacrylate) copolymer. Reproduced with permission [27]. Copyright 2019, American Chemical Society.

There are several variations for depositing polymer CVD films, with each having a direct parallel to a liquid phase synthesis method. While oxidative CVD (oCVD) has been used to deposit polymer thin films via step growth mechanisms, the majority of the literature focuses on chain growth polymerization via initiated CVD (iCVD). Typically, iCVD techniques are utilized for thermally initiated free-radical polymerizations, although cationic and anionic polymerizations are possible. While thermal energy sources are generally utilized for initiation, these can be substituted with radiation or plasma in photo initiated CVD (piCVD) and initiated plasma enhanced CVD (iPECVD) respectively [231], [233]. These iCVD processes can be modified by adding additional precursors to produce copolymer or cross-linked films, allowing greater control over film composition and structure [234]. Due to their prevalence in literature, this work will discuss a process model for iCVD films produced via thermally initiated free-radical polymerization.

4.1.1 iCVD Reactors and Parameters

A schematic for an iCVD reactor is presented in Figure 4.2A. The reaction chamber consists of gas inlets and outlets, a temperature-controlled substrate and an array of heated filaments at the top of the chamber. First, the monomer and precursors are selected, with several works having tabulated iCVD compatible monomer and initiator combinations [231], [233]. Since these are commonly liquid at room temperature, vapor is produced by heating vessels containing the liquid precursors. These monomer and initiator vapors are delivered into the reaction chamber (Steps 1 and 2), where the monomer adsorbs on the substrate surface (Step 3). While the monomer vapor is adsorbing, free-radical species are produced when the initiator vapor is dissociated by the heated filaments suspended throughout the reaction chamber (Step 4). These initiator radicals then diffuse to the surface and initiate surface polymerization with the adsorbed monomer (Step 5) [119]. By controlling processing parameters (substrate temperature, filament temperature, gas flow rates) film growth rates can be tuned from 10 nm per minute to 1 μm per minute [122]. Table 4.1 outlines several key considerations and associated processes parameters for iCVD systems [119].

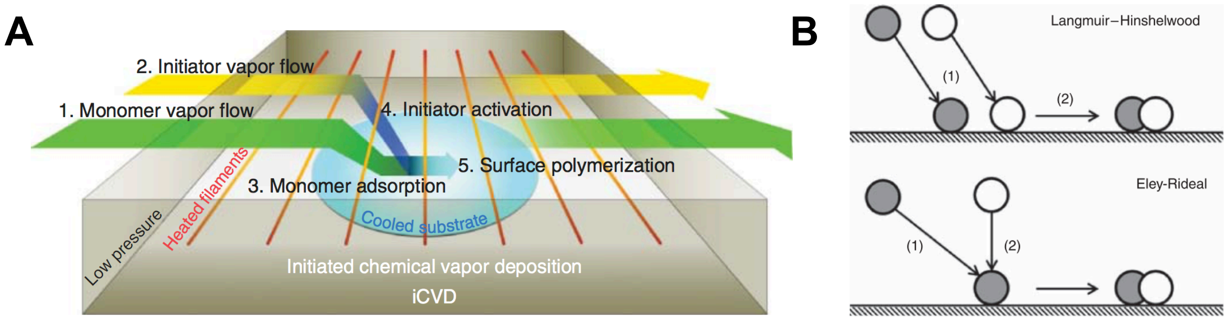

Figure 4.2: A) Generalized schematic for iCVD systems. Reproduced with permission [119]. Copyright 2015, Wiley-VCH. B) Modes for surface reactions with gas phase precursors [232]. Copyright 2015, Wiley-VCH.

Table 4.1: Design consideration and deposition parameters for iCVD systems. Summarized from [119].

System Components	Comments	Input Parameters
Vapor Delivery	Heating of vessels containing neat liquid precursors.	Source temperature: T_{sor}
Pressure Control	Generally 0.1-10 Torr, component partial pressures need to be below saturation pressure to prevent condensation.	Monomer partial pressure: P_m Initiator partial pressure: P_I Saturation pressure: P_{sat}
Temperature Control	Filament temperature (200-400 ºC) and substrate temperature (0-30 ºC) control radical species formation and surface concentrations respectively.	Filament temperature: T_{fil} Substrate Temperature: T_{sub}
Exhaust Management	Remove unreacted gaseous vapors and reaction byproducts to enable a continuous, steady flow system.	Gas flow rate: U_{gas}

As shown in Figure 4.2B surface polymerization is initiated by one of two mechanisms. In Langmuir-Hinshelwood initiation the reactants adsorb separately to the surface and the reaction then takes place between two adsorbed species. In Eley-Rideal initiation the first reactant, the monomer, adsorbs to the surface and initiation occurs when the gaseous species, the initiator radical, reacts with the adsorbed first reactant. The Eley-Rideal mechanism is likely the dominant mechanism for iCVD processes, as the time scale for the Langmuir-Hinshelwood surface reaction is about 10 times longer than the surface lifetime of adsorbed radicals [232]. The activated chain then propagates by reacting with more adsorbed monomer until chain growth is terminated [119].

4.1.2 Surface Reaction Process Model

A detailed process model for free-radical of iCVD poly(alkyl acrylate) films is included as part of the work by Lau and Gleason and has been adapted in Figure 4.3 [121], [235]. The mechanisms in Figure 4.3 generally agree with the process described by Figure 4.2A. The model begins with primary radical formation from initiator decomposition at the heated filaments (*i*), before then considering both primary radical (*ii*) and monomer adsorption (*iii*) at the surface. Here, it is assumed that the radicals on the surface react immediately, whereas the monomer is supplied in sufficient concentrations to reach equilibrium between gaseous and adsorbed species. Due to these conditions the model does not consider the desorption of either species. Surface polymerization then begins through an initiation step (*iv*) and the polymer chain propagates by reacting with adsorbed monomer (*v*). Chain growth is terminated by three mechanisms: coupling between active chains (*vi*), disproportionation between active chains (*vii*) or reaction with a freshly adsorbed primary radical (*viii*). Lau and Gleason also suggested that some primary radical concentration is lost at the surface due to recombination between radicals (*ix*) [235].

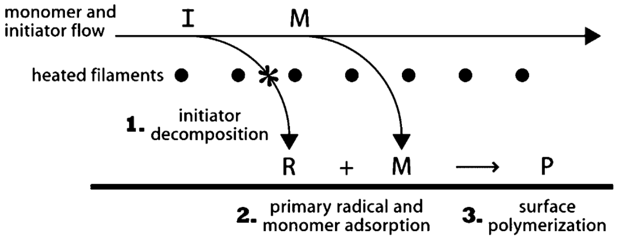

Gas phase reactions

i) Initiator decomposition

$$I_{(g)} \xrightarrow{k_d} 2R\cdot_{(g)}$$

Gas-to-surface processes

ii) Primary radical adsorption

$$R\cdot_{(g)} \xrightarrow{k_{ad,R}} R\cdot_{(ad)}$$

iii) Monomer adsorption

$$M_{(g)} \xrightarrow{k_{ad,M}} M_{(ad)}$$

Surface reactions

iv) Initiation

$$R\cdot_{(ad)} + M_{(ad)} \xrightarrow{k_i} M_1\cdot_{(ad)}$$

v) Propagation

$$M_n\cdot_{(ad)} + M_{(ad)} \xrightarrow{k_p} M_{n+1}\cdot_{(ad)}$$

vi) Termination by coupling

$$M_n\cdot_{(ad)} + M_m\cdot_{(ad)} \xrightarrow{k_{t,c}} M_{n+m\,(ad)}$$

vii) Termination by disproportionation

$$M_n\cdot_{(ad)} + M_m\cdot_{(ad)} \xrightarrow{k_{t,d}} M_{n\,(ad)} + M_{m\,(ad)}$$

viii) Termination by primary radical

$$M_n\cdot_{(ad)} + R\cdot_{(ad)} \xrightarrow{k_{t,R}} M_{n\,(ad)}$$

ix) Primary radical recombination

$$2R\cdot_{(ad)} \xrightarrow{k_{t,R'}} I_{(ad)}$$

Figure 4.3: Schematic and reaction mechanisms for free-radical polymerization by iCVD. Reproduced with permission [235]. Copyright 2006, American Chemical Society.

In assuming that only surface events are important Lau and Gleason [235] applied the kinetic equations for liquid free-radical polymerization as outlined and understood by Odian [236]. To find deposition rate it is crucial to solve for the rate of polymerization (R_p in *Eq. 4.1*), where $[M]$ is the volumetric monomer concentration at the surface and $[M\cdot]$ is the volumetric surface concentration of polymer radicals. Finding R_p also allows for the determination of the kinetic chain length (v in *Eq. 4.2*) from which the number degree of polymerization (X_n in *Eq. 4.3*), an important value for understanding polymer quality and properties, can be calculated [235], [236]. To eliminate intermediate radical concentrations a steady state assumption is made for primary radicals $[R\cdot]$ (*Eq. 4.4*) and polymer radicals *(Eq. 4.5*) using the reaction steps in Figure 4.3. In *Eq. 4.5.*, *r* represents the rate of primary radical adsorption to the substrate and is treated as a fitting parameter. This is done for convenience, as it allows one to ignore the complex gas-phase initiator decomposition and diffusion present among the heated filaments in iCVD systems and ignore radicals that are lost to side reactions before reaching the surface [235]. However, one can assume *r* will have dependence to the rate of decomposition (R_d in *Eq. 4.6*). This gives a direct dependency on the initiator partial pressure (P_I) and, through k_d and T_{gas}, filament temperature (T_{fil}) [236]. While not included in the model of Lau and Gleason [235] it may be possible expand the initiator efficiency (*f* in *Eq. 4.6*), which represents the fraction of primary radicals that initiate polymer chains, to include side reaction losses, and equate *r* to R_d if no mass transfer effects are present [236].

$$R_p = -\frac{d[M]}{dt} = k_p[M][M\cdot] \ (Eq. 4.1)$$

$$v = \frac{R_p}{R_i} = \frac{k_p[M][M\cdot]}{k_i[M][R\cdot]} \ (Eq. 4.2)$$

$$X_n = \frac{2v}{(2-a)} \ (Eq. 4.3)$$

$$r = k_i[M][R\cdot] + k_{t,R}[M\cdot][R\cdot] + 2k_{t,R'}[R\cdot]^2 \ (Eq. 4.4)$$

$$k_i[M][R\cdot] = 2k_{t,c}[M\cdot]^2 + 2k_{t,d}[M\cdot]^2 + k_{t,R}[M\cdot][R\cdot] \ (Eq. 4.5)$$

$$R_d = 2fk_d[I] = \frac{2fk_dP_I}{RT_{gas}} \ (Eq. 4.6)$$

$$V_{ad} = \frac{V_{ml}c\left({}^{P_M}/_{P_{M,sat}}\right)}{\left(1 - {}^{P_M}/_{P_{M,sat}}\right)\left[1 - (1-c)\left({}^{P_M}/_{P_{M,sat}}\right)\right]} \ (Eq. 4.7)$$

$$[M] = \frac{\rho_m V_{ad}}{MW_M V_{ml}} \ (Eq. 4.8)$$

By solving equations *Eq. 4.4* and *Eq. 4.5* the rate of polymerization can be written in terms of monomer concentration ($[M]$), *r* and the various rate constants (*k* in all equations). Therefore, it is necessary to numerically understand the monomer concentration at the surface. Monomer concentration can be found using the adsorbed volume (V_{ad} in *Eq. 4.7*). This volume can be found by fitting gas adsorption experiments with a Brunauer-Emmet-Teller (BET) equation (*Eq. 4.7*);

where V_{ml} is the volume of a single monolayer, c is the BET constant with exponential dependence on the substrate temperature (T_{sub}) and heat of adsorption, P_M is the monomer partial pressure and $P_{M,sat}$ is the monomer-saturated vapor pressure. The saturated vapor pressure is defined as the monomer vapor pressure when in equilibrium with liquid monomer and remains constant for a fixed substrate temperature (T_{sub}) [231], [235]. The adsorbed volume can then be converted to a volumetric monomer concentration using the monomer density (ρ_M) and molecular weight (MW_M) by *Eq. 4.8.* This allows for a direct determination of the polymerization rate in *Eq. 4.1* and, by knowing the fraction of chains terminated by coupling (a), the number average molecular weight in *Eq. 4.3* [235].

4.1.3 Effect of Operating Parameters on Deposition Rate

Based on the process model outlined in Figure 4.3 there are numerous mass transfer steps and surface reactions that can control the overall deposition rate. This rate controlling step can vary depending on the reactor's operating conditions and precursors, but three important parameters on the deposition rate are the filament temperature, substrate temperature and monomer saturation ratio. Figure 4.4A shows the deposition rate for polymerization of hexafluoropropylene oxide (HFPO) initiated with perfluorooctanesulfonyl fluoride (PFOSF) as a function of the filament temperature. This Arrhenius plot shows a linear trend with two rate-limiting regimes. Below 460 ^{o}C the deposition rate strongly depends on the filament temperature, indicating that the system operates in a reaction-limited regime where initiator decomposition (*Eq. 4.6*) is the rate determining step. Above 460 ^{o}C the deposition rate is much less strongly effected by temperature, indicating that the system now operates in a mass-transfer limited regime [119].

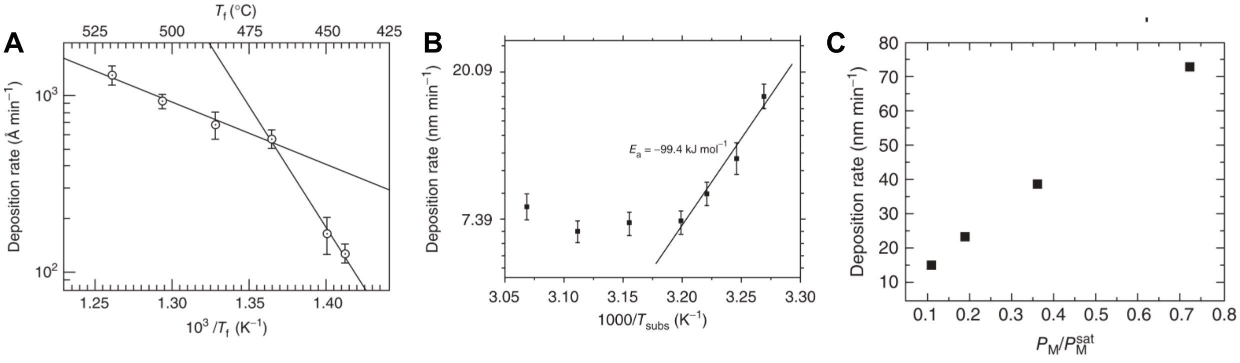

Figure 4.4: Dependence of deposition rate of A) HFPO monomer and PFOSF initiator on filament temperature, B) EGDA monomer and TBPO initiator on substrate temperature, and C) CHMA monomer and TBPO initiator on monomer saturation ratio. Compiled with permission from [119]. Copyright 2015, Wiley-VCH.

Similarly to the filament temperature, Figure 4.4B shows that iCVD systems, in this case ethylene glycol diacrylate (EGDA) polymerization initiated with *t*-butyl peroxide (TBPO), can operate in two different regimes depending on the substrate temperature (T_{sub}). Here, the maximum deposition rate occurs at the lowest substrate temperature and the positive slope indicates a negative activation energy. This shows that the system operates under conditions where monomer desorption, something not considered in the Figure 4.3 model, is a crucial rate limiting step. As the substrate temperature is increased above 39 °C the deposition rate becomes constant. This is hypothesized as being a regime in which surface reactions become increasingly important and monomer desorption is counteracted by increases in the surface reaction rate constants in *Eq. 4.1*, *Eq. 4.4* and *Eq. 4.5* [119].

Perhaps the most important parameter in iCVD systems is the monomer saturation ratio ($P_M/P_{M,sat}$) [231]. Based on the analysis for the process model in Figure 4.3, this ratio has a direct impact on the adsorbed monomer concentration, and directly impacts the deposition rate and number average degree of polymerization (*Eq. 4.3*) by changing the rate of polymerization (*Eq. 4.1*). Figure 4.4C shows the deposition rate for cyclohexyl methacrylate polymerized with TBPO initiator exhibits a linear dependence on the monomer saturation ratio, agreeing with the relationship between polymerization rate and monomer concentration in *Eq. 4.1* [119]. While increasing the monomer saturation ratio increases the growth rate, it should be noted that having a monomer saturation equal to 1 result in the formation of a liquid film on the substrate surface, a condition which is generally undesirable for CVD systems. As a result iCVD is carried out with a saturation ratio < 1, with increasing film conformality as the ratio decreases [231]. In special cases, a very low saturation ratio (< 0.03) results in polymerization conditions where the rate shows a second-order dependence on monomer concentrations, with a similar phenomenon being observed in liquid free radical polymerizations with low monomer concentration [119].

4.1.4 Concluding Remarks and Application in This Thesis

iCVD is a technique that allows for thin, conformal and pinhole free polymer films with a wide thickness range to be deposited on substrates for a variety of applications. While there are similarities with conventional CVD processes, a unique feature of iCVD is the initiator decomposition reaction that occurs in the gas phase well above the substrate. This reaction, coupled with the gas phase temperature gradient between the heated filament and substrate, makes understanding mass-transfer relationships in iCVD systems difficult. However, by making some simplifications a processes model can be developed for surface reaction limited deposition, where the deposition rate follows conventional free radical polymerization kinetics. Through these relationships the deposition rate can be controlled using the filament temperature, substrate temperature and, most importantly, the monomer saturation ratio.

Based on the information outlined above, the previous works of the Gleason Group [29], [122], [123], [237], [238] and the electrolyte chemistry first developed by Li *et al.* [27] the remainder of this chapter focuses on developing an iCVD process to deposit conformal co-polymer 3D electrolytes. Here, we demonstrate that the developed iCVD process is capable of producing conformal poly(hydroxyethyl methacrylate-*co*-ethylene glycol diacrylate) copolymer films on our vertically aligned CNTs. By utilizing a growth rate below ~ 4 nm/min we are able to not only achieve conformal electrolyte coatings on the exterior of the patterned CNT forests but also throughout the forest on the nanotubes themselves. Additionally, we dope poly(hydroxyethyl methacrylate-*co*-ethylene glycol diacrylate) with lithium salt to demonstrate that they operate as solid polymer electrolytes with ionic conductivities similar to those achieved by Li *et al.* [27] and amongst the highest demonstrated by 3D electrolyte technologies..

4.2 Experimental Methods

4.2.1 Initiated Chemical Vapor Deposition of Poly(hydroxyethyl methacrylate-co-ethylene glycol diacrylate) Thin Films

Initiated chemical vapor deposition (iCVD) reactions were performed in a homebuilt reactor system (Figure 4.5) consisting of a reactor chamber, a control module for the gas inlet lines, a vacuum pump system and a heater/chiller system to control the reactor stage temperature. To prevent unwanted monomer adsorption during deposition the monomer inlet lines and reactor body are wrapped in heating tape and respectively held at ~100 ^{o}C and ~40 ^{o}C. The reactor chamber pressure is measured using a Baratron capacitance manometer.

The reactor chamber is vented with ultrahigh purity N_2 (Airgas) (Figure 4.6A and Figure 4.6B) before the samples are loaded inside. Samples used in this work include vertically aligned carbon nanotubes (VA-CNTs, CNT forests) on either Cu foils or Si wafers and coated with LPCVD Si using the procedures outlined in Chapter 2, and ~1 cm x ~1cm pieces of blank Si wafers with a 300 nm oxide layer (WaferPro) or pieces of pieces of Indium-Tin-Oxide (ITO) coated glass (Figure 4.6C).

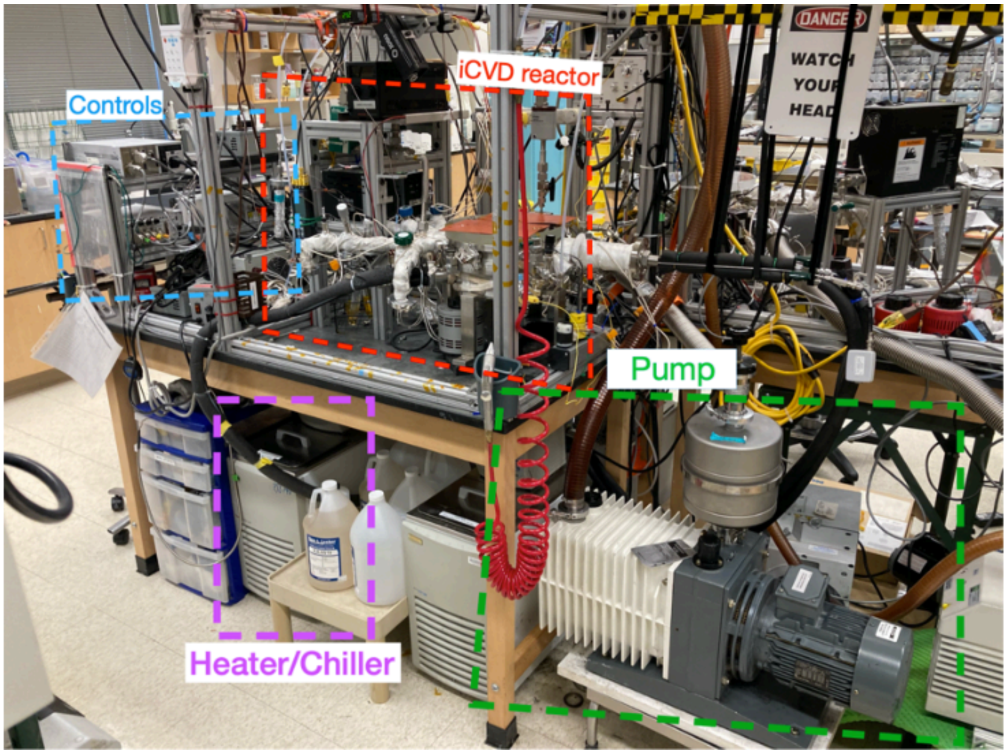

Figure 4.5: Picture of a homebuilt iCVD reactor showing the location of the reactor chamber, stage heater/chiller, vacuum system and reactor controls. Photo credit to Dr. Maxwell Robinson.

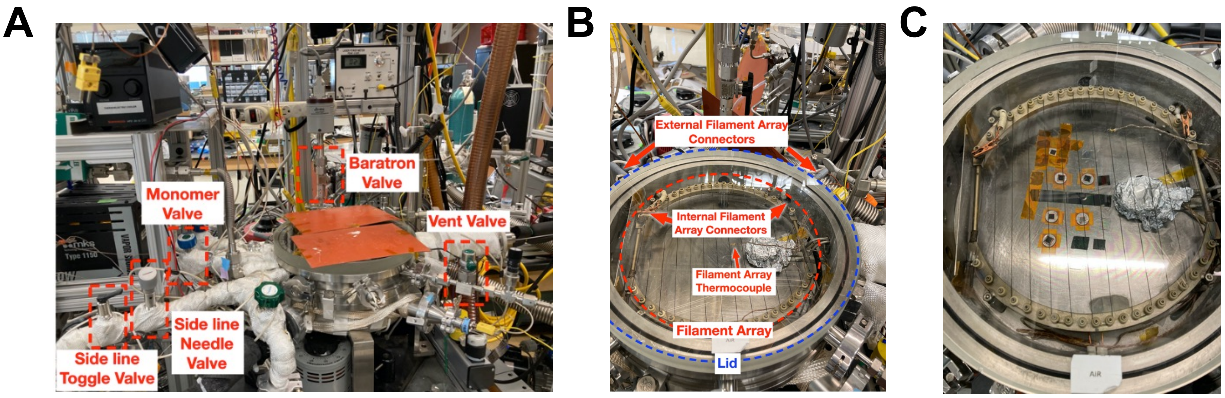

Figure 4.6: A) iCVD reactor chamber and inlet lines, B) filament array and associated connections inside the iCVD reactor chamber, and C) samples loaded inside iCVD reactor. A) and B) photo credit to Dr. Maxwell Robinson.

An additional wafer (WRS Materials) was cut into a thin section in the chamber and placed such that a He-Ne laser beam (JDSU) reflected off it and into an associated power meter (Meterologic) (Figure 4.6C and Figure 4.7) to enable *in-situ* laser interferometry monitoring of the iCVD film thickness during deposition. Following loading, an 80% Ni/20% Cr filament array was placed inside the reactor and was connected to a power source via alligator clips (Figure 4.6B). The electrical connection between the filament and power source was checked by ensuring a resistance of ~20-30 Ω across the filament array. After loading the samples and connecting the array the reaction chamber was sealed and allowed to pump down overnight at to a base pressure of ~10-12 mTorr.

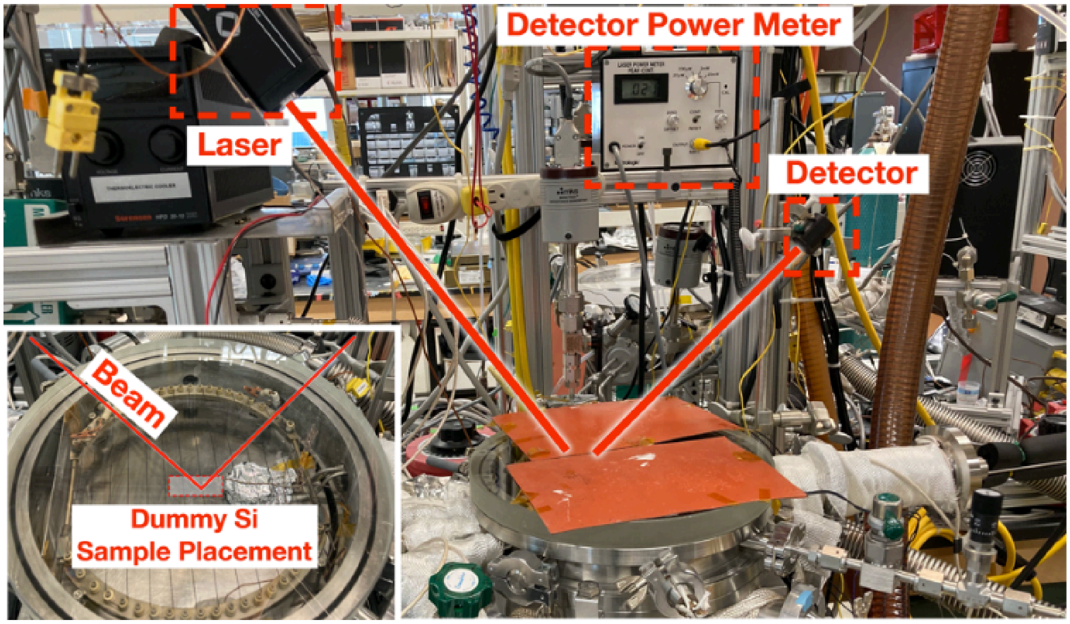

Figure 4.7: Photo showing location of dummy wafer to record laser intensity during iCVD runs. Photo credit to Dr. Maxwell Robinson.

After pumping down overnight a leak test is performed on the reactor to validate that the leak rate is 0.1-0.2 sccm. Following the leak test, the flow rates of the ultrahigh purity N_2 and 98% tert-butyl peroxide (TBPO, Sigma) are manually calibrated by tuning the mass flow controllers (MFC) associated with each line (Figure 4.8A). All flows were calibrated to be +/- 10% of the desired value. After calibration the N_2 and TBPO flows were temporarily turned off to calibrate the monomer flow rates.

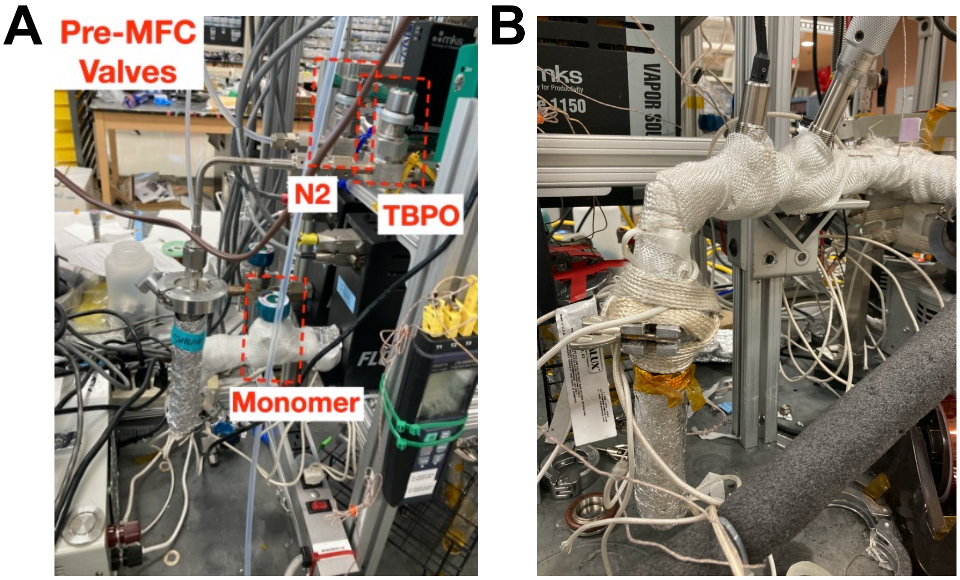

Figure 4.8: A) photo of N_2 inlet line, TBPO jar and inlet line and HEMA inlet line with their associated MFCs, and B) photo of EGDA jar with heating jacket and inlet line with the associated needle valve. A) photo credit to Dr. Maxwell Robinson.

Table 4.2: Input parameters used in poly(HEMA-*co*-EGDA) iCVD runs with a reactor pressure of 100 mTorr.

Recipe	Q_{N2} (sccm)	Q_{HEMA} (sccm)	P_{HEMA}/P_{Sat}	Q_{EGDA} (sccm)	P_{EGDA}/P_{Sat}	Q_{TBPO} (sccm)	Q_{Total} (sccm)
Poly(HEMA)	0.9	1.5	0.1	0	0	0.6	3
90HEMA	0.75	1.15-1.5	0.1	0.15	0.02	0.6	3
55HEMA	1.3	0.5	0.03	0.6	0.06	0.6	3

Glass jars containing 99% hydroxyethyl methacrylate (HEMA, Sigma) and 90% ethylene glycol diacrylate (EGDA, Sigma) were wrapped in heating jackets and attached to their respective inlet lines (Figure 4.8B). After being purged of air, the jars were heated to ~70-90 ^{o}C and held at temperature for 45 min to produce the required monomer vapor. Once steady flow was established the HEMA flowrate was calibrated using the associated MFC while the EGDA flowrate was calibrated using the associated needle valve. The HEMA and EGDA flows were selected to ensure saturation ratios < 0.1. The calibrated HEMA and EGDA jars were allowed to flow for 45 min before the N_2 and TBPO flows were restarted and held for 5 min to allow all the flows to stabilize.

The sample flow rates used for two recipes, one for pure poly(HEMA) (PHEMA), one with a high HEMA composition (90HEMA) and one with a lower HEMA (55HEMA) composition, and the associated saturation ratios are presented in Table 4.2. The saturation ratios ($P_{Reactant}/P_{Sat}$) in Table 4.2 were determined by dividing the reactant partial pressure by the saturation partial pressure at 40 °C. The saturation partial pressures were calculated using previously reported vapor pressures at temperatures ranging from 25 to 35 °C and extrapolating to 40 °C using the Clausius-Clapeyron Equation [27], [237], [238].

Once the flows are calibrated the reactor stage is heated to 40 °C and the reactor chamber pressure set to the desired value. Depositions were performed at 100 mTorr, with the pressure increased to 200 mTorr later in the deposition where noted. Once the pressure stabilized the power to the filament array was turned on, with the wires reaching ~200 °C, and a timer started. The laser power was recorded at the deposition start time, every 15 min for 100 mTorr chamber pressure and every 5 min for 200 mTorr chamber pressure. Once the desired film thickness was reached the power to the filament array was turned off, the inlet flows turned off and the samples were allowed to sit under vacuum at the 10 mTorr base pressure overnight before being removed the next morning. After sample removal the reactor chamber was cleaned with a razor blade, washed with isopropanol and left under vacuum (~10 mTorr) between depositions.

4.2.2 Doping of Poly(HEMA-co-EGDA) Thin Films and Electrochemical Impedance Spectroscopy Measurements

Poly(HEMA-*co*-EGDA) thin films on ~1 cm x ~ 1 cm Si wafers or ITO glass were prepared for conductivity measurements using a procedure similar to that of Li *et al.* [27]. For 90HEMA films 50 nm Au electrodes were deposited using the same sputtering system for CNT catalysts in Chapter 2. For 55HEMA films 50 nm Au electrodes were deposited by an evaporative deposition process. In both cases a shadow mask was used to control electrode spacing. For sputtering the electrodes are 3.5 mm in length and are spaced 0.3 mm apart. For evaporative deposition the interdigitated electrode spacing is 0.2 mm and the total electrode length is 7.2 cm. After Au electrode deposition, the samples were pumped down overnight in the glovebox antechamber before being transferred into an Ar filled glovebox (Airgas, MBraun Labstar) with O_2 and H_2O levels < 0.5 ppm. The samples were then allowed to soak overnight in a 0.3 M Lithium bis(trifluoromethanesulfonyl)imide (LiTFSI, Sigma) in anhydrous acetonitrile (Sigma) solution. The samples were removed from the 0.3 M LiTFSI in acetonitrile solution and allowed to dry in the glovebox on a hotplate at 120 °C for 1 h to remove all the acetonitrile. A schematic of the doping procedure is presented in Figure 4.9.

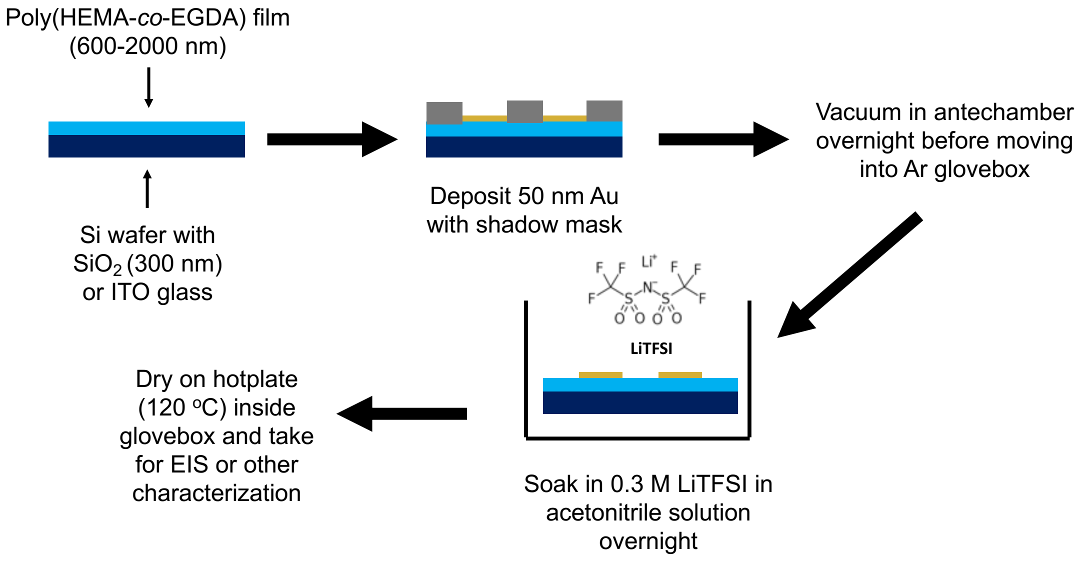

Figure 4.9: Schematic for process to dope poly(HEMA-*co*-EGDA) films with LiTFSI salts.

Following doping the poly(HEMA-*co*-EGDA) films were transported under Ar for electrochemical impedance spectroscopy (EIS) measurements. EIS measurements were performed under Ar using a Biologic VSP-300 potentiostat with a frequency between 100 mHz and 7 MHz for the 90HEMA film and 50 mHz and 5 MHz for the 55HEMA film. All EIS measurements used a 0 V bias and an AC amplitude of 100 mV. Five measurements were taken at each frequency and averaged together. The EIS spectra were fit using Biologic BT-Lab or ZView software.

4.2.3 Materials Characterization

Scanning electron microscopy (SEM) and energy dispersive x-ray (EDS) measurements were performed using the same equipment outlined for Si-CNT composite electrodes in Chapter 2.

Prior to Fourier transform infrared (FTIR) spectroscopy analysis the undoped films were kept under vacuum in the glovebox antechamber overnight to remove any adsorbed water. FTIR measurements were performed using a Bruker ALPHA II spectrometer in attenuated total reflectance mode (ATR-FTIR). Each measurement consisted of 128 scans with a 4 cm^{-1} resolution. Spectra were processed using the included OPUS software. This included performing background compensation, a baseline correction and normalizing the spectra to the highest peak intensity. The peak areas of interest were determined using the OPUS peak fitting tool.

4.3 Results and Discussion

4.3.1 Poly(HEMA-co-EGDA) Thin Film Characterization

The *in-situ* laser interferometry measurements recorded during the iCVD experiments enable control over the resulting thin film thickness and a determination of the poly(HEMA-*co*-EGDA) film growth rate (Figure 4.10). Previous runs with this iCVD system have determined that the completion of one laser interferometry period should correspond to ~200 nm of poly(HEMA-*co*-EGDA) thin film deposition. The plots of laser power versus deposition time are shown for a six period 90HEMA thin film at 100 mTorr in Figure 4.10A and a ten period 55HEMA thin film with variable reactor pressure in Figure 4.10C. Figure 4.10B shows that the actual thickness of the 90HEMA film (1.214 μm) is very close to the predicted value of 1.2 μm. Similarly, Figure 4.10D shows that the actual 2.098 μm thickness of the 55HEMA film is very close to the predicted value of 2.0 μm. Figure 4.10A and Figure 4.10C give a deposition rate of ~3-4 nm/min for 90HEMA and 55HEMA films at 100 mTorr. Figure 4.10C gives a deposition rate of ~5.5 nm/min for 55HEMA films at 200 mTorr.

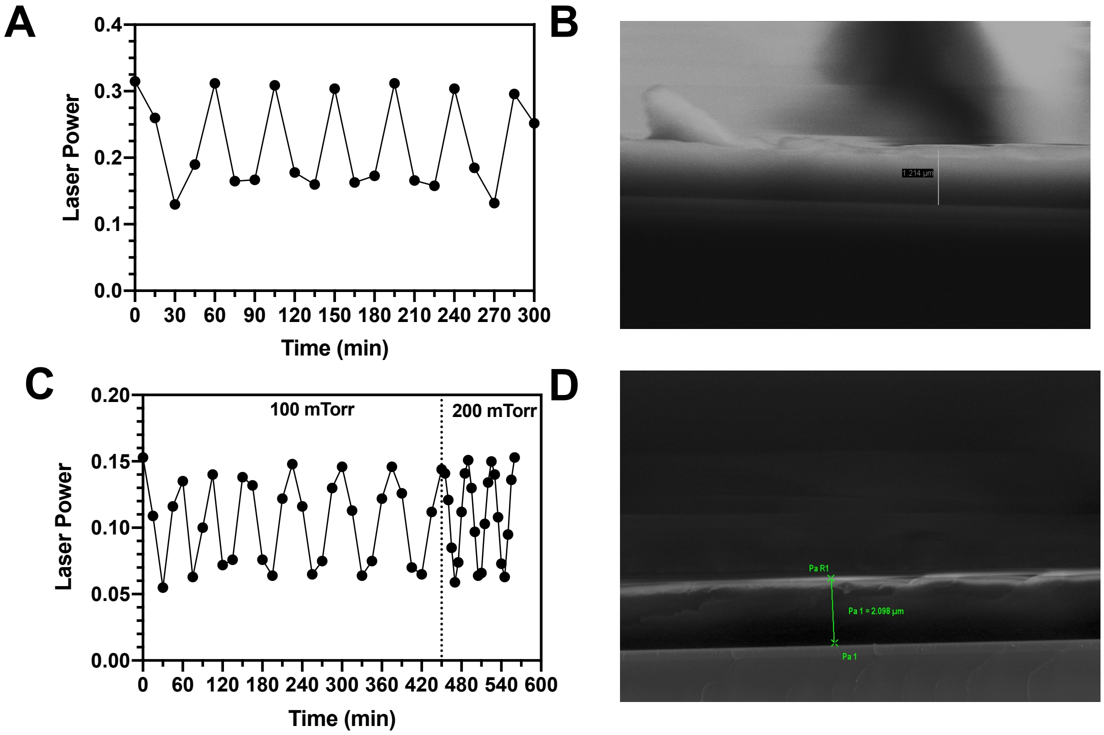

Figure 4.10: A) *In-situ* laser interferometry plot and B) SEM image of final film thickness for 90HEMA thin film at 100 mTorr. C) *In-situ* laser interferometry plot and D) SEM image of final film thickness for 55HEMA thin film.

The molecular structures of the TBPO, HEMA and EGDA reactants respectively are presented in Figure 4.11A through Figure 4.11C. Figure 4.11D shows FTIR spectra for PHEMA, 90HEMA and 55HEMA thin films on Si wafers and can be used to determine the composition of these iCVD films. The spectra in Figure 4.11D are representative of previously produced iCVD poly(HEMA) and poly(HEMA-*co*-EGDA) thin films [27], [237]. All three spectra contain a wide band at ~3700-3050 cm^{-1} corresponding to O—H stretching, a number of peaks in the in the 3050-2700 cm^{-1} range corresponding to C—H stretching and a peak at ~1720 cm^{-1} from C=O stretching.

These results indicate that the hydroxyl (O—H) groups in the HEMA monomer (Figure 4.11B), and the carbonyl (C=O) groups in the HEMA and EGDA (Figure 4.11C) are retained during the iCVD process [237].

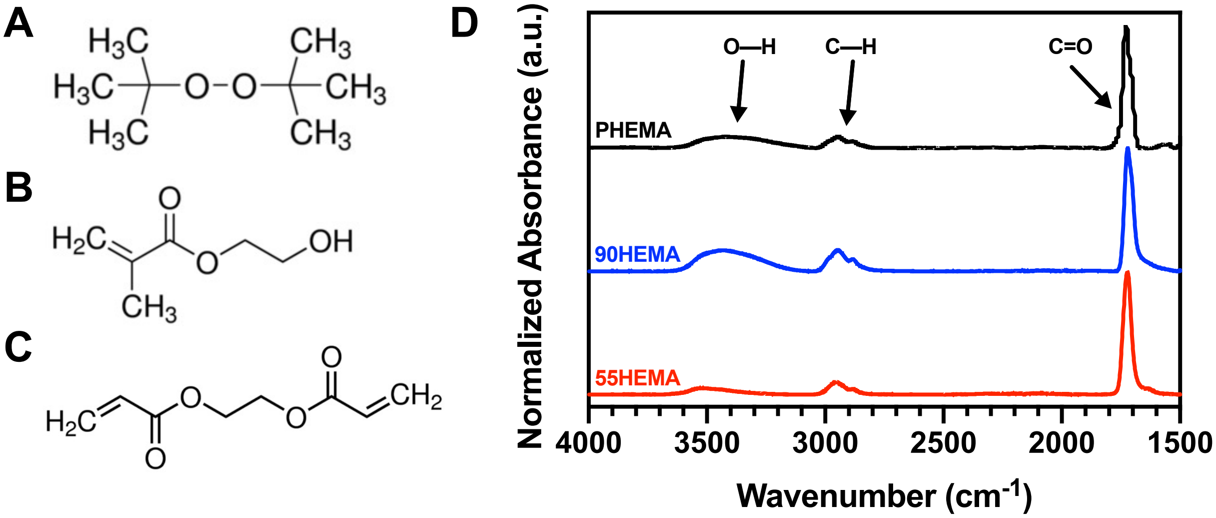

Figure 4.11: Molecular structures of the A) TBPO initiator, B) HEMA monomer and C) EGDA monomer used in this work. D) FTIR spectra for PHEMA, 90HEMA and 55HEMA iCVD thin films.

Furthermore, the information contained in the Figure 4.11D FTIR spectra can be utilized to estimate the composition of these copolymer thin films. This is done utilizing a formula initially developed by Chan *et al*. [237] and later utilized by both Yague *et al.* [238] and Li *et al.* [27]. The first step is to compute the ratio (r) of the C=O peak area to the O—H peak area in the PHEMA film (*Eq. 4.9*). The calculated r value for the PHEMA film in Figure 4.11D is 1.46. This ratio can then be used to calculate the contribution of HEMA to the C=O band in the copolymer films. The EGDA contribution to the C=O intensity can be determined by subtracting the HEMA contribution and dividing by two, since each EDGA monomer contains two C=O groups (Figure 4.11C). These two equations can be combined to calculate ratio of EGDA to HEMA (*Eq. 4.10*) in each film. *Eq. 10* can then be rearranged to calculate the mole fraction of HEMA in each film (*Eq. 4.11*).

Applying *Eq. 4.10* and *Eq. 4.11* to the 90HEMA and 55HEMA spectra in Figure 4.11D gives HEMA contents of ~87 mol.% and ~ 53 mol.%, respectively.

$$r = \frac{A_{C=O}}{A_{O-H}} \ (Eq. 4.9)$$

$$\frac{[EGDA]}{[HEMA]} = \frac{(A_{C=O} - rA_{O-H})/2}{rA_{O-H}} \ (Eq. 4.10)$$

$$\frac{[HEMA]}{[HEMA] + [EGDA]} = \frac{rA_{O-H}}{rA_{O-H} + (A_{C=O} - rA_{O-H})/2} \ (Eq. 4.11)$$

Table 4.3: Compositions obtained for multiple iCVD runs and their respective recipe.

Recipe	$A_{C=O}$	A_{O-H}	*r*	$\frac{[EGDA]}{[HEMA]}$	HEMA mol.%
P(HEMA)	54.98	37.54	1.46	0	100
90HEMA #1	84.77	44.48	-	0.151	87
90HEMA #2	7.49	3.836	-	0.167	86
90HEMA #3	17	10.5	-	0.053	95
55HEMA #1	61.16	17.47	-	0.695	59
55HEMA #2	15.83	3.77	-	0.935	52

A breakdown of the peak areas and calculated compositions for multiple runs of all three recipes is presented in Table 4.3. Here there is some run-run-run variation in the film composition. This is attributed to minor variations between runs in reactant flow rates due to the manual calibration of the HEMA MFC and EGDA needle valve. It is also noted that there is a tendency for the HEMA monomer inlet line to begin filling with polymer during the long deposition's times required to meet suitable film thickness. This unwanted polymerization may be a result of backflow of TBPO monomer to the HEMA jar.

4.3.2 Poly(HEMA-co-EGDA) Deposition on Vertically Aligned CNT Forests

In their work Li *et al.* demonstrated highly conformal poly(HEMA-*co*-EGDA) films on a number of TiO_2 microstructures with aspect ratios ranging from 1.15 from 3.85 (Figure 4.1C) . Li *et al.* deposited these films using saturations ratios ranging from 0.15 to 0.34 for HEMA and 0.14 to 0.72 for EGDA. Figure 4.12 shows that both the 90HEMA and 55HEMA recipes are capable of producing conformal polymer thin films over aligned Si-CNT pillars with an aspect ratio of 2.5. However, the objective is to use these iCVD films as either solid polymer or gel polymer electrolytes. Therefore, while coating the exterior of the CNT pillars is necessary it is also beneficial to ensure that the iCVD coating penetrates throughout the entirety of the Si-CNT structure create potential ionic conduction pathways.

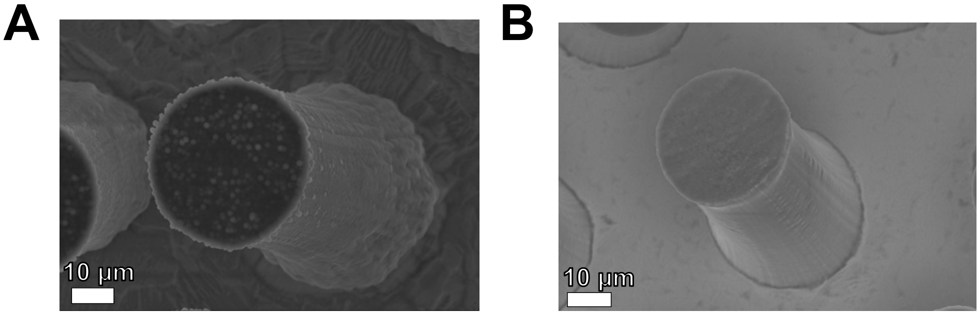

Figure 4.12: SEM images of A) 55HEMA and B) 90HEMA iCVD coatings on 40 µm diameter and ~100 40 µm tall Si-CNT pillars.

Figure 4.13 shows a 55HEMA deposition on a > 300 µm tall honeycomb patterned CNT forest. Similar to the CNT pillars in Figure 4.12, the SEM images of the forest exterior (Figure 4.13A and Figure 4.13B) demonstrate conformal 55HEMA coatings over these honeycomb structures with an ~100 aspect ratio. More impressively, Figure 4.13C and Figure 4.13D are SEM images of the internal cross section of these 55HEMA coated forests. Figure 4.13C and Figure 4.13D show that not only does the 55HEMA film coat the exterior of the CNT forest but that it also conformally coats the individual CNTs themselves.

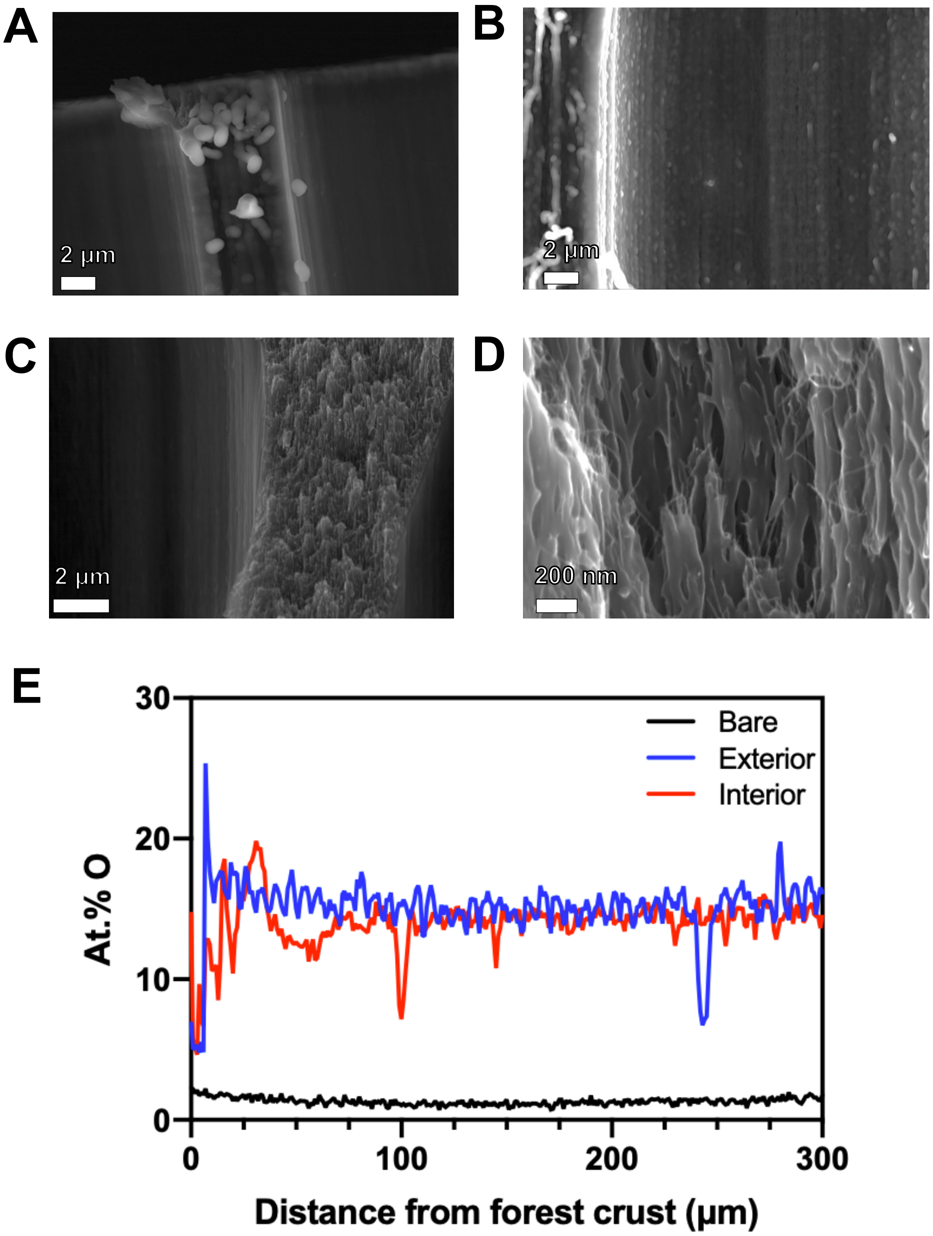

Figure 4.13: 55HEMA iCVD coating on A) and B) honeycomb CNT forest exterior, and C) and D) honeycomb CNT forest exterior. E) EDS linescan of 55HEMA coated forest compared with a bare uncoated forest). The forest is 300 µm tall and the honeycomb has 25 µm holes with 30 µm spacing.

This is impressive, as the aligned nanotubes have an aspect ratio > 25000. EDS results in Figure 4.13E show that this coating is consistent from the top to the bottom of the CNT forest interior and exterior. The high degree of conformality achieved in the iCVD coatings on the individual CNTs is attributed to the low saturation ratios utilized in these experiments (< 0.1, Table

4.1). Additionally, the 40 °C stage temperature puts the system in the operating regime where EGDA desorption also lowers the deposition rate to further increased conformality (Figure 4.4B) [119]. The downside of the low saturation ratio is that the deposition rate is low, 3-4 nm/min at a 100 mTorr deposition pressure; with > 1 μm depositions taking well over 5 h to complete.

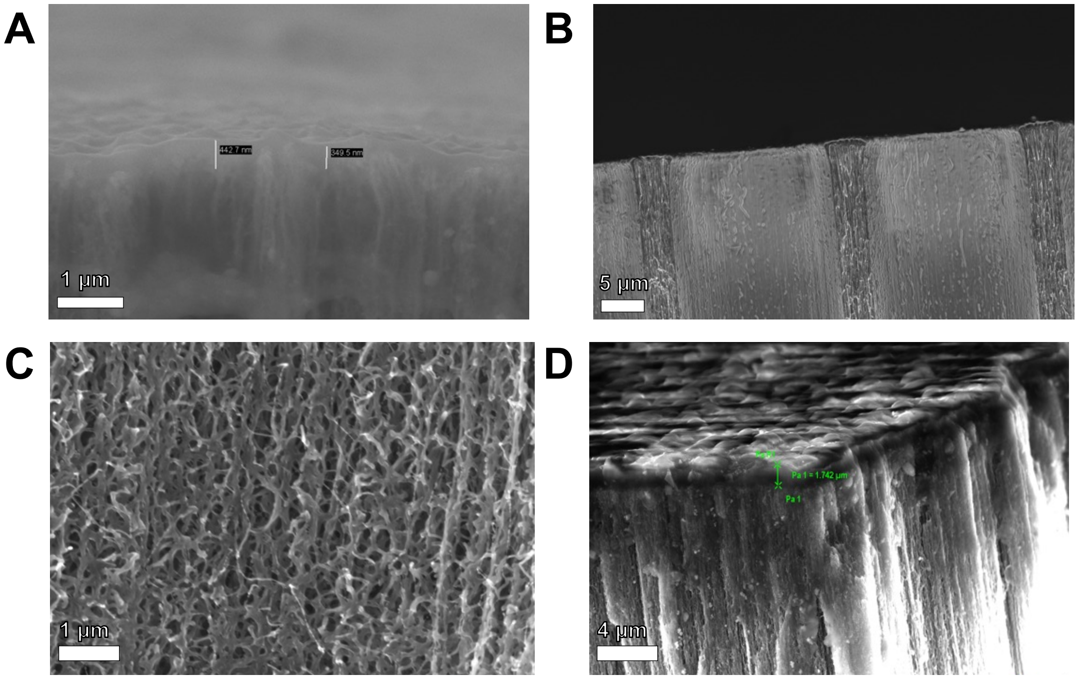

Figure 4.14: Cross section view of Si-CNT forests with A) six cycles at 100 mTorr 90HEMA deposition, B) and C) two cycles at 100 mTorr followed by four cycles at 200 mTorr 90HEMA deposition and D) seven cycles at 100 mTorr followed by three cycles at 200 mTorr 55HEMA deposition.

As demonstrated in Figure 4.10, the thickness of the poly(HEMA-*co*-EGDA) films deposited on flat substrates is easily tracked using the *in-situ* laser interferometry assembly. However, Figure 4.14A, shows that this same thickness is not necessarily achieved on the exterior of the CNT forests. The Si-CNT forest in Figure 4.14A was coated in the same run as the Si wafer in Figure 4.10B. While the 90HEMA film thickness on the Si wafer is very close to the expected value of 1.2 μm, the 90HEMA thickness on the exterior of the Si-CNT forest in Figure 4.14A is only in the range of 350-450 nm. While it is likely that the same amount of iCVD polymer is deposited on the top of the forest as is on the Si wafer, the greatly increased area of nanoporous aligned CNTs decreases the overall thickness of the exterior coating. This may be mitigated by modifying the deposition pressure mid-run. The Si-CNT forest in Figure 4.14A is subjected to six cycles at 100 mTorr, whereas the forest Figure 4.14B is subjected to two cycles at 100 mTorr followed by 4 cycles at 200 mTorr. The increase in deposition rate results in a build-up of iCVD polymer film at the top of the forest (Figure 4.14B). Similarly, the 55HEMA coated forest in Figure 4.14D is subjected to seven cycles at 100 mTorr followed by three cycles at 200 mTorr. The buildup in film is evident on the forest crust (Figure 4.14D), with the ~1.75 μm layer approaching the expected 2 μm thickness (Figure 4.10D).

It should be noted that increasing the pressure will also increase the saturation ratio, leading to a decrease in the conformality of the final film. This is seen in Figure 4.10C, where the dense 90HEMA coating does not extend all the way to the base of the aligned CNTs, with the thin coating likely being deposited during the first two cycles at 100 mTorr. If the initial 100 mTorr deposition is held performed for sufficiently long enough to achieve conformal coatings at the CNT level then additional cycles at 200 mTorr can be utilized to increase the thickness on the forest exterior, as in Figure 4.10D. this provides a significant level of flexibility when considering the Si-CNTs as a scaffold for 3D full cell development. The 100 mTorr deposition enables iCVD polymer electrolyte deposition through the Si-CNTs, enabling them to serve as a porous electrode, while the 200 mTorr deposition provides additional exterior thickness, allowing the exterior film to serve as a separator layer between the two electrodes and minimize the chance of a short circuit due to contact between the two electrodes.

4.3.3 Poly(HEMA-co-EGDA) Films as Solid Polymer Electrolytes

For these Poly(HEMA-*co*-EGDA) thin films to be utilized as electrolytes it is necessary to dope them with a Li-ion containing source. Following the procedure set by Li *et al.* [27] ~775 nm thick 90HEMA thin films (Figure 4.15A) on Si wafers were allowed to soak overnight under Ar in an acetonitrile solution containing 0.3 M LiTFSI salt, after which the films were dried to remove any residual solvent. Following doping the thin film thickness is ~ 1.05 μm (Figure 4.15B), an ~30% increase from the starting, which indicates LiTFSI salt incorporation throughout the film. This increase is slightly lower than the ~40% thickness increase observed by Li *et al*. for their 95 mol.% HEMA thin film, and may attributed to the ~5 mol.% increase in EDGA crosslinker in the 90HEMA films.

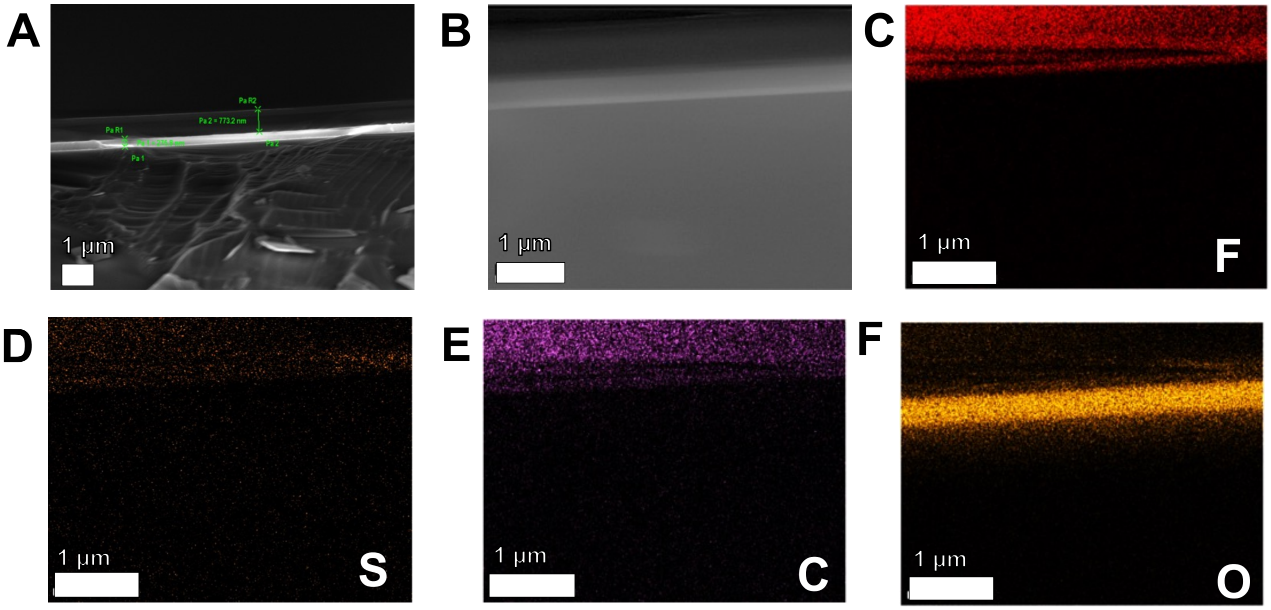

Figure 4.15: SEM images of A) undoped and B) LiTFSI doped 90HEMA thin films. C) through F) element specific EDS maps for LiTFSI doped 90HEMA thin film.

LiTFSI salt incorporation in the 90HEMA film is confirmed in Figure 4.15C through Figure 4.15F, where the F and S signals are exhibited throughout the entire 90HEMA film cross section. Due to the lack of F and S on the 90HEMA monomer and initiator these signals must be coming from atoms on the LiFTSI anion (Figure 4.9). FTIR analysis was performed on a doped and dried 90HEMA film. The spectra in Figure 4.16 indicate that the O—H, C—H and C=O peaks of the original film are retained while new peaks appear corresponding to the LiTFSI anions. The absence of a C≡N peak between 2220 cm^{-1} and 2260 cm^{-1} indicates the complete acetonitrile removal, confirming that any ionic conductivity will be a result of conduction by the doped 90HEMA film [27].

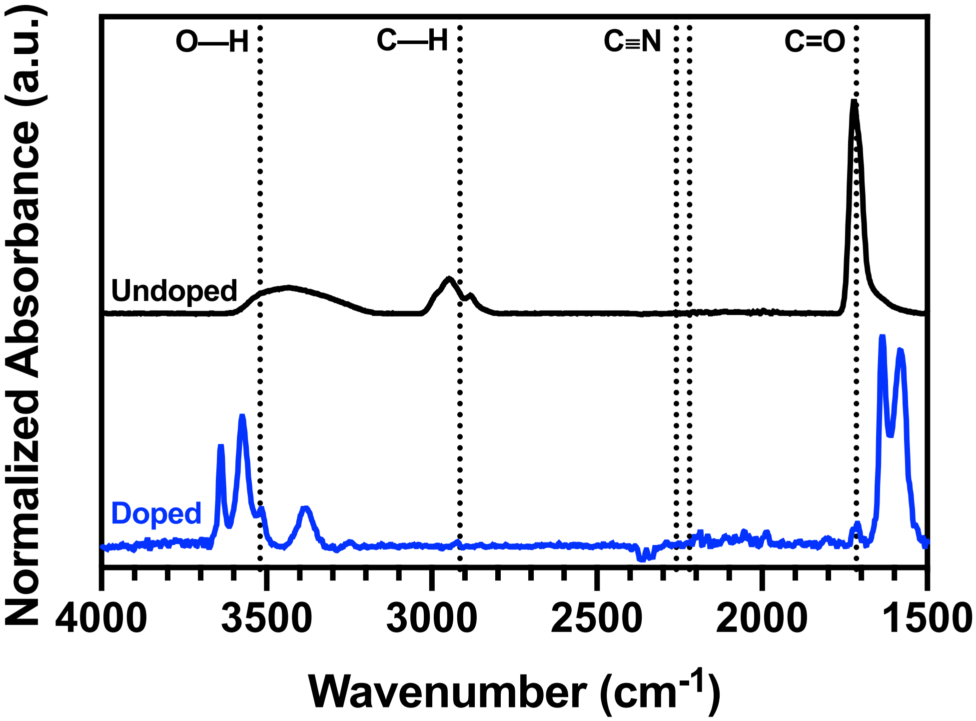

Figure 4.16: FTIR spectra for undoped and LiTFISI doped 90HEMA thin films.

EIS measurements were performed to determine the ionic conductivity of the LiTFSI doped 90HEMA thin films. The Nyquist plot in Figure 4.17 shows an elliptical shape at high frequencies that can be attributed to ion conduction through the iCVD polymer thin film. To determine ionic conductivity the elliptical shape was fit using a resistor and constant-phase element in parallel. The lower frequency region is characterized by a constant-phase element indicative of long-range ionic diffusion [27], [50]. The resistance from the equivalent circuit model in Figure 4.17, when combined with the post-doping ~1 μm film thickness and Au electrode spacing in the experimental methods, gives an ionic conductivity of ~2 x 10^{-5} S/cm. This is slightly higher than, but mostly consistent with, the ~6 x 10^{-6} S/cm conductivity measured by Li *et al.* [27]. Performing the same area specific resistance (ASR) as in Chapter 3 gives the 90HEMA thin film a 5 Ω cm^2 ASR, well below the 10 Ω cm^2 threshold established by Kazyak *et al.* [180] and putting it amongst the best 3D electrolyte candidates by this metric.

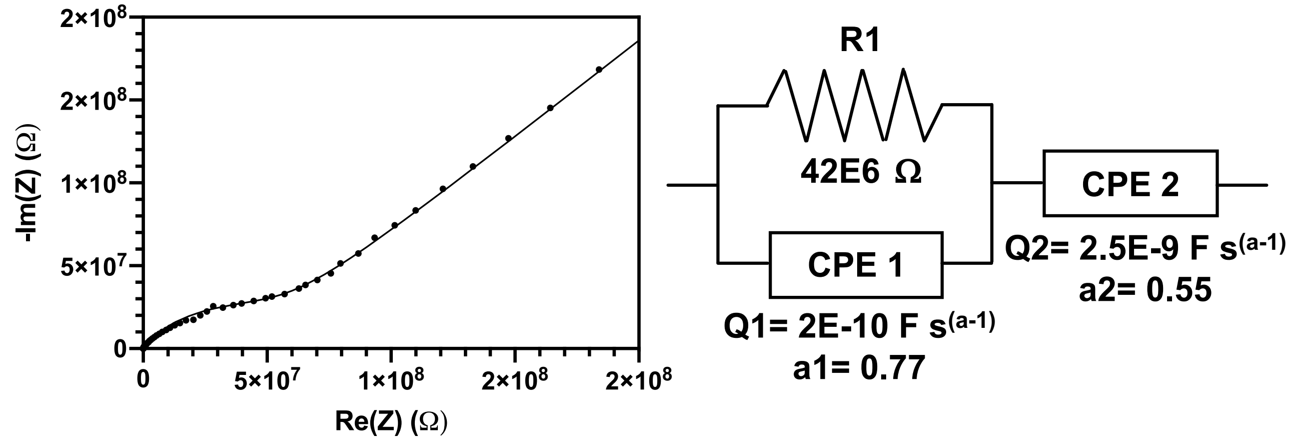

Figure 4.17: Nyquist plot and equivalent circuit model for LiTFSI doped 90HEMA thin film. The dots in Nyquist plot are the experimental data points while the fit is the solid line.

Li *et al.* observed that a 33.7 °C glass transition temperature for their 95 mol.% HEMA films. Since the 90HEMA film has a higher EGDA crosslinker concentration and the EIS measurements are performed at room temperature the likely ion conduction mechanism is ion hopping through percolated ionic clusters as proposed by Li *et al.* [27] and characteristic of conductive polymer glasses below their glass transition temperature [239], [240]. This percolation driven conduction, which is decoupled from the chain segmental relatation, may provide an explanation for the increase in ionic conductivity exhibited by the 90HEMA compared to Li *et al.*'s [27] thin films, as an small variations in the non-optimized doping process may lead to differences in post doping LiTFSI salt concentration. For the percolation based conduction mechanism the final LiTFSI concentration will have a significant effect on the ionic conductivity, as the free volume necessary for ion hopping is created when the Li-salt ions screen the dipole-dipole interactions between the polar functional groups on the polymer chains [27], [239], [240].

Future works should characterize and control the total LiTFSI content and distribution in these poly(HEMA-*co*-EGDA) iCVD films.

Furthermore, the increase in conductivity in the 90HEMA film when compared to the similar films produced by Li *et al.* may also be dependent on difference in free volume between the two films. In addition to salt concentration, the free volume in a polymer depends on the molecular weight. This is because the covalent bonds between backbone atoms are shorter than the intermolecular nearest neighbor distance. In low molecular weight polymers, the chain ends, which can be viewed as an impurity, represent a higher fraction of the material. This results in a decrease in the density and corresponding increase in the system free volume [241]. Having larger areas of free volume is critical to enable ion hopping conduction in polymer glass electrolytes [240]. In iCVD systems the molecular weight strongly corresponds with the deposition rate, which is controlled by the saturation ratio, with higher molecular weights being achieved at higher deposition rates [119]. The poly(HEMA-*co*-EGDA) iCVD films in this work are deposited at lower growth rates (3-4 nm vs.13-30 nm) and saturation ratios (0.02-0.1 vs.0.14-0.72) when compared to the work of Li *et al.* [27]. It is therefore reasonable to assume that the chains in the poly(HEMA-*co*-EGDA) films in this work have a shorter chain length, higher percentage of chain ends and therefore, a higher free volume which helps enable the observed increase in ionic conductivity.

Similar EIS measurements were performed on a LiTFSI doped 55HEMA film. The expected film thickness via *in-situ* laser interferometry is ~ 2 μm and EIS measurements were recorded at 25, 30, 40, 50 and 60 ^{o}C. The corresponding Nyquist plots and equivalent circuit model are shown in Figure 4.18, with the full fitting parameters, calculated ionic conductivity and ASR are presented in Table 4.4. Immediately noticeable is that the 8.09 x 10^{-10} S/cm room temperature ionic conductivity of the 55HEMA film is roughly five orders of magnitude lower than the 90HEMA film. This is also well below the 3.2 x 10^{-8} S/cm reported by Li *et al.* for their 55 mol.% HEMA thin films [27].

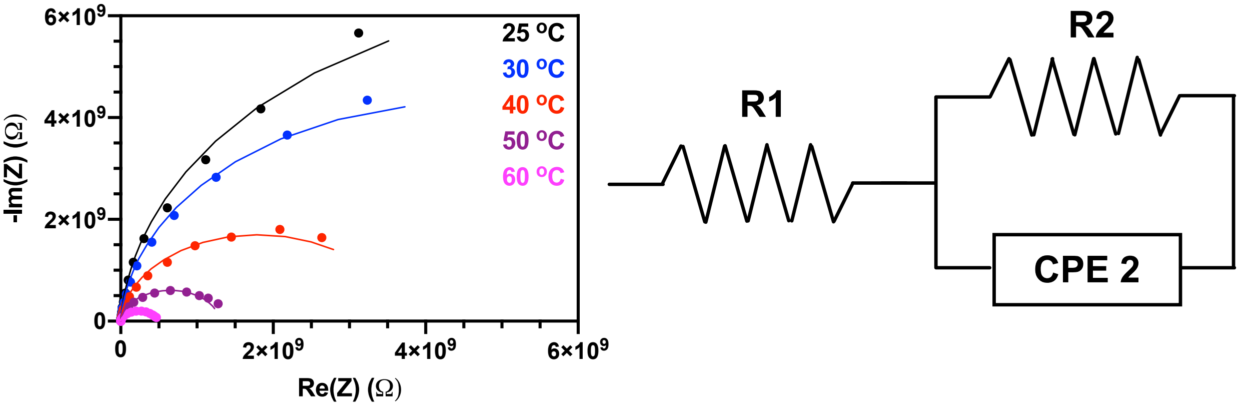

Figure 4.18: Nyquist plot and equivalent circuit model for LiTFSI doped 55HEMA thin film at various temperatures. The dots in Nyquist plot are the experimental data points while the fit is the solid line.

Table 4.4: Equivalent circuit model values, calculated ionic conductivity and calculated area specific resistance for LiTFSI dopped 55HEMA thin film at various temperatures.

Temperature (°C)	R1 (Ω)	R2 (Ω)	Q2 (F s$^{(a-1)}$)	a2	σ (S cm^{-1})	ASR (Ω cm^2)
25	624.7	1.32E10	3.96E-10	0.968	8.09E-10	3.21E5
30	618.3	9.03E9	4.08E-10	0.966	1.18E-9	2.20E5
40	615.8	3.61E9	4.39E-10	0.961	2.96E-9	8.79E4
50	599.4	1.30E9	4.74E-10	0.957	8.22E-9	3.16E4
60	633.6	4.3E8	5.19E-10	0.950	2.26E-8	1.10E4

Since conductivity is decoupled from polymer chain motion the decrease in conductivity can be attributed to the decrease in film polarity due to a decreased concentration of the HEMA hydroxyl groups that are necessary for the Li$^+$ to screen interchain interactions [27]. Due to the low ionic conductivity this 55HEMA film has ASR values that indicate its utilization as a solid polymer electrolyte would greatly hamper cell performance. One explanation for the drastically reduced conductivity is that the 55HEMA film is much thicker (~2 μm) then the ~300 nm films tested by Li *et al.* This increased thickness might reduce the LiTFSI salt's ability to fully infiltrate the polymer film during doping, leading to the observed decrease in room temperature ionic conductivity and similar negative effects of increased thickness on ionic conductivity have been observed for heavily crosslinked siloxane iCVD films [29].

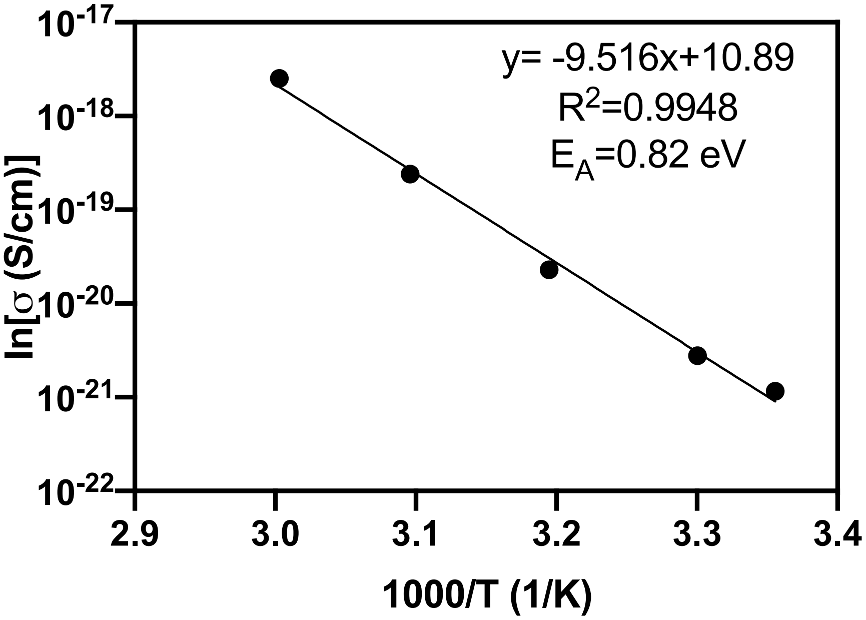

Figure 4.19: Arrhenius plot for LiTFSI doped 55HEMA thin film.

Figure 4.19 contains an Arrhenius plot for the LiTFSI doped 55HEMA film. The Arrhenius dependance indicates that the primary mode of ion conduction is through an ion hopping process and is decoupled from any long-range motion of the polymer chains [24]. This supports the proposition by Li *et al.* that the dominant ion conduction mechanism at low temperatures is ion hopping between salt clusters inside the polymer film [27], [239]. The Arrhenius plot also gives an activation energy (E_A) of 0.82 eV. This is significantly higher than the activation energies that have been measured for other solid electrolytes, with typical values ranging from ~0.2 eV for high conductivity sulfide glasses to ~0.5 eV for solid oxides [24]. This high activation energy is not surprising due to the 55HEMA's low ionic conductivity. Similar to the 90HEMA film, improvements in ionic conductivity may be achieved by optimizing the LiTFSI doping process.

Here, poly(HEMA-*co*-EGDA) films have been utilized as solid polymer electrolytes, as all solvent is removed after LiTFSI doping. Since poly(HEMA-*co*-EGDA) thin films are known to swell in polar solvents, another strategy to increase the ionic conductivity of more crosslinked films is to inject the films with conventional organic solvent electrolytes [27], [237], [238]. These polar aprotic solvents should swell the poly(HEMA-*co*-EGDA) films and enable them to function as gel polymer electrolytes, boosting their ionic conductivity. Although this does induce new safety risks due to the inherent flammability of these solvents [6], [7], [16].

4.4 Conclusions

iCVD is a chemical vapor deposition technique capable of depositing conformal polymer thin films on high aspect ratio features. Here, poly(HEMA-*co*-EGDA) thin films have been deposited on high aspect ratio vertically aligned CNTs. The coatings are conformal not only over the microstructured CNT forests (aspect ratio ~2.5) but also over the individual CNTs themselves (aspect ratio > 25000). The high conformality achieved is attributed to the low saturation ratio of the HEMA and EGDA monomers, which is kept < 0.1 during the deposition. These poly(HEMA-*co*-EGDA) films are then doped with LiTFSI salt to function as solid polymer electrolytes. Doped 90HEMA thin films exhibit conductivities on the order of 10^{-5} S/cm and, for a 1 μm thick films, an ASR of 5 Ω cm^2. This makes iCVD poly(HEMA-*co*-EGDA) thin films a leading candidate for 3D micro-battery full cell development. Despite this promising conductivity, future works should investigate the effects of LiTFSI, or other salt, concentration and distribution on ionic conductivity and determine other important electrochemical properties, such as verifying a suitable electrochemical stability window for full cell operation.

THIS PAGE IS LEFT INTENTIONALLY BLANK

Chapter 5- Fabrication and Simulation of 3D Full Cells with Micro-structured CNT Architectures

5.1 Introduction

After electrolyte deposition the final two steps in 3D full cell fabrication are to incorporate the second electrode and to attach the second current collector. Once these steps are completed the 3D full cell is ready to be cycled. Due to the difficulty in incorporating solid electrolytes and then preventing damage to that electrolyte when incorporating the second electrode there are far fewer works that attempt 3D full cell fabrication, instead focusing on the development of either 3D electrodes or conformal 3D electrolytes. In general, the 3D full cells containing a conformal electrolyte layer can be broken down into two categories, thin film nanobatteries and infiltrated micro-batteries. Thin film 3D nanobatteries are produced with layer thickness on the order of tens to hundreds of nanometers and are fabricated by thin film deposition processes such as atomic layer deposition (ALD) or sputtering. 3D micro-batteries are fabricated with feature thickness on the order of tens to hundreds of micrometers by conventional microfabrication techniques and often incorporate an infiltrated slurry-based electrode. Not considered here are 3D batteries that prevent electrode contact by controlling the spacing between the electrodes. [48], [159], [160].

Two examples of 3D thin film nanobatteries are presented in Figure 5.1. In Figure 5.1A Pearse *et al*. started fabricating their 3D nanobattery by reactively etching cylindrical pores into a Si substrate that would serve as a scaffold for battery deposition. Next, ALD was used to deposit 40 nm of a Ru current collector, 70 nm of LiV_2O_5 cathode, 50 nm of a LiPON-like electrolyte, 10 nm of SnN_x anode and, finally, a 25 nm TiN current collector. These 3D cells were able to cycle over 100 times and demonstrated a maximum discharge capacity of ~ 0.03 mAh/cm^2. More importantly the nanobatteries (AEF 4 and AEF 10) of Pearse *et al.* were able to access the majority of their discharge capacity at high current rates, while 2D planar cells (AEF 1) with an identical cell stack experienced significant capacity loss [37]. Talin *et al.* produced their cell stack by sputtering a 20/120 nm Ti/Pt current collector, a ~300 nm thick $LiCoO_2$ cathode, 500 nm of LiPON electrolyte, 100 nm of Si and 400 nm of Cu current collector onto a patterned Si micropillar array. While the cells produced by Talin *et al.* were able to successfully cycle, and achieved an areal capacity of 0.025 mAh/cm^2, they experienced capacity fading at higher currents. The authors attributed this to the non-uniform thickness and low ionic conductivity of their LiPON electrolyte [126]. The authors used finite element analysis simulations to determine that an order of magnitude increase in the ionic conductivity would result in significantly better full cell performance.

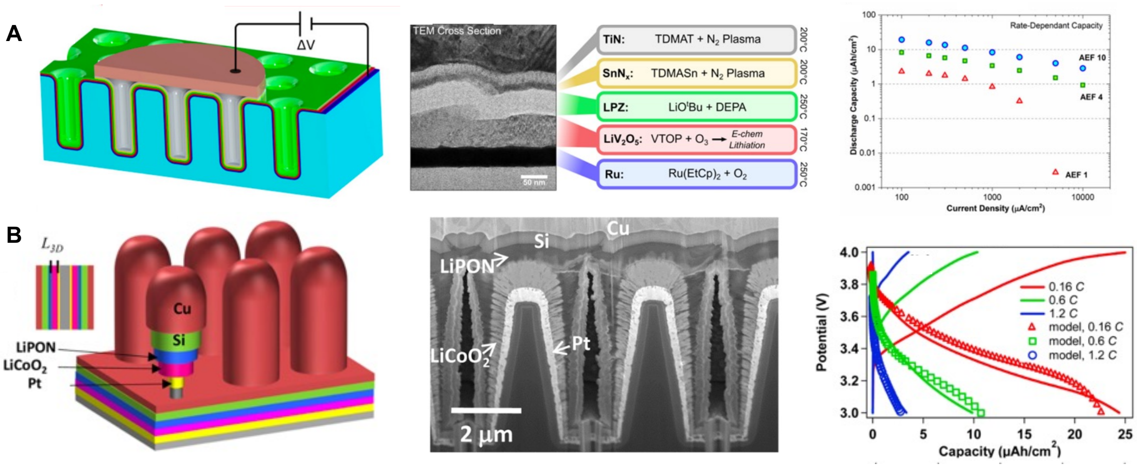

Figure 5.1: Schematics, electron microscopy cross sections and cycling performance of 3D thin film nanobatteries fabricated by A) ALD by Pearse *et al.* Reproduced with permission [37]. Copyright 2018, American Chemical Society. B) sputtering by Talin *et al.* Reproduced with permission from [126]. Copyright 2016, American Chemical Society.

Three examples of infiltrated 3D micro-batteries are presented in Figure 5.2. Hur *et al.* produced Si micropillar arrays by dry etching. These pillars are 400 µm tall, 100 µm in diameter and 200 µm in pitch. The Si pillar array was spin coated with a SU-8 photoresist and soaked in a Li-salt containing carbonate solution. A lithium nickel cobalt aluminum (NCA) containing slurry was infiltrated between the pillars before the entire stack was soaked in a propylene carbonate electrolyte and cycled (Figure 5.2A). These cells were cycled repeatedly with a cut off charging capacity of 0.5 mAh/cm^2. Despite stable cycling, high coulombic efficiency was obtained by discharging at a significantly lower current than the cell was charged at and the cells suffered from inefficient Si use and cracking [50].

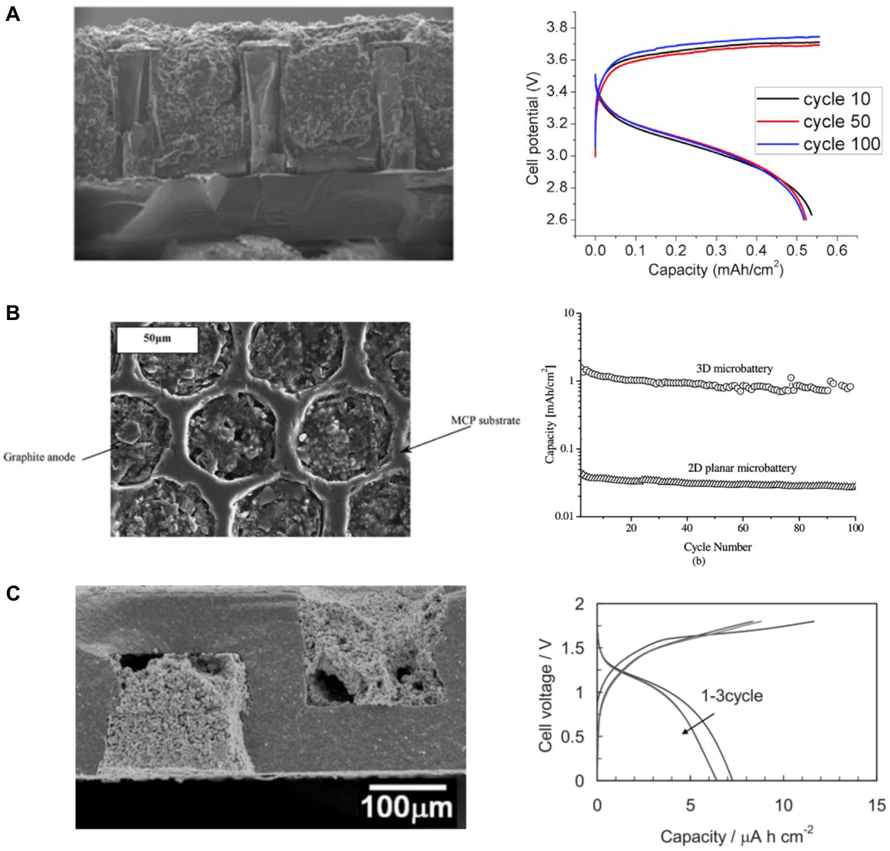

Figure 5.2: Electron microscopy images and cycling data for 3D micro-batteries fabricated by A) Hur *et al*. Reproduced with permission [50]. Copyright 2018, Elsevier. B) Nathan *et al*. Reproduced with permission [53]. Copyright 2005, IEEE. C) Kotobuki *et al.* Reproduced with permission [49]. Copyright 2010, IOP.

Nathan *et al*. started their fabrication by first coating a glass microchannel plate with an electrodeposited Ni current collector (Figure 5.2B). A second electrodeposition was performed to fabricate a molybdenum oxysulfide (MOS) cathode material. A gel polymer electrolyte was coated over the glass/Ni/MOS structure in a series of spin coating and vacuum pulling steps before mesocarbon microbeads were infiltrated into the holes using the same process [53]. Similar to the work of Hur *et al.* [50], Nathan *et al*. then soaked their cells in liquid electrolyte before cycling them 100 times. These cells were able to achieve an areal capacity of > 1 mAh/cm^2, which was significantly higher than the equivalent planar cell. Lastly, Kotobuki *et al.* (Figure 5.2C) took a different approach. Here the authors began by patterning a $Li_{0.35}La_{0.55}TiO_3$ (LLTO) electrolyte pellet into a dual sided honeycomb array. One side of the array was infiltrated with a $LiCoO_2$ nanoparticle slurry while the other side was infiltrated with a $Li_4Mn_5O_{12}$ slurry. This cell experienced a very low 0.0073 mAh/cm^2 capacity, due to poor ionic conductivity though the electrodes and large interfacial impedances at the LLTO/slurry interface [49].

The work in this chapter seeks to bridge the gap between thin film nanobatteries and infiltrated micro-batteries by fabricating a CNT-based full cell. Building upon the work of Chapter 2 and Chapter 4, initiated chemical vapor deposition (iCVD) poly(hydroxyethyl methacrylate-*co*-ethylene glycol diacrylate) (poly(HEMA-*co*-EGDA)) coated Si-CNT patterned electrodes are infiltrated with a lithium nickel manganese cobalt oxide (NMC) containing slurry. After evaluating the stability of the iCVD electrolyte, these slurry infiltrated cells are soaked in liquid electrolyte solutions to ensure suitable ionic conductivity throughout the cell and are placed in Swagelok cells for cycling. While some difficulties experienced during cell fabrication led to non-ideal performance, 2D finite element analysis (FEA) simulations are performed in COMSOL for ideal interdigitated CNT-based batteries to determine their theoretical specific energy and power, which are then compared with a simulation for a state-of-the art lithium-ion cell. The impact of cell geometry and electrolyte conductivity are also explored.

5.2 Experimental Methods

5.2.1 Si-CNT Composite Fabrication

Vertically aligned CNT forests with ~100 μm heights were grown on Cu foils using the process outlined in Chapter 2. Si-CNT composites were fabricated using either the low-pressure chemical vapor deposition process (LPCVD) process outlined in Chapter 2 or a plasma enhanced chemical vapor deposition (PECVD) process. PECVD amorphous Si (a-Si) depositions were performed in a Plasmatherm PECVD reactor by flowing 5% SiH_4 in He at 150 sccm into the reactor to establish a pressure of 500 mTorr. After flow had stabilized the RF power was set to 25 W for the desired 25 min deposition time. The deposited Si mass was determined using the same microbalance as Chapter 2.

5.2.2 iCVD Polymer Electrolyte Deposition

iCVD poly(HEMA-*co*-EGDA) films were deposited on Si-CNT composite electrodes using the same equipment and procedure outlined in Chapter 4. Prior to iCVD the Si-CNT electrodes were mounted on a 0.5" diameter stainless steel spacer using conductive Cu tape or Ni paste (Figure 5.3A). During deposition the backside of this spacer was covered in Kapton tape to prevent unwanted poly(HEMA-*co*-EGDA) deposition on the spacer (Figure 5.3B). An additional iCVD recipe for a 75 mol.% HEMA film (75HEMA) is presented in Table 5.1. All other iCVD parameters remained the same for the deposition.

Table 5.1: Recipe to produce film 75 mol.% HEMA poly(HEMA-*co*-EGDA) iCVD thin film.

Recipe	Q_{N2} (sccm)	Q_{HEMA} (sccm)	P_{HEMA}/P_{Sat}	Q_{EGDA} (sccm)	P_{EGDA}/P_{Sat}	Q_{TBPO} (sccm)	Q_{Total} (sccm)
75HEMA	1.2	0.8	0.05	0.4	0.04	0.6	3

5.2.3 Slurry Formation and Infiltration

A typical slurry with an 8:1:1 weight ratio of active material:conductive additive:binder was prepared for infiltration into the iCVD coated Si-CNT composites. $LiNi_{0.33}Mn_{0.33}Co_{0.33}$ (NMC, > 97.5%, particle size < 0.5 μm, Sigma Aldrich) and carbon black (~50 nm particle size, Cabot) were weighed outside the glove box before being ground together with a mortar and pestle. The mixture was then placed overnight in a BUCHI furnace under active vacuum and at 90 °C before being moved into the glovebox under vacuum. Inside the glovebox anhydrous N-methyl-2-pyrrolidone (NMP, 99.5%, Sigma) was mixed with polyvinylidene fluoride (PVDF, Sigma) to create a 5 wt.% PVDF in NMP solution at 60 °C . The PVDF was dried overnight under vacuum before being moved to the glovebox. The PVDF-NMP solution was then added to the dried NMC-carbon black powder and allowed to stir continuously at room temperature and 1500 RPM. To make it suitable for casing the NMC slurry was diluted with further NMP to give a solids concentration of ~0.27 g/mL.

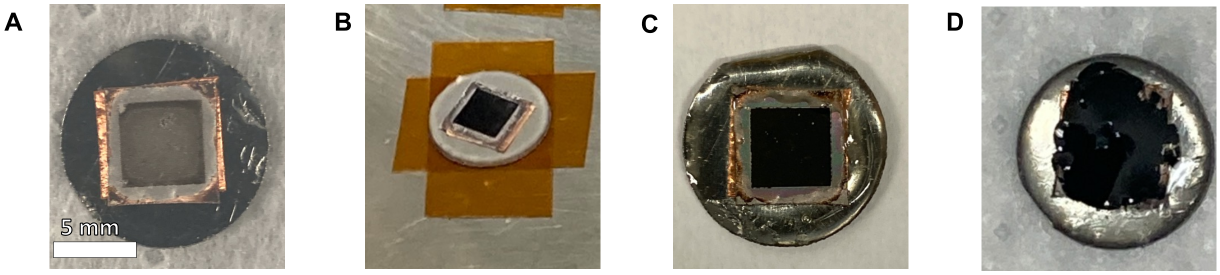

Figure 5.3: A) Si-CNT electrode mounted on stainless steel spacer with Cu tape, B) Si-CNT/spacer combination with Kapton tape on spacer backside to prevent unwanted iCVD polymer deposition, C) epoxy ring painted around iCVD coated Si-CNT electrode, D) full cell assembly after slurry infiltration and soaking overnight in liquid electrolyte.

iCVD coated Si-CNT electrodes were prepared for full cell fabrication using a procedure similar to that of Hur *et al.* [50]. As shown in Figure 5.3C, the stainless-steel spacer was painted with an epoxy (Devcon) that covered the edges of the CNT foil. This created a “dish” around the CNTs for slurry casting and prevents direct contact between the NMC slurry and the opposing current collector. Great care was taken to avoid unwanted epoxy infiltration into the CNT structure. The epoxy was allowed to dry for ~24 h before the assembly was dried under active vacuum in the glovebox antechamber overnight and moved into the Ar glovebox.

For slurry infiltration in the Ar glovebox the samples were first wet with a drop of anhydrous NMP. A micropipette was then used to cast 10 μL of slurry onto the sample. The sample was then placed under vacuum for 3 min to speed the NMP drying process. It should be noted that excessive drying results in slurry delamination. This process was repeated until the desired number of drops had been deposited. After slurry deposition the slurry coated cells were allowed to soak in a 1 M lithium bis(trifluoromethanesulfonyl)imide (LiTFSI, anhydrous, 99.99%, Sigma) in anhydrous propylene carbonate (PC, 99.7%, Sigma) or 1,3-dioxolane (DOL, 99.8%, Sigma) electrolyte. Following soaking (Figure 5.3D) the cell stack was loaded into the same Swagelok cells used in Chapter 2, capped with a stainless-steel spacer and transported to the battery cycler for testing.

5.2.4 Electrochemical Testing

All cycling was performed using the same Swagelok cells and BCS-805 battery cycler that was utilized for the Si-CNT half-cells in Chapter 2. Si-CNT half-cells with PECVD Si were fabricated using a 1 M LiTFSI in 1,3-dioxolane (DOL) electrolyte, Li-metal foil counter and reference electrode and Swagelok cells are identical to those in Chapter 2. Half-cell Galvanostatic cycling was preformed between 0.01 V and 2.0 V vs Li/Li^+. Full cell galvanostatic cycling was performed between 2.9 V and 4.1 V or 2.5 V and 4.2 V. The dQ/dV analysis was performed using Biologic's BT-Lab software.

5.2.5 Materials Characterization

Scanning electron microscopy (SEM), energy dispersive x-ray spectroscopy (EDS), Raman spectroscopy and optical microscopy were carried out using the equipment and settings outlined in Chapter 2. Fourier transform infrared spectroscopy (FTIR) was performed using the same equipment and settings outlined in Chapter 4.

CNT height profiles were captured using a Keyence VK-X1000 confocal laser microscope at 50X magnification. X-ray microscopy (XRM) was performed using a Zeiss Versa 620. For XRM the slurry infiltrated samples were transported to the equipment under Ar in a sealed plastic box and remained under Ar for the duration of the scan. For each scan the source was set at 60 kV and 108.25 μA with a LE2 source filter. Scans were performed using either a 4X or 20X optical lens and 1601 to 2401 projections were used in the reconstruction.

5.3 Experimental Results and Discussion

5.3.1 Poly(HEMA-co-EGDA) iCVD Polymer Electrolyte Stability

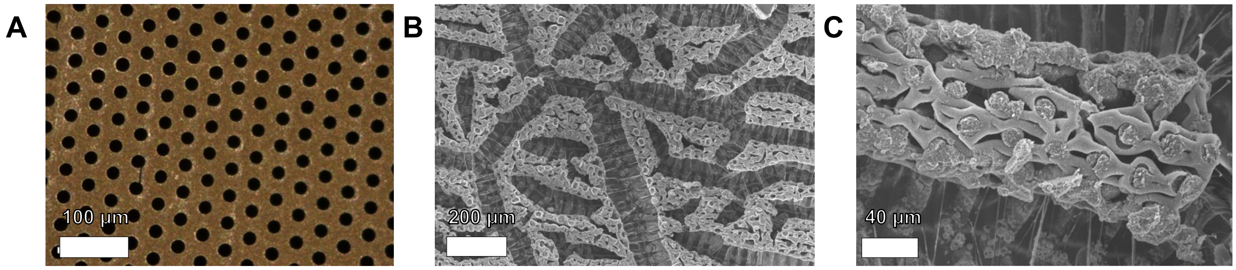

Figure 5.4: A) optical microscopy image of a honeycomb CNT forest coated with PECVD Si and a 90HEMA iCVD electrolyte. B) and C) SEM images of the same forest after coating with NMC slurry and drying under vacuum.

Early attempts to fabricate full cells utilizing 90HEMA electrolytes typically resulted in short circuited cells. Despite maintaining a pristine honeycomb structure (Figure 5.4A) following 90HEMA deposition, SEM analysis post slurry infiltration (Figure 5.4B) revealed significant damage to the honeycomb structure. Despite this damage some NMC slurry is still infiltrated into the honeycomb structure (Figure 5.4C).

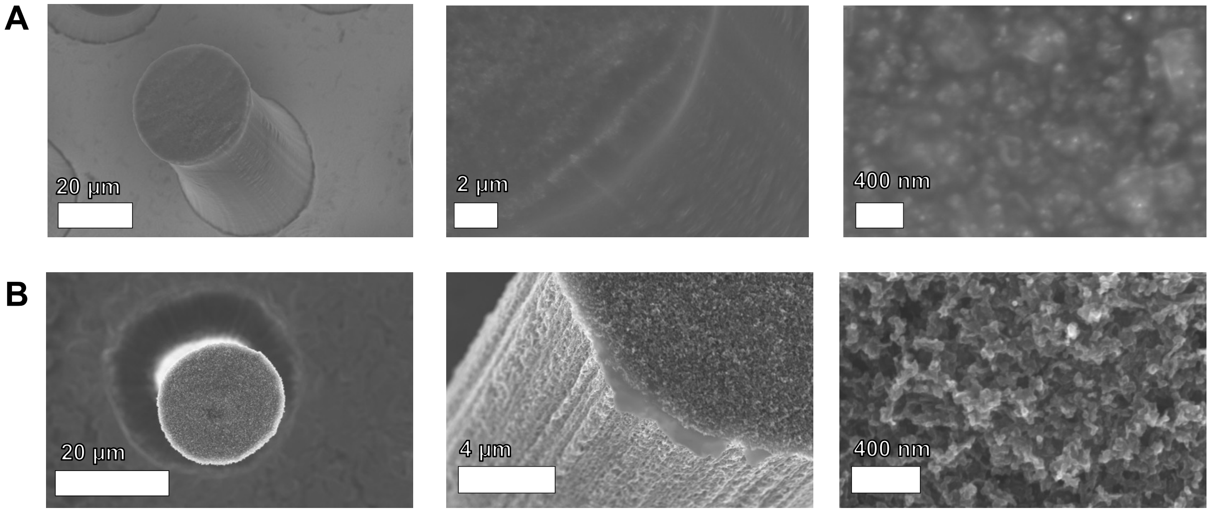

Figure 5.5: A) Pre- and B) post NMC casting and vacuum drying for 90HEMA coated LPCVD Si-CNTs. The CNTs are patterned in a pillar array with 40 µm diameter and 70 µm center-to-center spacing.

To determine the cause of this damage pure NMP was cast on 90HEMA coated LPCVD Si forests and then dried under vacuum. SEM images taken pre- (Figure 5.5A) and post (Figure 5.5B) NMC wetting of a 90HEMA coated pillar structured Si-CNT forest reveal that the once uniform 90HEMA coating does not survive exposure to NMP. It is known that poly(HEMA-*co*-EGDA) iCVD films swell in polar solvents [27], [237] and that lightly crosslinked poly(HEMA-*co*-EGDA) are not stable in water [238]. Similar to the experience of Yague *et al.*, here is believed, that despite having an excellent ionic conductivity, the 90HEMA films are insufficiently crosslinked [238]. As the NMP diffuses into the polymer network the resulting swelling results in polymer chain disentanglement that dissolves the 90HEMA film. Once the 90HEMA layer is dissolved the CNTs experience significant shrinking and densification. This is similar what was observed in previous works on using CNT forests as nanoporous stamps. In these works liquid infiltration resulted in forest shrinking and subsequent evaporation caused densification and mechanical damage to the CNT forest [59]. While increasing the Si coating on these pillars may help to prevent the observed densification [56], [59], the failure of the 90HEMA film greatly increases the chances of a short circuit. Figure 5.5 also exhibits an advantage of a pillar structured cell over the honeycomb design in Figure 5.4, as the discrete nature of the pillars results in significantly less damage to patterned CNT microstructure post NMP exposure.

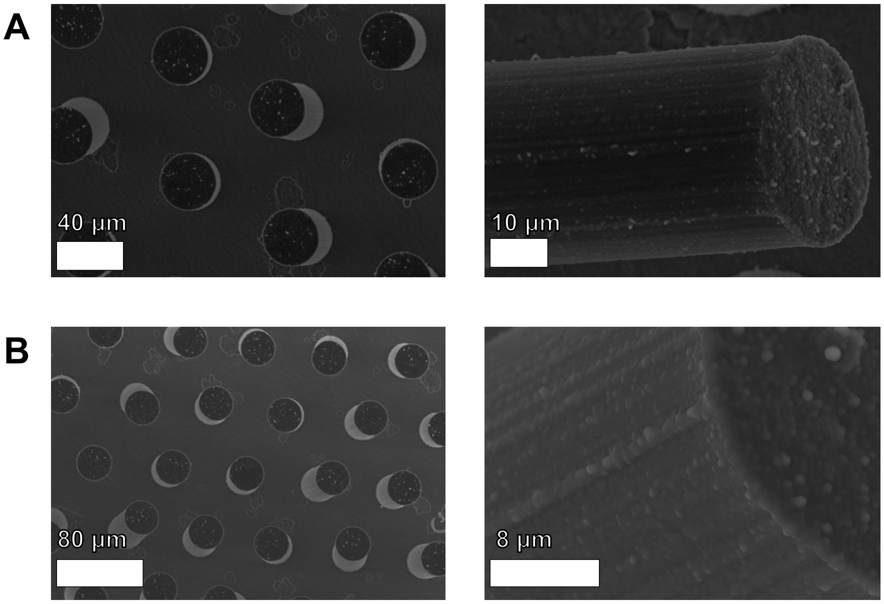

Figure 5.6: A) Pre- and B) post NMC casting and vacuum drying for 55HEMA coated LPCVD Si-CNTs. The CNTs are patterned in a pillar array with 40 µm diameter and 90 µm center-to-center spacing.

The poly(HEMA-*co*- EGDA) structural stability can be addressed by increasing the EGDA crosslinker concentration during deposition. Figure 5.6 shows Si-CNT pillars coated with a 55HEMA thin film pre- and post-exposure to drop cast NMC and drying under vacuum. Here, the more heavily crosslinked 55HEMA film maintains its structural integrity after the drying process, increasing its suitability for incorporation in full cell designs that include infiltrated slurry electrodes. However, it should be noted that the increase in crosslinker concentration will result in a significant decrease in the 55HEMA's ability to act as a solid polymer electrolyte. As discussed in detail in Chapter 4, decreasing the HEMA mol.% from ~90% to ~55% decrease the ionic conductivity from ~10^{-6} to 10^{-5} S/cm down to ~10^{-10} to 10^{-8} S/cm [27]. This decrease may be mediated by soaking the poly(HEMA-*co*-EGDA) thin films in liquid electrolyte solutions, as 55 mol.% poly(HEMA-*co*-EGDA) films have mesh sizes suitable for small molecule diffusion when swollen with polar solvent [238].

5.3.2 Slurry Infiltration Into Micro-structured CNT Pillar Arrays

After validating that the 55HEMA coatings maintain their mechanical stability after NMP contact, the samples are infiltrated with NMC slurry by drop casting and drying under vacuum. Figure 5.7 shows SEM images of a 55HEMA Si-CNT pillar array post NMC infiltration. In Figure 5.7A the slurry is clearly infiltrated between the pillar array. A zoom in (Figure 5.7B) shows that the 55HEMA coating on the pillar surface has survived the slurry infiltration process.

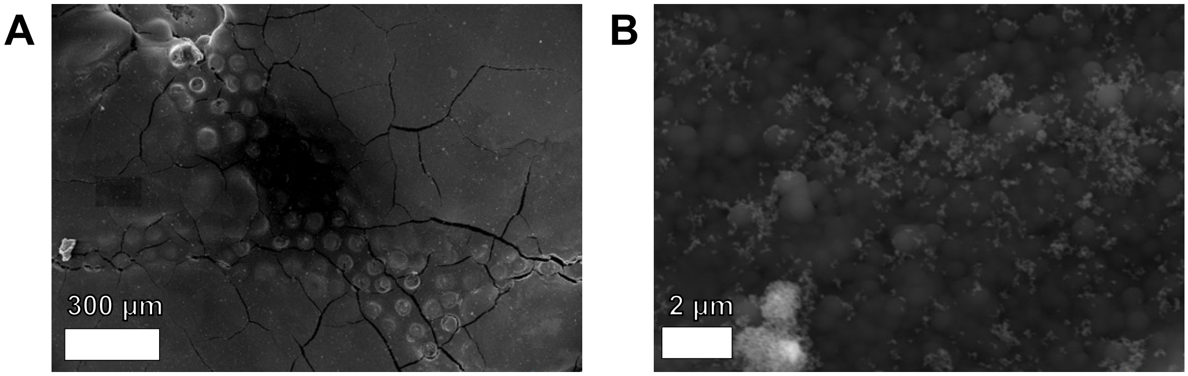

Figure 5.7: SEM images of A) a 55HEMA Si-CNT pillar array infiltrated with NMC slurry and B) the top of an individual 55HEMA Si-CNT pillar post NMC infiltration. The CNTs are patterned in a pillar array with 40 µm diameter and 90 µm center-to-center spacing.

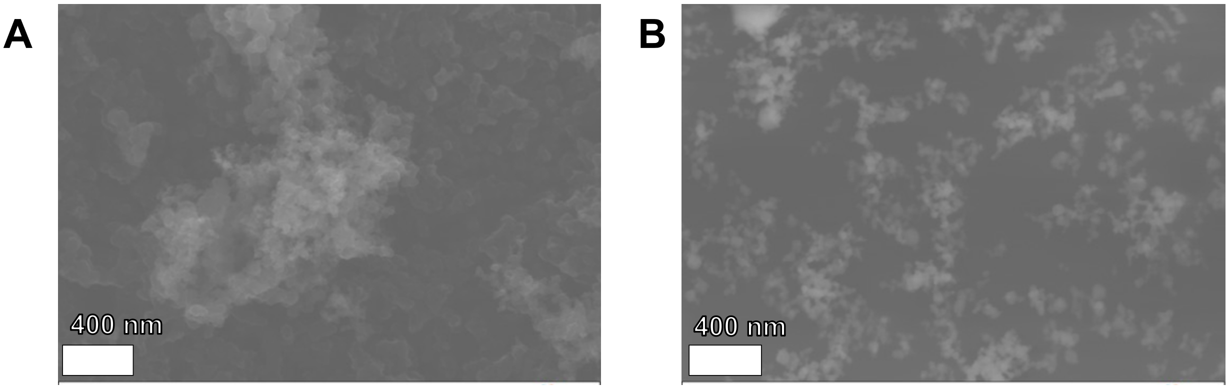

Figure 5.8: SEM images of the A) carbon black and B) NMC powders used in this work.

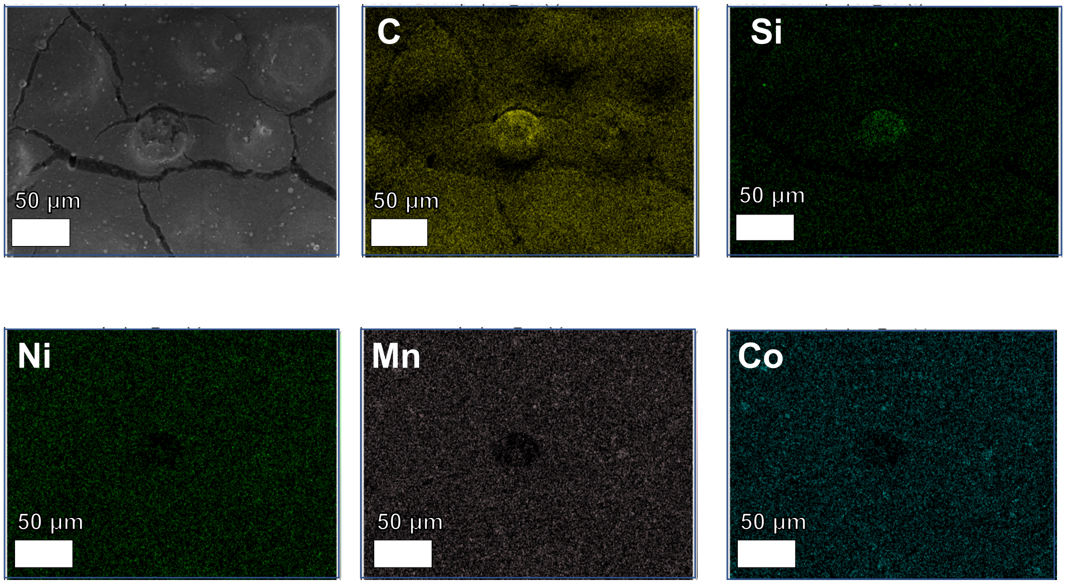

Figure 5.9: EDS analysis of a 55HEMA Si-CNT pillar array infiltrated with NMC slurry. The CNTs are patterned in a pillar array with 40 μm diameter and 90 μm center-to-center spacing.

The carbon black and NMC powders used in this work are presented in Figure 5.8A and Figure 5.8B respectively. Since the carbon black and NMC particles have similar dimensions, EDS mapping was performed to determine that both slurry components were successfully infiltrated. The EDS mapping in Figure 5.9 shows a uniform distribution of Ni, Mn and Co throughout the pillar array. Furthermore, while there are concentrations of C and Si at the top of the central pillar, the C signal is significant between the pillars. These results indicate that both the carbon black and NMC from the starting slurry have been infiltrated between the micro-structured CNT pillars.

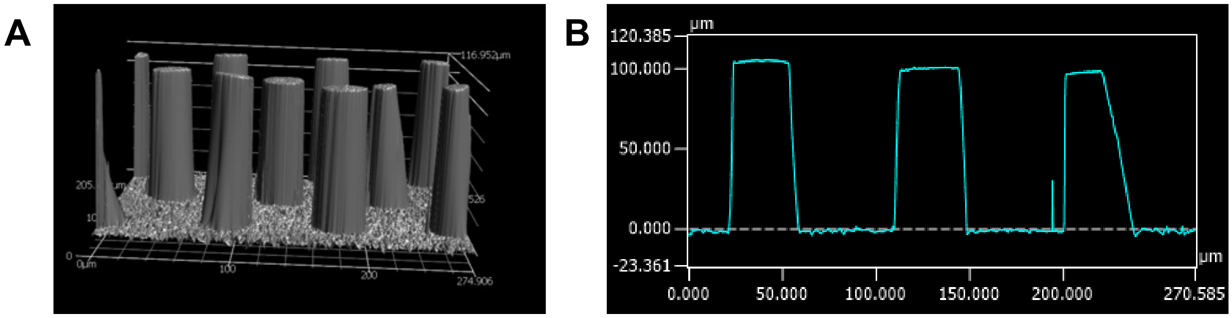

Figure 5.10: Confocal laser microscope A) 3D and B) 2D profiles of an array of vertically aligned CNT pillars. The CNTs are patterned in a pillar array with 40 μm diameter and 90 μm center-to-center spacing.

While the SEM and EDS analysis from Figure 5.7 and Figure 5.9 seem to indicate successful NMC electrode infiltration, it is necessary to verify that the slurry reaches the bottom of the pillar array and has not just formed a coating across the surface. Height profiles obtained by confocal laser microscopy (Figure 5.10) indicate that the CNT pillars infiltrated with slurry in Figure 5.7 are ~100 μm tall prior to any coating processes. XRM scans were performed on the sample in Figure 5.10 post NMC slurry infiltration to determine the depth of slurry infiltration. The results of a 4X scan are presented in Figure 5.11 and the results of a 20X scan in Figure 5.12. For each scan planar and sidewall slices are presented at the top, middle and bottom of the slurry layer. In both scans the thickness of the slurry layer is ~100 μm, in agreement with the slurry barely covering the CNT pillars in Figure 5.7 and the height of the CNT pillars themselves in Figure 5.10. At the top of the slurry layer the XRM shows mostly one uniform region of slurry. However, for the middle slice dark circles representing the 40 μm CNT pillars appear in the brightly colored slurry. The slurry is also present at the bottom of the forest, as the planar images near the Cu foil show both the round CNT pillars with the infiltrated slurry between, partially evident by the cracks within it. The combination of the SEM in Figure 5.7 and the XRM in Figure 5.11 and Figure 5.12 confirm that the drop casting followed by vacuum pulling successfully infiltrates the NMC slurry into the CNT pillar array.

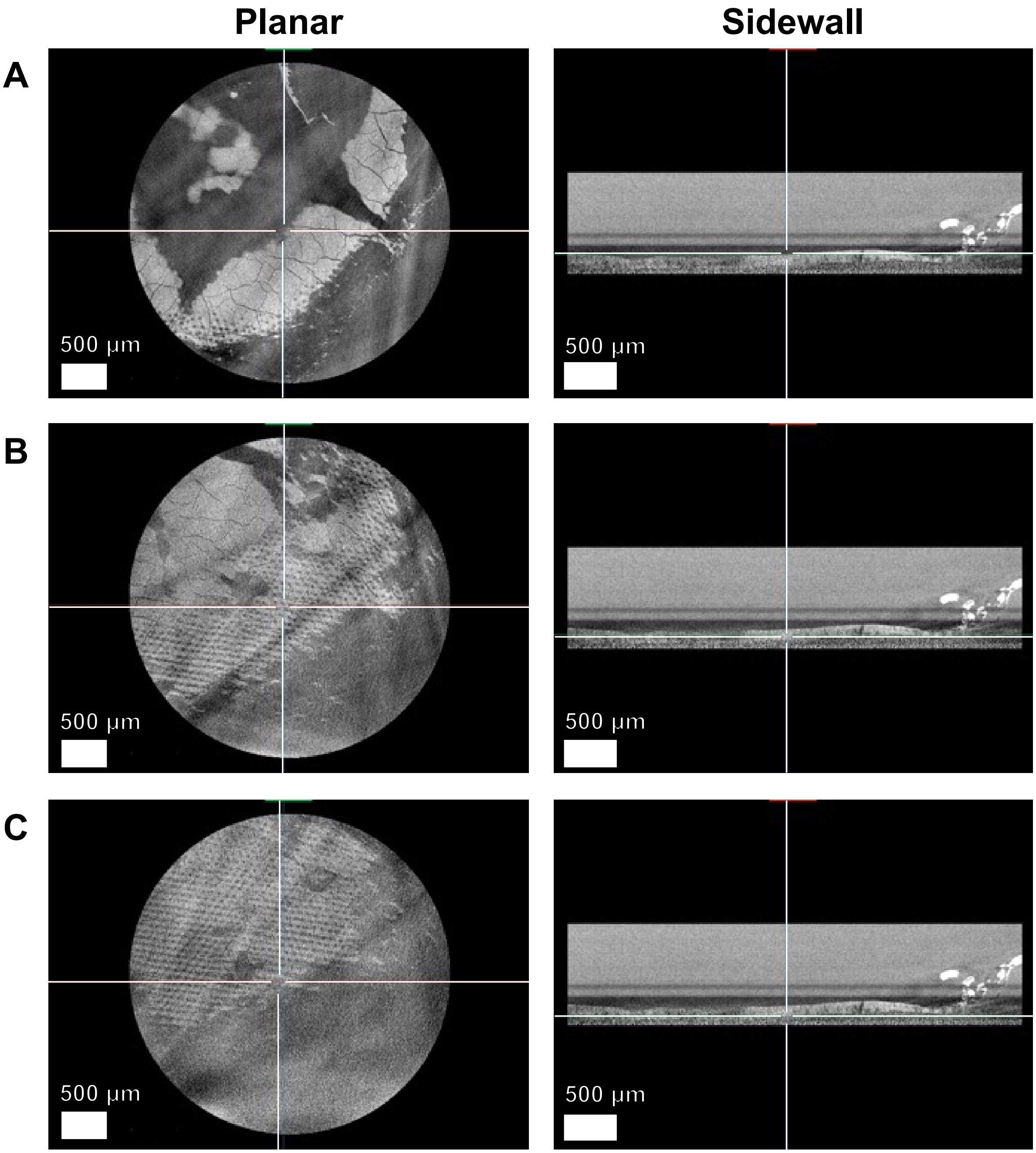

Figure 5.11: 4X XRM scan of NMC slurry infiltrated CNT pillars. The CNTs are patterned in a pillar array with 40 µm diameter and 90 µm center-to-center spacing. Planar and sideview images are presented for the A) top, B) middle and C) bottom of the CNT forest.

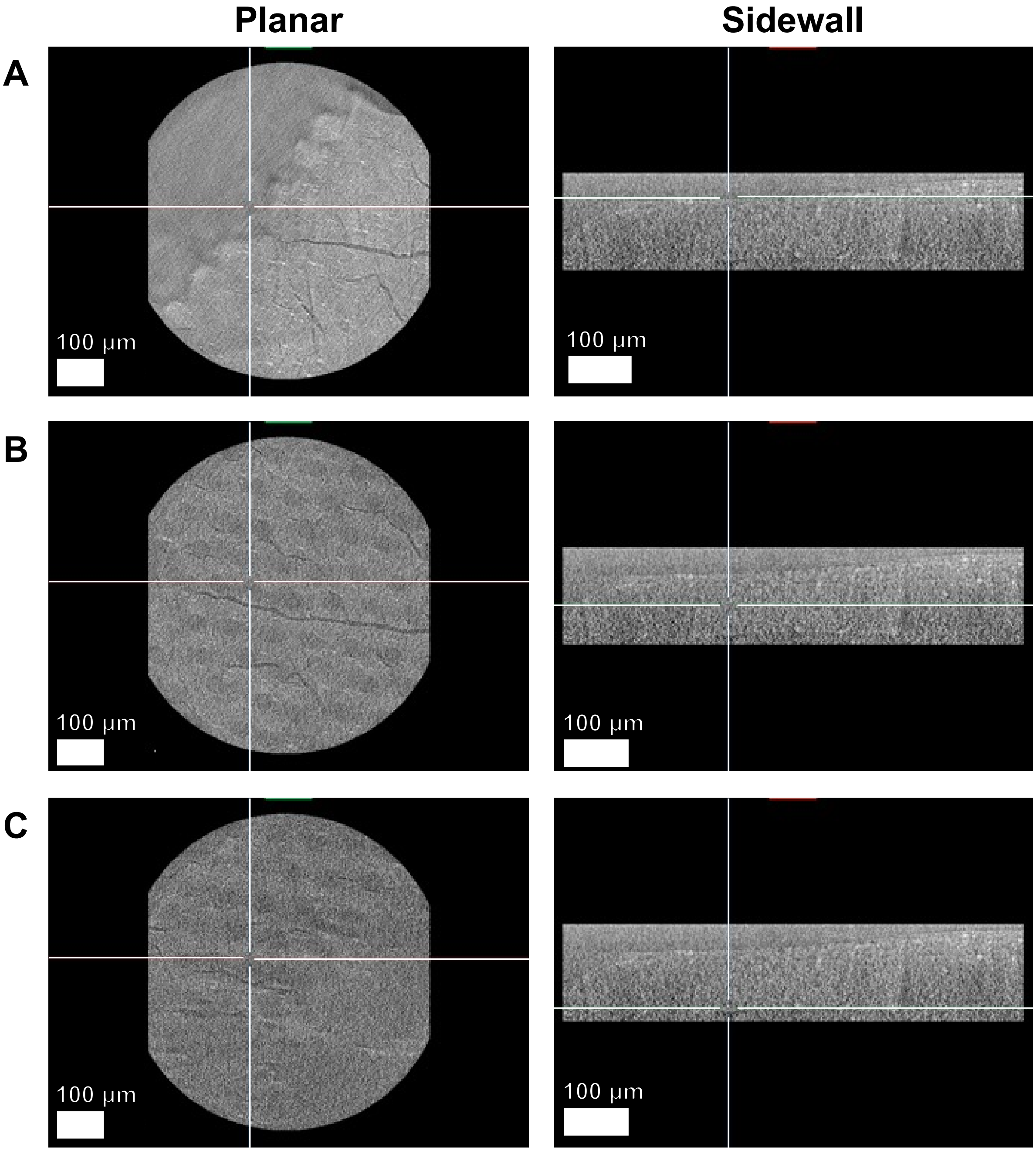

Figure 5.12: 20X XRM scan of NMC slurry infiltrated CNT pillars. The CNTs are patterned in a pillar array with 40 µm diameter and 90 µm center-to-center spacing. Planar and sideview images are presented for the A) top, B) middle and C) bottom of the CNT forest.

5.3.3 Planar NMC/75HEMA/Si-CNT Full Cell

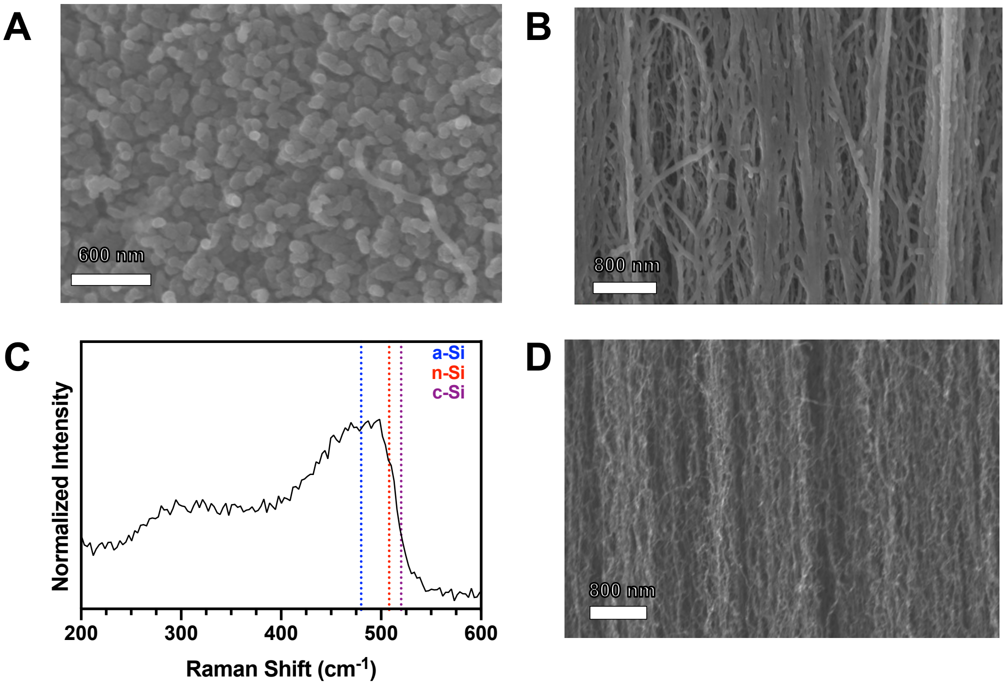

Figure 5.13: SEM images of PECVD Si on aligned CNT forest A) crust and B) exterior sidewall. C) Raman analysis of PECVD Si deposited on aligned CNTs. D) SEM of CNT forest interior post PECVD showing an absence of deposited Si.

Full cell fabrication began by growing ~100 μm tall non-patterned CNTs on Cu foil using the process outlined in Chapter 2. Following growth, the aligned CNTs were coated with a-Si using a PECVD process. A 25 min PECVD deposition resulted in a ~25 μg Si deposition on the forest, giving a 0.1 mg/cm^2 Si loading that is a full one to two orders of magnitude lower than the LPCVD depositions in Chapter 2. Post deposition SEM reveals that there is a substantial Si coating on the CNT forest surface (Figure 5.13A) and exterior sidewall (Figure 5.13B). Raman analysis of these CNT coatings (Figure 5.13C) shows a strong amorphous Si (a-Si) signal at ~480 cm^{-1} with a shoulder at ~508 cm^{-1} indicating a small amount of nanocrystalline Si (n-Si) in the coating [139], [140]. However, the SEM image in Figure 5.13D shows that the Si coating on the forest exterior in Figure 5.13A and Figure 5.13B does not extend to the forest interior, as there is no visible Si coating on the CNTs at the forest interior. This limitation is attributed the nature of the PECVD process, whereby the diffusion limitations of the reactive precursor species prevent interior coatings, and shows the strength of the reaction limited LPCVD deposition in developing high capacity electrodes [242].

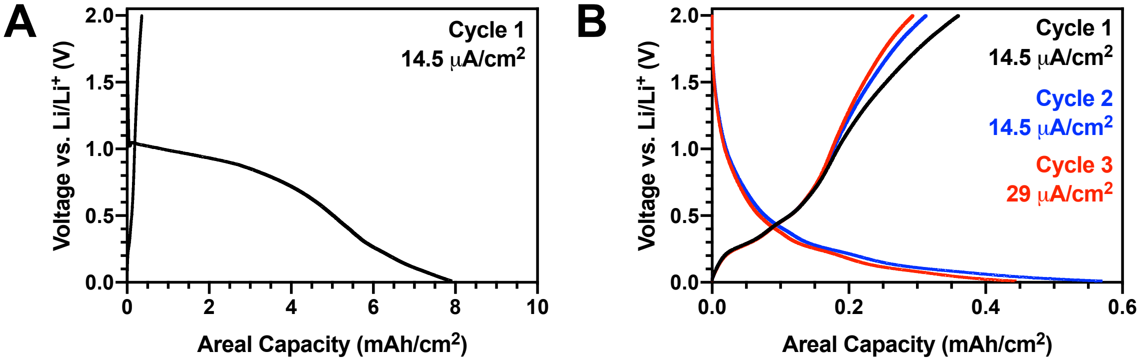

Figure 5.14: A) first cycle and B) subsequent cycle voltage profiles for a non-patterned PECVD Si-CNT electrode.

The voltage profiles for cycling a non-patterned PECVD Si-CNT electrode are presented in Figure 5.14. During the first cycle discharge (Figure 5.14A), there is a large plateau that starts at ~1 V vs. Li/Li$^+$ and makes up the majority of the discharge capacity. This plateau corresponds to solid electrolyte interphase (SEI) formation on the CNT surface and is responsible for the large irreversible first cycle capacity of CNT-based electrodes [66], [94]. This plateau is not visible in the LPCVD electrodes cycled in Chapter 2, as the LPCVD process conformally coats Si on all CNTs in the forest, and is attributed here to the inability of the PECVD process to coat CNTs in the forest interior cell (Figure 5.13D), which leaves them exposed to the electrochemical processes happening in the cell. Due to this irreversible process the first cycle coulombic efficiency is ~5%. Subsequent cycling (Figure 5.14B) shows a low reversible capacity, a low coulombic efficiency of 54% on cycle 2 and 66% on cycle 3, and noticeable capacity fading.

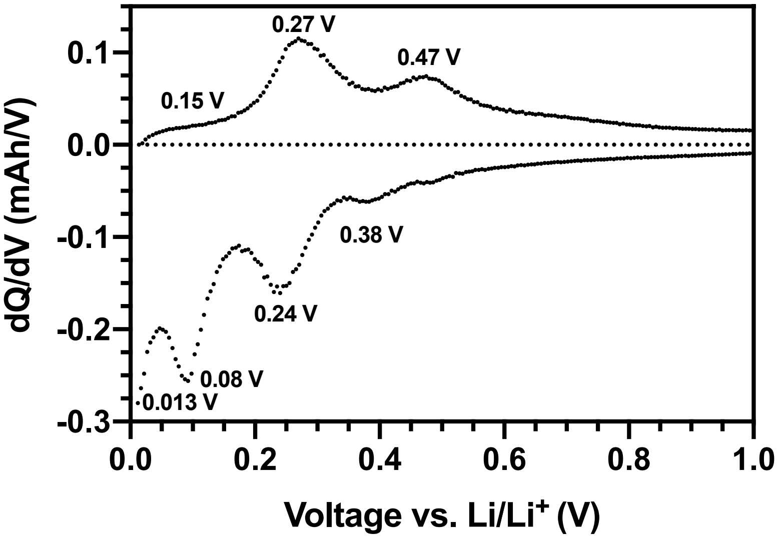

Figure 5.15: Cycle 3 dQ/dV plot for PECVD Si-CNT half-cell.

The voltage profiles for cycle 2 and cycle 3 (Figure 5.14B) contain additional plateaus not present in the LPCVD Si-CNT electrodes of Chapter 2. Similar to the LPCVD Si-CNT electrodes, the PECVD Si-CNT dQ/dV plot in Figure 5.15 shows reduction peaks at ~0.24 V and ~0.08 V that correspond to the formation of a-Li_2Si and a-$Li_{3.5}Si$, and oxidation peaks corresponding to the delithiation of these two phases at ~0.27 V and ~0.47 V [110], [145], [146]. Unlike the LPCVD Si-CNT electrode, the PECVD Si-CNT electrode shows a reduction peak starting at ~0.38 V and ending at ~0.13 V that results from Li^+ intercalation in the graphitic carbon present in the CNTs [243]. This reduction process is tied to an oxidation peak at ~0.15 where the Li^+ de-intercalates from the CNT. The voltage profiles in Figure 5.14B and dQ/dV plot definitively indicate that the PECVD Si-CNT electrode capacity comes both the CNT and Si components. The combination of irreversible CNT lithiation and known issues with Si expansion and contraction explain the low coulombic efficiency, capacity and capacity retention in Figure 5.14.

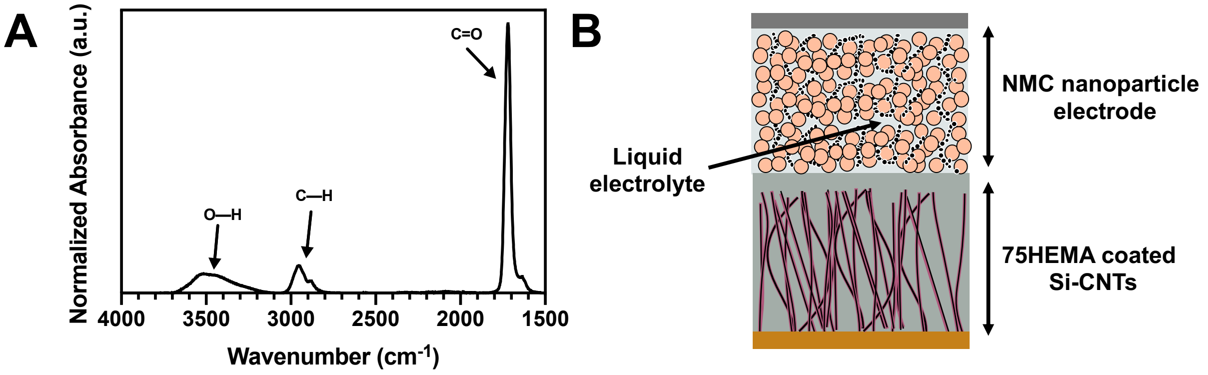

Figure 5.16: A) FTIR spectrum for 75HEMA iCVD thin film and B) schematic of planar NMC/75HEMA/Si-CNT full cell.

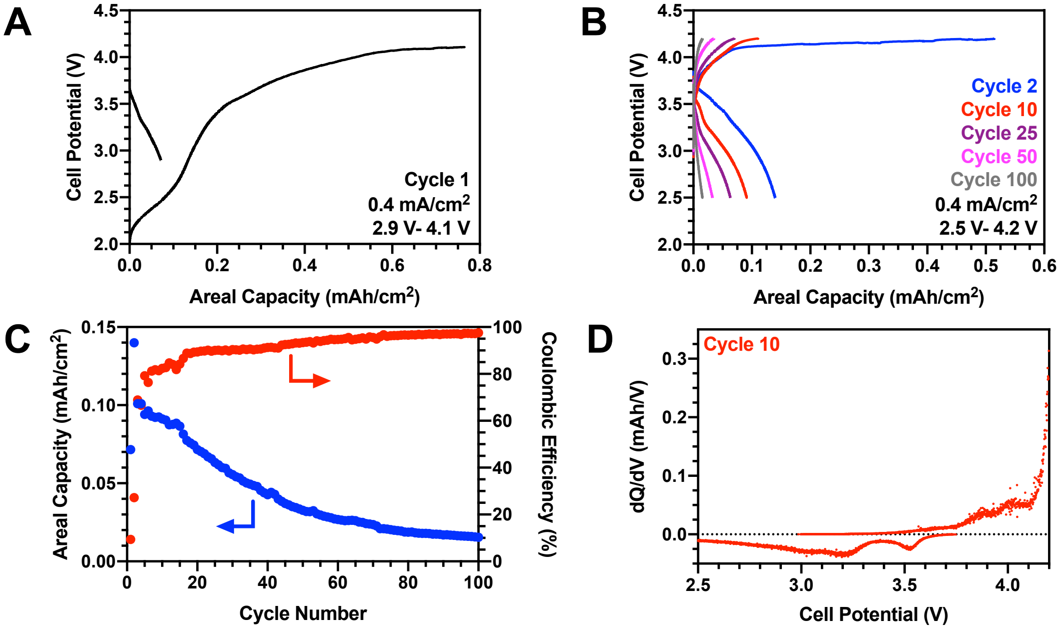

Figure 5.17: Voltage profiles of A) first cycle and B) subsequent cycles, B) areal capacity and coulombic efficiency and D) cycle 10 dQ/dV plot for NMC/75HEMA/Si-CNT full cell.

Following PECVD Si deposition, the non-patterned Si-CNT composite was coated with a ~1 µm thick 75HEMA thin film. Using the same analysis as Chapter 4 for the C=O and O—H peaks in Figure 5.16A gives a HEMA concentration of ~75 mol.%. After the iCVD process, the assembly was brough into the glovebox for NMC slurry and 1 M LiTFSI in DOL electrolyte infiltration. A schematic of the final cell structure is presented in Figure 5.16B, with the thin iCVD film separating the NMC nanoparticle and non-patterned Si-CNT electrodes and liquid electrolyte infiltrated throughout the entire cell. The cycling data for the planar NMC/75HEMA/Si-CNT full cell is presented in Figure 5.17. The first cycle (Figure 5.17A) shows a significant irreversible capacity loss, likely associated with irreversible SEI formation and lithiation of the exposed CNTs, and achieves a discharge capacity of 0.07 mAh/cm^2 when charged to 4.1 V and discharged to 2.9 V at 0.4 mA/cm^2. Upon further cycling at 0.4 mA/cm^2 between 2.5 V and 4.25 V, the usable discharge capacity jumps to 0.14 mAh/cm^2. This is comparable with the 2D planar micro-battery produced by Nathan *et al.* [53] and superior to the 3D cell of Kotobuki et al. [49]. Under these conditions the cell is capable of achieving 100 cycles (Figure 5.17B), although the usable discharge capacity fades upon repeated cycling and the coulombic efficiency is low for the majority of the cell lifetime (Figure 5.17C). The dQ/dV plot for the full cell (Figure 5.17D) is in good agreement with the dQ/dV plot for the PECVD Si-CNT half-cell (Figure 5.15) and other NMC/Si-CNT full cells [244]. This indicates the cell capacity is determined by both the Si and CNT components in the anode and, based on previously described mechanisms, explains the low coulombic efficiency and capacity. This full cell is, to the authors knowledge, the first known demonstrator of an iCVD polymer electrolyte, without the use of an additional separator, in a Li-ion full cell.

5.3.4 Interdigitated NMC/55HEMA/Si-CNT Full Cell

Interdigitated full cell development began by performing an LPCVD Si deposition on a ~100 μm tall CNT forest patterned as an array of pillars with 40 μm diameter and 70 μm center-to-center spacing. The forest was then coated with a ~2.2 μm thick 55HEMA film and, after NMC slurry infiltration, the cell was allowed to soak in 1 M LiTFSI in PC to create the full cell stack pictured in Figure 5.18A.

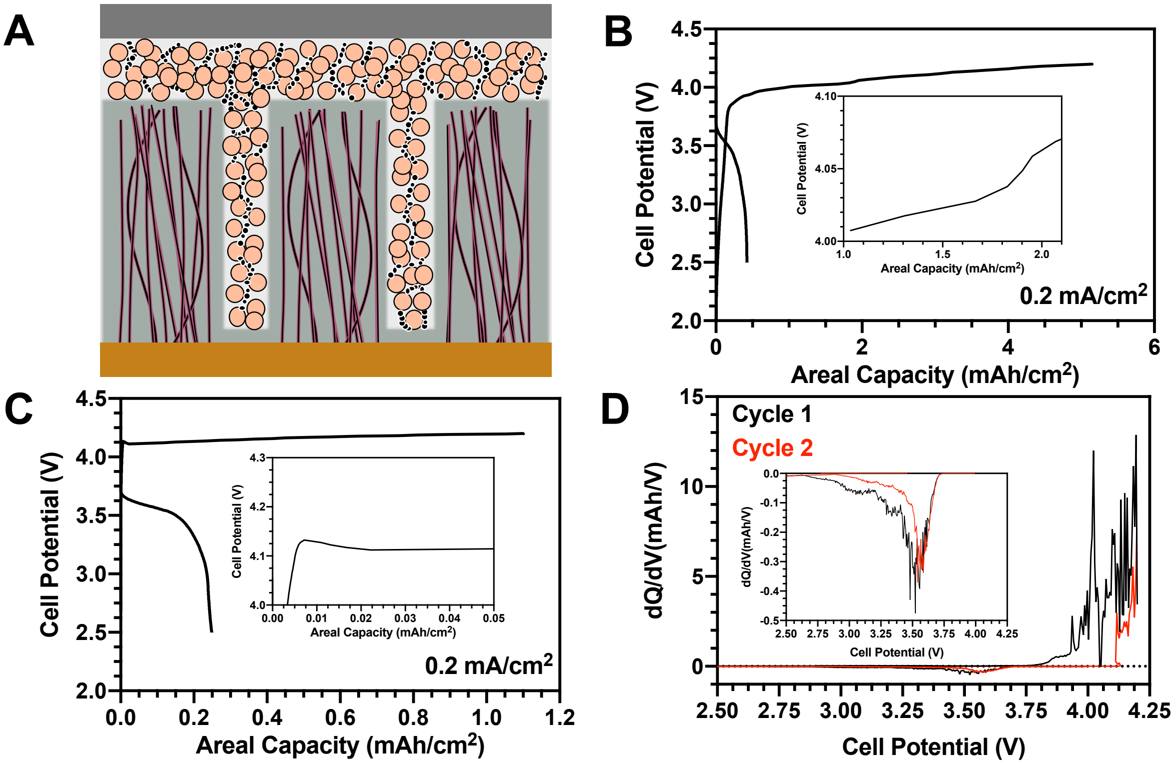

Figure 5.18: A) Schematic of interdigitated NMC/55HEMA/Si-CNT full cell, voltage profiles for B) first cycle with insert showing a kink in the voltage profile and C) second cycle with the insert showing the distinctive , and D) dQ/dV plots for the first two cycles with the insert showing the dQ/dV profile upon discharging.

The cell is successfully charged to 4.2 V and discharged down to 2.5 V at 0.2 mA/cm^2 (Figure 5.18B). The discharge capacity is 0.43 mAh/cm^2 with a coulombic efficiency of ~8%. For the first part of charging the voltage profile is in good agreement with those obtained by other NMC/Si full cells [146], [245]. Upon starting the second cycle (Figure 5.18C) the charging profile is noticeably different. There is an ~200 mV increases in the location of the voltage plateau compared to the first cycle and the appearance of a ~20 mV overpotential before the voltage plateau stabilizes. The shape of the voltage profile is more in line with the cycling behavior of an NMC/Li-metal half-cell [246], [247]. The overpotential in the Figure 5.18C insert can be attributed to the formation of an Li_2CO_3 layer on the NMC particles that impedes ionic transportation [247] or the nucleation overpotential required for Li-plating on the current collector [248]. The difference in the electrochemical process occurring in cycle 1 and cycle 2 is also evident in the dQ/dV plots (Figure 5.18D). Upon charging and discharging cycle 1 shows a dQ/dV profile in line with previous NMC/Si full cells [244], [246], [247]. However, the dQ/dV profile for the second discharge in the Figure 5.18D insert lacks the characteristic Si delithiation peak at ~3.1 V and agrees with the dQ/dV profile for a NMC/Li-metal half-cells [249], [250]. The small difference between the dQ/dV peak at ~3.55 V, and the kink in the cycle one voltage profile (Figure 5.18B insert) makes it difficult to tell if the Li-metal plating process begins in the first cycle or second cycle, but the presence of the dQ/dV Si delithiation peak at ~3.1 V indicates that the Si-CNT electrode is utilized during the first cycle. The cause and location of the Li-plating is currently unknown, but two hypotheses are that it may occur on the Cu foil if the Si-CNTs pillars become detached during cycling, as the inclusion of the NMC eliminates the space typically allotted for Si expansion, or on the stainless-steel spacer if it becomes exposed during cycling. While there is room much for future optimization, this first cycle demonstrates a proof-of-concept for a fully interdigitated CNT-based cell containing an iCVD electrolyte.

5.4 2D Simulations of Idealized Interdigitated CNT Full Cells

This section discusses the development and results of a 2D finite element analysis simulation for a full cell containing a Si-CNT negative electrode, iCVD poly(HEMA-*co*-EGDA)) solid polymer electrolyte and NMC slurry cathode. While there have been some difficulties assembling a full micro-structured CNT cell, the goal of this simulation is to determine the ideal theoretical performance of an interdigitated full cell built with a CNT architecture. All homogeneous 2D simulations in this work were performed using COMSOL's Battery Design Module. The 2D interdigitated designs were discharged at a variety of C-rates and then compared to a 1D simulation of an idealized, state-of-the-art (SOA) lithium-ion cell with thick (~55-65 μm) NMC and graphite electrodes. While not discussed in detail here, the SOA lithium-ion cell discharge simulations and material properties were based upon previous COMSOL simulations [251], with additional values taken from reviews on current lithium-ion full cells [1], [7], [8], [12] and a teardown of Tesla 4680 cell [252].

5.4.1 Interdigitated CNT-battery Geometry and Discharge Parameters

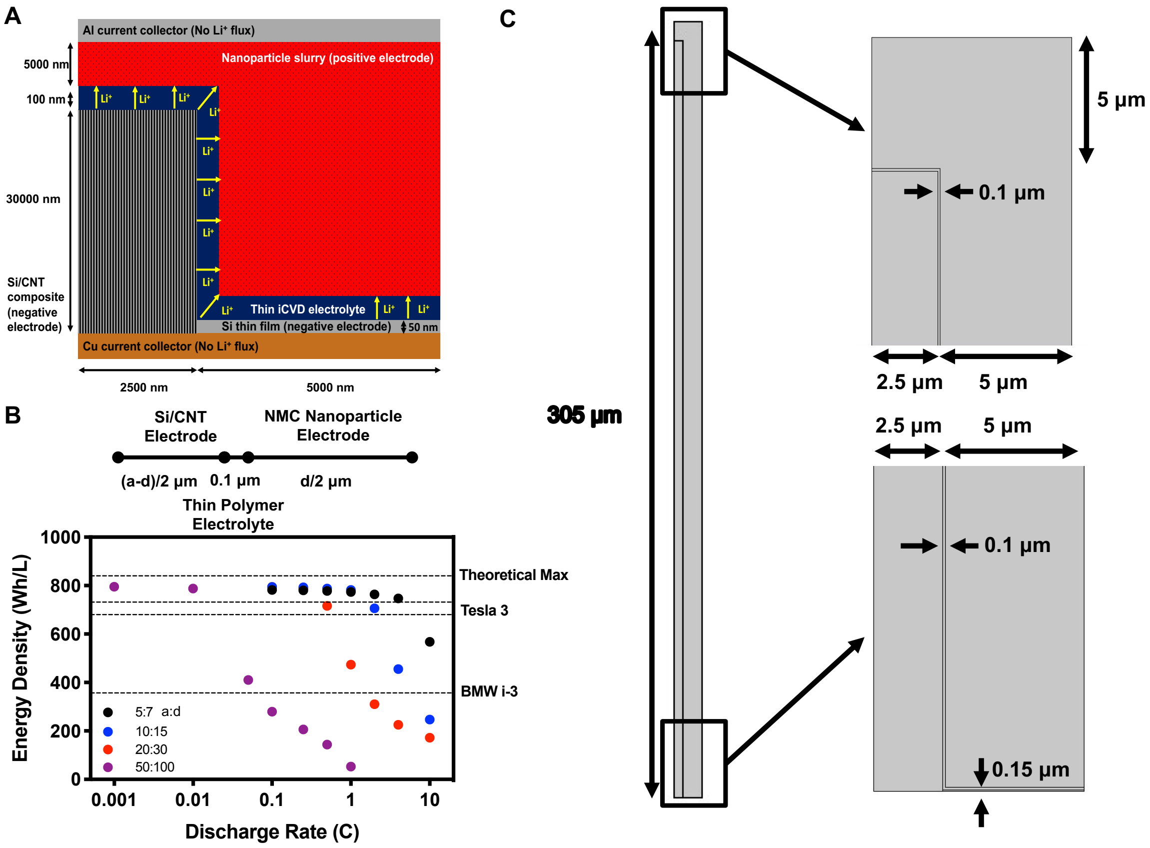

Figure 5.19: A) Schematic of an interdigitated full cell containing a Si-CNT anode, thin iCVD polymer electrolyte and NMC nanoparticle slurry cathode. B) Schematic and Ragone plot for 1D discharge simulation. C) Schematic for 2D discharge simulation of an interdigitated CNT full cell.

A schematic of the interdigitated CNT full cell used in the 2D simulations is presented in Figure 5.19A. The cell consists of an Si-CNT composite electrode, a thin film Si electrode and a NMC nanoparticle electrode. Together the Si-CNT composite and Si thin film comprise the negative electrode (anode) and the NMC nanoparticle slurry acts as the positive electrode (cathode) during discharge. The thickness of the iCVD polymer layer was chosen to be 0.1 µm. As discussed in Chapter 3, and as experimentally and computationally demonstrated by Talin *et al.* [126], the low conductivity of 3D electrolytes is often the cause of non-ideal performance in 3D cells and that this drop in performance can somewhat mitigated by minimizing the electrolyte thickness. In their experimental work on depositing iCVD poly(HEMA-*co*-EGDA) thin films Li *et al*. determined that ~0.1 μm was the minimum thickness to prevent dielectric breakdown in a 4 V system [27]. Ignoring difficulties in fabricating a cell with such a thin electrolyte layer, keeping the iCVD layer at 0.1 μm should help to minimize losses across the electrolyte layer.

The height of the Si-CNT electrode is set at 300 μm, which is the maximum consistently reproducible height of the CNT forests grown directly on Cu foil in Chapter 2. The Si thin film has a thickness 50 nm thickness and spans the bottom of the electrode. This thin Si coating is defect of the CVD processes used to deposit Si on the CNTs, as the nature of CVD ensures that Si will also be deposited on any exposed Cu foil. A series of quick 1D discharge simulations were performed to determine the optimal ratio of widths for the Si-CNT and NMC nanoparticle electrodes. These simulations, presented in Figure 5.19B, show that the interdigitated CNT design begins to overcome the energy and power density trade off when the NMC thickness is reduced to 10 μm with a corresponding Si-CNT thickness of 5 μm. While performance increases by further decreasing the electrode thicknesses to 5 μm and 2.5 μm (5:7) respectively, the 10:15 geometry is much easier to pattern via the photolithography process developed for patterning Cu foils in Chapter 2 and was therefore selected as a nice intermediary between performance and ease of fabrication. Due to the symmetric nature of a pillar or honeycomb design, the 10:15 geometry was modeled with a 2.5 μm thick Si-CNT electrode and a 5 μm thick NMC nanoparticle electrode. Figure 5.19C shows the full 2D geometry utilized in the COMSOL discharge simulations.

For the purpose of calculating the cell mass and volume, a 10 μm Cu foil is assumed to be underneath the Si-CNT and Si films and a 15 μm Al foil is assumed to be above the NMC nanoparticle slurry [7], [12]. In the COMSOL Battery design module the current density is applied to Al foil (top surface in Figure 5.19A and Figure 5.19C) and the Cu foil is selected as the electric ground (bottom surface in Figure 5.19A and Figure 5.19C) [251]. The 1C current is 63.9 A/m^2 and the cells were discharged at various C-rates until the potential reached a minimum of 3 V. For some high C-rates the simulations were terminated early due to issues with the solver reaching a singularity. All simulations were assumed to take place at room temperature (298 K)

5.4.2 Modeling iCVD Solid Polymer Electrolyte

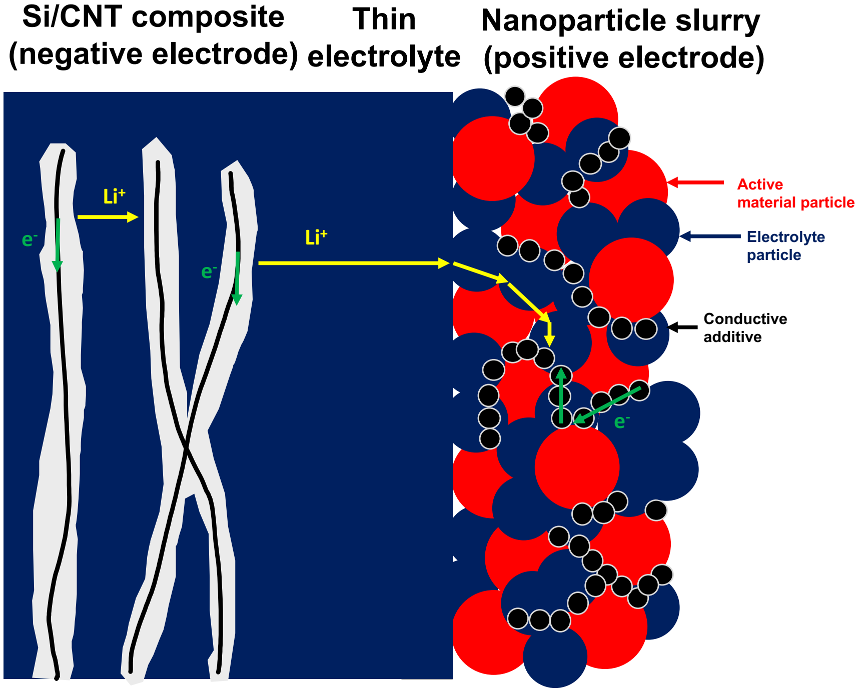

Figure 5.20: Schematic showing Li$^+$ diffusion from through an interdigitated CNT full cell during discharge.

Li-ion diffusion (Figure 5.20) through the iCVD polymer electrolyte layer was modeled using the Nernst-Planck equation. The electrolyte current density (i_{el}) is given by *Eq. 5.1*, where σ_{el} is the ionic conductivity, R is the ideal gas constant, F is the Faraday constant, T is the temperature, t_+ is the transference number of the cation species, φ_{el} is the electrolyte potential and c_{el} is the salt concentration in the electrolyte. This electrolyte current density is then used to calculate the Li$^+$ flux through the electrolyte (J_{el}) by *Eq. 5.2*, where D_{el} is the diffusivity of the salt species through the polymer and is related to the ionic conductivity by *Eq. 5.3*. Here, q_i is the salt species charge and k_B is the Boltzmann constant [126], [253], [254].

$$i_{el} = -\sigma_{el}\nabla\varphi_{el} + \frac{2\sigma_l RT}{F}(1 - t_+)\nabla ln(c_{el}) \quad (Eq.\ 5.1)$$

$$J_{el} = -D_{el}\nabla c_{el} + \frac{i_{el}t_+}{F}\ (Eq.\ 5.2)$$

$$\sigma_l = \frac{q_i^2 c_{el}}{k_B T} D_l\ (Eq.\ 5.3)$$

Table 5.2: Electrolyte properties used to model iCVD poly(HEMA-*co*-EGDA) electrolytes.

Parameter	Value	Units
Ionic conductivity (σ_{el})	6E-4	S/m
Diffusivity of salt species (D_{el})	3E-14	m^2/s
Salt concentration (c_{el})	1500	mol/m^3

Using the films produced in Chapter 2 and by Li *et al.* [27] the ionic conductivity of the iCVD poly(HEMA-*co*-EGDA) thin film is taken to be 6 x 10^{-4} S/m. However, as previously stated, little is known about the other electrochemical properties of these iCVD electrolytes. To fill in the gaps the salt concentration and transference number were estimated using typical values for polymer electrolytes [255] and the diffusion coefficient was estimated using the ionic conductivity and *Eq. 5.3*. These values are tabulated in Table 5.2.

5.4.3 Lithiation Processes of Porous Electrodes

In this work the Si-CNT, Si thin film and NMC nanoparticle electrodes were all modeled as porous electrodes. Charge transfer at the interface between active material and polymer electrolyte was modeled using a Butler-Volmer relationship (*Eq. 5.4*), where the electrode reaction current density (i_{loc}) is a function of the exchange current density (i_o) and the charge transfer coefficient (α) [126], [253]. The exchange current densities for NMC and Si were estimated using values from literature [256] and are presented in Table 5.3. The charge transfer coefficient is assumed to be 0.5. Li^+ transport inside the Si and NMC active material was assumed to occur by diffusional transport only and was governed by Fick's second law (*Eq. 5.5*) [126], [253]. The diffusion coefficients in the solid phase (D_s) for Si and NMC were estimated from literature [8], [126] and are also included in Table 5.3.

$$i_{loc} = i_0 \left(e^{\left(\frac{\alpha F \eta}{RT}\right)} - e^{\left(\frac{-(1-\alpha) F \eta}{RT}\right)} \right) (Eq.\ 5.4)$$

$$\frac{dc_s}{dt} - \nabla(D_s \nabla c_s) = 0\ (Eq.\ 5.5)$$

$$SOC = \frac{c_s}{c_{s,max}}\ (Eq.\ 5.6)$$

Table 5.3: Parameters used to model the materials in the interdigitated CNT battery porous electrodes.

Parameter	Si-CNT electrode	Si thin film	NMC nanoparticle electrode	Units
Exchange current density (*i_o*)	1	1	25	A/m^2
Solid diffusion coefficient (*Ds*)	1E-17	1E-17	4E-16	m^2/s
Maximum solid concentration ($c_{s,max}$)	316870	4316870	49620	mol/m^3
Starting solid concentration (c_{s0})	90500	90500	7450	mol/m^3
Active material thickness (r_p)	50E-9	50E-9	300E-9	m
Electronic conductivity (K_s)	1e7	4.5E-4	10	S/m

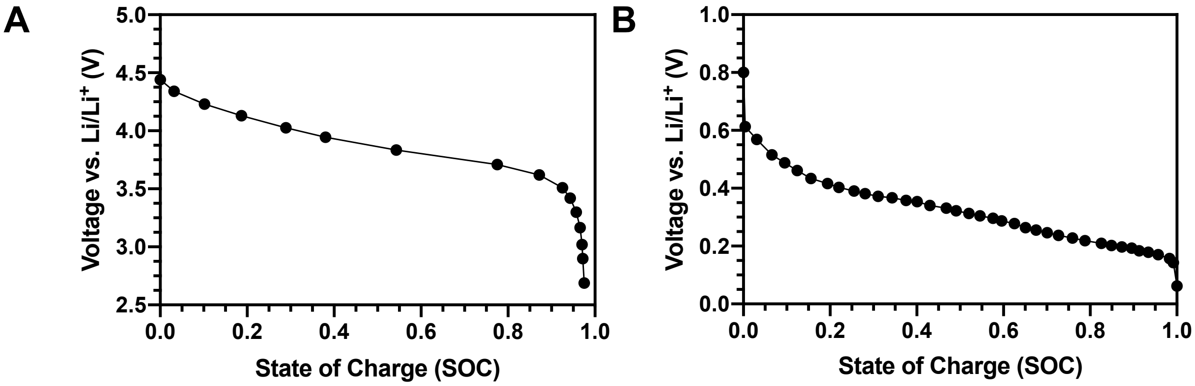

Figure 5.21: Voltage profiles a function of state-of-charge for A) NMC and B) Si utilized in these simulations.

The diffusion through the active material layers is also governed by the solid phase Li^+ concentration (c_s in *Eq. 5.5*). The voltage profiles for NMC and Si during discharge were taken from the COMSOL library and are presented in Figure 5.21, with the state-of-charge (SOC) being determined in *Eq. 5.6* by the solid phase Li^+ concentration and the maximum solid phase Li^+ concentration ($c_{s,max}$) [251]. The well-established maximum solid phase concentrations for NMC and Si were taken from literature and are also included in Table 5.3 [8]. The $c_{s,max}$ values can be converted to the expected Si and NMC specific capacities, ~3600 mAh/g and ~240 mAh/g respectively, by using the Faraday constant and the material's density [8], [246].

Other important electrode parameters included in Table 5.3 are the active material thickness (r_p), electronic conductivity (K_s) and starting solid Li^+ concentration (c_{s0}). For active material thickness, the Si coating on the CNTs and on the Cu foil was taken to be ~50 nm, which is achievable by the CVD processes used in Chapter 2. The NMC particle radius is taken to be 300 nm, very close to the commercially available NMC particles (500-600 nm diameter) used in the slurry infiltration experiments. The electronic conductivity for the Si-CNT electrode was taken to be the conductivity of CNTs [54], while the electrical conductivity of Si was used for the Si thin film [257] and the conductivity of carbon black was used for the NMC nanoparticle electrode [258]. Finally, the starting solid concentrations were such that the Si started at 30% lithiation, in agreement with the micro-battery work of Hur *et al.* [50] and the reversible specific capacity of the Si-CNT electrodes in Chapter 2 (~1100 mAh/g), and the NMC started at 15% lithiation [251].

5.4.4 Porous Electrode Structure

The next step in building the CNT-based interdigitated cell is to adequately describe the unique geometries of the Si-CNT and NMC nanoparticle electrodes. As a homogeneous model, the electrode structure is described by the volume fractions of the electrolyte (ε_{el}), active material

(ε_a) and conductive additive (ε_c). The NMC slurry was modeled using typical literature values to describe the volume fractions of each phase [7], [251], [259]. For the Si-CNT electrode the volume fraction of CNTs set at ~1% and was estimated using a CNT number density of ~4 x 10^9/cm^2 that had been established in previous works [64] and individual CNT radius of 5 nm. The Si volume fraction was determined by assuming the a ~50 nm Si coating on the individual CNTs that is in the realm of what is achievable by the LPCVD process outlined in Chapter 2. For both electrodes the remaining space not taken by active material or conductive additive is assumed to be filled by the iCVD polymer electrolyte. The Si thin film electrode is assumed to be made entirely of Si. The volume fractions for the three electrodes are tabulated in Table 5.4.

Table 5.4: Electrode volume fractions of the active material, conductive additive and electrolyte.

Parameter	Si-CNT electrode	Si thin film	NMC nanoparticle electrode	Units
Electrolyte volume fraction (ε_{el})	0.6	0	0.6	-
Active material volume fraction (ε_s)	0.399	1	0.3	-
Conductive additive volume fraction (ε_c)	0.001	0	0.1	-

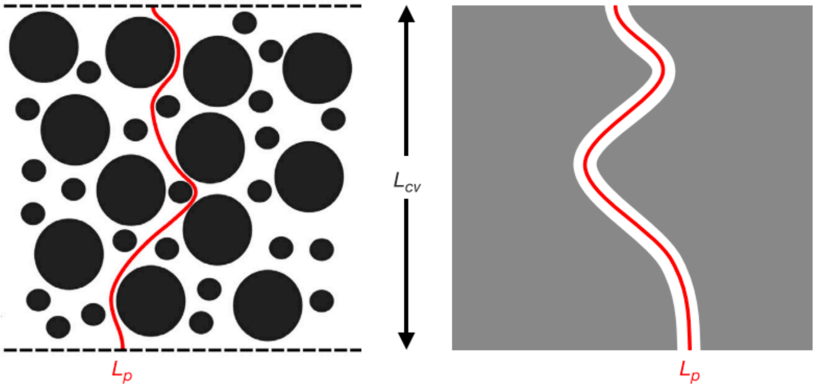

Figure 5.22: Schematic demonstrating how tortuosity often increases the length a species must travel (L_p) when compared to the electrode or membrane thickness (L_{cv}) [260].

$$\sigma_{eff} = \frac{\epsilon \sigma_0}{\tau} \quad (Eq.\ 5.7)$$

$$D_{eff} = \frac{\epsilon D_0}{\tau} \quad (Eq.\ 5.8)$$

$$\tau = \epsilon^{-n} \ (Eq.\ 5.9)$$

In a homogenous model it is also important to consider how the unique electrode structure influences the transport of both Li-ions through the electrolyte phase and electron transport through the conductive additive. As shown in Figure 5.22 the tortuous nature of both slurry and, although to a lesser extent, CNT electrodes result in the distance that either Li-ions or electrons must travel (L_p) often being far greater than the actual electrode thickness (L_{cv}). While these increased distances are not inherently a part of the homogeneous electrode geometry, they can be accounted for by utilizing effective values of the ionic or electrical conductivity (*Eq. 5.7*) or diffusion coefficient (*Eq. 5.8*). Here, the tortuosity (τ) is included to modify the transport property in a way that encapsulates the species path [260], [261].

Table 5.5: Bruggeman exponents to incorporate electrode tortuosity into the 2D interdigitated CNT battery model.

Parameter	Si-CNT electrode	Si thin film	NMC nanoparticle electrode	Units
Electronic conductivity Bruggeman exponent	N/A	N/A	2.3	-
Ionic conductivity Bruggeman exponent	2.3	N/A	2.3	-
Ionic diffusivity Bruggeman exponent	2.3	N/A	2.3	-

The next question that arises is how to estimate the tortuosity. In composite electrodes this is typically done by a Bruggeman relationship (*Eq. 5.9*) where the tortuosity is determined by the volume fraction of the media where the transport is taking place and an exponent *(n*). Typically the value of *n* is set to 0.5 but experimental works have shown that transport in battery slurries is better approximated by setting *n* equal to 2.3 [261]. The NMC nanoparticle electrode was assumed to use this modified Bruggeman relationship for the ionic conductivity, electrolyte diffusion coefficient and electrical conductivity. The same relationship was applied to the ionic conductivity and electrolyte diffusion coefficient in the Si-CNT electrode to represent the path that Li^+ ions would have to take as they snaked between the aligned nanotubes but the electronic conductivity was not modified to represent the direct electrical connection between the Si active material and current collector via the aligned CNT. No modifications were applied to the Si thin film electrode as it is a non-composite electrode. The Bruggeman coefficients used in this work are compiled with the volume fractions in Table 5.5.

5.4.5 Discharge Simulation Results

Discharge simulations at 0.1C, 0.5C, 1C and 2C and 6C were performed for the 2D interdigitated CNT battery presented in Figure 5.19C. The voltage profiles for these discharges are presented in Figure 5.23A. At low C-rates (0.1-1C) the CNT batteries exhibit an areal capacity greater than 60 Ah/m^2 (6 mAh/cm^2), which is competitive with state-of-the-art lithium-ion cells. This cell retains ~74% and 34% of its total capacity at 2C and 6C respectively. Previous 1D simulations indicate that the majority of this capacity loss comes from increased concentration overpotential and ohmic losses across the low conductivity iCVD polymer electrolyte at these increased current densities [251].

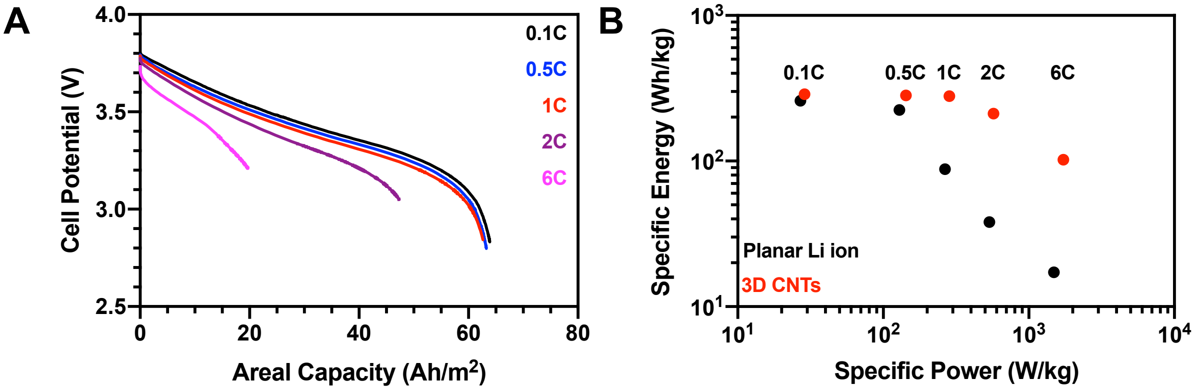

Figure 5.23: A) discharge voltage profiles and B) Ragone plot for 2D interdigitated CNT-based battery.

$$E_{sp} = \frac{1}{M}\int_0^{t_d} IV\, dt \; (Eq.\ 5.10)$$

$$P_{sp} = \frac{E_{sp}}{t_d} \; (Eq.\ 5.11)$$

The discharge curves in Figure 5.23A were used to calculate the specific energy and power density of the interdigitated CNT-based cell at each C-rate. The specific energy density (E_{sp}) was calculated by *Eq. 5.10*, where I is the discharge current, V is the cell voltage, M is the total cell mass, including Al and Cu current collectors, and t_d is the total discharge time. The specific power (P_{sp}) is then calculated by dividing the specific energy by the discharge time (*Eq. 5.11*) [261]. Figure 5.23B presents a Ragone plot for a 300 µm tall CNT cell and a state-of-the-art lithium-ion cell with 65 µm thick electrodes. At low C-rates the interdigitated CNT-based cell has an energy density approaching 290 Wh/kg, which is on par with the state-of-the-art lithium-ion cells [7], [252]. At higher C-rates the interdigitated CNT battery is able to utilize a significantly large portion of its energy density than the thick electrode lithium-ion cell, which begins to experience significant performance decreases at currents as low as 1C. This demonstrates the ability of the interdigitated design to allow for high specific energy and power densities due to the decreased diffusion Li^+ distance that is achieved by the thin iCVD polymer electrolyte layer and interdigitated structure.

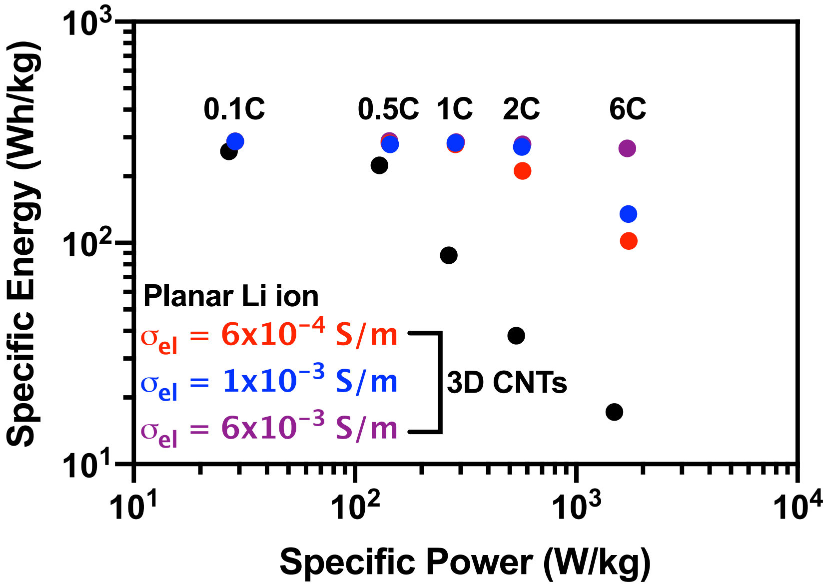

Figure 5.24: Ragone plot for interdigitated CNT-batteries with varying ionic conductivity.

Lastly, a parametric study was performed to determine the impact of ionic conductivity on interdigitated CNT-battery performance. Figure 5.24 shows the Ragone plot as the ionic conductivity is increased from 6 x 10^{-4} S/m to 10^{-3} S/m and eventually to 6 x 10^{-3} S/m. These results show that an order of magnitude increase to the iCVD polymer electrolyte conductivity enables the interdigitated CNT-cell to access its entire energy supply at currents as high as 6C. This also demonstrates that interdigitated full cells do not require electrolytes with ionic conductivities that match those used in planar systems. Due to the decreased diffusion distance between the electrodes the interdigitated CNT-battery is able to achieve peak performance using an electrolyte with an ionic conductivity (6 x 10^{-3} S/m) that is two to three orders of magnitude lower than the ionic conductivities of conventional liquid and solid electrolytes (10^{-1} to 10^{0} S/cm). This lowering of the ionic conductivity requirement for suitable 3D full cell performance is critical in furthering 3D battery development as, as was outlined in Chapter 2, development of suitable 3D electrolytes has been exceptionally challenging for the field.

5.5 Concluding Remarks

This work in this chapter has investigated the use of iCVD poly(HEMA-*co*-EGDA) thin films as polymer electrolyte and separator layers in full cells using an infiltrated NMC nanoparticle slurry and a Si-CNT electrode scaffold. In cells containing slurry infiltrated electrodes the EGDA crosslinker composition in the poly(HEMA-*co*-EGDA) film is a critical parameter for ensuring film mechanical stability. If the crosslinking concentration is too low, as in the case of a 95HEMA film, the iCVD polymer layer will dissolve during the slurry infiltration. This damages the underlying Si-CNT structure and results in a high short circuit probability. Increasing the crosslinker concentration improves the iCVD film stability, but as discussed in Chapter 2 largely decreases the ionic conductivity of the iCVD layer. This can be partially mitigated by impregnating the cell stack with a liquid electrolyte, which also ensures ionic conductivity through the NMC nanoparticle slurry. Future works should include understanding the effect of liquid electrolyte infiltration on ionic conductivity and determining the optimal EGDA crosslinker composition for high performance ionic conductivity and mechanical stability.

Using this iCVD poly(HEMA-*co*-EGDA) and liquid electrolyte combination two full cells were developed. First, a planar NMC/75HEMA/Si-CNT electrode was cycled for 100 cycles at 0.4 mA/cm^2. The dQ/dV plots demonstrate that the cell capacity is affected by both components in the Si-CNT positive electrode. The largely irreversible CNT lithiation, combined with the low PECVD Si loading, contribute to the low areal capacity and significant capacity fade upon repeated cycling. Next, a similar strategy is utilized to produce an NMC/55HEMA/Si-CNT interdigitated full cell built upon a CNT pillar array. This cell is able to survive one charge-discharge cycle before suffering from Li-plating issues. Further investigation is required to determine the origins of the Li-plating issues, although it is hypothesized that mechanical damage induced to high capacity LPCVD Si-CNTs during lithiation exposes Cu current collector or stainless-steel spacer. These two cells demonstrate the first known use of an iCVD polymer electrolyte layer in a full cell and a proof-of-concept for an interdigitated CNT battery.

Lastly, after performing a 1D parametric sweep to determine the appropriate starting dimensions, a 2D FEA simulation is performed in the COMSOL Battery Design module for an idealized interdigitated CNT full cell. The results show that at the current ionic conductivity achievable by conformal 3D electrolytes on these CNT full cells can offer specific energies competitive with existing Li-ion cells while offering a superior specific power. Additional specific power improvement can be obtained by further increases to the 3D electrolyte conductivity which enables full capacity utilization at high C-rates, although significant effort would be needed on the cell fabrication side to experimentally create and test such cells.

THIS PAGE IS LEFT INTENTIONALLY BLANK

Chapter 6- Conclusions, Contributions and Outlook

6.1 Conclusions

The overarching goal of this thesis was to demonstrate that vertically aligned carbon nanotube (CNT) forests could serve as a building block for thick electrode and, ultimately, 3D full cell development. Making this concept a reality began by developing a robust process to grow the patternable aligned CNTs directly on Cu foils. This was achieved by first coating Cu foil with a catalyst stack that incorporated a W diffusion barrier and could be patterned to control the resulting CNT microstructure. The catalyst coated Cu foils were then subjected to an atmospheric chemical vapor deposition process that, by precisely controlling the furnace moisture content, enabled the robust and repeatable growth of > 200 μm tall forests with honeycomb patterns. These CNT forests were then coated with Si by a low pressure chemical vapor deposition process (LPCVD) capable of achieving conformal coatings on the individual CNTs and allowing for high areal Si mass loadings.

The Si-CNT composites served as thick electrodes in Swagelok half-cells against a Li-metal foil counter electrode. Here, the honeycomb pattens were crucial in reducing capacity fading by providing room to accommodate the Si volume expansion and contraction that occurs during cycling. These honeycomb Si-CNT electrodes exhibited an areal capacity (~19.7 mAh/cm^2) approximately five times large than state-the-art lithium-ion cells and the cell lifetime could be extended by incorporating a fluoroethylene carbonate contain electrolyte. These honeycomb Si-CNT electrodes offer a desirable combination high areal, specific, retained and volumetric capacity when compared with other thick and 3D electrode designs.

After demonstrating this high-level performance for thick electrodes, the focus turns towards using the Si-CNT composite as a scaffold for interdigitated full cell development. Here, an initiated chemical vapor deposition (iCVD) process coats the Si-CNT composite with a poly(hydroxyethyl methacrylate-*co*-ethylene glycol diacrylate) (poly(HEMA-*co*-EGDA)) polymer. Careful control over the iCVD process pressure enables conformal poly(HEMA-*co*-EGDA) coating of both the individual Si-CNTs and the entire forest microstructure. When doped with Li-salts the ionic conductivity of these poly(HEMA-*co*-EGDA) thin films is on the order of 10^{-5} S/cm and amongst the highest recorded for conformal electrolyte technologies.

Full cells containing a Si-CNT electrode and iCVD electrolyte were produced by incorporating a $LiNi_{0.33}Mn_{0.33}Co_{0.33}O_2$ slurry-based electrode. The degree of crosslinking in the poly(HEMA-*co*-EDGA) electrolyte was a crucial parameter to prevent iCVD film dissolution during slurry infiltration. By incorporating adequate crosslinker, and soaking the entire cell stack in liquid electrolyte to ensure continuous ionic conductivity, a planar NMC/poly(HEMA-*co*-EDGA)/Si-CNT full cell was able to successfully complete 100 cycles. For an interdigitated NMC/poly(HEMA-*co*-EDGA)/Si-CNT, X-ray microscopy demonstrated that the NMC nanoparticle slurry had been successfully infiltrated between the CNT-structured pillars and Si lithiation and delithiation was observed on the first cycle to demonstrate a proof-of-concept for an interdigitated CNT-based full cell.

6.2 Original Contributions

The work in this thesis made the following original contributions to knowledge:

- Developed a robust process for growing tall CNTs directly on Cu foil by coupling a previously developed catalyst stack with optimized furnace growth conditions. A high furnace moisture content was critical to prevent amorphous carbon buildup from prematurely terminating CNT growth.

- Utilized these tall CNTs to produced patterned Si-CNT electrodes that increased Si loading and reduced capacity fading compared to non-patterned CNT electrodes in this work and others. The honeycomb Si-CNT electrodes exhibit a desirable combination of specific, areal and volumetric capacity when compared with other thick and structured electrodes.
- Controlled iCVD parameters to deposit poly(HEMA-*co*-EGDA) film with high conformality at both the individual CNT and the CNT forest exterior. Thin 90 mol.% HEMA films have an ionic conductivity amongst the highest reported for conformal electrolytes with nanoscale control.
- Produced planar and interdigitated NMC/poly(HEMA-*co*-EDGA)/Si-CNT full cell demonstrators that are the first known use of an iCVD electrolyte in a full cell application. This is a proof-of-concept for using vertically aligned CNTs as a scaffold for 3D battery development.

6.3 Outlook and Future Works

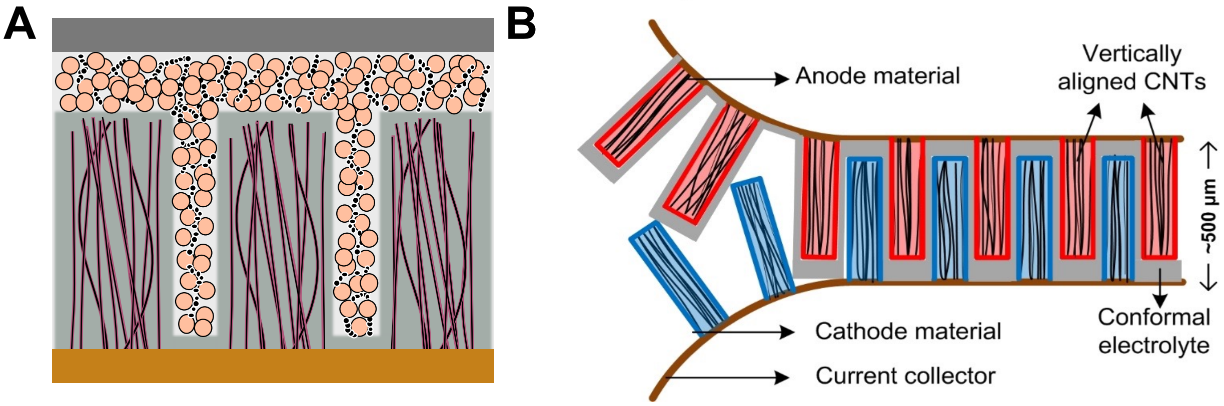

Figure 6.1: A) schematic of the interdigitated CNT full cell produced in this work and B) schematic of idealized interdigitated full cell produced by roll-to-roll processing.

The work in this thesis started with the growth of vertically aligned CNTs on Cu foils for use as thick Li-ion electrodes and culminated in the production of a proof-of-concept interdigitated full cell containing a patterned Si-CNT electrode, an iCVD polymer electrolyte and an NMC nanoparticle electrode (Figure 6.1A). While this is the first known demonstrated use of CNTs as a scaffold for 3D full cell development and iCVD electrolyte implementation in a full cell, the remainder of this section discusses the numerous avenues that can be investigated to improve both thick electrode and interdigitated full cell design and performance (Figure 6.1B).

1. Catalyst stack composition and patterning.
    a. The catalyst stack utilized in this work was based on one successfully used in a previous work [71]. While electronic connection between the Cu foil and CNTs via this catalyst stack has been demonstrated, further decreases in cell resistance may be achieved by optimizing the catalyst stack through reduction or elimination of the insulating Al_2O_3 layers.
    b. While the maskless lithography process is a versatile technique that allows for rapid modification of structured electrode designs, it is still a batch process that requires numerous steps. Implementation of roll-to-roll compatible patterning processes, such as laser-based electrostatic printing of catalyst particles [58] or laser ablation of catalyst particles of monolithic CNT forests [262], would allow for scalable electrode patterning.
2. Vertically aligned CNT growth on metal foils.
    a. The CNT growth in this thesis was performed using much higher moisture levels (~2400 ppm vs. ~220 ppm) then previous CNT growth works [61], [71]. While the robust CNT growth was attributed to the high moisture level, it is known that

    excessive moisture levels can begin to have detrimental effects on CNT growth. Further investigations should be performed at moisture levels between 220 ppm and 2400 ppm to determine the optimal moisture concentration for tall high quality CNT growth.

    b. Processes should be developed for tall CNT growth on Al foils to enable the use of thick 3D CNT cathodes that complement the Si-CNT anodes fabricated in this work.

3. Active material deposition on aligned CNTs.
    a. Due to laboratory user restrictions and cost the LPCVD Si depositions in this thesis were performed using a recipe optimized for thin film deposition on Si wafers. Increases in deposited Si quantity and more uniform distribution throughout the CNT forests may be achieved by performing studies that investigate the effect of reactor temperature and precursor gas pressure on Si deposition. A more extensive study on the CNT plasma etching step prior to Si-deposition may result in better Si uniformity and thickness by optimizing
    b. The CVD processes used in this work are energy intensive processes due high temperature and active vacuum requirements required to run the reactors. Alternative, less energy intensive processes, such as electrodeposition [263], should be investigated for producing Si-CNT composites.
    c. Processes can be developed for the deposition of cathode active materials, by processes such as atomic layer deposition [264] or nanoparticle infiltration [77], on aligned CNT forests on cathode compatible metal foils.
4. 3D electrolytes on aligned CNTs.

    a. The iCVD poly(HEMA-*co*-EGDA) electrolytes in this work have an ionic conductivity that is amongst the highest reported for conformal, nanoscale electrolyte. Future works should seek to uncover a better understanding of the mechanisms behind ion conduction in these copolymer films and how film properties such as molecular weight and salt concentration influence the observed conductivity. Additional electrochemical parameters, such as the electrochemical stability window, should also be addressed.
    b. Poly(HEMA-*co*-EGDA) is a rather unconventional electrolyte material that was selected in this work due to a previously demonstrated conductivity and reactor access. However, iCVD is a powerful and versatile technique for electrolyte deposition; so works investigating iCVD deposition of conventional electrolyte materials such as polyethylene oxide [265] may significantly improve the outlook of 3D battery designs.
5. Second electrode incorporation.
    a. The full cell produced in this work incorporated a NMC nanoparticle cathode (Figure 6.1A). Further advancements in performance should look to incorporate a CNT-based cathode (Figure 6.1B) as the NMC nanoparticle electrode lacks many of the structural advantages of a CNT-based electrode.
    b. As shown in Figure 6.1B the ideal 3D design would incorporate the solid polymer electrolyte throughout both electrodes, eliminating the need for the liquid electrolyte that ensures ionic conductivity through the NMC nanoparticle cathode in Figure 6.1A. This issue is not unique to the 3D CNT-based design, as maintaining ionic conductivity through the cathode is also a challenge for planar solid state cells

    [26]. While the "zip tie" fabrication in Figure 6.1B might be unfeasible to fabricate, pre-alignment of CNT electrodes, followed by an iCVD electrolyte deposition through the entire cell may allow for 3D full solid polymer cells.

6. System level fabrication and integration.
    a. Roll-to-roll processing steps, starting with those previously demonstrated for vertically aligned CNTs [57], should be investigated to determine the potential scale-up of all 3D electrode and full cell designs.
    b. The unique mechanical properties of coated CNT forests in compression [56] may serve as an interesting avenue to improve cell mechanical stability and for the possible use of aligned CNT electrodes to enable structural integration of cells. This would allow aligned CNTs to serve as the core of multifunctional energy storage devices that result in significant mass and volume savings at the pack and system level [266], [267].

THIS PAGE IS LEFT INTENTIONALLY BLANK

References

[1] T. Placke, R. Kloepsch, S. Dühnen, and M. Winter, “Lithium ion, lithium metal, and alternative rechargeable battery technologies: the odyssey for high energy density,” *J. Solid State Electrochem.*, vol. 21, no. 7, pp. 1939–1964, 2017, doi: 10.1007/s10008-017-3610-7.

[2] M. Armand and J. M. Tarascon, “Issues and challenges facing rechargeable lithium ion batteries,” *Nature*, vol. 414, no. November, pp. 359–367, 2001, doi: 10.1038/35104644.

[3] T. S. Arthur *et al.*, “Three-dimensional electrodes and battery architectures,” *MRS Bull.*, vol. 36, no. 7, pp. 523–531, 2011, doi: 10.1557/mrs.2011.156.

[4] M. Roberts *et al.*, “3D lithium ion batteries - From fundamentals to fabrication,” *J. Mater. Chem.*, vol. 21, no. 27, pp. 9876–9890, 2011, doi: 10.1039/c0jm04396f.

[5] M.-K. Song, S. Park, F. M. Alamgir, J. Cho, and M. Liu, “Nanostructured electrodes for lithium-ion and lithium-air batteries: the latest developments, challenges, and perspectives,” *Mater. Sci. Eng. R Reports*, vol. 72, no. 11, pp. 203–252, Nov. 2011, doi: 10.1016/j.mser.2011.06.001.

[6] X. B. Cheng, R. Zhang, C. Z. Zhao, and Q. Zhang, “Toward Safe Lithium Metal Anode in Rechargeable Batteries: A Review,” *Chem. Rev.*, vol. 117, no. 15, pp. 10403–10473, 2017, doi: 10.1021/acs.chemrev.7b00115.

[7] A. Ulvestad, “A Brief Review of Current Lithium Ion Battery Technology and Potential Solid State Battery Technologies,” 2018, doi: https://doi.org/10.48550/arXiv.1803.04317.

[8] N. Nitta, F. Wu, J. T. Lee, and G. Yushin, “Li-ion battery materials: Present and future,” *Mater. Today*, vol. 18, no. 5, pp. 252–264, 2015, doi: 10.1016/j.mattod.2014.10.040.

[9] “Specification of Product for Lithium-ion Rechargeable Cell, Model: ICR18650-32A,” 2011.

[10] J. Janek and W. G. Zeier, “A solid future for battery development,” *Nat. Energy*, vol. 1, p. 16141, 2016, doi: 10.1038/nenergy.2016.141.

[11] V. Etacheri, R. Marom, R. Elazari, G. Salitra, and D. Aurbach, “Challenges in the development of advanced Li-ion batteries: A review,” *Energy Environ. Sci.*, vol. 4, no. 9, pp. 3243–3262, 2011, doi: 10.1039/c1ee01598b.

[12] R. Schmuch, R. Wagner, G. Hörpel, T. Placke, and M. Winter, “Performance and cost of materials for lithium-based rechargeable automotive batteries,” *Nat. Energy*, vol. 3, no. 4, pp. 267–278, 2018, doi: 10.1038/s41560-018-0107-2.

[13] G. E. Blomgren, “The Development and Future of Lithium Ion Batteries,” *J. Electrochem. Soc.*, vol. 164, no. 1, pp. A5019–A5025, 2017, doi: 10.1149/2.0251701jes.

[14] “‘Advanced Battery Development III-USABC Battery Development Project,’” 2013. [Online]. Available: https://www.energy.gov/sites/prod/files/2014/05/f15/APR13_Energy_Storage_d_III_Adv_Battery_Dev_0.pdf.

[15] P. G. Bruce, S. A. Freunberger, L. J. Hardwick, and J. M. Tarascon, “LigO2 and LigS batteries with high energy storage,” *Nat. Mater.*, vol. 11, no. 1, pp. 19–29, 2012, doi: 10.1038/nmat3191.

[16] A. Varzi, R. Raccichini, S. Passerini, and B. Scrosati, “Challenges and prospects of the role of solid electrolytes in the revitalization of lithium metal batteries,” *J. Mater. Chem. A*, vol.

4, no. 44, pp. 17251–17259, 2016, doi: 10.1039/c6ta07384k.

[17] B. Liu, J. G. Zhang, and W. Xu, "Advancing Lithium Metal Batteries," *Joule*, vol. 2, no. 5, pp. 833–845, 2018, doi: 10.1016/j.joule.2018.03.008.

[18] M. T. McDowell, S. W. Lee, W. D. Nix, and Y. Cui, "25th anniversary article: Understanding the lithiation of silicon and other alloying anodes for lithium-ion batteries," *Adv. Mater.*, vol. 25, no. 36, pp. 4966–4985, 2013, doi: 10.1002/adma.201301795.

[19] J. W. Choi and D. Aurbach, "Promise and reality of post-lithium-ion batteries with high energy densities," *Nat. Rev. Mater.*, vol. 1, p. 16013, 2016, doi: 10.1038/natrevmats.2016.13https://www.nature.com/articles/natrevmats201613#supplementary-information.

[20] K. Takada, "Progress in solid electrolytes toward realizing solid-state lithium batteries," *J. Power Sources*, vol. 394, no. February, pp. 74–85, 2018, doi: 10.1016/j.jpowsour.2018.05.003.

[21] F. Zheng, M. Kotobuki, S. Song, M. O. Lai, and L. Lu, "Review on solid electrolytes for all-solid-state lithium-ion batteries," *J. Power Sources*, vol. 389, no. February, pp. 198–213, 2018, doi: 10.1016/j.jpowsour.2018.04.022.

[22] Z. Zhang *et al.*, "New horizons for inorganic solid state ion conductors," *Energy Environ. Sci.*, vol. 11, no. 8, pp. 1945–1976, 2018, doi: 10.1039/c8ee01053f.

[23] W. Zhao, J. Yi, P. He, and H. Zhou, "Solid-State Electrolytes for Lithium-Ion Batteries: Fundamentals, Challenges and Perspectives," *Electrochem. Energy Rev.*, vol. 2, no. 4, pp. 574–605, 2019, doi: 10.1007/s41918-019-00048-0.

[24] L. Fan, S. Wei, S. Li, Q. Li, and Y. Lu, "Recent Progress of the Solid-State Electrolytes for High-Energy Metal-Based Batteries," *Adv. Energy Mater.*, vol. 8, no. 11, pp. 1–31, 2018, doi: 10.1002/aenm.201702657.

[25] L. Yue *et al.*, "All solid-state polymer electrolytes for high-performance lithium ion batteries," *Energy Storage Mater.*, vol. 5, pp. 139–164, 2016, doi: 10.1016/j.ensm.2016.07.003.

[26] F. Hao, F. Han, Y. Liang, C. Wang, and Y. Yao, "Architectural design and fabrication approaches for solid-state batteries," *MRS Bull.*, vol. 43, no. 10, pp. 775–781, 2018, doi: 10.1557/mrs.2018.211.

[27] W. Li, L. C. Bradley, and J. J. Watkins, "Copolymer Solid-State Electrolytes for 3D Microbatteries via Initiated Chemical Vapor Deposition," *ACS Appl. Mater. Interfaces*, vol. 11, pp. 5668–5674, 2019, doi: 10.1021/acsami.8b19689.

[28] L. Chen, S. Venkatram, C. Kim, R. Batra, A. Chandrasekaran, and R. Ramprasad, "Electrochemical Stability Window of Polymeric Electrolytes," *Chem. Mater.*, vol. 31, no. 12, pp. 4598–4604, 2019, doi: 10.1021/acs.chemmater.9b01553.

[29] N. Chen *et al.*, "Nanoscale, conformal polysiloxane thin film electrolytes for three-dimensional battery architectures," *Mater. Horizons*, vol. 2, no. 3, pp. 309–314, Apr. 2015, doi: 10.1039/C4MH00246F.

[30] J. Lau, R. H. DeBlock, D. M. Butts, D. S. Ashby, C. S. Choi, and B. S. Dunn, "Sulfide Solid Electrolytes for Lithium Battery Applications," *Adv. Energy Mater.*, vol. 8, no. 27, pp. 1–24, 2018, doi: 10.1002/aenm.201800933.

[31] Y. Zhu, X. He, and Y. Mo, "Origin of Outstanding Stability in the Lithium Solid Electrolyte Materials: Insights from Thermodynamic Analyses Based on First-Principles Calculations," *ACS Appl. Mater. Interfaces*, vol. 7, no. 42, pp. 23685–23693, 2015, doi: 10.1021/acsami.5b07517.

[32] W. D. Richards, L. J. Miara, Y. Wang, J. C. Kim, and G. Ceder, “Interface Stability in Solid-State Batteries,” *Chem. Mater.*, vol. 28, no. 1, pp. 266–273, 2016, doi: 10.1021/acs.chemmater.5b04082.

[33] J. Schnell, F. Tietz, C. Singer, A. Hofer, N. Billot, and G. Reinhart, “Prospects of production technologies and manufacturing costs of oxide-based all-solid-state lithium batteries,” *Energy Environ. Sci.*, vol. 12, no. 6, pp. 1818–1833, 2019, doi: 10.1039/c8ee02692k.

[34] Y. Kuang, C. Chen, D. Kirsch, and L. Hu, “Thick Electrode Batteries: Principles, Opportunities, and Challenges,” *Adv. Energy Mater.*, vol. 9, no. 33, pp. 1–19, 2019, doi: 10.1002/aenm.201901457.

[35] H. Sun *et al.*, “Hierarchical 3D electrodes for electrochemical energy storage,” *Nat. Rev. Mater.*, vol. 4, no. 1, pp. 45–60, 2019, doi: 10.1038/s41578-018-0069-9.

[36] J. W Long, B. Dunn, D. R Rolison, and H. S White, “Three-Dimensional Battery Architectures,” *Chem. Rev.*, vol. 104, pp. 4463–4492, 2004, doi: 10.1021/cr020740l.

[37] A. J. Pearse *et al.*, “Three-Dimensional Solid-State Lithium-Ion Batteries Fabricated Via Conformal Vapor-Phase Chemistry,” *ACS Nano*, vol. 12, no. 5, pp. 4286–4294, 2018.

[38] J. F. M. Oudenhoven, L. Baggetto, and P. H. L. Notten, “All-solid-state lithium-ion microbatteries: A review of various three-dimensional concepts,” *Adv. Energy Mater.*, vol. 1, no. 1, pp. 10–33, 2011, doi: 10.1002/aenm.201000002.

[39] R. W. Hart, H. S. White, B. Dunn, and D. R. Rolison, “3-D microbatteries,” *Electrochem. commun.*, vol. 5, no. 2, pp. 120–123, 2003, doi: 10.1016/S1388-2481(02)00556-8.

[40] C. K. Chan *et al.*, “High-performance lithium battery anodes using silicon nanowires,” *Nat. Nanotechnol.*, vol. 3, p. 31, 2007, doi: 10.1038/nnano.2007.411https://www.nature.com/articles/nnano.2007.411#supplementary-information.

[41] P. H. L. Notten, F. Roozeboom, R. A. H. Niessen, and L. Baggetto, “3-D Integrated All-Solid-State Rechargeable Batteries,” *Adv. Mater.*, vol. 19, no. 24, pp. 4564–4567, 2007, doi: 10.1002/adma.200702398.

[42] F. Chamran, Y. Yeh, H. Min, B. Dunn, and C. Kim, “Fabrication of High-Aspect-Ratio Electrode Arrays for Three-Dimensional Microbatteries,” *J. Microelectromechanical Syst.*, vol. 16, no. 4, pp. 844–852, 2007, doi: 10.1109/JMEMS.2007.901638.

[43] P. L. Taberna, S. Mitra, P. Poizot, P. Simon, and J.-M. Tarascon, “High rate capabilities Fe3O4-based Cu nano-architectured electrodes for lithium-ion battery applications,” *Nat. Mater.*, vol. 5, no. 7, pp. 567–573, 2006, doi: 10.1016/j.cnsns.2018.02.037.

[44] M. M. Shaijumon, E. Perre, B. Daffos, P.-L. Taberna, J.-M. Tarascon, and P. Simon, “Nanoarchitectured 3D Cathodes for Li-Ion Microbatteries,” *Adv. Mater.*, vol. 22, no. 44, pp. 4978–4981, 2010, doi: 10.1002/adma.201001922.

[45] S. K. Cheah *et al.*, “Nanoelectrodes for Microbattery Applications,” *Nano Lett.*, vol. 9, no. 9, pp. 3230–3233, 2009.

[46] L. Bazin *et al.*, “High rate capability pure Sn-based nano-architectured electrode assembly for rechargeable lithium batteries,” *J. Power Sources*, vol. 188, no. 2, pp. 578–582, 2009, doi: https://doi.org/10.1016/j.jpowsour.2008.12.025.

[47] G. T. Teixidor, R. B. Zaouk, B. Y. Park, and M. J. Madou, “Fabrication and characterization of three-dimensional carbon electrodes for lithium-ion batteries,” *J. Power Sources*, vol. 183, no. 2, pp. 730–740, 2008, doi: https://doi.org/10.1016/j.jpowsour.2008.05.065.

[48] H.-S. Min *et al.*, “Fabrication and properties of a carbon/polypyrrole three-dimensional microbattery,” *J. Power Sources*, vol. 178, no. 2, pp. 795–800, 2008, doi:

https://doi.org/10.1016/j.jpowsour.2007.10.003.

[49] M. Kotobuki *et al.*, “Fabrication of Three-Dimensional Battery Using Ceramic Electrolyte with Honeycomb Structure by Sol–Gel Process,” *J. Electrochem. Soc.*, vol. 157, no. 4, pp. A493–A498, 2010, doi: 10.1149/1.3308459.

[50] J. I. Hur, L. C. Smith, and B. Dunn, “High Areal Energy Density 3D Lithium-Ion Microbatteries,” *Joule*, vol. 2, no. 6, pp. 1187–1201, 2018, doi: 10.1016/j.joule.2018.04.002.

[51] J. G. Werner, G. Rodriguez, H. Abruña, and U. Wiesner, “Block Copolymer Derived 3-D Interpenetrating Multifunctional Gyroidal Nanohybrid for Electrical Energy Storage,” *Energy Environ. Sci.*, vol. 11, 2018, doi: 10.1039/C7EE03571C.

[52] A. J. Pearse *et al.*, “Nanoscale Solid State Batteries Enabled by Thermal Atomic Layer Deposition of a Lithium Polyphosphazene Solid State Electrolyte,” *Chem. Mater.*, vol. 29, no. 8, pp. 3740–3753, 2017, doi: 10.1021/acs.chemmater.7b00805.

[53] M. Nathan *et al.*, “Three-dimensional thin-film Li-ion microbatteries for autonomous MEMS,” *J. Microelectromechanical Syst.*, vol. 14, no. 5, pp. 879–885, 2005, doi: 10.1109/JMEMS.2005.851860.

[54] M. F. L. De Volder, S. H. Tawfick, R. H. Baughman, and A. J. Hart, “Carbon Nanotubes: Present and Future Commercial Applications,” *Science (80-.).*, vol. 339, no. 6119, p. 535, 2013, doi: 10.1126/science.1222453.

[55] Z. Xiong, Y. S. Yun, and H.-J. Jin, “Applications of Carbon Nanotubes for Lithium Ion Battery Anodes,” *Materials (Basel).*, vol. 6, pp. 1138–1158, 2013, doi: 10.3390/ma6031138.

[56] A. Brieland-Shoultz *et al.*, “Scaling the Stiffness, Strength, and Toughness of Ceramic-Coated Nanotube Foams into the Structural Regime,” *Adv. Funct. Mater.*, vol. 24, no. 36, pp. 5728–5735, 2014, doi: 10.1002/adfm.201400851.

[57] E. Polsen *et al.*, “Continuous manufacturing of aligned carbon nanotubes for tough and multifunctional interface layers,” *Int. Conf. Compos. Mater.*, no. 1, 2009, [Online]. Available: http://iccm-central.org/Proceedings/ICCM17proceedings/Themes/TSAI/T1.1 Poulsen.pdf.

[58] E. S. Polsen, A. G. Stevens, and A. J. Hart, “Laser Printing of Nanoparticle Toner Enables Digital Control of Micropatterned Carbon Nanotube Growth,” *ACS Appl. Mater. Interfaces*, vol. 5, no. 9, pp. 3656–3662, 2013, doi: 10.1021/am400148t.

[59] S. Kim *et al.*, “Ultrathin high-resolution flexographic printing using nanoporous stamps,” *Sci. Adv.*, vol. 2, no. 12, 2016, doi: 10.1126/sciadv.1601660.

[60] W. Shi and D. L. Plata, “Vertically aligned carbon nanotubes: Production and applications for environmental sustainability,” *Green Chem.*, vol. 20, no. 23, pp. 5245–5260, 2018, doi: 10.1039/c8gc02195c.

[61] J. Li, M. Bedewy, A. O. White, E. S. Polsen, S. Tawfick, and A. J. Hart, “Highly Consistent Atmospheric Pressure Synthesis of Carbon Nanotube Forests by Mitigation of Moisture Transients,” *J. Phys. Chem. C*, vol. 120, no. 20, pp. 11277–11287, 2016, doi: 10.1021/acs.jpcc.6b02878.

[62] M. F. L. De Volder, S. H. Tawfick, R. H. Baughman, and A. J. Hart, “Carbon nanotubes: Present and future commercial applications,” *Science (80-.).*, vol. 339, no. 6119, pp. 535–539, 2013, doi: 10.1126/science.1222453.

[63] R. Rao *et al.*, “Carbon Nanotubes and Related Nanomaterials: Critical Advances and Challenges for Synthesis toward Mainstream Commercial Applications,” *ACS Nano*, vol.

12, no. 12, pp. 11756–11784, 2018, doi: 10.1021/acsnano.8b06511.

[64] N. T. Dee *et al.*, "Carbon-assisted catalyst pretreatment enables straightforward synthesis of high-density carbon nanotube forests," *Carbon N. Y.*, vol. 153, pp. 195–205, 2019, doi: 10.1016/j.carbon.2019.06.083.

[65] H. Zhao, C. Jacob, H. A. Stone, and A. J. Hart, "Liquid Imbibition in Ceramic-Coated Carbon Nanotube Films," *Langmuir*, vol. 32, no. 48, pp. 12686–12692, 2016, doi: 10.1021/acs.langmuir.6b03661.

[66] B. J. Landi, M. J. Ganter, C. D. Cress, R. A. DiLeo, and R. P. Raffaelle, "Carbon nanotubes for lithium ion batteries," *Energy Environ. Sci.*, vol. 2, no. 6, pp. 638–654, 2009, doi: 10.1039/b904116h.

[67] Y. Wu, J. Wang, K. Jiang, and S. Fan, "Applications of carbon nanotubes in high performance lithium ion batteries," *Front. Phys.*, vol. 9, no. 3, pp. 351–369, 2014, doi: 10.1007/s11467-013-0308-x.

[68] M. Bedewy, B. Farmer, and A. J. Hart, "Synergetic Chemical Coupling Controls the Uniformity of Carbon Nanotube Microstructure Growth," *ACS Nano*, vol. 8, no. 6, pp. 5799–5812, 2014, doi: 10.1021/nn500698z.

[69] C. R. Oliver *et al.*, "Statistical analysis of variation in laboratory growth of carbon nanotube forests and recommendations for improved consistency," *ACS Nano*, vol. 7, no. 4, pp. 3565–3580, 2013, doi: 10.1021/nn400507y.

[70] H. B. Abdullah, I. Ramli, I. Ismail, and N. A. Yusof, "Hydrocarbon sources for the carbon nanotubes production by chemical vapour deposition: A review," *Pertanika J. Sci. Technol.*, vol. 25, no. 2, pp. 379–396, 2017.

[71] B. R. Lettiere, C. A. C. Chazot, K. Cui, and A. John Hart, "High-Density Carbon Nanotube Forest Growth on Copper Foil for Enhanced Thermal and Electrochemical Interfaces," *ACS Appl. Nano Mater.*, vol. 3, no. 1, pp. 77–83, 2020, doi: 10.1021/acsanm.9b01595.

[72] M. F. L. De Volder, S. J. Park, S. H. Tawfick, D. O. Vidaud, and A. J. Hart, "Fabrication and electrical integration of robust carbon nanotube micropillars by self-directed elastocapillary densification," *J. Micromechanics Microengineering*, vol. 21, no. 4, 2011, doi: 10.1088/0960-1317/21/4/045033.

[73] C. C. Chiu, T. Y. Tsai, and N. H. Tai, "Field emission properties of carbon nanotube arrays through the pattern transfer process," *Nanotechnology*, vol. 17, no. 12, pp. 2840–2844, 2006, doi: 10.1088/0957-4484/17/12/002.

[74] M. J. Kim *et al.*, "Efficient transfer of a VA-SWNT film by a flip-over technique," *J. Am. Chem. Soc.*, vol. 128, no. 29, pp. 9312–9313, 2006, doi: 10.1021/ja062872s.

[75] S. Jessl, D. Copic, S. Engelke, S. Ahmad, and M. De Volder, "Hydrothermal Coating of Patterned Carbon Nanotube Forest for Structured Lithium-Ion Battery Electrodes," *Small*, p. 1901201, 2019, doi: 10.1002/smll.201901201.

[76] K. Evanoff *et al.*, "Towards ultrathick battery electrodes: Aligned carbon nanotube-enabled architecture," *Adv. Mater.*, vol. 24, no. 4, pp. 533–537, 2012, doi: 10.1002/adma.201103044.

[77] F. Pawlitzek, H. Althues, B. Schumm, and S. Kaskel, "Nanostructured Networks for Energy Storage: Vertically Aligned Carbon Nanotubes (VACNT) as Current Collectors for High-Power Li4Ti5O12(LTO)//LiMn2O4(LMO) Lithium-Ion Batteries," *Batteries*, vol. 3, no. 4, p. 37, 2017, doi: 10.3390/batteries3040037.

[78] S. Dörfler, M. Hagen, H. Althues, J. Tübke, S. Kaskel, and M. J. Hoffmann, "High capacity vertical aligned carbon nanotube/sulfur composite cathodes for lithium-sulfur batteries,"

Chem. Commun., vol. 48, no. 34, pp. 4097–4099, 2012, doi: 10.1039/c2cc17925c.

[79] W. Lu, A. Goering, L. Qu, and L. Dai, "Lithium-ion batteries based on vertically-aligned carbon nanotube electrodes and ionic liquid electrolytes," *Phys. Chem. Chem. Phys.*, vol. 14, no. 35, pp. 12099–12104, 2012, doi: 10.1039/C2CP40726D.

[80] K. Moyer-Vanderburgh *et al.*, "Growth and Performance of High-Quality SWCNT Forests on Inconel Foils as Lithium-Ion Battery Anodes," *ACS Appl. Mater. Interfaces*, 2022, doi: 10.1021/acsami.2c18396.

[81] S. Talapatra *et al.*, "Direct growth of aligned carbon nanotubes on bulk metals," *Nat. Nanotechnol.*, vol. 1, p. 112, 2006, doi: 10.1038/nnano.2006.56https://www.nature.com/articles/nnano.2006.56#supplementary-information.

[82] E. P. Kitsyuk, T. L. Kulova, A. A. Pavlov, and A. M. Skundin, "Formation and study of thin-film lithium-ion batteries using CNT/silicon composite material as an anode," *Russ. Microelectron.*, vol. 46, no. 2, pp. 88–94, 2017, doi: 10.1134/S1063739717020044.

[83] A. Gohier *et al.*, "High-rate capability silicon decorated vertically aligned carbon nanotubes for li-ion batteries," *Adv. Mater.*, vol. 24, no. 19, pp. 2592–2597, 2012, doi: 10.1002/adma.201104923.

[84] E. Roumeli, M. Diamantopoulou, M. Serra-Garcia, P. Johanns, G. Parcianello, and C. Daraio, "Characterization of vertically aligned carbon nanotube forests grown on stainless steel surfaces," *Nanomaterials*, vol. 9, no. 3, pp. 18–25, 2019, doi: 10.3390/nano9030444.

[85] X. Li, M. Baker-Fales, H. Almkhelfe, N. R. Gaede, T. S. Harris, and P. B. Amama, "Rational modification of a metallic substrate for CVD Growth of Carbon Nanotubes," *Sci. Rep.*, vol. 8, no. 1, pp. 1–10, 2018, doi: 10.1038/s41598-018-22467-7.

[86] S. Miura *et al.*, "Millimeter-tall carbon nanotube arrays grown on aluminum substrates," *Carbon N. Y.*, vol. 130, pp. 834–842, 2018, doi: 10.1016/j.carbon.2018.01.075.

[87] J.-M. Bonard *et al.*, "Synthesis of carbon nanotubes over Fe catalyst on aluminium and suggested growth mechanism," *Carbon N. Y.*, vol. 41, no. 3, pp. 539–547, 2003.

[88] U. Pakdee and B. Duangsawat, "Buffer Film Assisted Growth of Dense MWCNTs on Copper Foils for Flexible Electrochemical Applications," *J. Nanomater.*, vol. 2017, 2017, doi: 10.1155/2017/1867414.

[89] G. Zhong *et al.*, "Growth of high quality, high density single-walled carbon nanotube forests on copper foils," *Carbon N. Y.*, vol. 98, pp. 624–632, 2016, doi: 10.1016/j.carbon.2015.11.047.

[90] S. Sepahvand, P. Safaei, and Z. Sanaee, "Growth of Carbon Nano Tubes on Copper Substrate Suitable for Lithium Ion Battery Anode," *Procedia Mater. Sci.*, vol. 11, no. 2013, pp. 634–638, 2015, doi: 10.1016/j.mspro.2015.11.100.

[91] M. Ezzedine, F. Jardali, I. Florea, M. R. Zamfir, and C. S. Cojocaru, "Nanostructuring Strategies for Silicon-based Anodes in Lithium-ion Batteries: Tuning Areal Silicon Loading, SEI Formation/Irreversible Capacity Loss, Rate Capability Retention and Electrode Durability," *Batter. Supercaps*, vol. 6, no. 3, 2023, doi: 10.1002/batt.202200451.

[92] E. Teblum *et al.*, "Millimeter-tall carpets of vertically aligned crystalline carbon nanotubes synthesized on copper substrates for electrical applications," *J. Phys. Chem. C*, vol. 118, no. 33, pp. 19345–19355, 2014, doi: 10.1021/jp5015719.

[93] G. Li, S. Chakrabarti, M. Schulz, and V. Shanov, "Growth of aligned multiwalled carbon nanotubes copper substrates by chemical vapor deposition," *J. Mater. Res.*, vol. 24, no. 9, pp. 2813–2820, 2009, doi: 10.1557/jmr.2009.0339.

[94] S. H. Ng *et al.*, “Flexible free-standing carbon nanotube films for model lithium-ion batteries,” *Carbon N. Y.*, vol. 47, no. 13, pp. 2976–2983, 2009, doi: 10.1016/j.carbon.2009.06.045.

[95] R. Paul, V. Etacheri, V. G. Pol, J. Hu, and T. S. Fisher, “Highly porous three-dimensional carbon nanotube foam as a freestanding anode for a lithium-ion battery,” *RSC Adv.*, vol. 6, no. 83, pp. 79734–79744, 2016, doi: 10.1039/c6ra17815d.

[96] L.-F. Cui, Y. Yang, C.-M. Hsu, and Y. Cui, “Carbon−Silicon Core−Shell Nanowires as High Capacity Electrode for Lithium Ion Batteries,” *Nano Lett.*, vol. 9, no. 9, pp. 3370–3374, 2009, doi: 10.1021/nl901670t.

[97] K. Evanoff *et al.*, “Ultra strong silicon-coated carbon nanotube nonwoven fabric as a multifunctional lithium-ion battery anode,” *ACS Nano*, vol. 6, no. 11, pp. 9837–9845, 2012, doi: 10.1021/nn303393p.

[98] L.-F. Cui, L. Hu, J. W. Choi, and Y. Cui, “Light-Weight Free-Standing Carbon Nanotube-Silicon Films for Anodes of Lithium Ion Batteries,” *ACS Nano*, vol. 4, no. 7, pp. 3671–3678, 2010, doi: 10.1021/nn100619m.

[99] S. L. Chou, Y. Zhao, J. Z. Wang, Z. X. Chen, H. K. Liu, and S. X. Dou, “Silicon/single-walled carbon nanotube composite paper as a flexible anode material for lithium ion batteries,” *J. Phys. Chem. C*, vol. 114, no. 37, pp. 15862–15867, 2010, doi: 10.1021/jp1063403.

[100] J. Fu *et al.*, “Ultrathin Si/CNTs paper-like composite for flexible Li-Ion battery anode with high volumetric capacity,” *Front. Chem.*, vol. 6, no. DEC, pp. 1–9, 2018, doi: 10.3389/fchem.2018.00624.

[101] L. Hu *et al.*, “Silicon-carbon nanotube coaxial sponge as Li-ion anodes with high areal capacity,” *Adv. Energy Mater.*, vol. 1, no. 4, pp. 523–527, 2011, doi: 10.1002/aenm.201100056.

[102] B. Luo *et al.*, “Freestanding carbon-coated CNT/Sn(O2) coaxial sponges with enhanced lithium-ion storage capability,” *Nanoscale*, vol. 7, no. 48, pp. 20380–20385, 2015, doi: 10.1039/c5nr06613a.

[103] K. Fu *et al.*, “Aligned carbon nanotube-silicon sheets: A novel nano-architecture for flexible lithium ion battery electrodes,” *Adv. Mater.*, vol. 25, no. 36, pp. 5109–5114, 2013, doi: 10.1002/adma.201301920.

[104] S. Luo, K. Wang, J. Wang, K. Jiang, Q. Li, and S. Fan, “Binder-free LiCoO 2/carbon nanotube cathodes for high-performance lithium ion batteries,” *Adv. Mater.*, vol. 24, no. 17, pp. 2294–2298, 2012, doi: 10.1002/adma.201104720.

[105] A. Busnaina *et al.*, “A Layered Carbon Nanotube Architecture for High Power Lithium Ion Batteries,” *J. Electrochem. Soc.*, vol. 161, no. 6, pp. A989–A995, 2014, doi: 10.1149/2.052406jes.

[106] H. Wang *et al.*, “A binder-free high silicon content flexible anode for Li-ion batteries,” *Energy Environ. Sci.*, vol. 13, no. 3, pp. 848–858, 2020, doi: 10.1039/c9ee02615k.

[107] R. Epur *et al.*, “Scribable multi-walled carbon nanotube-silicon nanocomposites: A viable lithium-ion battery system,” *Nanoscale*, vol. 7, no. 8, pp. 3504–3510, 2015, doi: 10.1039/c4nr04288c.

[108] C. Xie *et al.*, “Flexible and Robust Silicon/Carbon Nanotube Anodes Exhibiting High Areal Capacities,” *J. Colloid Interface Sci.*, vol. 625, no. 5, pp. 871–878, 2022, doi: 10.1016/j.jcis.2022.06.082.

[109] S. H. Park *et al.*, “High areal capacity battery electrodes enabled by segregated nanotube

networks," *Nat. Energy*, vol. 4, no. July, 2019, doi: 10.1038/s41560-019-0398-y.

[110] W. Wang and P. N. Kumta, "Nanostructured hybrid silicon/carbon nanotube heterostructures: Reversible high-capacity lithium-ion anodes," *ACS Nano*, vol. 4, no. 4, pp. 2233–2241, 2010, doi: 10.1021/nn901632g.

[111] J. Liu, B. Wang, Q. Sun, R. Li, T. K. Sham, and X. Sun, "Atomic Layer Deposition of Hierarchical CNTs@FePO4 Architecture as a 3D Electrode for Lithium-Ion and Sodium-Ion Batteries," *Adv. Mater. Interfaces*, vol. 3, no. 21, 2016, doi: 10.1002/admi.201600468.

[112] S. Ahmad, D. Copic, C. George, and M. De Volder, "Hierarchical Assemblies of Carbon Nanotubes for Ultraflexible Li-Ion Batteries," *Adv. Mater.*, vol. 28, no. 31, pp. 6705–6710, 2016, doi: 10.1002/adma.201600914.

[113] H. Wu and Y. Cui, "Designing nanostructured Si anodes for high energy," *Nano Today*, vol. 7, pp. 414–429, 2012, doi: dx.doi.org/10.1016/j.nantod.2012.08.004.

[114] C. P. Rhodes, J. W. Long, and D. R. Rolison, "Direct Electrodeposition of Nanoscale Solid Polymer Electrolytes via Electropolymerization of Sulfonated Phenols," *Electrochem. Solid-State Lett.*, vol. 8, no. 11, pp. A579–A584, 2005, doi: 10.1149/1.2050508.

[115] C. P. Rhodes, J. W. Long, M. S. Doescher, B. M. Dening, and D. R. Rolison, "Charge insertion into hybrid nanoarchitectures: mesoporous manganese oxide coated with ultrathin poly(phenylene oxide)," *J. Non. Cryst. Solids*, vol. 350, pp. 73–79, 2004, doi: https://doi.org/10.1016/j.jnoncrysol.2004.06.050.

[116] C. P. Rhodes, J. W. Long, M. S. Doescher, J. J. Fontanella, and D. R. Rolison, "Nanoscale Polymer Electrolytes: Ultrathin Electrodeposited Poly(Phenylene Oxide) with Solid-State Ionic Conductivity," *J. Phys. Chem. B*, vol. 108, no. 35, pp. 13079–13087, 2004, doi: 10.1021/jp047671u.

[117] J. Liu *et al.*, "Atomic layer deposition of lithium tantalate solid-state electrolytes," *J. Phys. Chem. C*, vol. 117, no. 39, pp. 20260–20267, 2013, doi: 10.1021/jp4063302.

[118] A. C. Kozen, A. J. Pearse, C. F. Lin, M. Noked, and G. W. Rubloff, "Atomic Layer Deposition of the Solid Electrolyte LiPON," *Chem. Mater.*, vol. 27, no. 15, pp. 5324–5331, 2015, doi: 10.1021/acs.chemmater.5b01654.

[119] K. K. S. Lau, *Growth Mechanism, Kinetics, and Molecular Weight*. 2015.

[120] S. R. Gowda, A. L. M. Reddy, M. M. Shaijumon, X. Zhan, L. Ci, and P. M. Ajayan, "Conformal Coating of Thin Polymer Electrolyte Layer on Nanostructured Electrode Materials for Three-Dimensional Battery Applications," *Nano Lett.*, vol. 11, no. 1, pp. 101–106, 2011, doi: 10.1021/nl102919m.

[121] K. K. S. Lau and K. K. Gleason, "Initiated Chemical Vapor Deposition (iCVD) of poly(alkyl acrylates): An experimental study," *Macromolecules*, vol. 39, no. 10, pp. 3688–3694, 2006, doi: 10.1021/ma0601619.

[122] N. Chen, D. H. Kim, P. Kovacik, H. Sojoudi, M. Wang, and K. K. Gleason, "Polymer Thin Films and Surface Modification by Chemical Vapor Deposition: Recent Progress," *Annu. Rev. Chem. Biomol. Eng.*, vol. 7, no. 1, pp. 373–393, 2016, doi: 10.1146/annurev-chembioeng-080615-033524.

[123] B. Reeja-Jayan *et al.*, "A Group of Cyclic Siloxane and Silazane Polymer Films as Nanoscale Electrolytes for Microbattery Architectures," *Macromolecules*, vol. 48, no. 15, pp. 5222–5229, 2015, doi: 10.1021/acs.macromol.5b00940.

[124] N. Chen, B. Reeja-Jayan, A. Liu, J. Lau, B. Dunn, and K. K. Gleason, "ICVD Cyclic Polysiloxane and Polysilazane as Nanoscale Thin-Film Electrolyte: Synthesis and Properties," *Macromol. Rapid Commun.*, vol. 37, no. 5, pp. 446–452, 2016, doi:

10.1002/marc.201500649.

[125] N. J. Trujillo, Q. Wu, and K. K. Gleason, "Ultralow dielectric constant tetravinyltetramethylcyclotetrasiloxane films deposited by initiated chemical vapor deposition (iCVD)," *Adv. Funct. Mater.*, vol. 20, no. 4, pp. 607–616, 2010, doi: 10.1002/adfm.200900999.

[126] A. A. Talin *et al.*, "Fabrication, Testing, and Simulation of All-Solid-State Three-Dimensional Li-Ion Batteries," *ACS Appl. Mater. Interfaces*, vol. 8, no. 47, pp. 32385–32391, 2016, doi: 10.1021/acsami.6b12244.

[127] K. McKelvey, A. A. Talin, B. Dunn, and H. S. White, "Microscale 2.5D Batteries," *J. Electrochem. Soc.*, vol. 164, no. 12, pp. A2500–A2503, 2017, doi: 10.1149/2.0771712jes.

[128] V. Zadin, H. Kasemägi, A. Aabloo, and D. Brandell, "Modelling electrode material utilization in the trench model 3D-microbattery by finite element analysis," *J. Power Sources*, vol. 195, no. 18, pp. 6218–6224, 2010, doi: 10.1016/j.jpowsour.2010.02.056.

[129] K. Zhu *et al.*, "Mesoporous TiO2 Spheres as Advanced Anodes for Low-Cost, Safe, and High-Areal-Capacity Lithium-Ion Full Batteries," *ACS Appl. Nano Mater.*, vol. 3, no. 2, pp. 1019–1027, 2020, doi: 10.1021/acsanm.9b02594.

[130] K. Narita, M. A. Citrin, H. Yang, X. Xia, and J. R. Greer, "3D Architected Carbon Electrodes for Energy Storage," *Adv. Energy Mater.*, p. 2002637, 2020, doi: 10.1002/aenm.202002637.

[131] C. Zheng, B. Yang, S. Yarlagadda, T. Chou, and K. K. Fu, "Low Tortuous, Highly Conductive, and High-Areal-Capacity Battery Electrodes Enabled by Through-thickness Aligned Carbon Fiber Framework," *Nano Lett.*, vol. 20, no. 7, pp. 5504–5512, 2020, doi: 10.1021/acs.nanolett.0c02053.

[132] H. Kim, D. wook Kim, H. Todoki, N. Zettsu, and K. Teshima, "Three-dimensional assembly of multiwalled carbon nanotubes for creating a robust electron-conducting network in silicon-carbon microsphere-based electrodes," *Sci. Rep.*, vol. 10, no. 1, pp. 1–11, 2020, doi: 10.1038/s41598-020-58338-3.

[133] D. Mariappan *et al.*, "Dynamics of Liquid Transfer from Nanoporous Stamps in High-Resolution Flexographic Printing," *Langmuir*, 2019, doi: 10.1021/acs.langmuir.9b00460.

[134] M. Hagen *et al.*, "Lithium-sulphur batteries - Binder free carbon nanotubes electrode examined with various electrolytes," *J. Power Sources*, vol. 213, pp. 239–248, 2012, doi: 10.1016/j.jpowsour.2012.04.004.

[135] R. A. DiLeo, B. J. Landi, and R. P. Raffaelle, "Purity assessment of multiwalled carbon nanotubes by Raman spectroscopy," *J. Appl. Phys.*, vol. 101, no. 6, 2007, doi: 10.1063/1.2712152.

[136] B. J. Landi, H. J. Ruf, C. M. Evans, C. D. Cress, and R. P. Raffaelle, "Purity assessment of single-wall carbon nanotubes, using optical absorption spectroscopy," *J. Phys. Chem. B*, vol. 109, no. 20, pp. 9952–9965, 2005, doi: 10.1021/jp044990c.

[137] D. N. Futaba, K. Hata, T. Yamada, K. Mizuno, M. Yumura, and S. Iijima, "Kinetics of water-assisted single-walled carbon nanotube synthesis revealed by a time-evolution analysis," *Phys. Rev. Lett.*, vol. 95, no. 5, pp. 1–4, 2005, doi: 10.1103/PhysRevLett.95.056104.

[138] G. K. Simon, B. Maruyama, M. F. Durstock, D. J. Burton, and T. Goswami, "Silicon-coated carbon nanofiber hierarchical nanostructures for improved lithium-ion battery anodes," *J. Power Sources*, vol. 196, no. 23, pp. 10254–10257, 2011, doi: 10.1016/j.jpowsour.2011.08.058.

[139] P. Yogi *et al.*, "Quantifying the Short-Range Order in Amorphous Silicon by Raman Scattering," *Anal. Chem.*, vol. 90, no. 13, pp. 8123–8129, 2018, doi: 10.1021/acs.analchem.8b01352.

[140] B. Li, D. Yu, and S. Zhang, "Raman spectral study of silicon nanowires," *Phys. Rev. B - Condens. Matter Mater. Phys.*, vol. 59, no. 3, pp. 1645–1648, 1999, doi: 10.1103/PhysRevB.59.1645.

[141] D. Mazouzi *et al.*, "Very high surface capacity observed using Si negative electrodes embedded in copper foam as 3D current collectors," *Adv. Energy Mater.*, vol. 4, no. 8, 2014, doi: 10.1002/aenm.201301718.

[142] X. Yang and A. L. Rogach, "Electrochemical Techniques in Battery Research: A Tutorial for Nonelectrochemists," *Adv. Energy Mater.*, vol. 9, no. 25, pp. 1–10, 2019, doi: 10.1002/aenm.201900747.

[143] L. Hu *et al.*, "Excellent Cyclic and Rate Performances of SiO/C/Graphite Composites as Li-Ion Battery Anode," *Front. Chem.*, vol. 8, no. May, pp. 1–8, 2020, doi: 10.3389/fchem.2020.00388.

[144] X. Y. Zhou, J. J. Tang, J. Yang, J. Xie, and L. L. Ma, "Silicon@carbon hollow core-shell heterostructures novel anode materials for lithium ion batteries," *Electrochim. Acta*, vol. 87, pp. 663–668, 2013, doi: 10.1016/j.electacta.2012.10.008.

[145] M. J. Loveridge *et al.*, "Towards High Capacity Li-ion Batteries Based on Silicon-Graphene Composite Anodes and Sub-micron V-doped LiFePO 4 Cathodes," *Sci. Rep.*, vol. 6, no. November, 2016, doi: 10.1038/srep37787.

[146] N. P. Wagner, A. Tron, J. R. Tolchard, G. Noia, and M. P. Bellmann, "Silicon anodes for lithium-ion batteries produced from recovered kerf powders," *J. Power Sources*, vol. 414, no. January, pp. 486–494, 2019, doi: 10.1016/j.jpowsour.2019.01.035.

[147] M. Wetjen, D. Pritzl, R. Jung, S. Solchenbach, R. Ghadimi, and H. A. Gasteiger, "Differentiating the Degradation Phenomena in Silicon-Graphite Electrodes for Lithium-Ion Batteries," *J. Electrochem. Soc.*, vol. 164, no. 12, pp. A2840–A2852, 2017, doi: 10.1149/2.1921712jes.

[148] A. Ulvestad *et al.*, "Crystallinity of Silicon Nanoparticles: Direct Influence on the Electrochemical Performance of Lithium Ion Battery Anodes," *ChemElectroChem*, vol. 7, no. 21, pp. 4349–4353, 2020, doi: 10.1002/celc.202001108.

[149] V. Etacheri *et al.*, "Exceptional electrochemical performance of Si-nanowires in 1,3-dioxolane solutions: A surface chemical investigation," *Langmuir*, vol. 28, no. 14, pp. 6175–6184, 2012, doi: 10.1021/la300306v.

[150] T. Jaumann, J. Balach, M. Klose, S. Oswald, J. Eckert, and L. Giebeler, " Role of 1,3-Dioxolane and LiNO 3 Addition on the Long Term Stability of Nanostructured Silicon/Carbon Anodes for Rechargeable Lithium Batteries ," *J. Electrochem. Soc.*, vol. 163, no. 3, pp. A557–A564, 2016, doi: 10.1149/2.1011603jes.

[151] J. Wang *et al.*, "Improving cyclability of Li metal batteries at elevated temperatures and its origin revealed by cryo-electron microscopy," *Nat. Energy*, vol. 4, no. 8, pp. 664–670, 2019, doi: 10.1038/s41560-019-0413-3.

[152] G. M. Hobold *et al.*, "Moving beyond 99.9% Coulombic efficiency for lithium anodes in liquid electrolytes," *Nat. Energy*, vol. 6, no. 10, pp. 951–960, 2021, doi: 10.1038/s41560-021-00910-w.

[153] A. Nurpeissova, A. Adi, A. Aishova, A. Mukanova, S. S. Kim, and Z. Bakenov, "Synergistic effect of 3D current collector structure and Ni inactive matrix on the electrochemical

performances of Sn-based anodes for lithium-ion batteries," *Mater. Today Energy*, vol. 16, p. 100397, 2020, doi: 10.1016/j.mtener.2020.100397.

[154] Y. Cui *et al.*, "High Performance Solid Polymer Electrolytes for Rechargeable Batteries: A Self-Catalyzed Strategy toward Facile Synthesis," *Adv. Sci.*, vol. 4, no. 11, 2017, doi: 10.1002/advs.201700174.

[155] L. Qie, C. Zu, and A. Manthiram, "A High Energy Lithium-Sulfur Battery with Ultrahigh-Loading Lithium Polysulfide Cathode and its Failure Mechanism," *Adv. Energy Mater.*, vol. 6, no. 7, pp. 1–7, 2016, doi: 10.1002/aenm.201502459.

[156] J. Cui *et al.*, "Effect of continuous pressures on electrochemical performance of Si anodes," *Mater. Today Energy*, vol. 20, p. 100632, 2021, doi: 10.1080/10643389.2012.728825.

[157] J. Van Mierlo *et al.*, "Beyond the state of the art of electric vehicles: A fact-based paper of the current and prospective electric vehicle technologies," *World Electr. Veh. J.*, vol. 12, no. 1, pp. 1–26, 2021, doi: 10.3390/wevj12010020.

[158] R. Sheil and J. P. Chang, "Synthesis and integration of thin film solid state electrolytes for 3D Li-ion microbatteries," *J. Vac. Sci. Technol. A*, vol. 38, no. 3, p. 032411, 2020, doi: 10.1116/1.5142859.

[159] J. H. Pikul, H. Gang Zhang, J. Cho, P. V. Braun, and W. P. King, "High-power lithium ion microbatteries from interdigitated three-dimensional bicontinuous nanoporous electrodes," *Nat. Commun.*, vol. 4, pp. 1732–1735, 2013, doi: 10.1038/ncomms2747.

[160] K. Sun, T.-S. Wei, B. Y. Ahn, J. Y. Seo, S. J. Dillon, and J. A. Lewis, "3D Printing of Interdigitated Li-Ion Microbattery Architectures," *Adv. Mater.*, vol. 25, no. 33, pp. 4539–4543, 2013, doi: 10.1002/adma.201301036.

[161] D. T. Hallinan, I. Villaluenga, and N. P. Balsara, "Polymer and composite electrolytes," *MRS Bull.*, vol. 43, no. 10, pp. 759–767, 2018, doi: 10.1557/mrs.2018.212.

[162] C. Cao, Z. Bin Li, X. L. Wang, X. B. Zhao, and W. Q. Han, "Recent advances in inorganic solid electrolytes for lithium batteries," *Front. Energy Res.*, vol. 2, no. JUN, pp. 1–10, 2014, doi: 10.3389/fenrg.2014.00025.

[163] Y. Ren, K. Chen, R. Chen, T. Liu, Y. Zhang, and C. W. Nan, "Oxide Electrolytes for Lithium Batteries," *J. Am. Ceram. Soc.*, vol. 98, no. 12, pp. 3603–3623, 2015, doi: 10.1111/jace.13844.

[164] K. J. Kim, M. Balaish, M. Wadaguchi, L. Kong, and J. L. M. Rupp, "Solid-State Li–Metal Batteries: Challenges and Horizons of Oxide and Sulfide Solid Electrolytes and Their Interfaces," *Adv. Energy Mater.*, vol. 11, no. 1, 2021, doi: 10.1002/aenm.202002689.

[165] M. Balaish, J. C. Gonzalez-Rosillo, K. J. Kim, Y. Zhu, Z. D. Hood, and J. L. M. Rupp, "Processing thin but robust electrolytes for solid-state batteries," *Nat. Energy*, vol. 6, no. 3, pp. 227–239, 2021, doi: 10.1038/s41560-020-00759-5.

[166] A. Jetybayeva, B. Uzakbaiuly, A. Mukanova, S. T. Myung, and Z. Bakenov, "Recent advancements in solid electrolytes integrated into all-solid-state 2D and 3D lithium-ion microbatteries," *J. Mater. Chem. A*, vol. 9, no. 27, pp. 15140–15178, 2021, doi: 10.1039/d1ta02652f.

[167] S. Moitzheim, B. Put, and P. M. Vereecken, "Advances in 3D Thin-Film Li-Ion Batteries," *Adv. Mater. Interfaces*, vol. 6, no. 15, pp. 1–17, 2019, doi: 10.1002/admi.201900805.

[168] J. Mindemark, M. J. Lacey, T. Bowden, and D. Brandell, "Beyond PEO—Alternative host materials for Li+-conducting solid polymer electrolytes," *Prog. Polym. Sci.*, vol. 81, pp. 114–143, 2018, doi: 10.1016/j.progpolymsci.2017.12.004.

[169] Y. Jiang *et al.*, "Development of the PEO Based Solid Polymer Electrolytes for All-Solid

State Lithium Ion Batteries," *Polymers (Basel).*, vol. 10, no. 11, p. 1237, 2018, doi: 10.3390/polym10111237.

[170] N. Kamaya *et al.*, "A lithium superionic conductor," *Nat. Mater.*, vol. 10, no. 9, pp. 682–686, 2011, doi: 10.1038/nmat3066.

[171] J. F. Wu *et al.*, "Gallium-doped Li7La3Zr2O12 garnet-type electrolytes with high lithium-ion conductivity," *ACS Appl. Mater. Interfaces*, vol. 9, no. 2, pp. 1542–1552, 2017, doi: 10.1021/acsami.6b13902.

[172] W. J. Kwon *et al.*, "Enhanced Li+ conduction in perovskite Li3XLa2/3-x□1/3-2xTiO3 solid-electrolytes via microstructural engineering," *J. Mater. Chem. A*, vol. 5, no. 13, pp. 6257–6262, 2017, doi: 10.1039/c7ta00196g.

[173] E. C. Bucharsky, K. G. Schell, A. Hintennach, and M. J. Hoffmann, "Preparation and characterization of sol-gel derived high lithium ion conductive NZP-type ceramics Li1 + x AlxTi2 - X(PO4)3," *Solid State Ionics*, vol. 274, pp. 77–82, 2015, doi: 10.1016/j.ssi.2015.03.009.

[174] B. Wang, B. S. Kwak, B. C. Sales, and J. B. Bates, "Ionic conductivities and structure of lithium phosphorus oxynitride glasses," *J. Non. Cryst. Solids*, vol. 183, no. 3, pp. 297–306, 1995, doi: https://doi.org/10.1016/0022-3093(94)00665-2.

[175] J. Sastre, A. Priebe, M. Döbeli, J. Michler, A. N. Tiwari, and Y. E. Romanyuk, "Lithium Garnet Li7La3Zr2O12 Electrolyte for All-Solid-State Batteries: Closing the Gap between Bulk and Thin Film Li-Ion Conductivities," *Adv. Mater. Interfaces*, vol. 7, no. 17, 2020, doi: 10.1002/admi.202000425.

[176] Y. Su *et al.*, "LiPON thin films with high nitrogen content for application in lithium batteries and electrochromic devices prepared by RF magnetron sputtering," *Solid State Ionics*, vol. 282, pp. 63–69, 2015, doi: 10.1016/j.ssi.2015.09.022.

[177] H. Chen, H. Tao, X. Zhao, and Q. Wu, "Fabrication and ionic conductivity of amorphous Li-Al-Ti-P-O thin film," *J. Non. Cryst. Solids*, vol. 357, no. 16–17, pp. 3267–3271, 2011, doi: 10.1016/j.jnoncrysol.2011.05.023.

[178] N. Kuwata, N. Iwagami, Y. Matsuda, Y. Tanji, and J. Kawamura, "Thin Film Batteries with Li3PO4 Solid Electrolyte Fabricated by Pulsed Laser Deposition," *ECS Trans.*, vol. 16, no. 26, pp. 53–60, 2019, doi: 10.1149/1.3111821.

[179] S. I. Furusawa, H. Tabuchi, T. Sugiyama, S. Tao, and J. T. S. Irvine, "Ionic conductivity of amorphous lithium lanthanum titanate thin film," *Solid State Ionics*, vol. 176, no. 5–6, pp. 553–558, 2005, doi: 10.1016/j.ssi.2004.08.020.

[180] E. Kazyak *et al.*, "Atomic layer deposition and first principles modeling of glassy Li3BO3-Li2CO3 electrolytes for solid-state Li metal batteries," *J. Mater. Chem. A*, vol. 6, no. 40, pp. 19425–19437, 2018, doi: 10.1039/c8ta08761j.

[181] N. S. Ergang, M. A. Fierke, Z. Wang, W. H. Smyrl, and A. Stein, "Fabrication of a Fully Infiltrated Three-Dimensional Solid-State Interpenetrating Electrochemical Cell," *J. Electrochem. Soc.*, vol. 154, no. 12, pp. A1135–A1139, 2007, doi: 10.1149/1.2794288.

[182] B. Sun, D. Rehnlund, M. J. Lacey, and D. Brandell, "Electrodeposition of thin poly(propylene glycol) acrylate electrolytes on 3D-nanopillar electrodes," *Electrochim. Acta*, vol. 137, pp. 320–327, 2014, doi: 10.1016/j.electacta.2014.06.008.

[183] M. E. Abdelhamid *et al.*, "Electrochemically Controlled Deposition of Ultrathin Polymer Electrolyte on Complex Microbattery Electrode Architectures," *J. Electrochem. Soc.*, vol. 166, no. 3, pp. A5462–A5469, 2019, doi: 10.1149/2.0601903jes.

[184] K. Dokko, J. Sugaya, H. Nakano, T. Yasukawa, T. Matsue, and K. Kanamura, "Sol–gel

fabrication of lithium-ion microarray battery," *Electrochem. commun.*, vol. 9, no. 5, pp. 857–862, 2007, doi: https://doi.org/10.1016/j.elecom.2006.11.025.

[185] K. Yoshima, H. Munakata, and K. Kanamura, "Fabrication of micro lithium-ion battery with 3D anode and 3D cathode by using polymer wall," *J. Power Sources*, vol. 208, pp. 404–408, 2012, doi: https://doi.org/10.1016/j.jpowsour.2012.02.045.

[186] S. Tan, S. Walus, J. Hilborn, T. Gustafsson, and D. Brandell, "Poly(ether amine) and cross-linked poly(propylene oxide) diacrylate thin-film polymer electrolyte for 3D-microbatteries," *Electrochem. commun.*, vol. 12, no. 11, pp. 1498–1500, 2010, doi: 10.1016/j.elecom.2010.08.017.

[187] H. Nakano, K. Dokko, J. ichi Sugaya, T. Yasukawa, T. Matsue, and K. Kanamura, "All-solid-state micro lithium-ion batteries fabricated by using dry polymer electrolyte with micro-phase separation structure," *Electrochem. commun.*, vol. 9, no. 8, pp. 2013–2017, 2007, doi: 10.1016/j.elecom.2007.05.020.

[188] B. Sun, I. Y. Liao, S. Tan, T. Bowden, and D. Brandell, "Solid polymer electrolyte coating from a bifunctional monomer for three-dimensional microbattery applications," *J. Power Sources*, vol. 238, pp. 435–441, 2013, doi: 10.1016/j.jpowsour.2013.04.058.

[189] P. Sun, X. Li, J. Shao, and P. V. Braun, "High-Performance Packaged 3D Lithium-Ion Microbatteries Fabricated Using Imprint Lithography," *Adv. Mater.*, vol. 2006229, pp. 1–7, 2020, doi: 10.1002/adma.202006229.

[190] D. S. Ashby, C. S. Choi, M. A. Edwards, A. A. Talin, H. S. White, and B. S. Dunn, "High-Performance Solid-State Lithium-Ion Battery with Mixed 2D and 3D Electrodes," *ACS Appl. Energy Mater.*, vol. 3, no. 9, pp. 8402–8409, 2020, doi: 10.1021/acsaem.0c01029.

[191] B. Sun *et al.*, "Toward Solid-State 3D-Microbatteries Using Functionalized Polycarbonate-Based Polymer Electrolytes," *ACS Appl. Mater. Interfaces*, vol. 10, no. 3, pp. 2407–2413, 2018, doi: 10.1021/acsami.7b13788.

[192] C. S. Choi, J. Lau, J. Hur, L. Smith, C. Wang, and B. Dunn, "Synthesis and Properties of a Photopatternable Lithium-Ion Conducting Solid Electrolyte," *Adv. Mater.*, vol. 30, no. 1, pp. 6–11, 2018, doi: 10.1002/adma.201703772.

[193] M. Nasreldin *et al.*, "High performance stretchable Li-ion microbattery," *Energy Storage Mater.*, vol. 33, no. July, pp. 108–115, 2020, doi: 10.1016/j.ensm.2020.07.005.

[194] Y. He, S. Chen, L. Nie, Z. Sun, X. Wu, and W. Liu, "Stereolithography Three-Dimensional Printing Solid Polymer Electrolytes for All-Solid-State Lithium Metal Batteries," *Nano Lett.*, vol. 20, no. 10, pp. 7136–7143, 2020, doi: 10.1021/acs.nanolett.0c02457.

[195] E. H. Kil *et al.*, "Imprintable, bendable, and shape-conformable polymer electrolytes for versatile-shaped lithium-ion batteries," *Adv. Mater.*, vol. 25, no. 10, pp. 1395–1400, 2013, doi: 10.1002/adma.201204182.

[196] J. Schnell *et al.*, "All-solid-state lithium-ion and lithium metal batteries – paving the way to large-scale production," *J. Power Sources*, vol. 382, no. December 2017, pp. 160–175, 2018, doi: 10.1016/j.jpowsour.2018.02.062.

[197] J. Li, C. Ma, M. Chi, C. Liang, and N. J. Dudney, "Solid electrolyte: The key for high-voltage lithium batteries," *Adv. Energy Mater.*, vol. 5, no. 4, 2015, doi: 10.1002/aenm.201401408.

[198] N. Suzuki, S. Shirai, N. Takahashi, T. Inaba, and T. Shiga, "A lithium phosphorous oxynitride (LiPON) film sputtered from unsintered Li3PO4 powder target," *Solid State Ionics*, vol. 191, no. 1, pp. 49–54, 2011, doi: 10.1016/j.ssi.2011.04.001.

[199] D. L. Xiao, J. Tong, Y. Feng, G. H. Zhong, W. J. Li, and C. L. Yang, "Improved

performance of all-solid-state lithium batteries using LiPON electrolyte prepared with Li-rich sputtering target," *Solid State Ionics*, vol. 324, no. May, pp. 202–206, 2018, doi: 10.1016/j.ssi.2018.07.011.

[200] D. Li, Z. Ma, J. Xu, Y. Li, and K. Xie, "High temperature property of all-solid-state thin film lithium battery using LiPON electrolyte," *Mater. Lett.*, vol. 134, pp. 237–239, 2014, doi: 10.1016/j.matlet.2014.07.092.

[201] E. J. Jeon, Y. W. Shin, S. C. Nam, W. Il Cho, and Y. S. Yoon, "Characterization of all solid-state thin film batteries with V 2O5 thin film cathode by using ex-situ and in-situ process," *Proc. - Electrochem. Soc.*, vol. 3, pp. 70–80, 2000, doi: 10.1149/1.1354609.

[202] C. Lethien, M. Zegaoui, P. Roussel, P. Tilmant, N. Rolland, and P. A. Rolland, "Micro-patterning of LiPON and lithium iron phosphate material deposited onto silicon nanopillars array for lithium ion solid state 3D micro-battery," *Microelectron. Eng.*, vol. 88, no. 10, pp. 3172–3177, 2011, doi: https://doi.org/10.1016/j.mee.2011.06.022.

[203] Y. S. Park, S. H. Lee, B. Il Lee, and S. K. Joo, "All-Solid-State Lithium Thin-Film Rechargeable Battery with Lithium Manganese Oxide," *Electrochem. Solid-State Lett.*, vol. 2, no. 2, pp. 58–59, 1999, doi: 10.1149/1.1390733.

[204] P. Schichtel, M. Geiß, T. Leichtweiß, J. Sann, D. A. Weber, and J. Janek, "On the impedance and phase transition of thin film all-solid-state batteries based on the Li4Ti5O12 system," *J. Power Sources*, vol. 360, pp. 593–604, 2017, doi: 10.1016/j.jpowsour.2017.06.044.

[205] S. W. Song, H. Choi, H. Y. Park, G. B. Park, K. C. Lee, and H. J. Lee, "High rate-induced structural changes in thin-film lithium batteries on flexible substrate," *J. Power Sources*, vol. 195, no. 24, pp. 8275–8279, 2010, doi: 10.1016/j.jpowsour.2010.06.113.

[206] B. Fleutot *et al.*, "Characterization of all-solid-state Li/LiPONB/TiOS microbatteries produced at the pilot scale," *J. Power Sources*, vol. 196, no. 23, pp. 10289–10296, 2011, doi: 10.1016/j.jpowsour.2011.07.018.

[207] Y. Yoon, C. Park, J. Kim, and D. Shin, "The mixed former effect in lithium borophosphate oxynitride thin film electrolytes for all-solid-state micro-batteries," *Electrochim. Acta*, vol. 111, pp. 144–151, 2013, doi: 10.1016/j.electacta.2013.08.053.

[208] S. J. Lee, H. K. Baik, and S. M. Lee, "An all-solid-state thin film battery using LISIPON electrolyte and Si-V negative electrode films," *Electrochem. commun.*, vol. 5, no. 1, pp. 32–35, 2003, doi: 10.1016/S1388-2481(02)00528-3.

[209] H. Ohtsuka and Y. Sakurai, "Characteristics of Li/MoO3-x thin film batteries," *Solid State Ionics*, vol. 144, no. 1–2, pp. 59–64, 2001, doi: 10.1016/S0167-2738(01)00889-X.

[210] P. S. Maydannik, T. O. Kaariainen, and D. C. Cameron, "Continuous atomic layer deposition: Explanation for anomalous growth rate effects," *J. Vac. Sci. Technol. A Vacuum, Surfaces, Film.*, vol. 30, no. 1, p. 01A122, 2012, doi: 10.1116/1.3662861.

[211] K. Lahtinen, P. Maydannik, P. Johansson, T. Kääriäinen, D. C. Cameron, and J. Kuusipalo, "Utilisation of continuous atomic layer deposition process for barrier enhancement of extrusion-coated paper," *Surf. Coatings Technol.*, vol. 205, no. 15, pp. 3916–3922, 2011, doi: 10.1016/j.surfcoat.2011.02.009.

[212] J. Liu, H. Zhu, and M. H. A. Shiraz, "Toward 3D Solid-State Batteries via Atomic Layer Deposition Approach," *Front. Energy Res.*, vol. 6, no. March, pp. 1–5, 2018, doi: 10.3389/fenrg.2018.00010.

[213] M. Nisula, Y. Shindo, H. Koga, and M. Karppinen, "Atomic Layer Deposition of Lithium Phosphorus Oxynitride," *Chem. Mater.*, vol. 27, no. 20, pp. 6987–6993, 2015, doi: 10.1021/acs.chemmater.5b02199.

[214] B. Put *et al.*, "Plasma-Assisted ALD of LiPO(N) for Solid State Batteries," *J. Electrochem. Soc.*, vol. 166, no. 6, pp. A1239–A1242, 2019, doi: 10.1149/2.1191906jes.

[215] S. Shibata, "Thermal Atomic Layer Deposition of Lithium Phosphorus Oxynitride as a Thin-Film Solid Electrolyte," *J. Electrochem. Soc.*, vol. 163, no. 13, pp. A2555–A2562, 2016, doi: 10.1149/2.0371613jes.

[216] T. Fujibayashi, Y. Kubota, K. Iwabuchi, and N. Yoshii, "Highly conformal and high-ionic conductivity thin-film electrolyte for 3D-structured micro batteries: Characterization of LiPON film deposited by MOCVD method," *AIP Adv.*, vol. 7, no. 8, 2017, doi: 10.1063/1.4999915.

[217] B. Wang, J. Liu, Q. Sun, R. Li, T. K. Sham, and X. Sun, "Atomic layer deposition of lithium phosphates as solid-state electrolytes for all-solid-state microbatteries," *Nanotechnology*, vol. 25, no. 50, 2014, doi: 10.1088/0957-4484/25/50/504007.

[218] M. Létiche *et al.*, "Atomic Layer Deposition of Functional Layers for on Chip 3D Li-Ion All Solid State Microbattery," *Adv. Energy Mater.*, vol. 7, no. 2, pp. 1–12, 2017, doi: 10.1002/aenm.201601402.

[219] E. Kazyak *et al.*, "Atomic Layer Deposition of the Solid Electrolyte Garnet Li7La3Zr2O12," *Chem. Mater.*, vol. 29, no. 8, pp. 3785–3792, 2017, doi: 10.1021/acs.chemmater.7b00944.

[220] Y. Hu, A. Ruud, V. Miikkulainen, T. Norby, O. Nilsen, and H. Fjellvåg, "Electrical characterization of amorphous LiAlO2 thin films deposited by atomic layer deposition," *RSC Adv.*, vol. 6, no. 65, pp. 60479–60486, 2016, doi: 10.1039/c6ra03137d.

[221] J. S. Park *et al.*, "Ultrathin lithium-ion conducting coatings for increased interfacial stability in high voltage lithium-ion batteries," *Chem. Mater.*, vol. 26, no. 10, pp. 3128–3134, 2014, doi: 10.1021/cm500512n.

[222] B. Wang *et al.*, "Atomic Layer Deposited Lithium Silicates as Solid-State Electrolytes for All-Solid-State Batteries," *ACS Appl. Mater. Interfaces*, vol. 9, no. 37, pp. 31786–31793, 2017, doi: 10.1021/acsami.7b07113.

[223] Y. C. Perng *et al.*, "Synthesis of ion conducting LixAlySizO thin films by atomic layer deposition," *J. Mater. Chem. A*, vol. 2, no. 25, pp. 9566–9573, 2014, doi: 10.1039/c3ta14928e.

[224] B. Wang *et al.*, "Atomic Layer Deposition of Lithium Niobium Oxides as Potential Solid-State Electrolytes for Lithium-Ion Batteries," *ACS Appl. Mater. Interfaces*, vol. 10, no. 2, pp. 1654–1661, 2018, doi: 10.1021/acsami.7b13467.

[225] N. Hornsveld, B. Put, W. M. M. Kessels, P. M. Vereecken, and M. Creatore, "Plasma-assisted and thermal atomic layer deposition of electrochemically active Li2CO3," *RSC Adv.*, vol. 7, no. 66, pp. 41359–41368, 2017, doi: 10.1039/c7ra07722j.

[226] L. Chen *et al.*, "Novel ALD Chemistry Enabled Low-Temperature Synthesis of Lithium Fluoride Coatings for Durable Lithium Anodes," *ACS Appl. Mater. Interfaces*, vol. 10, no. 32, pp. 26972–26981, 2018, doi: 10.1021/acsami.8b04573.

[227] J. Xie *et al.*, "Atomic Layer Deposition of Stable LiAlF4 Lithium Ion Conductive Interfacial Layer for Stable Cathode Cycling," *ACS Nano*, vol. 11, no. 7, pp. 7019–7027, 2017, doi: 10.1021/acsnano.7b02561.

[228] Y. Cao, X. Meng, and J. W. Elam, "Atomic Layer Deposition of LixAlyS Solid-State Electrolytes for Stabilizing Lithium-Metal Anodes," *ChemElectroChem*, vol. 3, no. 6, pp. 858–863, 2016, doi: 10.1002/celc.201600139.

[229] M. Shoji, H. Munakata, and K. Kanamura, "Fabrication of all-solid-state lithium-ion cells

using three-dimensionally structured solid electrolyte Li 7 La 3 Zr 2 O 12 pellets," *Front. Energy Res.*, vol. 4, no. AUG, pp. 1–7, 2016, doi: 10.3389/fenrg.2016.00032.

[230] E. Cohen *et al.*, "Novel rechargeable 3D-Microbatteries on 3D-printed-polymer substrates: Feasibility study," *Electrochim. Acta*, vol. 265, no. 2018, pp. 690–701, 2018, doi: 10.1016/j.electacta.2018.01.197.

[231] K. K. Gleason, *Overview of Chemically Vapor Deposited (CVD) Polymers*, vol. 1, no. Cvd. 2015.

[232] S. Baxamusa, "Conformal Polymer CVD," 2015, pp. 87–109.

[233] K. K. Gleason, "Nanoscale control by chemically vapour-deposited polymers," *Nat. Rev. Phys.*, vol. 2, no. 7, pp. 347–364, 2020, doi: 10.1038/s42254-020-0192-6.

[234] Y. Mao, "Copolymerization and Crosslinking," *CVD Polym. Fabr. Org. Surfaces Devices*, pp. 45–63, 2015, doi: 10.1002/9783527690275.ch3.

[235] K. K. S. Lau and K. K. Gleason, "Initiated Chemical Vapor Deposition (iCVD) of poly(alkyl acrylates): A kinetic model," *Macromolecules*, vol. 39, no. 10, pp. 3695–3703, 2006, doi: 10.1021/ma0601621.

[236] G. Odian, *Principles of Polymerization*, 4th ed. Hoboken: John Wiley & Sons, Ltd, 2004.

[237] K. Chan and K. K. Gleason, "Initiated chemical vapor deposition of linear and cross-linked poly(2-hydroxyethyl methacrylate) for use as thin-film hydrogels," *Langmuir*, vol. 21, no. 19, pp. 8930–8939, 2005, doi: 10.1021/la051004q.

[238] J. L. Yague and K. K. Gleason, "Systematic control of mesh size in hydrogels by initiated chemical vapor deposition," *Soft Matter*, vol. 8, p. 2890, 2012, doi: 10.1039/c2sm07137a.

[239] D. R. MacFarlane, F. Zhou, and M. Forsyth, "Ion conductivity in amorphous polymer/ salt mixtures," *Solid State Ionics*, vol. 113, no. 115, pp. 193–197, 1998.

[240] M. Forsyth, D. R. MacFarlane, and A. J. Hill, "Glass transition and free volume behaviour of poly(acrylonitrile)/LiCF3so3 polymer-in-salt electrolytes compared to poly(ether urethane)/LiClO4 solid polymer electrolytes," *Electrochim. Acta*, vol. 45, no. 8–9, pp. 1243–1247, 2000, doi: 10.1016/S0013-4686(99)00387-4.

[241] P. C. Hiemenz and T. P. Lodge, *Polymer Chemistry*, Second. Boca Raton: CRC Press, 2007.

[242] R. Birney, F. Placido, J. Kavanagh, S. Lapp, and D. Wojcieszak, *OPTICAL AND PHYSICAL STUDIES OF DLC NANOFILMS*. 2010.

[243] R. Bhandavat and G. Singh, "Stable and efficient li-ion battery anodes prepared from polymer-derived silicon oxycarbide-carbon nanotube shell/core composites," *J. Phys. Chem. C*, vol. 117, no. 23, pp. 11899–11905, 2013, doi: 10.1021/jp310733b.

[244] W. Zhang, S. B. Son, H. Guthrey, and C. Ban, "Mitigation of rapid capacity decay in silicon-LiNi0.6Mn0.2Co0.2O2 full batteries," *Energy Storage Mater.*, vol. 49, pp. 111–121, 2022, doi: 10.1016/j.ensm.2022.03.025.

[245] R. S. Young, H. Yu, and M. N. Obrovac, "Enhancing NMC/silicon alloy full cell cycling by adding water to the electrolyte," *J. Appl. Electrochem.*, vol. 51, no. 10, pp. 1501–1507, 2021, doi: 10.1007/s10800-021-01594-6.

[246] R. C. Lee, J. Franklin, C. Tian, D. Nordlund, M. Doeff, and R. Kostecki, "The origin of impedance rise in Ni-Rich positive electrodes for lithium-ion batteries," *J. Power Sources*, vol. 498, no. March, p. 229885, 2021, doi: 10.1016/j.jpowsour.2021.229885.

[247] H. Liu, A. J. Naylor, A. S. Menon, W. R. Brant, K. Edström, and R. Younesi, "Understanding the Roles of Tris(trimethylsilyl) Phosphite (TMSPi) in LiNi0.8Mn0.1Co0.1O2 (NMC811)/Silicon–Graphite (Si–Gr) Lithium-Ion Batteries," *Adv. Mater. Interfaces*, vol. 7, no. 15, 2020, doi: 10.1002/admi.202000277.

[248] P. Biswal, S. Stalin, A. Kludze, S. Choudhury, and L. A. Archer, “Nucleation and Early Stage Growth of Li Electrodeposits,” *Nano Lett.*, vol. 19, no. 11, pp. 8191–8200, 2019, doi: 10.1021/acs.nanolett.9b03548.

[249] J. Choi, L. Dong, C. Y. Yu, C. O’Meara, E. Lee, and J. H. Kim, “Relationship of Chemical Composition and Moisture Sensitivity in LiNixMnyCo1−X−YO2 for Lithium-Ion Batteries,” *J. Electrochem. Energy Convers. Storage*, vol. 18, no. 4, 2021, doi: 10.1115/1.4051208.

[250] M. J. Herzog, N. Gauquelin, D. Esken, J. Verbeeck, and J. Janek, “Increased Performance Improvement of Lithium-Ion Batteries by Dry Powder Coating of High-Nickel NMC with Nanostructured Fumed Ternary Lithium Metal Oxides,” *ACS Appl. Energy Mater.*, vol. 4, no. 9, pp. 8832–8848, 2021, doi: 10.1021/acsaem.1c00939.

[251] “1D Isothermal Lithium-Ion Battery Tutorial,” COMSOL Multiphysics, 2012, pp. 1–32.

[252] “Tesla’s 4680-Type Battery Cell Teardown: Specs Revealed.” https://insideevs.com/news/598656/tesla-4680-battery-cell-specs/.

[253] *Battery Design Module User’s Guide*. COMSOL Multiphysics, 2022.

[254] M. Park, X. Zhang, M. Chung, G. B. Less, and A. M. Sastry, “A review of conduction phenomena in Li-ion batteries,” *J. Power Sources*, vol. 195, no. 24, pp. 7904–7929, 2010, doi: 10.1016/j.jpowsour.2010.06.060.

[255] D. T. Hallinan and N. P. Balsara, “Polymer Electrolytes,” *Annu. Rev. Mater. Res.*, vol. 43, no. 1, pp. 503–525, 2013, doi: 10.1146/annurev-matsci-071312-121705.

[256] T. Swamy and Y.-M. Chiang, “Electrochemical Charge Transfer Reaction Kinetics at the Silicon-Liquid Electrolyte Interface,” *J. Electrochem. Soc.*, vol. 162, no. 13, pp. A7129–A7134, 2015, doi: 10.1149/2.0181513jes.

[257] M. Ashuri, Q. He, and L. L. Shaw, “Silicon as a potential anode material for Li-ion batteries: Where size, geometry and structure matter,” *Nanoscale*, vol. 8, no. 1, pp. 74–103, 2016, doi: 10.1039/c5nr05116a.

[258] D. Pantea, H. Darmstadt, S. Kaliaguine, L. Sümmchen, and C. Roy, “Electrical conductivity of thermal carbon blacks: Influence of surface chemistry,” *Carbon N. Y.*, vol. 39, no. 8, pp. 1147–1158, 2001, doi: 10.1016/S0008-6223(00)00239-6.

[259] M. Mastali, M. Farkhondeh, S. Farhad, R. A. Fraser, and M. Fowler, “ Electrochemical Modeling of Commercial LiFePO 4 and Graphite Electrodes: Kinetic and Transport Properties and Their Temperature Dependence ,” *J. Electrochem. Soc.*, vol. 163, no. 13, pp. A2803–A2816, 2016, doi: 10.1149/2.1151613jes.

[260] B. Tjaden, S. J. Cooper, D. J. Brett, D. Kramer, and P. R. Shearing, “On the origin and application of the Bruggeman correlation for analysing transport phenomena in electrochemical systems,” *Curr. Opin. Chem. Eng.*, vol. 12, pp. 44–51, 2016, doi: 10.1016/j.coche.2016.02.006.

[261] M. Doyle, “Comparison of Modeling Predictions with Experimental Data from Plastic Lithium Ion Cells,” *J. Electrochem. Soc.*, vol. 143, no. 6, p. 1890, 1996, doi: 10.1149/1.1836921.

[262] E. S. Polsen, D. Q. McNerny, B. Viswanath, S. W. Pattinson, and A. John Hart, “High-speed roll-to-roll manufacturing of graphene using a concentric tube CVD reactor,” *Sci. Rep.*, vol. 5, pp. 0–12, 2015, doi: 10.1038/srep10257.

[263] N. J. Fritz *et al.*, “Chemical Analysis of High Energy Density Electrodeposited Silicon Anodes for Lithium-Ion Batteries,” *ECS Meet. Abstr.*, vol. MA2022-01, no. 22, p. 1121, 2022, doi: 10.1149/MA2022-01221121mtgabs.

[264] J. Liu *et al.*, “Rational Design of Atomic-Layer-Deposited LiFePO4 as a High-Performance Cathode for Lithium-Ion Batteries,” *Adv. Mater.*, vol. 26, no. 37, pp. 6472–6477, 2014, doi: 10.1002/adma.201401805.

[265] R. K. Bose, S. Nejati, D. R. Stufflet, and K. K. S. Lau, “Graft polymerization of anti-fouling PEO surfaces by liquid-free initiated chemical vapor deposition,” *Macromolecules*, vol. 45, no. 17, pp. 6915–6922, 2012, doi: 10.1021/ma301234z.

[266] T. J. Adam *et al.*, “Multifunctional composites for future energy storage in aerospace structures,” *Energies*, vol. 11, no. 2, 2018, doi: 10.3390/en11020335.

[267] L. E. Asp and E. S. Greenhalgh, “Structural power composites,” *Compos. Sci. Technol.*, vol. 101, pp. 41–61, 2014, doi: https://doi.org/10.1016/j.compscitech.2014.06.020.